Thesis for the degree of Doctor of Philosophy

Soundings of the ionospheric HF radio link between Antarctica and Spain

Ahmed Gamal Ads

Enginyeria i Arquitectura La Salle
Electronics and Telecommunications Department

Barcelona, October 2013

Soundings of the ionospheric HF radio link between Antarctica and Spain

Ahmed Gamal Ads
Research Group in Electromagnetism and Communications (GRECO)
Enginyeria i Arquitectura La Salle
Universitat Ramon Llull
Quatre Camins, 30
08022 Barcelona, Spain
E-mail: aads@salle.url.edu

Advisor:
Joan Ramon Regué Enginyeria i Arquitectura La Salle, Universitat Ramon Llull, Barcelona, Spain.

This work has been funded with grant number BES-2008-00948 by the FPI Scholarship from the ministry of Education and Science in the Spanish Government.

This thesis has been prepared using LaTeX.

Abstract

The HF electromagnetic waves with a frequency range from 2 MHz to 30 MHz can be reflected by means of the ionospheric layers for distances beyond 100 km. Even in some cases, they can reach the other side of the Earth. Along with the utilization of satellite communications, the ionosphere reserved its importance of being a very attractive transmission medium. The cost of the HF ionospheric transceiver is a way less expensive than using a satellite link. Also, it can be used for military and surveillances purposes overseas and in unapproachable lands.

However, the main drawback of the HF ionospheric communications is that the characteristics of the transmission medium depend largely on parameters that are varying over time, such as the Smoother Sunspot Number (SSN), Solar Flux, hour of the day, season, etc.

The Department of Electronics and Telecommunications at La Salle, Ramon Llull University has been cooperated with the Ebro Observatory in a scientific project called the Antarctica project. The main objective of this project is to connect the Spanish Antarctic Station Juan Carlos I (SAS) in Livingston, Antarctica and the Ebro Observatory (OE) in Roquetes, Spain. That SAS-OE link has a length of 12700 km and it aimed to transmit measurements collected from geomagnetic and geophysics sensors located at the SAS towards the OE.

The research work done in this thesis is part of this project. First, design and implementation of the transmission platform called POTASIO using the *Software Defined Radio* (SDR) technique to perform the Oblique Incidence Sounding (OIS) of the SAS-OE ionospheric link is reviewed. All the updates that have taken place to the previous SDR platform (SODIO) are explained, including the components that raised the accuracy of both frequency and time synchronization between transmitter and receiver. The availability and the Frequency of Largest Availability (FLA) of the SAS-OE link has been obtained from the narrowband sounding technique throughout three consecutive surveys from 2009 to 2012. Besides that, wideband sounding of the SAS-OE link has taken place to estimate the wideband Signal to Noise Ratio (SNR), the time dispersion (*composite multipath spread*), frequency dispersion (*composite Doppler spread* and *Doppler frequency shift*), and the propagation time.

Second, analyze the SAS-OE link availability, FLA, and the predicted Maximum Usable Frequency from the Rec533 model (MUFRec533) over the three surveys. Consequently, there has been an investigation of the day-to-day and inter-day variations of various parameters (e.g., Total Electron Density (TEC), critical frequency of the F2 layer (foF2), and F2 layer Maximum Usable Frequency for ground distance MUF(3000)) that have been measured at four Vertical Incidence Sounding (VIS) stations located over the SAS-OE link path throughout three consecutive surveys (2009/2010, 2010/2011, and 2011/2012).

Finally, the correlation between the FLA of the SAS-OE ionospheric link and the MUF(3000) obtained from VIS stations located close to the reflection points of the same link has been studied. Therefore, the minimum propagated frequencies for the oblique SAS-OE link have been determined throughout the three survey.

Keywords: Ionosphere, HF, communications, Oblique Incidence Sounding, Vertical Incidence Sounding, Ionospheric Channel Characterization.

Acknowledgements

My PhD is almost over but I can not finish it without looking back and thanking all the people that in one way or the other helped me to make it possible. It is not difficult to imagine that I would like to start by giving my deepest special thanks to Eman. For her infinite support, for being always there no matter how far I am and how long it takes me to come back, but specially for sharing all my dreams.

Special thanks to my parents who always trusted me and encouraged me to go on. You know there are no words to thank you all you have done for me during the last 27 years.

To my advisors Joan Lluís Pijoan, Joan Ramon Regué, and Marc Deumal for believing in me and for pushing me to go further and further. Thanks also for giving me always the freedom to draw new paths in our research activities.

I am also very thankful to Juraj Gazda and Peter Drotár from the Technical University of Košice, Slovakia and Kaarti Salvan from the VIT, India for our joint cooperation.

To all my colleagues from the Department of Telecommunications and Electronics, La Salle, Ramon Llull University, specially, Pau Bergadá. And, thanks also to David Altadill from Ebro Observatory.

My deepest thanks to my new family in Barcelona: Ahmed Helmi, Ahmed shokry, Ashraf Abdelfattah, and Eslam El Malkawy.

This work has been funded by the Spanish Government under the projects CGL2006-12437-C02-01, CTM2008-03536-E, CTM2009-13843-C02-02 and CTM2010-21312-C03-03. The author has an FPI grant of BES-2008-00948 from the Spanish Government.

Dedicated to Eman, Asia, Moaaz, and my family...

Contents

Abstract iv

Acknowledgements vi

List of Figures xiii

List of Tables xix

Abbreviations xxi

Preface iii

I Introduction 3

1 The Ionosphere 5
1.1 Introduction . . . 5
1.2 The Sun . . . 6
1.2.1 Smother sunspot number . . . 7
1.2.2 Disturbance Storm Time (Dst) index . . . 8
1.2.3 A- and K-index . . . 9
1.2.4 Solar Flux . . . 10
1.3 The structure of the ionosphere . . . 10
1.3.1 D Layer . . . 11
1.3.2 E Layer . . . 12
1.3.3 F Layer . . . 12
1.4 Solar disturbances and their effects on the ionosphere . . . 13
1.5 Ionospheric propagation . . . 15

2 HF ionospheric communications 23
2.1 Introduction . . . 23
2.2 Ionospheric channel characterizations . . . 24
2.2.1 Channel availability . . . 25

2.2.2 Frequency dispersion . . . 25
2.2.3 Time dispersion . . . 26
2.2.4 Noise . . . 27
2.2.5 Interference . . . 28
2.3 Ionospheric channel study . . . 28
2.3.1 Modeling . . . 29
2.3.1.1 Channel modeling . . . 29
2.3.1.2 Physical modeling . . . 30
2.3.2 Prediction . . . 31
2.3.3 Sounding . . . 32
2.3.3.1 Vertical Incidence Sounding . . . 33
2.3.3.2 Oblique Incidence Sounding . . . 35
2.3.4 Simulation . . . 36
2.3.5 Noise and interference . . . 37
2.4 HF ionospheric modems . . . 38
2.4.1 Automatic Link Establishment . . . 41
2.5 Applications . . . 42

3 An OIS system between Antarctica and Spain 47
3.1 Introduction . . . 47
3.2 *Software defined radio* . . . 49
3.3 SAS-OE ionospheric link . . . 50
3.4 The POTASIO platform . . . 53
3.4.1 Introduction . . . 53
3.4.2 *XTremeDSP-IV* development board . . . 59
3.4.3 The *Cyanide* board . . . 60
3.4.4 *Hardware* description of the transmitter . . . 62
3.4.5 *Hardware* description of the receiver . . . 66

II Contributions 71

4 Oblique sounding of the ionospheric HF radio link 73
4.1 Introduction . . . 73
4.2 Link description . . . 75
4.3 Wideband theoretical basics . . . 78
4.3.1 Characterizations of wideband channel . . . 80
4.3.2 Wideband sounding techniques . . . 84
4.3.2.1 Pulse compression techniques . . . 84
4.3.2.2 Periodic pulses sounding technique . . . 88
4.4 Structure of the channel sounding . . . 88
4.5 Analysis algorithms of channel sounding . . . 89
4.5.1 Algorithms of the narrowband sounding . . . 90
4.5.1.1 First algorithm . . . 92
4.5.1.2 Second algorithm . . . 92

4.5.1.3 Third algorithm . . . 93
4.5.1.4 Fourth algorithm . . . 93
4.5.1.5 Windowing algorithm . . . 93
4.5.1.6 Time framing algorithm . . . 97
4.5.2 Algorithms of the wideband sounding . . . 100
4.6 Results . . . 114
4.6.1 Narrowband sounding . . . 115
4.6.2 Wideband sounding . . . 119
4.6.2.1 Wideband SNR estimation . . . 119
4.6.2.2 *Composite multipath spread* . . . 122
4.6.2.3 *Composite Doppler spread* . . . 127
4.6.3 Propagation Time . . . 131
4.6.4 *Doppler frequency shift* . . . 133
4.7 Concluding remarks . . . 134

5 Vertical and Oblique soundings variation **141**
5.1 Introduction . . . 141
5.2 Oblique incidence sounding . . . 144
5.3 Vertical incidence sounding . . . 145
5.4 Solar activity . . . 148
5.5 Oblique incidence sounding, data, and results . . . 150
5.5.1 2009/2010 survey . . . 151
5.5.2 2010/2011 survey . . . 152
5.5.3 2011/2012 survey . . . 154
5.6 Vertical incidence sounding, data, and results . . . 157
5.6.1 Day-to-day variation . . . 157
5.6.1.1 foF2 day-to-day results . . . 157
5.6.1.2 MUF(3000) day-to-day results . . . 163
5.6.2 Inter-day variation . . . 168
5.6.2.1 TEC inter-day variation results . . . 168
5.6.2.2 foF2 inter-day variation results . . . 174
5.6.2.3 MUF(3000) inter-day variation results . . . 178
5.7 VIS and OIS parameters comparison . . . 182
5.8 Concluding remarks . . . 186

6 Conclusions and future lines **191**

Bibliography **197**

List of Figures

1.1 SSN values and the average from 1995 to 2012. 8
1.2 The digram of the *Ray theory* concept. 17
1.3 A simple digram of the *Snell's law*. 18
1.4 Sample of ionogram obtained in the Ebro Observatory, Roquetes, Spain at 07 of September 2012, 15:55 UTC 20

2.1 Sample of an ionogram obtained in the OE, Roquetes, Spain at 07 of September 2012, 15:55 UTC 34
2.2 A simple HF communications channel model. 39

3.1 Classification of technologies according to the efficiency and versatility. 55
3.2 Functional block diagram of the digital devices in the transmitter. . . . 56
3.3 A map shows the location of SAS (*Base Juan Carlos I*) in Livingston Island. 57
3.4 Approximate location of the transmitting antenna at the *Pico Radio*. . 58
3.5 The installations of yagi and monopole antennas at OE during 2009/2010. 58
3.6 The development board *XTremeDSP-IV*. 59
3.7 The implementation block of the *XTremeDSP-IV* development board. . 61
3.8 The *Cyanide* board. 61
3.9 Front view of the waterproof sealed box. 63
3.10 Rear view of the waterproof sealed box. 64
3.11 The antenna adapter with monopole antenna at the transmission side. . 64
3.12 A simplified block diagram of the transmitter. 65
3.13 A diagram of the wireless network installed at SAS. 66
3.14 The cabinet where the receiver placed. 67
3.15 A simplified block diagram of the receiver. 67
3.16 The filtering and amplification unit at the closet of the receiver. 68
3.17 Filtering and amplification block of the receiver. 68

4.1 The location of the receiver at OE, Spain. 75
4.2 The location of the transmitter at the SAS, Antarctica. 76
4.3 The locations of the transmitter, receiver, and the approximation path of the link. 77
4.4 The sunrise times at the four reflection hops. 78
4.5 The sunset times at the four reflection hops. 78
4.6 The sounding organization. 90

4.7 Narrowband signal filtered with the ideal rectangular window function with a carrier frequency of 15.5 MHz at 10:00 UTC. 95
4.8 Highly interfered narrowband signal filtered with the ideal rectangular window function with a carrier frequency of 20 MHz at 17:00 UTC. . . 95
4.9 The time response of the four window functions (*Blackman*, *Hanning*, *Flattop*, and *Kaiser*). 96
4.10 4 seconds of 20 MHz narrowband signal at 17:00 UTC shows the difference between the four window functions. 97
4.11 Narrowband signal filtered with the four different window functions with a carrier frequency of 15.5 MHz at 10:00 UTC. 98
4.12 Narrowband signal filtered with the ideal and *Kaiser* window functions with a carrier frequency of 15.5 MHz at 10:00 UTC. 98
4.13 Ideal window compared with the other four window filters on a highly interfered narrowband signal with a carrier frequency of 20 MHz at 17:00 UTC. 99
4.14 Ideal window compared with the *Kaiser* window on a highly interfered narrowband signal with a carrier frequency of 20 MHz at 17:00 UTC. . 99
4.15 Ideal window compared with the other four window filters on a noisy narrowband signal with a carrier frequency of 3 MHz at 00:00 UTC. . . 101
4.16 A block diagram of the analysis algorithms of the wideband received signal. 102
4.17 A correlated version of the received sounding signal (10 seconds long). . 103
4.18 A correlated version of the received sounding signal (clipped to 2 seconds long). 104
4.19 An example of the channel matrix in 3D view. 104
4.20 An example of the channel matrix in 2D view. 105
4.21 A 3D representation of the *scattering function* of a received sounding signal. 106
4.22 A 2D representation of the *scattering function* of a received sounding signal. 106
4.23 Sounding signal of 18.5 MHz at 11:00 UTC. A correlation of 10 seconds and 2 seconds of the received signal with the original sequence depicted at the top right and left frames respectively. At the middle right and left frame, channel impulse response in 3D and top-view. *Scattering function* in 3D and top-view are depicted at the bottom right and left frames respectively. 107
4.24 Sounding signal of 16 MHz at 17:00 UTC. A correlation of 10 seconds and 2 seconds of the received signal with the original sequence depicted at the top right and left frames respectively. At the middle right and left frame, channel impulse response in 3D and top-view. *Scattering function* in 3D and top-view are depicted at the bottom right and left frames respectively. 108
4.25 The *power delay profile* of a received sounding signal. 111
4.26 An example of the corresponding integral function (*power delay profile*). 112
4.27 The *Doppler power profile* of a received sounding signal. 112

4.28 An example of the corresponding integral function (*Doppler power profile*). 113
4.29 An example of the *scattering function*. 113
4.30 SNR estimation of the narrowband ionospheric channel as a function of hour and frequency of sounding. 116
4.31 The channel availability measured over 2009/2010, as a percentage of the time frames that exceeded 6 dB. 116
4.32 The channel availability during 2009/2010, where 70% of the time frames have SNR higher than 3 dB and 50% higher than 6 dB. 118
4.33 Wideband SNR values estimated during 2009/2010, as a function of the hour and the frequency of sounding. 121
4.34 The *composite multipath spread* measurements as a function of the sounding frequency and hour from 00:00 to 11:00 UTC. 125
4.35 The *composite multipath spread* measurements as a function of the sounding frequency and hour from 12:00 to 23:00 UTC. 126
4.36 The *composite Doppler spread* measurements as a function of the sounding frequency and hour from 00:00 to 11:00 UTC. 128
4.37 The *composite Doppler spread* measurements as a function of the sounding frequency and hour from 12:00 to 23:00 UTC. 129
4.38 *Scattering functions* and their corresponding time *delay* and *Doppler* frequency for different sounding frequencies and times. 130
4.39 A correlated version of the received sounding signal (clipped to 2 seconds long). 132
4.40 Average propagation time as a function of sounding frequencies. 132
4.41 Average *Doppler frequency shift* during the 24 hours. 133

5.1 The SAS-OE ionospheric link path and the approximate locations of the VIS stations and reflection hops. 143
5.2 An ionogram obtained from the VIS system in OE, Roquetes, Spain at 16 of May 2013, 11:10 UTC 146
5.3 SSN values and the average during the period from 1995 to 2012. . . . 148
5.4 The sunrise times at four reflection hops of the SAS-OE link and four VIS stations located along the link path. 149
5.5 The sunset times at four reflection hops of the SAS-OE link and four VIS stations located along the link path. 150
5.6 Comparison between the inter-day variation of the FLA, MUFRec533, and the channel availability of the SAS-OE link during the 2009/2010 survey. 152
5.7 Comparison between the inter-day variation of the FLA, MUF Rec 533, and the channel availability of the SAS-OE link throughout the 2010/2011 survey. 153
5.8 Comparison between the inter-day variation of the FLA, MUFRec533, and the channel availability over the 2011/2012 survey. 155
5.9 The FLA inter-day variation during the 2009/2010, 2010/2011, and 2011/2012 surveys. 156

5.10 The day-to-day variation of the foF2 during two weeks of January 2010 (2009/2010 survey) at the four VIS stations (PSJ5J, AS00Q, EA036, and EB040). 158
5.11 The day-to-day variation of foF2 throughout two weeks of January 2011 (2010/2011 survey) at the four VIS stations (PSJ5J, AS00Q, EA036, and EB040). 159
5.12 The day-to-day variation of foF2 during two weeks of January 2012 (2011/2012 survey) at the four VIS stations (PSJ5J, AS00Q, EA036, and EB040). 160
5.13 The day-to-day variation of foF2 during three surveys at Port Stanley station. 160
5.14 The day-to-day variation of foF2 over three surveys at Ascension station. 161
5.15 The day-to-day variation of foF2 throughout three surveys at El Arenosillo station. 161
5.16 The day-to-day variation of foF2 during three surveys at OE station. . 162
5.17 The day-to-day variation of MUF(3000) during two weeks of January 2010 (2009/2010 survey) at the four VIS stations (PSJ5J, AS00Q, EA036, and EB040). 163
5.18 The day-to-day variation of MUF(3000) throughout two weeks of January 2011 (2010/2011 survey) at the four VIS stations (PSJ5J, AS00Q, EA036, and EB040). 164
5.19 The day-to-day variation of MUF(3000) during two weeks of January 2012 (2011/2012 survey) at the four VIS stations (PSJ5J, AS00Q, EA036, and EB040). 165
5.20 The day-to-day variation of MUF(3000) throughout three surveys at Port Stanley station. 165
5.21 The day-to-day variation of MUF(3000) over three surveys at Ascension station. 166
5.22 The day-to-day variation of MUF(3000) during three surveys at El Arenosillo station. 166
5.23 The day-to-day variation of MUF(3000) during three surveys at OE station. 167
5.24 Inter-day variation of the TEC at Port Stanley station during 2009/2010, 2010/2011, and 2011/2012. 170
5.25 Inter-day variation of the TEC at Ascension station throughout 2009/2010, 2010/2011, and 2011/2012. 171
5.26 Inter-day variation of the TEC at El Arenosillo station during 2009/2010, 2010/2011, and 2011/2012. 172
5.27 Inter-day variation of the TEC at the OE station throughout 2009/2010, 2010/2011, and 2011/2012. 173
5.28 Inter-day variation of the foF2 at Port Stanley station during 2009/2010, 2010/2011, and 2011/2012. 174
5.29 Inter-day variation of the foF2 at the Ascension station over 2009/2010, 2010/2011, and 2011/2012. 175
5.30 Inter-day variation of the foF2 at El Arenosillo station throughout 2009/2010, 2010/2011, and 2011/2012. 176

5.31 Inter-day variation of the foF2 at the OE station during 2009/2010, 2010/2011, and 2011/2012. 177
5.32 Inter-day variation of the MUF(3000) at the Port Stanley station during 2009/2010, 2010/2011, and 2011/2012. 178
5.33 Inter-day variation of the MUF(3000) for the Ascension over 2009/2010, 2010/2011, and 2011/2012. 179
5.34 Inter-day variation of the MUF(3000) at El Arenosillo station throughout 2009/2010, 2010/2011, and 2011/2012. 180
5.35 Inter-day variation of the MUF(3000) at the OE station during 2009/2010, 2010/2011, and 2011/2012. 181
5.36 A comparison between MUF(3000) inter-day variation of the VIS stations throughout the 2009/2010 survey, the FLA of the OIS system, and the minimum MUF(3000). 182
5.37 A comparison between MUF(3000) inter-day variation of the VIS stations during the 2010/2011 survey, the FLA of the OIS system, and the minimum MUF(3000). 184
5.38 A comparison between MUF(3000) inter-day variation of the VIS stations over the 2011/2012 survey, the FLA of the OIS system, and the minimum MUF(3000). 184
5.39 Comparison of the minimum inter-day variations of MUF(3000) throughout the 2009/2010, 2010/2011, and 2011/2012 surveys. 185

List of Tables

1.1 K- and A-index measurements and the corresponding geomagnetic condition. 9

4.1 The locations of the transmitter, receiver, and the four reflection hop. . 76
4.2 The configuration setup for the narrowband sounding during the 2009/2010 survey. 92
4.3 A brief comparison between the four window functions. 96
4.4 The configuration setup for the wideband sounding during 2009/2010 survey. 102
4.5 The dynamic range of the *multipath* and *Doppler* measurements (all values expressed in dB). 110
4.6 Maximum *composite multipath spread* values that exceeded 2.5 ms. . . 124
4.7 The degradation of the *composite multipath spread* values throughout the day. 124
4.8 Maximum *composite Doppler spread* values that exceeded 2 Hz. 127

5.1 The locations of the VIS stations and the reflection hops of the OIS link from the SAS to OE (SAS-OE). 143
5.2 The start, end, and number of operating days for each of the three surveys. 145
5.3 The frequency range where the channel was available during the three surveys summarized into 4 time segments of the daytime and nighttime regions. 156
5.4 Maximum foF2 values measured at the four VIS stations during three surveys. 162
5.5 Maximum MUF(3000) values recorded at the four VIS stations during three consecutive surveys. 167
5.6 Maximum foF2 and MUF(3000) values that measured at the four VIS stations during three surveys. 187

Abbreviations

SAS	Spanish Antarctic Station
OE	Ebro Observatory
FOT	Frequency of Optimum Traffic
EUV	Extreme Ultraviolet
SSN	Smoother Sunspot Number
Dst	Disturbance Storm Time
CME	Coronal Mass Ejection
PCA	Polar Cap Absorption
TID	Traveling Ionospheric Disturbance
SPE	Solar Proton Events
ALE	Automatic Link Establishment
SDR	Software Defined Radio
OIS	Oblique Incidence Sounding
VIS	Vertical Incidence Sounding
PLC	Power Line Communications
SNR	Signal to Noise Ration
TEC	Total Electron Density
PSK	Phase Shift Keying
QAM	Quadrature Amplitude Modulation
DoD	Department of Defense of the United Sates of America
MIL-STD	Military Standard
FED-STD	Federal Standard
ITS	Institute of Telecommunication Science
STANAG	Standard Agreement
NATO	North Atlantic Treaty Organization
ARQ	Automatic Re-Quest
MMHS	Military Message Handling System
HMTP	HF Mail Transfer Protocol

LQA	Link Quality Analysis
ARCS	Automatic Radio Control System
ACS	Automatic Channel Selection
ALM	Automatic Link Maintenance
HF-GCS	Global Communications System HF air/ground/air Network
SHARES	SHAred RESources
FNARS	FEMA National Radio System
COTHEN	Customs Over-the-Horizon Network
DRM	Digital Radio Mondiale
HAL	Hardware Abstraction Layer
INL	Integral NonLinearity
DSP	Digital Signal Processing
FPGA	Field Programmable Gate Arrays
CPLD	Complex programmable logic device
UTM	Unidad de Tecnología Marina
SANDICOM	Sounding System for Antarctic Digital Communications
ASIC	Application Specific Integrated Circuits
WLAN	Wireless Local Area Network
ZBT SRAM	Zero-Bus Turnaround Static Random-Access Memory
LED	Light-Emitting Diode
JTAG	Joint Test Action Group
PCI	Personal Computer Interface
TTL	TransistorTransistor Logic
CMOS	Complementary MetalOxideSemiconductor
GPS	Global Positioning System
PPS	Pulse Per Second
OCXO	Oven Controlled Crystal Oscillator
UTP	Unshielded Twisted Pair
TCP/IP	Transmission Control Protocol/Internet Protocol
LNA	Low Noise Amplifier
AGC	Automatic gain control
GRECO	Research Group in Electromagnetism and Communications
ISI	Intersymbol Interference
FFT	Fast Fourier Transform
IFFT	Inverse Fast Fourier Transform
WSS	Wide Sense Stationary

WSSUS	Wide Sense Stationary Uncorrelated Scattering
SAW	Surface Acoustic Wave
VGA	Variable Gain Amplifier
DDC	Digital Down Converter
MDR	Maximum Dynamic Range
VOACAP	Voice of America Coverage Analysis Program
FLA	Frequency of Largest Availability
WIOBSS	Wuhan Ionospheric Oblique Backscattering Sounding System
MRF	Maximum Received Frequency
PSJ5J	Port Stanley
AS00Q	scension Island
EA036	El Arenosillo
UMLCAR	Center for Atmospheric Research at the University of Massachusetts Lowell
AIS	Advanced Ionospheric Sounder
INGV	Istituto Nazionale di Geofisica e Vulcanologia
DPS	Digital Portable Sounder
UV	Ultraviolet
SFU	Solar Flux Unit
TECU	Total Electron Contents Unit

Preface

Since Marconi's first empirical evidence of the existence of the ionosphere region early in the XX century, the ionosphere has been used in the means of long distance communications where there is no feasible line of sight. Hence, the long distance ionospheric communications have been used for several purposes, such as military and amateur communications, remote access, and emergency cases. The long distance ionospheric communications utilize the ionosphere as a reflection surface for the HF electromagnetic waves. Along with the satellite communications revolution, the ionospheric communications experienced a setback for some decades. However, recently with the introduction of the digital techniques to be applied in the HF ionospheric links, a growing interest for ionospheric links is observed both in business and science.

Some part of the work presented in this thesis is a continuation to what have been presented in [1]. It has been developed within the Research Group in Electromagnetism and Communications (GRECO) of Electronics and Telecommunications department, La Salle, Ramon Llull University. Since 1997, GRECO has the responsibility of developing an ionospheric link aiming to connect the Spanish Antarctic Station Juan Carlos I (SAS), Antarctica with the Ebro Observatory (OE) in Spain. The research activities that have been carried out by GRECO are focused mainly in obtaining the knowledge of the ionospheric channel. Besides that, GRECO had applied several advanced digital techniques to that link (channel estimation, spread spectrum, multiuser access systems, OFDM modulation, etc.) in order to send the magnetic data gathered at the SAS in Antarctica to OE in Spain.

The most important scientific projects carried out by GRECO are described briefly as:

1. TIC97/0787-C02, and the subsequent special action CICYT TIC 99/1284-E with the main objective of establishing a simplex HF ionospheric link between INTA

in El Arenosillo, Spain and La Salle, Barcelona, Spain using a spread spectrum technique.

2. Since 2003, and as large step forward, the projects REN2003-08376-C02-01, CGL2005-24213-E, CGL2006-12437-C02-01, CTM2008-03536-E, CTM2009-13843-C02-02, and CTM2010-21312-C03-03 have been carried out with the following objectives:

   (a) Oblique Incidence Sounding (OIS) over the SAS-OE link in order to obtain the ionospheric channel characterizations;

   (b) a scientific survey has been taking place every year since 2003 in order to have a complete time series of the oblique soundings;

   (c) the design of the physical layer, which had to be suitable for low power and high speed data transmission system;

   (d) the implementation of the whole transceiver (transmitter, receiver, and two antennas);

   (e) the geomagnetic station in SAS is being updated and improved throughout the lifetime of each project;

   (f) the analysis of the behavior of the ionospheric link between SAS and OE;

   (g) investigate the relationship between the quality of the SAS-OE link and the geomagnetic and solar activities.

From 2003 to 2012, those projects were aiming to study this very long ionospheric link of 12700 km from the radio communications point of view. Such link can be used as an alternative to satellite communications for connecting the SAS (high-latitude) with OE (mid-latitude). Usually, the measurements obtained from the geomagnetic and geophysics sensors located in SAS are gathered to be transmitted through this ionospheric link during the austral summer (November to March), while the scientific survey takes place. Finally, we are aiming to implement a transmission system able to operate 365 days per year.

In that context, the objectives of this thesis are:

1. Characterization of the ionospheric channel of the long-haul link from SAS to OE by achieving the followings:

   (a) the SNR estimation;

(b) the availability of the ionospheric link (SAS-OE);

(c) *composite multipath spread* measurements;

(d) *composite Doppler spread* measurements;

(e) the propagation time of the signal;

(f) *Doppler frequency shift* measurements;

(g) the Frequency of Largest Availability (FLA) measurements.

2. Study of the solar activity effects on the link from the physical and communications point of view, through complementing several parameters obtained from our OIS system and Vertical Incidence Sounding (VIS) stations located along the path of the SAS-OE link. The investigation of the VIS's parameters include the following:

   (a) inter-day variation of the critical frequency of the F2 layer (foF2);

   (b) inter-day variation of the Maximum Usable Frequency for a single hop transmission reflected at the F2 layer (MUF(3000));

   (c) day-to-day variations of the foF2 and MUF(3000);

   (d) inter-day variation of the Total Electron Contents (TEC).

Towards achieving the previous objectives, this thesis is arranged as following - Chapter 1 presents a description of the Sun, solar activity, and its effect on the ionosphere composition. Besides that, there will be an explanation of the structure of the ionosphere, and the principles of the ionospheric propagation.

Consequently, general characterization of the ionospheric channel is presented in Chapter 2, along with explanations of modeling, prediction, and simulation of the ionospheric channel. Also in Chapter 2, we will present several standards for manufacturing the HF modems along with the concept of the Automatic Link Establishment (ALE). Finally, there will be a brief remarking of the HF modem's applications.

In Chapter 3, there will be a description of the *Software Defined Radio* (SDR) technique, which has been used in the implementation of the OIS system. In addition, the characteristics of the SAS-OE ionospheric link will be explained in deep. Throughout the lifetime of the project, three main SDR systems (SANDICOM, SODIO, and POTASIO) were implemented. Since the POTASIO platform was used in the work referenced in this thesis, the specifications of the POTASIO platform are defined in Chapter 3.

In the 2009/2010 survey, the analysis time and the frequency band was extended to 24 hours per day and to the whole HF band (2 MHz to 30 MHz). Therefore, in Chapter 4, we will present the algorithms dedicated to analyze the received signals from the narrowband and wideband soundings. Thus, there will be a discussion of new measurements of the absolute propagation time and the *Doppler frequency shift*, that together with the SNR estimation, channel availability of the SAS-OE link, *composite multipath spread*, and *composite Doppler spread* from the complete set of measurements.

Through Chapter 5, we present inter-day and day-to-day variations of the MUF(3000), foF2, and TEC parameters that were recorded at four VIS stations located along the SAS-OE link throughout three consecutive surveys (2009/2010, 2010/2011, and 2011/2012). Moreover, the availability of the ionospheric channel from SAS to OE has been studied and compared to Rec533 model over the same time period. In order to understand the ionospheric link behavior from both the scientific and communications point of view, this paper presents the likeness between parameters obtained from the OIS system and the VIS stations located along the link path. To that end, the OIS system has been established to link the SAS base and OE, and since 2004, two VIS units were installed at both SAS and OE. Finally, during these three surveys, the influence of the solar activity on both the VIS and OIS results are studied and both the outcomes and the conclusions are presented in Chapter 5.

Part I

Introduction

Chapter 1

The Ionosphere

This chapter is organized as follows. The Sun activities and the interplanetary medium will be described in Section 1.2. Then, the structure of the ionosphere and a brief description of the ionospheric layers (D, E, and F) will be explained in Section 1.3. The ionization levels of each layer is different according to the day, season, and the solar cycle. Along with the ionization variations, the ionosphere is subjected to disturbances that modifies the overall behavior of the ionosphere. Section 1.4 describes these disturbances, such as the Magnetic Storms, Sporadic E, Solar Flare, etc. Finally, several parameters that characterized the ionospheric layers will be introduced in Section 1.5, such as the Maximum Usable Frequency (f_{MUF}), Lowest Usable Frequency (f_{LUF}), Frequency of Optimum Traffic (FOT), D layer absorption, etc.

1.1 Introduction

The ionosphere has the highest electron density among the other regions of the atmosphere. Therefore from the radio communications point of view, the ionosphere is used to propagate the radio signals in a variety of applications throughout the last century. *Oestred* in 1819 discovered the relations between electricity and magnetism. Then depending on the those relations, *Maxwell* put forward the theory of the electromagnetism in 1864.

The first hypothesis about the existence of electrically ionized regions in the atmosphere has been mentioned back in the 19^{th} century. Such hypotheses have been proved by *Marconi* in 1901, who established the first long-haul transatlantic radio experiment

and came up with empirical evidence of the ionosphere utilization as a propagation layer for the radio waves [2]. The long distance link that has been used in the *Marconi* experiments cannot be demonstrated by sight because of the curvature of the Earth that realized firstly by *Heaviside* [3] and *Kennelly* [4]. So that, in the cases of no line of sight existence between the transmitter and the receiver, the electromagnetic waves should be reflected by an ionized region in the atmosphere of the Earth. Such region named as ionosphere by *Robert Watson-Watt* in 1926 [5]. The first complete theory of the ionosphere was demonstrated depending on the height and electron density that have been measured by *Appleton* [6] and *Berkner* [7].

1.2 The Sun

Through this section, we will describe the Sun and different measurements of the solar activity (Smoother Sunspot Number (SSN), Solar Flux, A- and K-index, etc.). Finally, study how the emissions received from the Sun influence the physical formation of the ionosphere.

The distribution of the electron density through the ionosphere is varying according to the electromagnetic radiations coming from the Sun or as it called the *Solar Radiation*. Consequently, the characteristics of each layer of the ionosphere is obtained regarding the variations in the Sun's behavior. As the Sun is radiating more emissions during the daytime period, the electron density raised; however, the electron density does not completely disappear shortly after sunset, where no radiations received from the Sun.

The Sun is a medium sized star at the center of the *Solar System* with radius of 1,392,684 km [8], located about 150 million km from the Earth, and is radiating several types of electromagnetic radiations, which is one of the several consequences of the nuclear fusion process that are taking places at the core. The electromagnetic radiations that have being emitted from the Sun have three different types with various wavelengths, that include the following:

- *Extreme Ultraviolet* (EUV) with wavelength range from 100 to 1000 Å;
- *Soft X-rays* with wavelength range from 10 to 100 Å;
- *Hard X-rays* with wavelength range from 1 to 10 Å.

Those three types of electromagnetic rays are being emitted in daily bases towards the Earth, along with the solar matter, which is consisting of electrons and protons particles with energies varied between 1.5 and 10 keV. Such charged particles are being released in streams from the upper surface of the Sun, forming what we called the solar winds. The solar wind is heading towards the Earth with an average speed of 400 km/s through a *quiet* solar day. The magnetic field of the Earth is affected largely by the solar winds as explained in [9, 10]. Throughout a solar wind, the magnetic field becomes more compressed on the side facing the Sun, and stretched out on the side away from the Sun.

A highly disturbed geomagnetic field caused by a solar wind shock wave, takes the name of geomagnetic storm. This type of storms affect the radio communications that utilize the ionosphere at all latitudes. As several frequencies from the HF band are absorbed and others are reflected, the ionospheric HF communications can not be relied on during the geomagnetic storms. Therefore, the magnetic field of the Earth is a critical parameter in the HF ionospheric communications.

In order to measure the solar activity in daily, monthly, and annually basis, several parameters were introduced, such as the Disturbance Storm Time (Dst), K- and A-index, along with the sunspots recordings and the Solar Flux measurements. Below we will discuss briefly each of these parameters.

1.2.1 Smother sunspot number

The sunspots represent dark areas appear on the surface of the Sun with temperatures ranging from 3000^oK to 4500^oK [11]. That could be quite cold comparing to the temperature of the rest of the surface, which is about 6000^oK. As it is moving on the surface of the Sun, it expands and contracts in size, and takes place and disappears, with a lifetime ranging from hours to months. Therefore, the daily readings of the sunspots numbers are fluctuating considerably. In order to overcome these fluctuations, the readings are smoothed mathematically to take out the erratic nature of the readings. So the elemental trend can be seen, which leads to a number called the SSN [12].

With a periodicity median of 11 years, occasionally there were solar cycles with lifetime less or more than 11 years. The magnitude of the SSN is ranging from virtually zero to around two hundred as maximum SSN value. Figure 1.1 shows the SSN values

for around complete solar cycle from 1995 to 2012, which are decisively affecting the electron density distribution through the ionospheric layers.

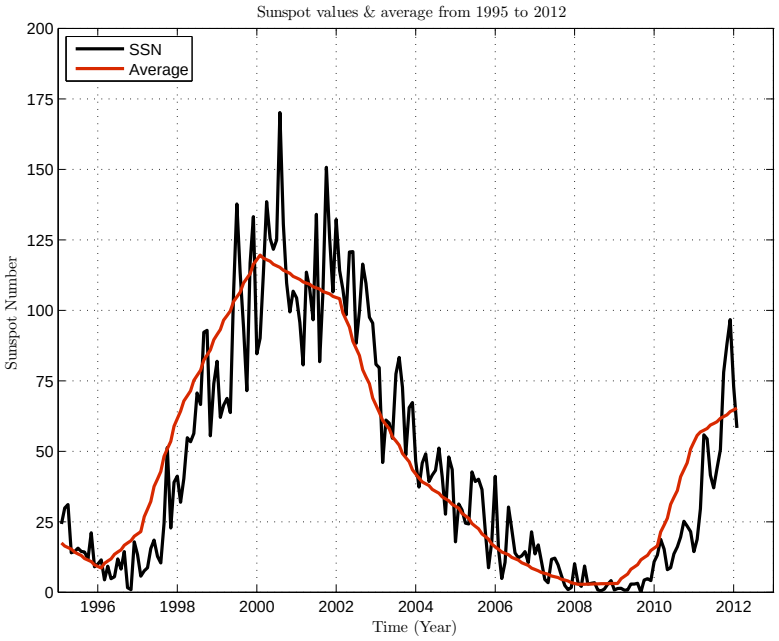

Figure 1.1: SSN values and the average from 1995 to 2012.

During the time period, where maximum SSN values are recorded, the sunspots have intense magnetic fields and, so that, the surface of the Sun becomes highly disturbed.

These magnetic fields energize largely a region of the Sun known as the chromosphere, which lie just above the surface. Subsequently, more EUV and *X-ray* waves are being emitted, which will lead to step up the electron density distribution through the ionospheric layers. Otherwise, throughout the period of the solar cycle minimum, the chromospheres are significantly quiet and the levels of the EUV emissions are very low.

Later on, through Chapter 5, we will discuss the effect of the solar activity increment on the ionospheric propagation throughout three consecutive surveys (see, Chapter 3 for further details regarding the survey period).

1.2.2 Disturbance Storm Time (Dst) index

Another important reading to measure the magnetic storm with respect to the time is the Disturbance Storm Time (Dst) index [13]. The Dst represents a geomagnetic

index, which monitors the magnetic storm level world widely, and it is constructed by averaging the horizontal component of the magnetic field at magnetograms located in mid-latitude and equatorial areas.

During the quiet periods of the magnetic storms, Dst lies between -20 and +20 nano-Tesla (nT). A geomagnetic storm is defined by changes in the Dst index. Negative Dst values indicate a magnetic storm is in progress, the more negative Dst values represent more intense magnetic storm. The size of a geomagnetic storm is classified as following - moderate (-50 nT > minimum Dst > -100 nT), intense (-100 nT > minimum Dst > -250 nT), and super storm (minimum Dst $\leq$ -250 nT).

1.2.3 A- and K-index

The variations in the magnetic field of the Earth are measured by the daily A-index and the three-hour K-index [14]. The A-index is a daily average planetary geomagnetic activity index based on local K-index. An average of eight K-indices (three-hour) lead to A-index with a linear scale from 0 to 400. The HF electromagnetic waves are highly propagating in case of A-index less than 15, and that is particularly appeared on the lower HF band. The K-index is a local index of geomagnetic activity computed every three hours at a variety of observing locations around the world.

Usually, K-index less than 3 is a good indicator of quiet conditions for the electromagnetic waves propagation of the low HF band. Best degree of HF propagation occurs when K-index is less than 5.

Table 1.1 is summarized the conditions of the magnetic field according to the A-index and K-index values.

K-index	A-index	Geomagnetic Conditions
0	0-3	Quiet
1	4-6	Quiet to Unsettled
2	7-14	Unsettled
3-4	15-47	Active
5	48-79	Minor Storm
6	80-131	Major Storm
7	132-207	Severe Storm
8-9	208-400	Very Severe Storm

Table 1.1: K- and A-index measurements and the corresponding geomagnetic condition.

1.2.4 Solar Flux

Finally, the Solar Flux values are measuring the daily amount of the energy received from the Sun. It can vary from very low around 50 (at the minimum period of the solar cycle) to the maximum of 300 throughout the solar cycle maximum. Solar Flux values higher than 200 will make very long distance ionospheric links possible with high HF band. A range of Solar flux values from 50 to almost 80, during the minimum of the solar cycle, is going to yield in poor long distance communications with low HF band.

Generally, an increment in the Solar Flux values for a period of several days, is indicating great improvement in the long distance HF communications over the same time period. For any given Solar Flux value, HF ionospheric communications are improved, while the geomagnetic field conditions are quiet, and become worse, for example, during a geomagnetic storm.

1.3 The structure of the ionosphere

The ionosphere represents a region of the upper atmosphere, and it is distinguished due to the high electron density, which lead to propagate the HF electromagnetic waves from one point to another. As explained in [15], the ionosphere is composed of different types of gases. Along with the difference in heights of the ionospheric layers, the density and composition of these gases vary constantly depending on the observation time through the day.

The solar radiations, during the daytime period, are strong enough to modify the molecular structure of the atmospheric layers. The differences in the electron density distribution of each layer are consequences of the molecular structure modifications through this layer. Specifically, some of the electrons can gain enough energy to break the tie that binds them together with the molecular core. Therefore, these electrons become free by the means of the previous processes. The negatively charged electrons and the positive ionized molecules are forming the *plasma* gas.

The ions in the ionosphere are too massive and the response to the rapid oscillations of a radio wave is too slow. Thus, they have little effect on the radio wave propagation. However, the free electron are over 20,000 times lighter than the ion and do respond quickly to the radio wave propagation.

The ionization, photodissociation, and recombination processes are playing a major rule in giving the *plasma*, a dynamic status as explained in [16]. Along with the time of the day, the structure of the *plasma* gas is continuously changing. Over the nighttime period from sunset to sunrise, and opposite to the daytime period, ionized air zones are reduced significantly due to the drastic decline of the solar radiations. The intensity of the ionization gained from the solar radiations increases with height; however, the concentration of the ionized gas decreases. So, it is reasonable to expect that the electron density will pass to the maximum at some altitudes.

The ionosphere region begins around 50 km from the surface of the Earth during the daytime, which over the nighttime, it changes to 100 km. The ions concentration is reaching values greater than 10^6 per cubic centimeter at lower heights. At very high altitudes, the atmospheric layers become very thin and the ionization levels are very low. Obviously the characteristics of the ionosphere are not homogeneous along with increasing the altitude, since each type of particles has its own ionization characteristics and different recombination times. Note that the ionosphere divided into different layers depending on height and time of day, below the D, E, F layers will be discussed.

Chronologically, the first discovered layer has been given the name of E as Sir. *Edward Appleton* called it referred to the electric vector of the reflected wave. Later, it found that the ionized zone extended to lower latitudes. So for continuity, D layer gave to the lower heights. Likewise, the area has a sufficient ionization density that situated above E layer called the F layer. According to the observation time of the day and the altitude, the F layer divided into F1 and F2 due to different ionization characteristics that have been appeared.

1.3.1 D Layer

The D layer is the nearest layer to the Earth, between 50 and 90 km, the D layer is often seen laying with electron densities between 100 and 10^4 e/cm^3 [17]. It resulted mainly from *X-ray* radiations that have enough ability to penetrate further into the atmosphere. After nightfall, and since the ionization source has disappeared, the D layer will be completely vanishing throughout the nighttime interval.

When a radio electromagnetic wave enters the D layer it sets the free electrons in a vibrating state. As they are vibrating and colliding with the nearby molecules, some energy is lost after each collision. Consequently, these electromagnetic waves that

entered the D layer will be attenuated with attenuation levels inversely proportional to the square of frequency. Therefore, the radio waves transmitted with low frequencies are completely absorbed by the mean of the D layer.

1.3.2 E Layer

The E layer extends from 90 km to approximately 150 km, with electron density of around 10^5 e/cm^3. Also, this layer is known as the *Kennelly-Heaviside* layer or simply the *Heaviside* layer [18]. Herein this layer, the ionization process is due to soft *X-ray* and far EUV solar radiation.

The vertical structure of the E layer is primarily determined by the competing effects of ionization and recombination processes. At oblique incidence, this layer can only reflect radio waves having frequencies lower than around 10 MHz and may contribute a bit to absorb higher frequencies. After sunrise, an increment in the maximum height of the E layer will raise the frequency range to which the radio waves can travel to further distance by reflection. At the nighttime period, the E layer disappears rapidly because the primary source of ionization is no longer present.

1.3.3 F Layer

The F layer or as it has been called the *Appleton* layer refereeing to the English physicist *Edward Appleton* [19], is the most important layer among the ionospheric layers. With the highest range of altitudes from 150 km to around 800 km, the F layer has much less density of the composition gases. The electrons are set in motion, but as fewer collisions take place, the signals tend to bend away from the highest ionization area. In other words, the signal will be refracted back towards the Earth's surface.

At noontime, the ionization density of the F layer raised to the maximum, and consequently, it declines slowly after sunset to just before dawn. During the nighttime period, the F layer usually locates at higher altitudes in summer, especially in latitudes close to the Equator. Practically, the F layer comprises two different layers during the daytime period, the F1 and F2 layers, meanwhile over the nighttime, they are being merged.

First - F1 layer extends from around 150 km to 220 km, with approximately $5 * 10^5$ e/cm^3 during the noontime and solar cycle minimum, that increases to about $2 * 10^6$

e/cm^3 during solar cycle maximum. Such electron density falls down to less than 10^4 e/cm^3 throughout the nighttime period.

Second - F2 layer exists from approximately 220 km to approximately 800 km, this layer is the only one that exists throughout the whole day. Due to its higher electron density, which helps in reflecting the HF electromagnetic waves during the whole day, the F2 layer is the most important layer.

1.4 Solar disturbances and their effects on the ionosphere

Through this section we are describing some phenomenons that are often unpredictable, and lead to a set of disturbances associated to events take place on the Sun. When one or more of these phenomenons appear, it significantly change the characteristics of the ionosphere.

Usually, all types of disturbances have a large influence on the HF ionospheric communications over the whole HF band. At some cases, the user might take advantage of these disturbances. Herein, we are highlighting this list of solar disturbances that leads to ionospheric disturbances:

1. The *Solar Flares* are generating *X-ray* and EUV emissions, and radio bursts [20]. It is considered to be a consequence of releasing magnetic energy generated in the atmosphere of the Sun. They have a similar nature as the solar wind; however, they are sudden and have more intense energy.

2. The *Coronal Mass Ejections* (*CMEs*) imply a large scale disturbance propagation from the outer corona into the solar wind [21]. They involve expulsions on the surface of the Sun and tend to occur simultaneously to *Solar Flares*; so that, their frequency vary along with the cycle of the SSN.

3. The *Coronal Holes* are considered to be sources of the solar winds that lead to ionospheric and geomagnetic storms by disturbing the magnetosphere of the Earth.

4. The *Polar Cap Absorption* (PCA) appears firstly in high-latitude, and then expands toward the equator. Also, it last from one hour to around 60 hours or

more depending on the latitude and the duration of the protons source on the Sun.

5. The ionospheric storms are very critical type of disturbances due to their lifetime that could reach several days and the bad effects on the HF ionospheric communications. There are several types of these storms, such as:

   - *Magnetic storm* is a fast temporal variation in Earth's magnetic field [22], and tends to be happened by the increment of the particles radiations from the Sun towards the Earth.
   - *D layer Storms* that lead to *Sudden Commencement Absorption* and *Auroral Absorption*.
   - *F region Storms* reduce the critical frequency of the F2 layer (foF2); and so, the Maximum Usable Frequency for a single hop transmission reflected at the F2 layer (MUF(3000)).

6. Sometimes irregular ionization zones occur, such as the *Spread-E* phenomena, which occurs in the E layer and the *Spread-F* that exists through the F layer [23].

7. The *Sporadic-E* represent areas of relatively high electron density [24]. So it is significantly affecting the electromagnetic propagation, allowing ionospheric communications links that would otherwise not possible to be establish. There is no union agreement on the causes of this phenomenon, although it is usually associated with meteorological torments.

8. The *Sudden Commencement Absorption*, which has a short period of time compared to the PCA, but at the same time it has enough intensity to disturb the HF ionospheric communications.

9. The *Traveling Ionospheric Disturbances* (*TIDs*) are being defined by some irregularities in the electron density through the ionosphere that are moving from the polar regions towards the Equator [25]. Such disturbances often appear simultaneously to *Solar Flares* and *Magnetic Storms*.

10. Sometimes the Sun ejects large amounts of protons called *Solar Proton Events* (*SPEs*) that reach the Earth, and due to the Earth's magnetic field, they are shifted towards the poles [26].

1.5 Ionospheric propagation

The idea behind the utilization of the ionosphere in the radio communications through HF range, is that the ionosphere is acting as a mirror and able to refract the electromagnetic waves back to the surface of the Earth. Since the ionosphere region surrounds the Earth, it has being used for establishing very long ionospheric links, where transmitter and receiver have no line of sight.

The usage curve of the ionosphere as transmission medium was increasing until the first appearance of the satellite communications, which were being constantly preferred due to the high data rate and wide coverage provided by the satellites. That all relegated the communications through the ionosphere to the background for around a decade.

Along with the revolution of the digital era, the ionospheric communications took back its share through deploying the digital signal processing, Automatic Link Establishment (ALE) technique, *Software Defined Radio* (SDR) technique, etc.

As explained previously, the ionosphere is an anisotropic and inhomogeneous medium, with a variable electron density N that is depending on the altitude h. The incoming electromagnetic waves interact with the ionized layers of the ionosphere, and depending on the height of the layer and the electron density distribution, the waves may be reflected back to the Earth or passed into the space. The oscillation frequency of an electron in induced electric field created by the displacement of the *plasma* is given by the angular *plasma* frequency f_N:

$$f_N^2 = 4\pi^2 f_N^2 = \frac{Ne^2}{\epsilon_0 m} \tag{1.1}$$

where N is the electron density per cubic meter, $e \approx 1.602 * 10^{-8}$ C and $m \approx 9.607 * 10^{-31}$ kg are the charge and mass of an electron, respectively, and $\epsilon_0 \approx 8.854 * 10^{-12}$ kg defines the dielectric constant.

The angular gyro-frequency f_H determines the oscillation frequency of an electron in imposed magnetic field, and it is defined by:

$$f_H = \frac{eB}{m} \tag{1.2}$$

where B is the magnitude of the magnetic flux density of the imposed magnetic field; therefore, the magnetic field of the Earth has a strong effect on the ionospheric radio wave propagation.

The constitutive relations in the *Magneto-ionic theory* combine the forces imposed on the free electrons, which include the electric force from the incoming electromagnetic wave, the force imposed on the moving electron by the magnetic field of the Earth, and the force exerted when electron collides with a neutral particle. The resulting set of *Maxwell* equations can be solved for waves propagation in ionized medium with external magnetic fields. That resulted in the *Appelton* formula for calculating the refractive index n of the ionosphere as transmission medium, which is determined by:

$$n^2 = \frac{X}{1 - jZ - \frac{Y_T^2}{2(1-X-jZ)} \pm \sqrt{\frac{Y_T^4}{4(1-X-jZ)^4} + Y_L^2}} \tag{1.3}$$

where

$$X = \frac{f_N^2}{f^2}, \tag{1.4}$$

$$Y_L = \frac{eB_L}{mf}, \tag{1.5}$$

$$Y_T = \frac{eB_T}{mf}, \tag{1.6}$$

$$Z = \frac{\nu}{f} \tag{1.7}$$

and f is the wave frequency of the electromagnetic radio wave, L and T subscripts refer to the transverse and longitudinal components of the magnetic field, and ν is the collision frequency between the electrons and neutral molecules. The $\pm$ in Equation 1.3 shows that the refractive index may take two different values, positive and negative. That means the ability of supporting the propagation of two characteristic modes. The two modes were commonly referred to *Ordinary wave* and the *Extraordinary wave*.

In order to study the refraction of the electromagnetic waves in the ionosphere, we assume the Earth as a flat model. Furthermore, according to the *Ray theory* that is shown in Figure 1.2, the electromagnetic wave is considered as a ray, which is perpendicular to the wave front, marking the direction of propagation.

The simplest ionospheric propagation medium for the analysis, is one with the absence of the imposed magnetic field ($Y_L = Y_T = 0$) and without collision ($Z = 0$). In

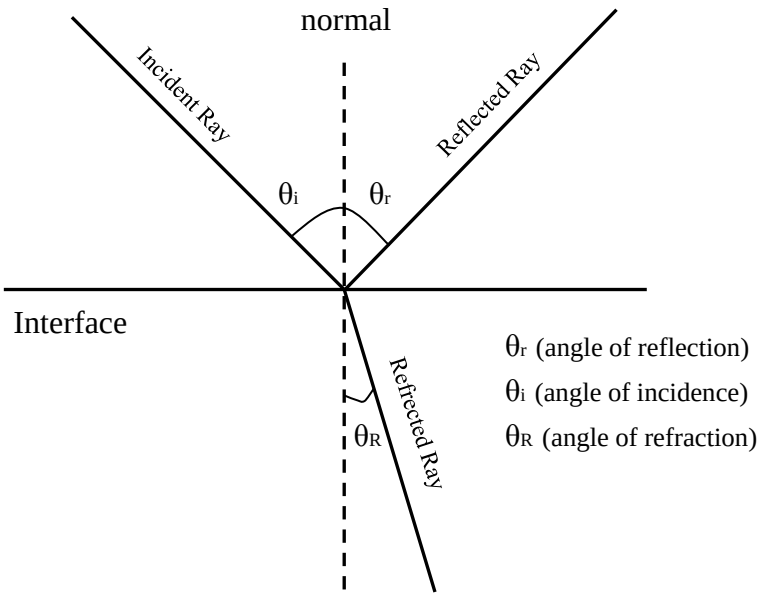

Figure 1.2: The digram of the *Ray theory* concept.

such case the refractive index has only a real part:

$$\Re\{n\}^2 = 1 - X = 1 - \frac{f_N^2}{f^2} = 1 - k\frac{N}{f^2} \tag{1.8}$$

where $k = 80.5$, N is in e/cm^3, f is in Hz, and only single propagation mode is present. Figure 1.3 shows the θ_0 that determines the angle of incidence of the electromagnetic wave on the plane separating two different mediums, measured from the perpendicular to the plane. The angle of incidence is then complement the elevation angle measured with respect to the Earth surface. The electromagnetic wave could incidence upon the ionosphere in two forms vertically and obliquely. As this wave is emitted to the ionosphere, the electron density will increase and the wave characteristics change according to the *Snell's law*:

$$\frac{\sin(\theta_0)}{\sin(\theta_1)} = \frac{n_1}{n_0} \tag{1.9}$$

where n_0 is the refractive index of the origin medium, θ_0 presents the angle of incidence, n_1 is the refractive index of the destination medium, and θ_1 defines the refraction angle.

For the sake of discussion we start with the vertical incidence where the incidence angle θ_0 equals to zero. At the reflection case,

$$n_1 = \sin(\theta_0) \tag{1.10}$$

and since $\theta_0 = 0$ then

$$n_1 = 0 \tag{1.11}$$

Thus, a reflection will take place in case of the equality between the angular *plasma* frequency f_N and wave frequency f. Finally, f_N represents the maximum *plasma* frequency or the critical frequency of the medium at a certain height h. For a vertical incidence, such critical frequency determines whether the waves will be reflected or not.

Then, as shown in Figure 1.3, *Snell's law* will be applied in the case of oblique incidence ($\theta_0 > 0$). Generally, with a constant value of the incident wave frequency f, increased altitude of the ionospheric layer h, and increased electron density N; therefore, the refractive index from Equation 1.8 is going to decrease. Equation 1.9 shows that in case of $n_0 > n_1$, this will result in $\sin(\theta_0) < \sin(\theta_1)$; so that, the electromagnetic waves will be curved into the Earth.

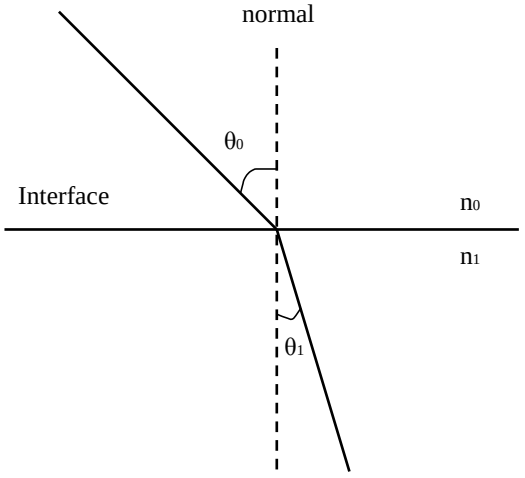

Figure 1.3: A simple digram of the *Snell's law*.

Apply the Equation 1.9 successively on the ionospheric layers that located at greater heights will yield in:

$$n_0 \sin(\theta_0) = n_1 \sin(\theta_1) = n_2 \sin(\theta_2) = ... = n_k \sin(\theta_k) \tag{1.12}$$

The closest layers to the surface of the Earth have a unitary refractive index. So for an incident wave sent from such layers, the reflection conditions of an oblique incidence lead to returning back the electromagnetic waves towards the Earth with a forced refraction angle θ_R of 90 degrees. Accordingly, apply Equation 1.12 will yield in:

$$\sin(\theta_0) = n_k \rightarrow \sin(\theta_0) = \sqrt{1 - \frac{f_N^2}{f^2}} \tag{1.13}$$

where f_N defines the critical frequency of a vertical incidence for the height h, which hereafter will be referred to the critical frequency for vertical incidence reflection f_ν.

The relationship between f_ν at a certain height h and the maximum frequency for oblique incidence f_{ob} reflected at the same height h and the incidence angle θ_0 can be obtained through isolating the frequency f in Equation 1.13. Ultimately, the resulted relationship is called the *Secant Act* and its is defined as:

$$f_{ob} = f_\nu \sec(\theta_0) \tag{1.14}$$

In order to establish an oblique ionospheric link, very important parameter has to be known in advance is the f_{MUF}. The higher the height of the ionospheric layer, the larger the electron density; and so, from Equation 1.14, the f_ν will increase. Otherwise, the incidence angle will decrease; and so that, it is going to affect the altitude oppositely.

An optimum height for reflecting the electromagnetic waves has to be known previously, and consequently from Equation 1.14, the f_{MUF} will be the result to establish a specific ionospheric link. Practically, the f_{MUF} is limiting the frequency range need to launch an ionospheric transmission link, and usually it lays in the HF range. The f_{MUF} is measured at a certain time and position of the ionosphere through applying the *Secant Act* on the ionograms.

The electron density N at any point depends on the location, height, and the time. Through the Vertical Incidence Sounding (VIS) stations that spread around the world, we can measure the $N(x, y, h, t)$ for a given position (x_0, y_0). Consequently, the *Secant Act* can be applied to the ionograms, see Figure 2.1, for obtaining the f_{MUF}. Besides

that, these ionograms (see, for example, Figure 2.1) are providing several important parameters, such as the heights of the E and F layers, TEC, MUF(3000), foF2, etc., (appear at the left side of the ionogram).

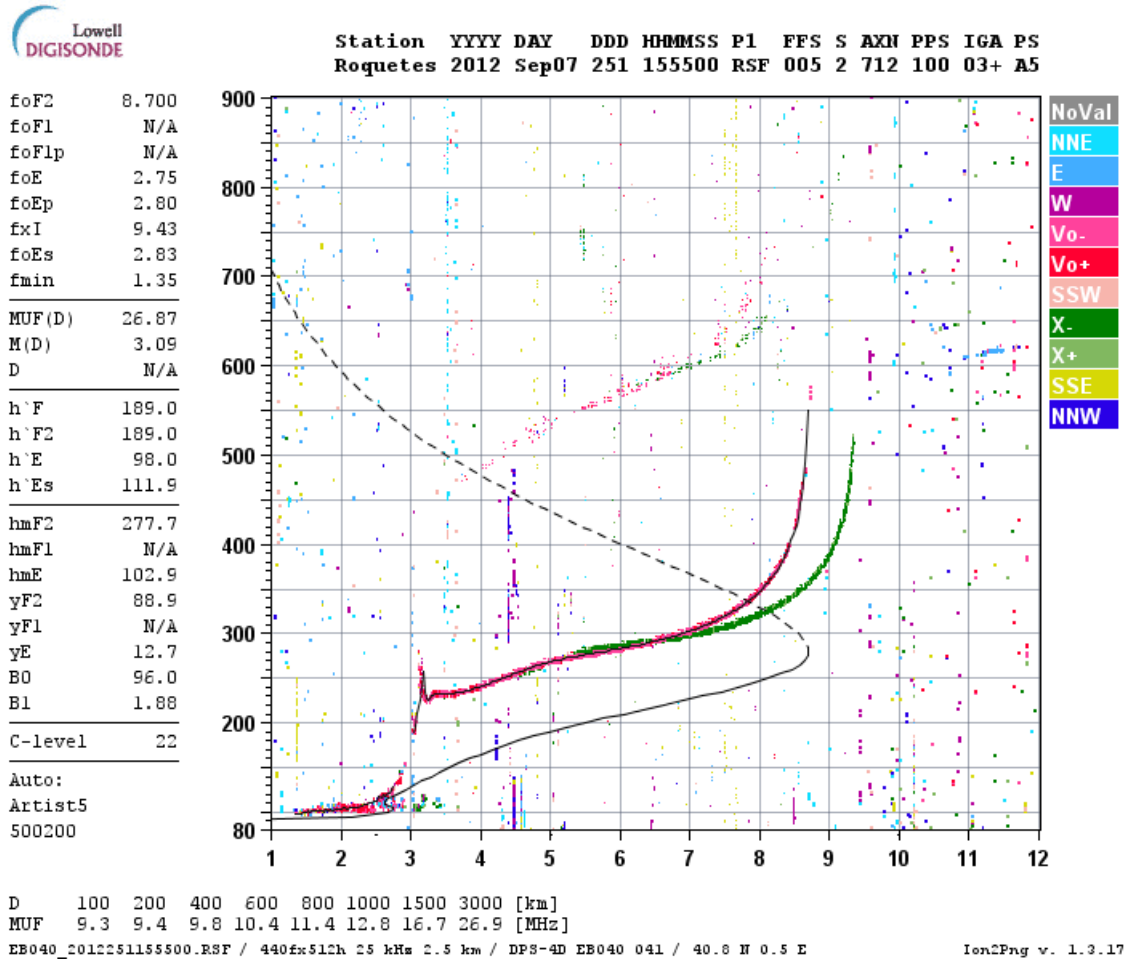

Figure 1.4: Sample of ionogram obtained in the Ebro Observatory, Roquetes, Spain at 07 of September 2012, 15:55 UTC

Chapter 2

HF ionospheric communications

In the previous chapter, we have discussed the Sun as the ionization source for the ionosphere, the structure of the ionosphere, and the principles of the ionospheric communications. Consequently through this chapter, in Section 2.2, there will be an explanation of the parameters that characterize an ionospheric channel. That is followed by Section 2.3, which is dedicated to study the ionospheric channel through several processes, such as the modeling, prediction, simulation, and sounding. During Section 2.4, we will define the Automatic Link Establishment (ALE) concept and the main standards in the HF modems field. Finally, some of the applications of the HF ionospheric communications will be explained in Section 2.5.

2.1 Introduction

Recently, research activities on the ionosphere could be divided into two main research lines, the geophysics and the radio communications. Through this chapter, we demonstrate a brief explanation of the ionospheric communications using the HF band. In all aspects, studying the ionosphere as a propagation medium for the HF electromagnetic waves should start with understanding the behavior of the ionosphere.

Firstly, from the geophysics point of view, the majority of the research activities are devoted to investigate the ionosphere itself, such as the chemical processes that are forming the structure of the ionospheric layers. Then, studying the influence of

the magnetic field of the Earth and the solar activity on the behavior of the ionosphere in daily, monthly, and annually basis. These are the main objects for several investigations carrying out by scientific workshops around the world.

With respect to the radio communications interests, which represent the second research line in the ionospheric investigations, the behavior of the ionosphere towards the HF electromagnetic waves propagation is the main concern. Specifically, assigning the time/frequency regions where the HF electromagnetic waves are strongly propagating through the ionosphere. That is mainly depending on the development of both transmitter and receiver equipments in order to optimize the performance of the ionospheric channel. Since our research group is primarily focusing on the communications engineering field, this chapter will focus on the second research line.

The interoperability between different HF ionospheric modems became more difficult, since the development of the HF ionospheric modems was firstly conducted by separate manufacturers. Organizations started to pay more attention to the standardization of the HF ionospheric modems because of the incompatibility among different equipments. Several years of experience have agglutinated together in order to choose best frequencies and times to establish an ionospheric link. Consequently, ALE technology was developed to automatically establish communications over the ionosphere, besides improving the efficiency of radio spectrum use.

2.2 Ionospheric channel characterizations

In order to use the ionosphere as medium for transmitting electromagnetic waves, the behavior of the ionosphere has to be extensively studied daily, monthly, and annually. From the radio communications standpoint, the characteristics of the ionospheric channel are summarized into five main parameters: channel availability; noise; interference; time dispersion; frequency dispersion.

The coincidence of the distorting phenomena and many other unpredicted variations in the ionosphere, makes it one of the most complicated wireless channel for the radio communications purposes. Below, we will describe briefly each of these parameters. Later on, in Chapter 4, there will be deep explanation of the availability of the Spanish Antarctica Station Juan Carlos I to Ebro Observatory (SAS-OE) link, and both time and frequency dispersion parameters, which have been obtained during the 2009/2010 survey.

2.2.1 Channel availability

Practically, HF communications through the ionosphere can be established between any two locations in the world depending on the transmission power of the system and the characteristics of the ionosphere at the transmission time.

For optimizing the utilization of any ionospheric link, a specific range of frequencies shall be used throughout certain time period of the day. That is called the channel availability, which if being known in advance, will improve dramatically the performance of the link. According to the experiments that have been taken place since the first ionospheric link establishment, there are general facts controlling the propagation of electromagnetic waves through the ionosphere.

The availability of the SAS-OE link (12700 km long) during the 2009/2010 survey will be studied in deep through Chapter 4. Then in Chapter 5, we are going to extend the study of the SAS-OE link availability to 2010/2011 and 2011/2012; besides that, the influence of the solar activity variability on the link availability.

2.2.2 Frequency dispersion

The frequency dispersion of a channel is characterized by spreading the signal frequencies that are reaching the receiver, while originally these frequencies were transmitted as single frequency. In both representative ways (*composite Doppler spread* and *Doppler frequency shift*), the frequency dispersion is unlike time dispersion, since it can occur only when the channel varies with time. In case of the ionospheric *multipath* propagation, a diversity of frequency dispersion represents the time fading of the HF electromagnetic waves.

Doppler frequency shift

The relative motion between the transmitter and receiver will result in the *Doppler frequency shift* (f_d). Furthermore, the movement of the signal reflector/retractor medium can lead to *Doppler frequency shift*. It has either positive or negative values regarding whether the transmitter is moving towards or away from the receiver, or according the movement of the reflector/refractor medium. In the case of the ionospheric communications, usually the transmitter and receiver are static; therefore, the *Doppler frequency shift* results from the appearance, disappearance, and the movements of the

ionospheric layer. The *Doppler frequency shift* can be expressed as:

$$f_d = \frac{\upsilon_m}{c} f_c \tag{2.1}$$

where υ_m represents the transmitter relative motion with respect to the receiver, c is the speed of light, and f_c determines the transmitted frequency.

Doppler spread

The *Doppler spread* is a measure of the spectral broadening caused by the time rate of change of the mobile radio channel and is defined as the range of frequencies over which the received *Doppler* spectrum is essentially non-zero. The inverse of the ν_c measures the stationary of the transmission channel and it is called the *Coherence time*. There are several facts that affect the *Doppler spread* values, including the following:

- the electron density distribution through the ionospheric layers, which depends largely on the existence of the layers throughout the day;
- the *Spread-F* phenomenon;
- the absorption variations of the emitted electromagnetic waves;
- finally, the ionospheric layers existence and disappearance, which is taking place constantly over the day.

Both *composite Doppler spread* and *Doppler frequency shift* values, which have been measured from wideband sounding the SAS-OE ionospheric link during the 2009/2010 survey, will be introduced in deep through Chapter 4.

2.2.3 Time dispersion

The ionosphere can be considered a typical *multipath* channel that is due to having different layers with varied electron density distribution. So, the transmitted electromagnetic waves will refract in the ionosphere and finally reach the receiver at separated moments and the duration of the received signal will be greater than the original. That is called the time dispersion property of the ionospheric channel.

Besides the influence of the ionosphere on the electromagnetic waves, the magnetic field of the Earth is contributing somehow on the time dispersion of the channel. It

is dividing the electromagnetic wave into two different components, *Ordinary* and *Extraordinary* components. Therefore, these components of the incidence wave will refract in the ionosphere through different layers with various speeds, and finally reach the receiver at separated times.

The wideband sounding of the SAS-OE link has offered *composite multipath spread* measurements along with the propagation time values throughout the 2009/2010 survey. Later on, each of the time dispersion parameters will be explained extensively in Chapter 4.

2.2.4 Noise

In case of sounding the ionospheric channel, noise can make one or several frequencies useless during specific time over the day. Also, several types of noise will degrade the SNR values of data transmission system; therefore, affect largely the performance of the system.

In order to neglect the destructive influence of the noise on the HF ionospheric systems, the transmitter and receiver sites have to be selected carefully according to the noise sources and levels. This could be the first step to establish a reliable and successful ionospheric link. Below, there will be some of the crucial types of noise that affect largely any ionospheric link [27].

Atmospheric Noise

It is resulted from the lightning of the tropical thunderstorms, and since it is moving through the ionosphere, this type is affecting vast areas of the Earth [28]. It has a form of short bursts that occur randomly in time. However, it also has a recurrent form with a period of around one hour.

The *Atmospheric Noise* is greater in the equatorial areas, and along with moving towards the high-latitude areas, it becomes lower and has no effect on the ionospheric communications.

Man-made Noise

The *Man-made Noise* is produced by the humans, such as the machines, power lines, etc. Firstly, it decreases along with increasing the transmission frequency, and is often highly dependent on the area. Specifically, in urban and industrial areas this type of

noise is the most crucial type. Selecting a horizontally polarized antennas or using a narrower bandwidth may help in reducing the effects of the *Man-made Noise*.

Galactic Noise

The *Galactic Noise* is raised originally from the space, and specifically from our galaxy [28]. Particularly, it becomes relevant when the receiver is located in very quiet rural areas and the link is set to the high band of HF, besides that is greater at lower frequencies.

2.2.5 Interference

Besides the noise, several sources generate high levels of interference, which degrade the benefits of any HF ionospheric communications system. Usually, an interference mean that the same frequency is used by two different operators, which makes the transmission over this frequency imposed to high levels of interference during a specific time. There are several sources of the interference, *Man-made* and natural, we are highlighting the following:

- Users who are transmitting on a specific range of frequencies for amateur purposes, can generate great influence over the same range.
- The frequency reutilization will cause significant amount of interference, which is regarding to the small number of available channels for HF communications.
- The Power Line Communications (PLC) technology that is operating with the HF band over the electric power lines will produce high levels of interference [29].

The amount of the interference that is produced by radio transmitter can be controlled by cutting transmitting antennas to the correct frequency, limiting bandwidth, and using electronic filtering network and metallic shielding.

2.3 Ionospheric channel study

In order to study an ionospheric communications link using the HF band, several procedures are involving in varying degrees [30, 31], these include: modeling, prediction, sounding, and simulation the ionospheric channel.

2.3.1 Modeling

Modeling the ionosphere is one way to study the characterization of the ionosphere as a transmission channel for the HF band. It means describing the ionosphere as a function of several interchangeable variables, such as the solar activity, location, geomagnetic activity, etc. There are several approaches for modeling the ionosphere under two main classifications: the physical modeling and the channel modeling. Below we will describe both types of modeling.

2.3.1.1 Channel modeling

As explained in [32], those models are aiming to obtain the characterizations of the ionosphere as a wireless transmission channel. Mainly, modeling the ionosphere as a channel means reproducing a statistical behavior of the ionosphere. So, obtain the characteristics of an ionospheric link at a certain moment is not an intention of the channel models.

An important aspect has to be taken into account in case of modeling the ionospheric channel, is replicating the typical conditions in order to design, verify, and compare the functionality and performance of the algorithms used in the system.

From all the characteristics of the ionospheric channel, which have been described early in the previous section, the channel models should include at least the simulation of the time and frequency dispersion, SNR estimation, noise, and the interference.

Below we distinguish between two channel models according to the incorporation of the time or frequency dispersion. Firstly, depending on whether the channel model includes simulation of the frequency dispersion, we will classify:

- Static models, which is only used to simulate the ionosphere at a particular state, and it does not consider any *Doppler spread* values.
- Dynamic models that takes into account the frequency and time dispersion. So we are distinguishing two different channel models:

  Narrowband models: This type is used with small bandwidth signal. Each receiving path has a complex coefficient that changes normally with *Rayleigh* distribution. This type of channels are corresponding unanimously the *Watterson* model [33], which is the most accepted model in the HF ionospheric field.

Wideband models: Signals with very large bandwidth have to be handled with these wideband models. The *taps* of each FIR filter evolve according to set of random variables, which are often *Gaussian* and correlated in time. The *multipath spread* is modeled for each path as a finite impulse response filter with coefficients that are typically specified from measuring the *power delay profile* [34, 35].

2.3.1.2 Physical modeling

The physical model of the ionosphere represents the electron density distribution modeling through both E and F layer of the ionosphere. Unlike channel modeling, the physical models are intended to reproduce the characteristics of the ionosphere at any particular moment. There are different types of physical models, a brief description of three different types will be mentioned below:

Physical models

The *Physical models* are based on the mathematical solutions of the equations that control the *plasma* of the ionosphere, and depend on the solar radiation and other boundary conditions [36]. In practice, the use of these models is limited due to the high levels of complexity and large amount of computations required for the implementation.

Parametric models

The *Parametric models* are depending on the parameterization of the *Physical models* according to the solar activity during a specific period of observation time, such as [37, 38], the magnetic field of the Earth, and the geographical area of interest.

Empirical models

The *Empirical models* are based on interpolation processes of measurements arrays recorded at ionosonde stations around the globe, for examples see, [39, 40]. Since these stations are not covering the ionosphere completely; so that, it is not fully sampled and the recorded data are insufficient. That is limiting the performance of the *Empirical models*, such as the ITU-R PI.533 model (Rec533) and the ITU-R P1239-3 model [41], which is the most notable one.

2.3.2 Prediction

Before the revolution of the digital era, and in order to optimize the utilization of the ionospheric transmission link, data tables are used to specify the best frequencies at a given time according to pre-organized knowledge from the previous experiments. Therefore, the operators of the HF ionospheric communications link will have more control and satisfactory results.

Recently, the large development of the computational capacity provided by the computer systems has facilitated the implementation of several complex models of electron density distribution. Those new models are considering the operation at different areas around the globe (mid-latitude, equatorial, and high-latitude), besides that, the magnetic field information. So, that will lead to predict several important parameters for handling any ionospheric transmission link.

The main idea behind the prediction models is predicting the state of ionosphere based on the historical and current availability of certain physical parameters, which are directly related to the ionosphere (Maximum Usable Frequency (f_{MUF}), critical frequencies, etc.) or indirectly (solar activity, geomagnetic information, etc.). Regarding the radio communications point of view, there are two techniques of predictions as below:

- Short-term predictions lead to specifying the current state of the ionosphere or during few hours as well. Measurements obtained from satellites, radars, ionosondes, etc., can be incorporated practically in *real-time* to result in prediction models that can provide a 4D ionospheric model. For better short-term predictions, two techniques have been introduced as follows:
  - The *NowCast* technique [42] - is describing the current state of the ionosphere through *real-time* measurements incorporated practically from different sources, such as Oblique Incidence Sounding (OIS), Vertical Incidence Sounding (VIS), satellites, radars, etc.
  - The *ForeCast* technique [43] - is predicting the f_{MUF} values for several hours, by monitoring both the activity associated to the magnetic field of the Earth and the solar activity; so that, *ForeCast* technique can predict the ionospheric disturbances in advance.

Short-term prediction can optimize effectively the HF band that is used for the ionospheric communications. And, average the *NowCast* and *ForeCast* techniques lead to the medium-term predictions, which used to make a frequency plan including the best frequencies to establish HF communications through the ionosphere.

- Long-term predictions, which aim to predict the monthly averages of the Maximum Usable Frequency for ground distance reflected at the F2 layer (MUF(3000)) and the critical frequency of F2 layer (foF2) that lead to frequency plan of high availability to use with the *broadcast* systems.

There are two types of prediction models depending on the deployed techniques for prediction. The first type, which is associating more sophisticated models along with virtual geometry techniques, such as the SKYCOM, AMBCOM, and IONORAY, etc. Due to the high levels of complexity that appeared in large amount of computations, these types of models offer more accurate predictions and more parameters. The IONORAY model is able to evaluate a point-to-point ionospheric transmission link considering the measurements of the magnetic field of the Earth.

The other type of models is depending only on the virtual geometric techniques, such as the ASAPS [44], ICEPAC [45], REC533 [46], IONCAP [47], etc. These types result in less number of parameters for the sake of the computation time. Besides that, in case of ionospheric disturbances over the link path, the predictions may not be too accurate. Operators, who use these simulators, are able to specify several important parameters, such as the antenna type, frequency range, etc.

2.3.3 Sounding

Sounding the ionospheric channel could be used as an indicator for the state of the ionosphere with a specific range of frequencies at certain time. The channel sounding can be performed through two main techniques, taking their name from the modality of emitting the sounding tones towards the ionosphere (obliquely (OIS) and vertically (VIS)).

From the radio communications perspective, the characterizations of the ionosphere can be obtained through sounding the ionosphere obliquely as introduced in [48, 49]. Usually, OIS systems are used for sounding short links as very long links. Synchronized

transmitter and receiver units are transmitting and receiving signals in regular basis with different bandwidth and transmission frequencies.

From the physical standpoint, the parameters measured from the VIS systems located at stations over the world, stand for describing the structure of the ionosphere. These stations are vertically emitting electromagnetic pulses with different frequencies towards the ionosphere. Consequently, the pulses are reflected by the ionospheric layers, and then the VIS systems generate graphs called ionograms from the received pulses.

Ionograms obtained from VIS systems, such as the one appeared in Figure 2.1, are different from the ionograms that can be obtained from OIS systems. These VIS ionograms are used to be an indicator of the critical frequencies, heights, MUF(3000), Lowest Usable Frequency (f_{LUF}), and Total Electron Content (TEC) of the different layers of the ionosphere.

The OIS system presented several important advantages for understanding the electromagnetic waves propagation over the VIS system, despite any additional complications. Firstly, it enables the investigations on how the electromagnetic waves travel over the ionospheric link by re-creating real life propagation scenarios. Secondly, OIS receiving station can detect several OIS transmitting stations using a pre-defined schedule of the transmission frequency. Finally, it provides monitoring of the ionosphere over unapproachable areas, e.g., oceans.

2.3.3.1 Vertical Incidence Sounding

The VIS systems are sharing the same principles with the OIS systems; nevertheless, the geometry of the VIS systems is more straightforward. The VIS ionosondes are transmitting vertically electromagnetic radio pulses within the HF range towards the ionosphere. During 1925, *Breit* and *Tuve* have introduced the first VIS platform using pulse technique.

Usually, the whole transceiver (transmitter, transmission and receiving antennas, and receiver) is in the same location. So, the receiving antenna detects several echoes back from the ionosphere. At a particular frequency, the propagation time of the electromagnetic radio signal indicates the height of the reflection layer.

The critical frequencies of the ionospheric layers could be obtained from the ionograms through the asymptotes and the virtual heights of the ionospheric layers. At

the critical frequency, the emitted electromagnetic radio wave reaches the maximum resonant frequency of the layer, and once the critical frequency of a layer is exceeded, the radio wave is no longer reflected by the layer, and continues moving until it encounters the next layer of higher electron density and correspondingly higher critical frequencies. Eventually, if the frequency exceeds the maximum critical frequency of all the layers, the radio wave will continue into the space.

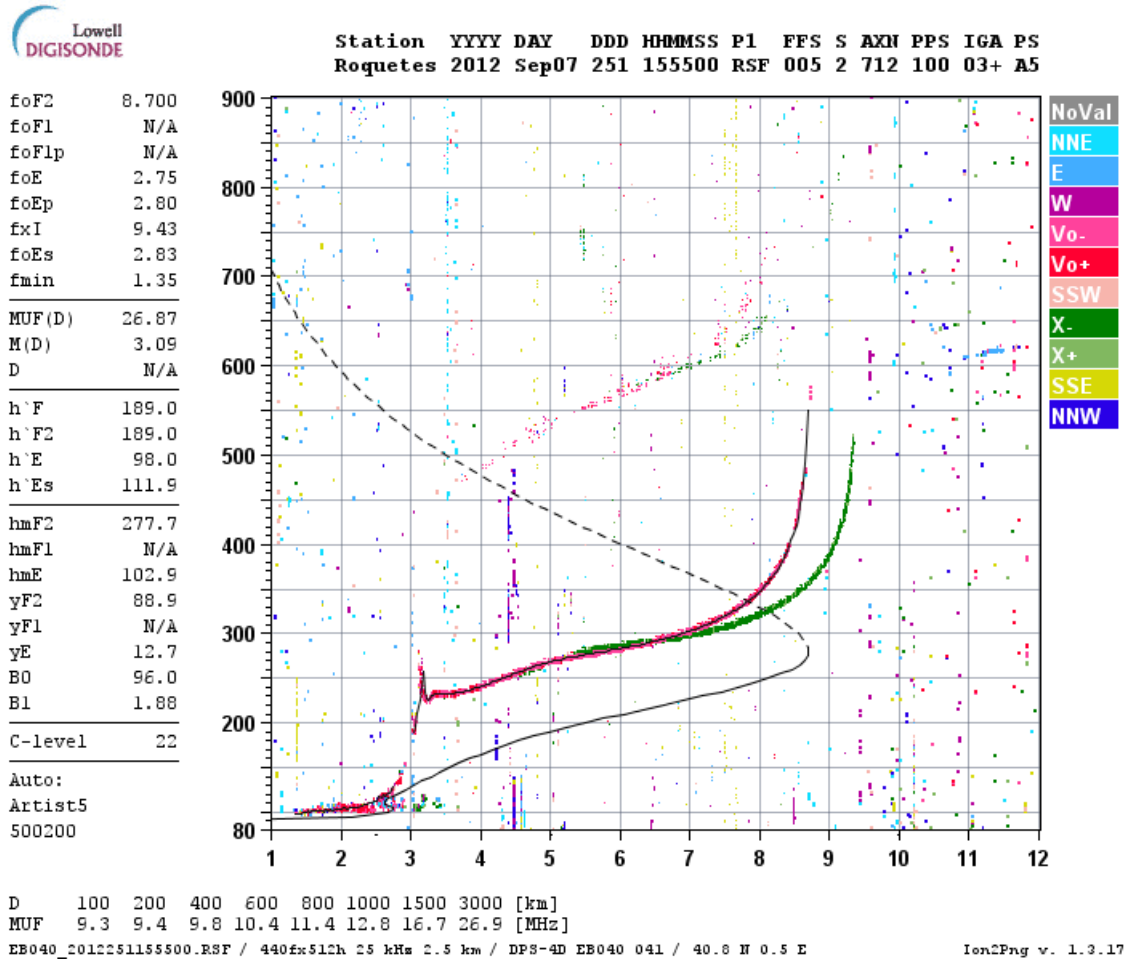

FIGURE 2.1: Sample of an ionogram obtained in the OE, Roquetes, Spain at 07 of September 2012, 15:55 UTC

As shown in Figure 2.1, at the case of splitting the electromagnetic waves into *Ordinary* and *Extraordinary* components by the interaction with the Earth's magnetic field, here it appears the red trace. The red trace defines the *Extraordinary* ray that means the component of the incident radio wave perpendicular to the magnetic field direction. On the other hand, the green trace in the ionogram represents the returned echoes from the *Ordinary* component of the transmitted radio signal, which is parallel with the direction of the magnetic field of the Earth.

For obtaining the features of received electromagnetic radio waves through the ionosphere, such as the relative phase, propagation time, *multipath spread*, amplitude, and polarization, it is necessary to know the propagation path of the waves from the transmitter to the receiver. Here, it comes the need to more details about the electron density profile associated with each ionospheric layer, which could be extracted as well from the ionograms as illustrated in Figure 2.1.

There are various groups of parameters regarding the virtual height and critical frequency of each layer:

- **virtual heights**: virtual height of the E layer (h'E); virtual height of the F layer (h'F); virtual height of the F2 layer (h'F2);
- **critical frequencies**: critical frequency of the E layer (foE); critical frequency of the F1 layer (foF1); critical frequency of the F2 layer (foF2); critical frequency of *Extraordinary* trace (fxI).

All these parameters besides the MUF(3000) will be stored and, later on be used in prediction models to produce the ionospheric *forecast*.

2.3.3.2 Oblique Incidence Sounding

In the OIS systems, the narrowband or wideband electromagnetic pulses are conveyed obliquely towards the ionosphere, which will be reflected or refracted by the ionospheric layers. In addition, such radio pulses are more prone to the effects of the ionospheric variations since these pulses are taking more time to reach the receiver. Recently, several set of architectures and methods have been introduced, such as the WHISPER [50], DAMSON [51], and SCIPION [52].

The situation of the *multipath* propagation in the OIS techniques is further complicated than in the VIS because the transmitted signals can take different paths to reach the receiver. Besides that, it is imposed to different sources of signal distortion and loss. Over and above, analyzing the resulted parameters is more complicated due to the geometry of the OIS links.

An OIS system offers clear lay out of the available frequency band to establish an ionospheric link, also, the frequency band where no link can be launched. The available frequencies have to be updated according to the ionospheric variability and the

emissions from Sun. A variety of parameters will be obtained from both narrowband and wideband OIS systems, such as time and frequency dispersion, channel availability, SNR estimation, signal phase stability, propagation time, etc.

In the narrowband sounding, the OIS systems are transmitting electromagnetic pulses repetitively with very small bandwidth. Otherwise in the wideband sounding, PN-sequences, such as *Gold*, *Kasami*, *Barker*, etc., are noted for its good autocorrelation properties and the occupation of selectable bandwidth. In case of the wideband OIS systems, the receiver is responsible for generating the channel impulse response, and consecutively the *scattering function* that includes the time and frequency dispersion values (*composite multipath spread*, *composite Doppler spread*, and *Doppler frequency shift*) [53]. There are some parameters that need very accurate instruments to be measured, such as the propagation time, *Doppler frequency shift*, and the arriving angle.

Historically, most of the OIS surveys have been conducted at mid-latitude locations. That is the reason behind including finished surveys carried out by the DAMSON project, which came up with systematic OIS measurements of the ionosphere through high-latitude zones [51].

Recently (since 2009), our OIS system is sounding the SAS-OE transmission link in order to complete a time series of the channel soundings (entire HF band and during 24 hours per day) as introduced in Chapter 4 and [49], along with invistigating the solar activity influence on the OIS parameters as explained in 5 and [54].

2.3.4 Simulation

Simulating the ionospheric link before the actual establishment will increase the probability of having a successful link with minimum number of failure occasions as introduced in [55]. That is due to allowing the development of different algorithms with various goals, verifying these algorithms within controlled environment of pre-defined conditions as introduced in [56, 57].

Besides that, it gives the ability of doing multiple comparisons of algorithms at different environments, in order to select the most reliable one. Typically, any simulator has to include the following models: noise model; interference pattern; channel model; pre-defined ionospheric conditions. Such conditions will lead to simulate the ionospheric link in near *real-time* situations. The specifications of the following aspects is

necessary for which different simulators will reproduce identical conditions: channel coefficients, interpolation techniques, etc.

There are several recommendations that include various ionospheric conditions, different scenarios of simulation the ionospheric links. For example, the CCIR 520-2 recommendation [55], offers three different scenarios for simulating poor, moderate, and good channel, along with various parameters of different values associated with each channel scenario.

A highly efficient implementation of any simulation system of ionospheric link has to be conducted at two levels, *Off-line* and *Real-time*.

Off-line

The algorithms usually programmed on PCs, with the support of specialized *software*, such as the MATLAB and `C++`. So, the algorithms used in both the transmitted and receiver are implemented, verified, and finally came up with the best one, all that is done at the *Off-line* level.

Real-time

Usually, it is implemented on specialized *hardware* and with the *Software Defined Radio* (SDR) techniques. Consequently, it comes the importance of verifying the equipment in *Real-time* level. Using SDR techniques is not requiring any modification or adaptation of the equipment under test. Besides that, allow simulating the characteristics of the ionosheric channel with respect to the time and frequency dispersion, noise, etc. Typically, it allows the simulation of attenuation, in a form of which you can test some parameters of the radio transceiver, e.g., the sensitivity.

2.3.5 Noise and interference

The noise and interference levels are limiting the benefits of the HF communications systems. Several surveys have measured the noise characteristics that affect the ionospheric propagation at different areas of the world [58], with different environments [59], etc. These surveys came up with several measurements that have been collected in the CCIR reports [60]. Such reports show the noise maps for the entire globe and for different seasons.

There is a diversity of noise sources that affect communications ionospheric as previously mentioned in Section 2.2. The measurements show that the statistical distribution of the noise is neither *Gaussian* nor stationary. Both the *Atmospheric noise* [61], and *Man-made noise* [62] have a manifestly impulsive nature, and are often limiting the benefits of the HF systems. In order to carry out reliable simulations, the models have to be developed based on noise measurements of different types.

Interference in a communications channel mainly results from other communications established elsewhere at the same frequency. The amount of interference varied upon the propagation conditions of the ionosphere, which also depends on the time of day, season, solar activity, etc. In several parts of the world, several surveys have been carried out to measure the interference levels, such as in [63], and consequently all the interference statistics will be incorporated in the ionospheric channels simulators.

2.4 HF ionospheric modems

Through the capability of refracting the electromagnetic waves in the ionosphere, HF communications channel transfers the signals beyond line of sight, connecting transmitter located hundreds or even thousands kilometers away from the receiver. The automated HF radio systems have to identify and coordinate the usable range of frequencies, since it is largely affected by the refractive and absorptive characteristics of the ionospheric layers.

Currently, selecting the transmission frequency is the motivation behind collecting various types of measurements, combining them with several prediction techniques, which may lead to the f_{MUF} of the link. Then, ALE protocols have being developed to provide high reliable and quick way to initiate connections between different HF radio stations over the intervals of variability of the HF ionospheric propagation. Besides that, it is handling the HF spectrum utilization in case of busy or fall channels.

Bounded by treaty limits on radiated power and by several types of noise (galactic, *Atmospheric noise*, and *Man-made noise*), a normal HF radio channel of 3 kHz is resulting in low and fluctuating SNR values. As stated previously through this chapter, the transmitted signals reach the receiver from one or more ionospheric layers via refraction, which are in motion most of the time. So, the receiver receives multiple replicas of the original signal having independent, time-varying path losses and phase

shifts. Thus, that will lead to *multipath* interference, deep fades, and impulsive (non-*Gaussian*) noise. All that will degrade the SNR estimation, which requires the ALE to select a new transmission frequency and may be setting up a new channel.

Figure 2.2 shows a simple HF communications channel with HF modem, which is used in recent experiments of evaluating the modem performance. In this Figure - $s(t)$ is the transmitted signal; $d(t)$ defines the ionospheric disturbances; $r(t)$ determines the output signal of the HF communications channel; $p(t)$ is the output signal of the HF modem.

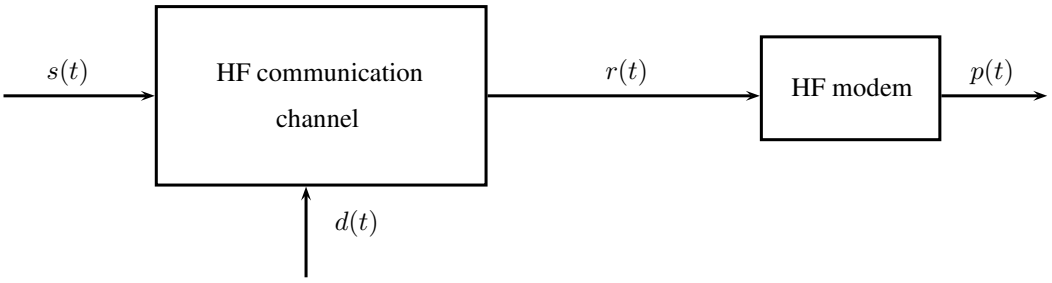

FIGURE 2.2: A simple HF communications channel model.

The HF radio modems apply a suite of techniques to address channel problems ranging up to few seconds. Recently, the large steps in the digital signal processing technology have made the utilization of the adaptive equalizers more practical; and so, permitting high performance HF data modems, such as in [64], [65], etc. Those are able to use Phase-Shift Keying (PSK) or even Quadrature Amplitude Modulation (QAM) as we will describe later.

Various manufactures around the world have introduced several modems in the field of HF communications via ionosphere. Since that lead to quick development of the HF ionospheric communications; however, the incompatibility among several systems appeared as crucial issue for the manufacturers and users as well [66]. In order to overcome this drawback, standardizing the protocols of the HF modems come to the surface as a long term solution.

From United States of America, the *Department of Defense of the United States of America* (DoD) issued the military standard MIL-STD and the *Institution of the Telecommunication Science* (ITS) proposed the federal standard FED-STD. From the other side of the Atlantic, the standard agreement STANAG introduced by the *North Atlantic Treaty Organization* (NATO). All the standards introduced by the previous organizations can be classified into three generations as below:

- The first generation (1G) was prior starting the standardization processes, and referred to the privately owned modems.
- The second generation (2G) included the first standards, such as STANAG 5066 [67], MIL-STD-188-110A [68], FED-STD-1052, etc.
- The standards of the third generation (3G) offer high data rates and/or advanced ALE protocols, such as the STANAG 4539 [69], MIL-STD-188-110C [64], MIL-STD-188-141C [65], etc.

Along with each generation, the corresponding standards are covering at least one of the following categories.

Physical category

Usually standards in this category handle parameters related to the physical issues of the modem, such as the channel coding, frame structure, modulation schemes, training sequences, etc. The first generation of standards (MIL-STD-188) proposed general requirements of long haul data modems.

First, the MIL-STD-188-110A [68] has operated with bit rate ranging from ranging from to 4800 to 9600 b/s over a 4 kHz voice frequency channel with a QAM full duplex modulation technique, and 4800 b/s (4800 b/s encoded or 2400 b/s with a convolution code of *rate* 1/2) over a 3 kHz HF radio channel with an 8-PSK modulation technique. Then in 2000, the MIL-STD-188-110B [70] has been revealed with a bit rate of 9600 b/s with conventional code and 12800 b/s encoded with the ability to implement a 64-QAM technique. Consequently, the MIL-STD-188-110C [64] published in 2011 for the design and development of new data modems with data rates up to 120,000 b/s.

Other standards that specify the physical layer of the HF modems are, for example, STANAG 4539 [69] that allows bit rate up to 12800 b/s encoded and 9600 b/s coded with a convolution code of *rate* 1/2 and punctured of *rate* 3/4.

Link layer category

In this category, standards are responsible for establishing the communication through the ionosphere, maintain it, ensure the information to be received free of errors, and finally terminating the communication. The Automatic Re-Quest (ARQ) and ALE are the main protocols dedicated to identify the link layer specifications, such as in the STANAG 4539 [69], MIL-STD-188-141C [65], etc.

Application category

Usually different standards are offering the same protocols for applications. However, in some cases each standard defines its own application protocols or requires specific set of protocols. The STANAG 4406 Edition 2 as an example [71], specified the *Military Message Handling System* (MMHS). Also, the *HF Mail Transfer Protocol* (HMTP) and IP-over-HF operation has been standardized in the STANAG 5066 Edition 3 [72].

To increase the versatility of a standard, usually it covers several categories, such as the STANAG 5066-Edition 3 that included ARQ protocol, besides the HMTP from both the link layer and application categories, respectively.

2.4.1 Automatic Link Establishment

Along with using the ionosphere in various applications, the communications through it has to be governed automatically. So, this was the idea that fostered the development of the ALE protocols that are aiming to establish, manage, and terminate the communications through the ionosphere. Continually, the ALE protocol uses the quality information obtained previously in form of tables called Link Quality Analysis (LQA) tables.

The two main concerns of the ALE protocols are the interference levels and the transmission frequency selection; hence, it needs a wide range of available frequencies to mitigate the interference effects and has more freedom to choose frequencies with availability. Besides handling the communications, the ALE protocols are sounding the channel to complete the LQA tables, and then share it among other ionospheric stations.

In parallel to the standards issued by the United States of America, the NATO published the STANAG series. Consistently with developing the standards of the HF modems, the ALE protocols are ongoing upgraded. Back in the 80s, the first generation of the ALE protocols emerged on the initiative of the HF equipment manufactures. Then, the DoD introduced the military standard MIL-STD-188-141A in 1988 [73], and the equivalent civil standard FED-STD-1045 was during 1990 [74]. The standards of the second generation, such as the MIL-STD-188-141C [65], MIL-STD-188-110C [64], etc., offered a robust, reliable, and interoperable ALE protocols.

A cooperative development effort among industry, government, and academia resulted in a third generation protocol suite that was recently standardized in MIL-STD-188-141C [65] at 2011. The STANAG 4539 [69], which is called *Automatic Radio Control System* (ARCS), and consisted of three levels as following:

- The *Automatic Channel Selection* (ACS) is responsible for choosing the best frequencies, taking into account aspects of propagation, network load, and unwanted traffic.
- The ALE is establishing, managing, and terminating the communication.
- The *Automatic Link Maintenance* (ALM) is monitoring the communication parameters and take appropriate actions if necessary.

Some of the key features of the third generation ALE protocols are (see for example, [75]): faster link establishment; highly supportive to the Internet protocols; connecting at lower SNR; higher throughput.

2.5 Applications

The HF electromagnetic waves with frequency range from 2 MHz to 30 MHz can be reflected by means of the ionospheric layers for distance further than 100 km easily. Even it can reach the other side of the Earth at some cases. Along with the utilization of the satellite communications, the ionosphere reserved its importance of being very attractive transmission medium for the next reasons:

1. The cost of the whole transmission system (transmitter and receiver) is a way less expensive than using a satellite link.
2. It has the advantage of being very attractive tool for military and surveillance purposes overseas and unapproachable lands.
3. The visibility of the ionosphere over any location in the Earth; therefore, it can be used for emergency purposes and development countries around the world.

As nothing is perfect, some of the drawbacks have to be taken into account when using HF ionospheric communications system are listed below:

1. high levels of interference, since the ionosphere is used in several applications and high number of operators around the world;

2. high levels of noise from several sources that reduce the SNR values and he performance of the systems;

3. the frequency range where the ionospheric link is available, is varied over 24 hours per day due to the ionization levels.

A substantial increase in bit rate from 300 b/s to 120,000 b/s is offered by the current HF systems throughout a few years. Nowadays, we have the ability to create networks of computers with ALE by using the third generation ALE standards that have opened the door to investigate new applications that previously were unfeasible.

Remote sites can be linked together into HF sub-networks, with multiple gateways into the information infrastructure to improve the robustness of connectivity to these sites. An automatic HF modems network can be connected to already serve network for emergency connection. *Man-made* and environmental disasters are affecting segments of the HF modems networks. As a solution, backup network of automated HF radio stations will quickly detect and bridge such faults to carry high-precedence traffic.

From disaster areas to combat theaters, the transportability, low-cost, and long-haul of HF radio make the ionosphere a primary quick response medium. So it can be considered as a rapid deployment networks. In [76] discusses the possibilities and limitations of a network topology formed by different nodes, where each node has different transmitters and receivers. If what previously mentioned was achieved, resulted a greater capacity, redundancy, diversity and quality of service, etc.

There are many HF networks in operation, many of them promoted by the United States of America, such as *The global communications system HF air/ground/air network* (HF-GCS) [77], *SHAred RESources* (SHARES) [78], *FEMA National Radio System* (FNARS) [79], *Customs Over-the-Horizon Network* (COTHEN), etc. The functioning of these networks demonstrates the success of the HF modems standardization, and more specifically, great achievements in efficiency and interoperability.

The HF modem networks, as a first step, can be integrated into existing IP networks to act as a backup link [80], and later on be fully integrated within the network. The interconnection of the HF modems in networks, and then the integration of these networks with other heterogeneous IP networks has motivated the emergence of new

applications, such as electronic mail HMTP [81] and *HF-Messenger* [82] that enables the transmission of text files, faxes, images, emails, etc. Despite that many services are available only for military or government needs, there are also commercial applications designated for other sectors.

The United States Navy for administrative and logistics messaging uses the *Battle Force Electronic Mail* in HF radio ground-wave propagation paths between ships in a battle group. Also, **Bushmail** [83] is a company that offers email service across Africa based on low-power HF links, while **Arinc** through the *GLOBALink* solution [84], provides coverage in polar regions using HF systems for communications between aircraft.

For communications with mobile platforms beyond line of sight, HF ionospheric modems provide an economical alternative to the communications via satellite. The ALE protocols have shown high mitigation against the link-level connectivity problems that formerly plagued the HF connectivity. Automated *HF Node Controllers* (HFNCs) integrate individual voice and data terminals, as well as the networks aboard larger platforms, into high bandwidth, low-cost stationary infrastructure.

The use of HF for voice transmission has undergone significant improvements [85]. The former analogue point to point links are being replaced by digital encoded and encrypted ones, with integrated HF modems in the telephone networks [86], make the HF communications being alternative mean of communications to cables and satellites. Besides the voice transmission, in [87, 88], there are experiments to investigate the efficiency of using HF communications systems in transmitting images. In 1980, **Marconi Communications** installed HF communications systems that integrate voice and data traffics, protocols and topology updates, and network services as described in [89].

The old AM radio systems that located within the LF, MF and HF bands are replaced with the Digital Radio Mondiale (DRM) initiative [90] that resulted from a collaboration of several organizations in the field; therefore, the quality of sound has increased significantly.

Chapter 3

An OIS system between Antarctica and Spain

Section 3.1 is devoted to introduce some general considerations for the HF ionospheric communications field. Consequently through Section 3.2, there will be an explanation of the Software Defined Radio (SDR) technique, followed by full description of the ionospheric link between the Spanish Antarctic Station Juan Carlos I (SAS) and Ebro Observatory (OE) (SAS-OE) in Section 3.3. Finally, the third SDR transmission platform (POTASIO) that has been used over the SAS-OE link will be explained in Section 3.4.

3.1 Introduction

Strong variability, time dispersion, high levels of interference, several types of noise, and the frequency dispersion, are the main challenges that face any communications system via the ionosphere. Therefore, HF communications through the ionosphere were famously characterized as the solution provided low bit rate, highly subjected to noise, and little robust. Also, as a consequence, most of the operators were changed to other means of communications, such as the satellites.

Throughout the analog era of transceivers, there was a huge lack of devices that could diminish the negative effects of the variability of the ionospheric channel characteristics. So, in any case, nothing could be done analogously to improve the achievable quality levels of the HF ionospheric systems.

Recently, the utilization of several digital techniques in the HF ionospheric systems is opening the doors for various expectations. The substantial increase in the computational capabilities, offers several devices that are carrying out very complex digital signal processing techniques. So that, the utilization of the ionospheric communications has raised and reached its previous position among other means of communications.

The work of this thesis is referred to results obtained from a complete HF ionospheric communications system during several surveys, which we called *radiomodem*. Practically, it consists of three main components, transmitter, receiver, and transmission and reception antennas. Hence, this transmission platform (*radiomodem*) is responsible for generating and transmitting the signal at SAS, and then receiving at OE. Besides these general tasks, there are other internal operations that are performed by the *radiomodem*, such as modulation, demodulation, coding, decoding, equalization, time and frequency synchronization, etc.

Starting with the transmitter, which is a device to manage frequency and transmission power to the baseband signal. The most important functions of the transmitter is divided into mixing, filtering, and amplification. The signal is amplified analogously, while mixing and filtering tasks can be performed either in analog or digital domain. Consequently, the prepared signal will be transmitted through the transmission antenna (monopole) at the transmitter side. The receiver is very similar to the transmitter, it has the responsibility for amplifying, filtering, and lowering the received signals to the baseband version.

Several characteristics of the physical layer are specified by communications standards, such as transmission bandwidth, equalization, modulation, etc.; and then, all the equipments must to meet these standards to be approved.

The establishment of a transmission link bounced by the ionosphere should take into account the following aspects: link availability; time dispersion (*composite multipath spread*); frequency dispersion (*composite Doppler spread* and *Doppler frequency shift*); signal attenuation; noise; interference. The ability of having available ionospheric link with certain frequency range at specific time, is depending on:

- the antenna characteristics at both transmitter and receiver;
- signal attenuation due to the total length of the link;
- output transmission power at the transmitter side;

- filtering and amplification stages, which are conducted at the receiving side;
- Signal to Noise Ratio (SNR) estimation;
- time and frequency dispersion measurements.

3.2 *Software defined radio*

The SDR technique was firstly introduced in [91] with the aim of using the digital technology to implement multi-service, multi-standard, flexible, and reconfigurable *software*. During the last few years, several research groups have used techniques, such as high performance A/D/A converters, *real-time* integrated circuits, and the *Hardware* Abstraction Layer (HAL), to develop new transmission systems that in one or more of those aspects can be considered as SDR platform.

The A/D/A converters that have been installed in the *radiomodem* of the SAS-OE link offered up to 125 MS/s, 16-bit of resolution, and *Integral NonLinearity* (INL) of about 3 LSB. These converters are highly noted for the HF ionospheric communications systems because of allowing the digitization of the entire HF band. Thus, that will lead to improve the architecture of the *radiomodem* SDR platform significantly, through minimizing the number of the analogue components.

We are noting herein two types of *real-time* digital devices, Digital Signal Processing (DSP) units and programmable logic devices (Field Programmable Gate Arrays (FPGA) and Complex programmable logic device (CPLD)). They have high computational capability, high implementation efficiency, and re-configurability. Generally, the DSP is easier to write, edit, and delete the demanded algorithms. Meanwhile, FPGAs and CPLDs are more efficient from the energy standpoint and allow higher processing speeds due to the possibility of parallelizing the execution of the algorithms [92].

The *hardware* abstractions routines allow programming the communications algorithms with *hardware* independence with high efficient implementation. Also, make the algorithms more capable of carrying out *real-time* dynamic configurability services [93] and offer direct access to the *hardware* resources.

In [94], there is an extensive study of applying SDR technology to the HF communications systems. Two architectures of digital channel simulators were proposed in [56, 95] using the SDR implementations.

Regarding our project, which is essentially an Oblique Incidence Sounding (OIS) operating over the SAS-OE link, an explanation of the architectural design of the transceiver is found in [96]. A *real-time* proposal to implement *hardware* receivers for the *Digital Radio Mondiale* (DRM) standard is described in [97].

3.3 SAS-OE ionospheric link

Since our project is classified as a scientific project, the link between the SAS to OE (SAS-OE) has no exclusive allocation of bandwidth. Internationally, the ITU and, the CNAF in Spain [98], are in charge of regulating the use of the radio spectrum. Also, the project should not limit to one or few frequencies due to the main objective, which is investigating the availability and the characteristics of the ionospheric channel. Therefore, to reconcile this objective with the recommendations of ITU and CNAF, series of decisions are being adopted with the intention to minimize the interference with the other systems:

- high bandwidth modulation with low power spectral density;
- maximum transmission power of 200 Watts;
- the period of using a specific frequency for transmission;
- the possibility of changing the transmission frequency in case of any interference.

The work carried out within the project REN2003-08376-C02-01 is funded by the Spanish ministry of science and innovation and developed jointly by La Salle engineering and architecture, Barcelona, Spain and the OE, Roquetes, Spain. Both institutions belong to the Ramon Llull University in Barcelona, Spain. The overall objectives of this project are:

- analysis of the ionospheric behavior over SAS in Antarctica through Vertical Incidence Sounding (VIS) system;
- design a suitable physical layer for low power data transmission over the SAS-OE link;
- investigate the effects of the solar and magnetic activities on the electromagnetic wave propagation through the ionosphere;

- implement the whole *radiomodem* SDR platform, and then apply frequent *hardware* updates to the platforms according to the latest available technologies;
- conduct consecutive sounding surveys of the SAS-OE ionospheric link by using OIS technique.

In order to satisfy the previous objectives of the project, we ended up with a road map to be tracked, with the following millstones:

- design, implement, and install transmitter and receiver units at SAS and OE, respectively;
- measure the interference levels and noise at the receiver location;
- obtain the narrowband and wideband availability of the SAS-OE link, and the time and frequency dispersion of the channel;
- determine the frequency plan depending on the previous surveys as introduced in [99];
- correlate measurements from both sounding systems, our OIS system and four VIS stations located close to the SAS-OE link path.

The observatory of Ebro has several areas of expertise including the seismic, weather, geomagnetism, ionosphere, climate, and solar activity. The staff of OE firstly installed a geomagnetic observatory at SAS during the 1995/1996 survey. Starting from 1998, the measurements from geomagnetic observatory in SAS were transmitted in hour basis to OE through two different satellite systems, *Meteosat* or *GOES*.

The utilization of the satellite communications has several advantages, such as coverage of very remote areas; however, the main weak point is the high cost. Besides that, transmissions from polar latitudes towards the equatorial orbits are facing some difficulties, e.g., antenna pointing. Consequently, the main motivation of the project was to propose an alternative way to satellite communications in order to transmit all the geomagnetic measurements from the geomagnetic sensors at SAS to be analyzed later in OE.

Along with being an alternative communications technique, the cost of the design, implement, and operate the HF ionospheric systems is very low. All the latest communications techniques can be installed, which is considered key benefit of the HF communications systems.

With total distance of around 12700 km, the transmitter is located at the SAS (62.6 S, 60.4 W), with departure azimuth angle of 45.5 degrees (northeast). The SAS has several modules dedicated to habitability, laboratories, warehouses, etc., and usually is operated from November to March, which is famously named the austral summer. Throughout this period, SAS is inhabited by technicians from the Unidad de Tecnología Marina (UTM) and academics from various fields (geologists, biologists, physicists, engineers, etc.). In Roquetes, Spain, the receiver is placed at the OE (40.8 N, 0.5 E) with an arrival azimuth angle of 206.2 degrees (southwest).

The *hardware* of the *radiomodem* platform has been updated several times since 2003/2004 survey. Three main SDR platforms were installed at the transmitter (SAS) and the receiver (OE) locations. The first generation of platforms is called Sounding System for Antarctic Digital Communications (SANDICOM), it was described in [100]. A proposition of the channel sounding test carried out during the 2003/2004 survey (9 days throughout the period from December 2003 to January 2004) from the SANDICOM platform, channel characteristics, and other preliminary results were published in [101]. *Composite multipath spread* measurements between 1.5 and 6 ms and *composite Doppler spread* between 0.4 and 2 Hz have been obtained in 3 kHz bandwidth.

During the 2005/2006 survey, the second generation SODIO has started with a new digital platform using FPGA, and Application Specific Integrated Circuits (ASIC) with high speed A/D and D/A converters as explained in [96]. The results obtained by the SODIO system have been introduced in [48]. The system had some limitations in both sounding time (00:00 UTC to 11:00 UTC and 18:00 UTC to 23:00 UTC), frequency (4.5 MHz to 16.5 MHz), and also in measuring capabilities. For the previous reasons, the characteristics of the ionospheric channel, the propagation time, and *Doppler frequency shift* during the daytime period, could not be obtained. The limitation of the operating time of the system to 18 hours was due to changing the configurations of the system, which were carried out manually by the staff in the SAS.

Finally, during the 2009/2010 survey, a third generation of the SDR platforms called POTASIO was installed in both SAS and OE, which will be deeply explained in the following section.

3.4 The POTASIO platform

Very complex design of a radio system is doomed to failure. Therefore the complexity of the POTASIO SDR platform has to be minimized as most; besides that, using the benefits of each existing technology or programming language and working in the most appropriate layer in each moment. The detection and correction of an error or even making an improvement to the system is being handled in a way to be as simple as possible, which is a key success factor.

This section is organized as following, basic principles of designing the POTASIO platform, and then there will be a description of the two main *hardware* boards of the system, and finally, *hardware* presentation of the transmitter at SAS and the receiver at OE.

3.4.1 Introduction

In principle, the final prototype of the transmission system shall be capable of transmitting the collected data in nearly *real-time* from the geomagnetic sensors placed at SAS. Since the development work in this project is integrated and being carried out successively; therefore, we have attempted to take advantages of the best virtues of the two previous *radiomodem* platforms (SANDICOM and SODIO). In addition, it aims to meet the commitment of consumption/versatility in the best possible way.

As a device must be capable of supporting the cruelty of winter, it is equipped enough to be left outdoors. For ease of system management, a wireless LAN (WLAN) access point has been installed with additional fiber optic interface. Along this section, we will explain all the virtues and limitations of the design. Essentially, the benefits of any digital radio system appear to be assessed, nevertheless considering the characteristics of the environment where the system will operate.

Regarding the integration nature of the system, we avoided at all costs that the amount of *hardware* components could increase over the years and this involves adding external components. Therefore, this design should consider the future needs and must have enough flexibility to adapt. Furthermore, conglomerating the *hardware* provides the maximum protection of equipment against the extreme conditions of work in which it must work continuously and properly.

As the surrounding environment of the system in Antarctica represents the extreme case in terms of weather (strong winds, rain, snow, etc.), the whole transmission system located in Antarctica equipped with sufficient protection against the weather. All the electronic devices have a range of working temperatures. So, we have worked on keeping the equipment always within the ranges of temperature and humidity. Furthermore, the sealing system should prevent the condensation from being occur. Since any liquids produced by this phenomenon will freeze, expand, and finally damage the electronic devices.

Also, the design of the system has considered all cases and experiments that aimed to be conducted. From a simple sounding test of the ionospheric link, geomagnetic data transmissions in *real-time* with different bandwidths, or even any other experiment that need to be performed throughout HF band.

Even though many advantages, digital technology also has few disadvantages. The sensitivity of the system comes marked by the resolution of the A/D converters. No less important are the limitations with respect to the operation frequencies of the A/D and D/A converters. This, despite being a general major problem, it is not when it comes to HF band, since the boundaries of the sampling frequency of these devices are around 125 MS/s with a resolution of 16 bits, which are more than enough to sample a signal that at the worst case scenario will be 30 MHz.

We must take into account this commitment (flexibility/efficiency), regarding the device selection phase that have to be able to perform transmitting and receiving digital data or even sounding the ionospheric radio channel. Moreover, the choice of technology or combination of several, is notably influencing the development time and cost of the project. Figure 3.1 shows a list of various available technologies [48], which are ordered from left to right as most to least efficient and from right to left as more or less flexible.

From the energy consumption and efficiency point of view, ASIC devices were the preferred ones. Since it has the *hardware* adequate to develop all the desirable functions, and capable of solving algorithms of high computational complexity at very high frequencies.

Despite being more efficient from a consumer standpoint, it would be totally impractical from economic standpoint, as small- or medium-scale production of these devices is usually very expensive. In addition, it requires a huge effort in human resources;

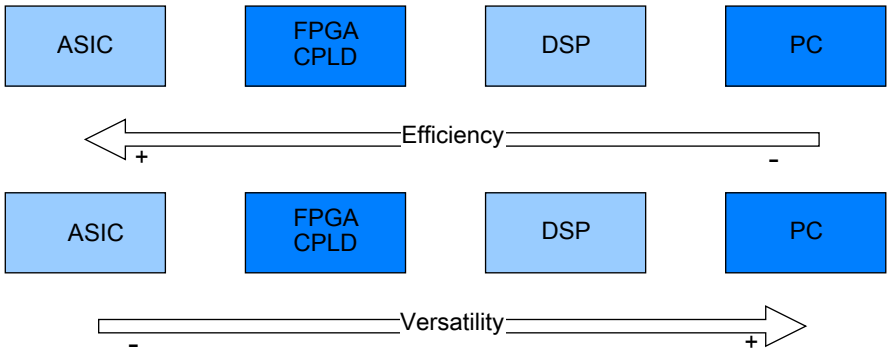

Figure 3.1: Classification of technologies according to the efficiency and versatility.

therefore, long development time. Another major drawback is that this device is dedicated only for the algorithm that is designed for. In case of improving or changing the applied algorithm, the ASIC is obsolete and should be replaced by a new one.

The investigations that have been conducted, came up with a hyper design through combining FPGA or ASIC with PC or DSP unit. The FPGA and ASIC chips are dedicated to higher computational cost; on the other hand, the non-computational functions are solved by using the PC or the DSP unit. The higher the working level, the easier managing and configuring the peripherals according to configuration files or commands from the operator. Programming the demanded algorithms is the only obstacle that faces the utilization of PC or DSP unit.

Figure 3.2 shows a functional block diagram of the entire digital portion of the transmitter. The receiver has very similar scheme except in some components, such as D/A instead of A/D, signal demodulator and decoder instead of modulator and coder at the transmitter side.

The design appeared in Figure 3.2 supports different modes of operation, as the user operates the system in *real-time* through configuration files. One or more control units must set up all the blocks and make all the appropriate interconnections.

This structure can perform two sounding techniques, the narrowband and wideband, that besides the magnetic data transmission. Firstly - in case of the narrowband sounding, is simple to cancel one of the two CICs branches and let a proportional value of the desired amplitude to the other branch in order to generate the narrowband tones.

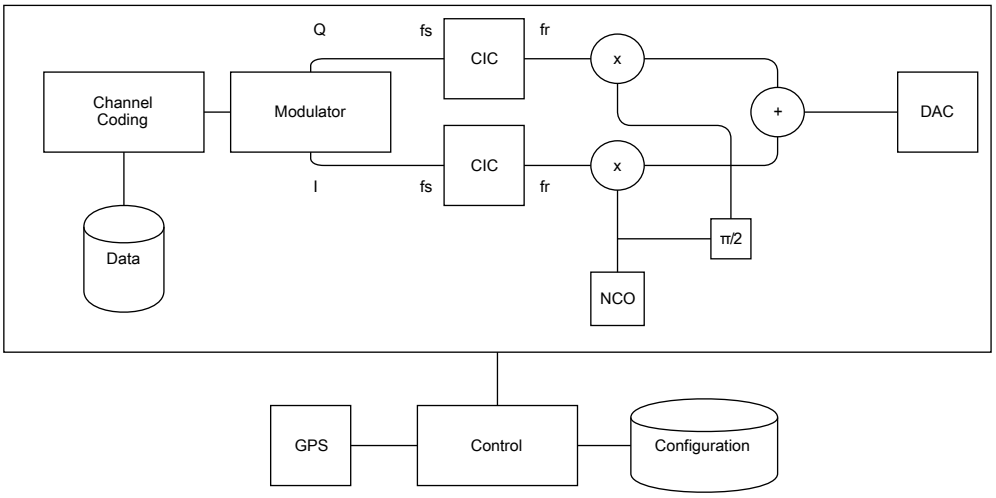

Figure 3.2: Functional block diagram of the digital devices in the transmitter.

Secondly - the wideband sounding is carried out through going directly to the modulator, ignoring everything that last in the chain, then generate the IQ, raise the frequency and finally transmit the signal.

Thirdly - the data transmission of the geomagnetic sensors, which is already subjected to source coding before the storage, starts with consulting the directory where the data is stored, then continue following the previous path of the wideband sounding.

Locations of transmitter and receiver

The POTASIO platform was firstly installed at both SAS and OE during December 2009. In Antarctica the transmitter is located on a hill called *Pico radio* as illustrated in Figure 3.3 for the following reasons:

- The distance between *Pico radio* and SAS (about 500 meters straight) is not very long; so that:
  - The maintenance of the antenna structure or the *radiomodem* platform can be done daily without any need for long journeys or requiring an intervention of the technicians to the site.
  - The section of the single phase AC power cables for an expected consumption of about 1 kW is 12 mm^2, that gives an acceptable solution for the logistical constraints in the Base.

- Near the top of the hill showed in Figure 3.4, there is about 1000 square meters of clear area, which is suitable for installing the monopole antenna and all associated equipments.

- The *Pico radio* hill elevated to about 100 feet above sea level. In the direction of Roquetes (northeast azimuth of 46.5 degree) on the island there are two relevant orographic obstacles:

  – Heights from 300 meters to about 7 km, corresponding to the slopes of *Pico Burdick*. Therefore, installing the transmitter in *Pico Radio* link is unobstructed for vertical angles greater than 1.5 degrees.

  – A peak of about 200 meters height located 2.5 km away, between *Punta Hesperides* and *Monte Charrua*.

- The distance between *Pico radio* and the location of the geomagnetic sensors near *Punta Polaca* (less than 400 meters in a straight line) is not excessive; thereafter, the expected losses of the RF cable that unites both locations is of 8 dB order at 10 MHz.

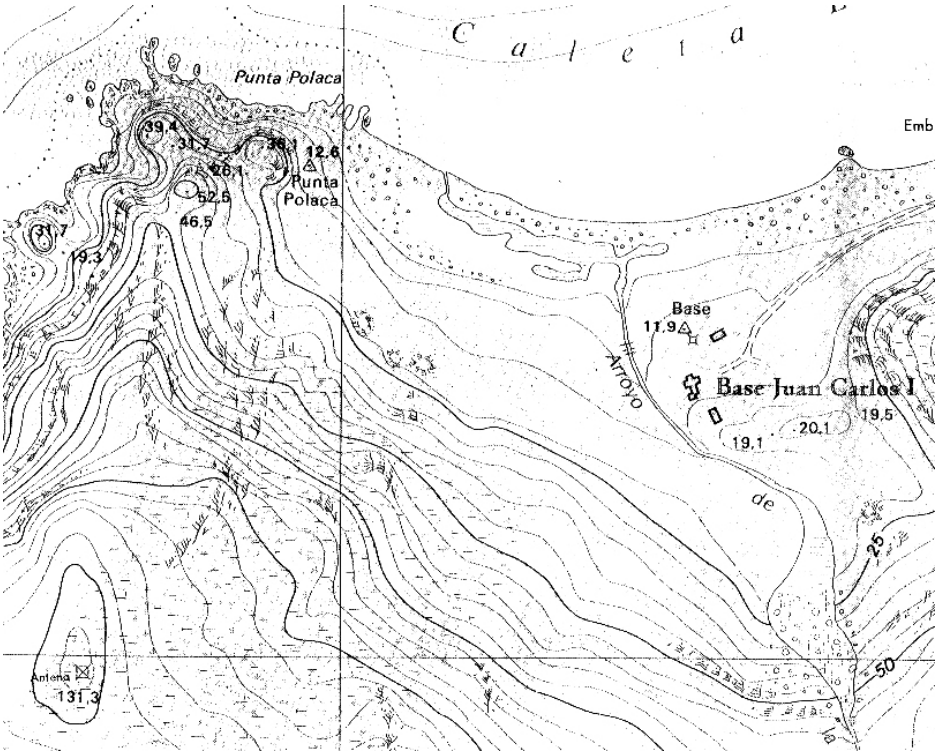

Figure 3.3: A map shows the location of SAS (*Base Juan Carlos I*) in Livingston Island.

Figure 3.4: Approximate location of the transmitting antenna at the *Pico Radio*.

Figure 3.5: The installations of yagi and monopole antennas at OE during 2009/2010.

The great novelty of this system is the ability of receiving simultaneously from two antennas with different polarizations: 5-element yagi and monopole. In this way, we take advantage of the two propagation modes with different polarizations, *Ordinary* and *Extraordinary*.

As a first approach and due to the size of its active element, the yagi antenna has been adopted to work at three different frequencies around 15 MHz during 2009/2010. Instead, the monopole operates at the whole HF band, as long as the impedance adapts. Therefore, also needs antenna adapter and, the transmitter by switching a relay to send a tone, it is activating the adapter to launch an algorithm looking for the impedance that minimizes the ROE for that frequency. Figure 3.5 illustrates a photography of two antennas, yagi and monopole, which have been installed at OE. Throughout both 2010/2011 and 2011/2012, there were three receiving antennas at OE working with the entire HF band, monopole, yagi, and V-antenna.

3.4.2 *XTremeDSP-IV* development board

This board is responsible for carrying out all the operations that require high computational capabilities. It is capable of generating the RF signal from the baseband data and vice versa, and controlling all the peripherals of the transmitter. Similarly, two boards have been installed at both the transmitter and receiver, with functions could be configured through the user *firmware* installed on the FPGA. Figure 3.6 shows the *XTremeDSP-IV* board [102].

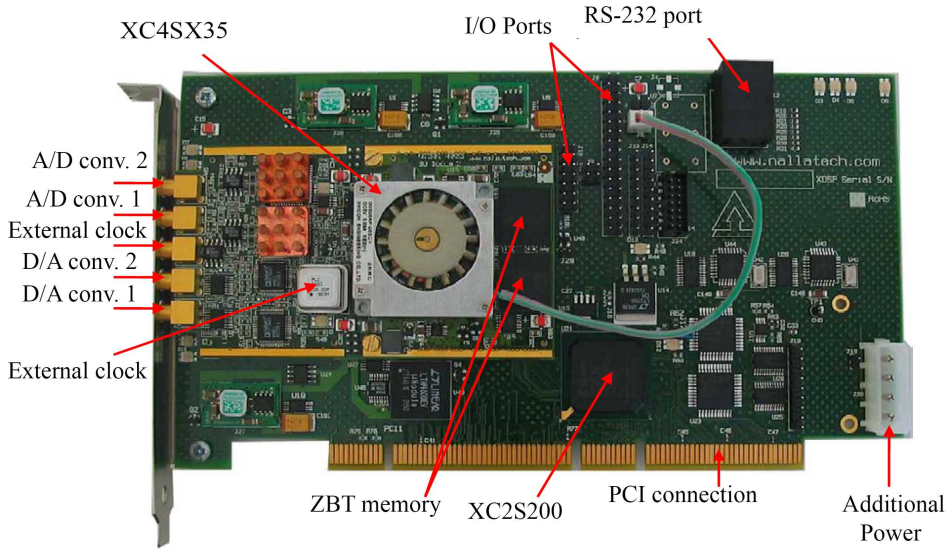

Figure 3.6: The development board *XTremeDSP-IV*.

The main *Virtex-4 XC4VSX35-10FF668* FPGA chip from XILINX is designed by the user, and dedicated to control the peripherals and handle the arithmetic functions.

It contains 34560 logic cells besides 192 DSP slices. Besides the *Virtex-4 XC4VSX35-10FF668* chip, there is another one (*Virtex-II-XC2V80 4CS144*) has the responsibility to set up the system clock and both the D/A and A/D converters. In terms of the data memorizing capabilities, there are two *ZBT SRAM* memory banks of 512 kW (kiloword) and 32 bit. Finally, through the pre-configuration feature, it handles the interface between the PCI bus and the *Virtex-4 XC4VSX35-10FF668*.

For the sake of synchronization, the board has been prepared with an internal oscillator of 100 MHz. Aside from the internal one, the board can be connected to another external clock, and more, it has the ability of programming up to three different clocks via *software*. In addition, it has a serial port, several LEDs, additional input power, and JTAG in order to configure the FPGAs.

A PCI connection is responsible for connecting the *Spartan-II XC2S200* FPGA chip and the PCI bus. Also, it supports 33 MHz mode with bus width of 32 bits; therefore, theoretically it can reach throughput rate up to 132 MB/s in order to communicate with the application *software*. The user has I/O ports of 12 pins available on the *P-Link* bus and up to 28 pins in the *Adjacent-IN* bus. Moreover, it accepts logic levels of 0 and 3.3 Volts.

The D/A converters provide two independent channels with the *AD9772* converters of 14 bits and support sample rate up to 160 MS/s. Besides the A/D converters, which also has two independent channels with *AD6645* converters of 14 bits and sample rate of 105 MS/s.

Figure 3.7 shows the same functional block diagram appeared in Figure 3.2; however, the blocks marked with light blue are fully performed by the *XTremeDSP-IV* board, and the ones marked with red are not fully conducted by the board.

3.4.3 The *Cyanide* board

As seen previously, this system is powerful enough to be responsible of processing the RF signal digitally, communicate with the *embedded*-PC, and control the majority of the peripherals need for the system to work. However, each peripheral device has its own electrical and mechanical specifications at both input and output ports. Therefore, we need a bridge interface between the 0 and 3.3 Volts signals of the FPGA and TTL signals, open collector or CMOS, which works with different peripherals. In addition, it must do any conversions need of the required voltage levels.

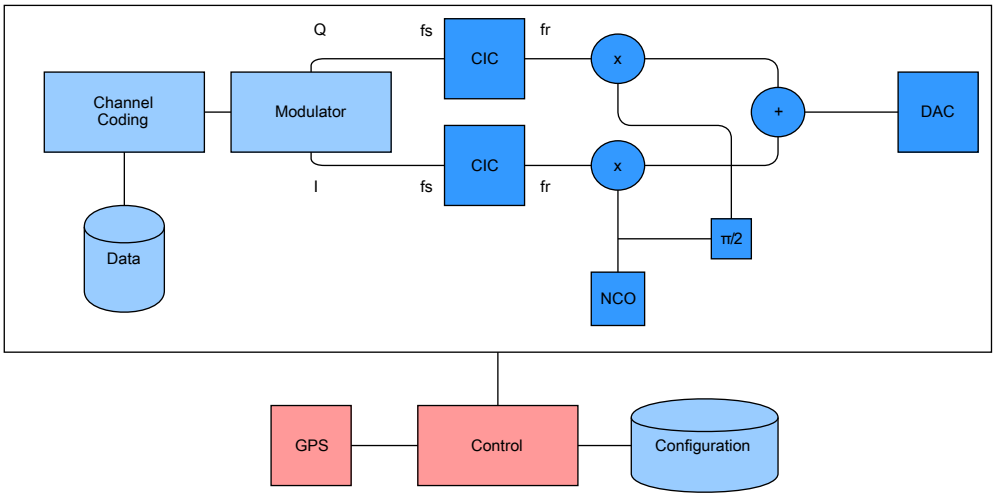

Figure 3.7: The implementation block of the *XTremeDSP-IV* development board.

Moreover, in most cases the connectors of the I/O ports have to be mechanically adjust to provide the signal to each component. For the previous reasons, we have initiated the design of the *Cyanide* solution, which meets the needs of I/O for both transmitter and receiver. The reason behind the decision of designing one board instead of two different ones is the cost saving involved in make a single spin, and the flexibility that supposes to make it able to run either of the two boards, especially in the testing phase. The *Cyanide* board and its major components are shown in Figure 3.8.

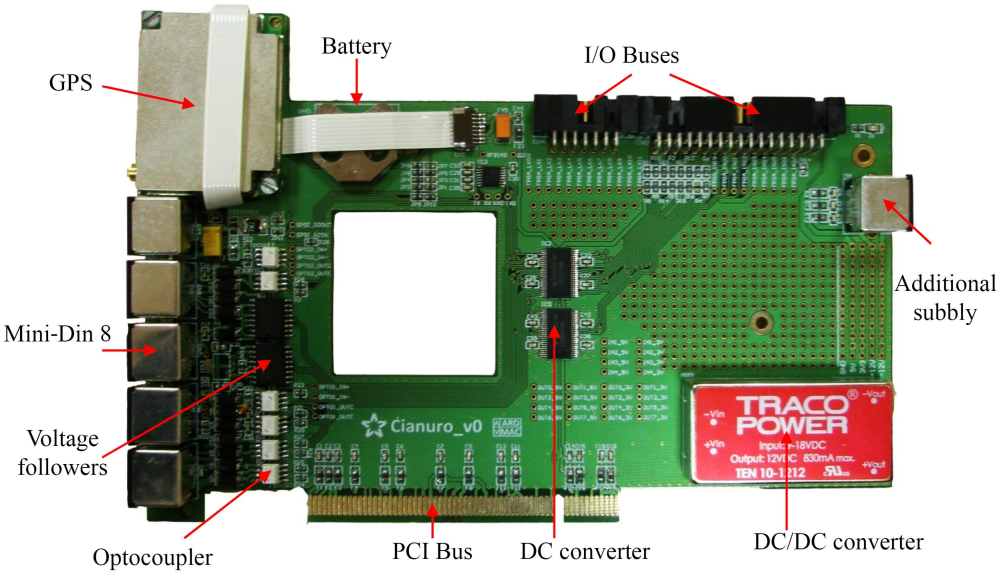

Figure 3.8: The *Cyanide* board.

The objectives we have aimed to reach at the implementation phase, were minimizing the cables length to connect the *Cyanide* board, and maximizing the integration capacity. The design of this board fits the electrical and the mechanical specifications of the PCI bus, and allows integration into the *embedded*-PC at transmission side, or into the *conventional*-PC at reception side.

The current dimensions of the *Cyanide* board allow new GPS unit to be easily installed as shown in Figure 3.8. In addition to a battery that keeps feeding the GPS unit in case of any power interruptions. The FPGA chip has been provided with signals by an I/O bus, and additional power source connected to the *BeOne* board if necessary.

A DC/DC converter for the sake of a +12 Vdc to -12 Vdc conversion, which is necessary to power some bipolar amplifiers of the front-end A/D of the POTASIO platform. A PCI connection to provide a power supply of +12 Vdc, and does fit the board at the PCI slot. Mini-Din 8 connectors to carry different signals to the various peripherals of the transmission platform.

There are several DC converters to convert signals from 0 and 3.3 Vdc to 0 and 5 Vdc, respectively in both directions. The optocoupler units turn the 0 and 5 Vdc TTL signals to an open collector in both directions. The utilization of inputs and outputs optocouplers is greatly enhancing the immunity to noise and interference. In order to ensure the necessary input current to the DC converters, voltage followers have been deployed for that purpose.

3.4.4 *Hardware* description of the transmitter

The transmitter unit is covered with a fully sealed waterproof case, which serves as a protection against rain and moisture with an electromagnetic shielding. Everything related to the digital signal processing lay inside this sealed box, concentrated within an *embedded*-PC, and all the analog and RF power, handing out a maximum power of 250 watts. In addition, it also contains the necessary devices in order to implement a WLAN network, with a redundant fiber optic connection to access the *embedded*-PC remotely. Figure 3.9 illustrates a photograph of the front side of the waterproof sealed box shown the power amplifier unit and other components.

An outstanding attention is dedicated to maximize the electromagnetic compatibility of each component, since the transmission antenna located few meters from the

Figure 3.9: Front view of the waterproof sealed box.

transmitter, and it is generating strong electromagnetic field. As mentioned previously, the material of the waterproof box acts as electromagnetic shield. Therefore, the problems usually appear with the holes that let the signals (power, control, and RF) pass. All these signals properly filtered to protect the entire system that stands inside the box. In addition, we have used connectors able to work in the severe weather with guarantee. Figure 3.10 shows some of the wires and connectors coming out from the waterproof case.

A mast of the WLAN and GPS antennas lies above the waterproof box. The antenna adapter *SG-235* from **SGC** is located just few meters from the waterproof box as illustrated in Figure 3.11. It has the responsibility of adjusting the impedance of the monopole antenna [103], through receiving control signals from the transmitter, and then adapting the impedance of the antenna and the RF signal delivers to the monopole antenna.

The adaptation process is crucial to continue correctly; nevertheless, the wave level remains negligible, which will decrease the overall efficiency of the system. This translates into low radiated power because the amplifier injects the reflected power to the power transistor. In order to improve the adaptation, manual adaptive control is implemented to force the antenna to be adapted. The POTASIO is responsible for generating the control signals, and the *Cyanide* board adjusts the electric levels.

Figure 3.10: Rear view of the waterproof sealed box.

Figure 3.11: The antenna adapter with monopole antenna at the transmission side.

A PC unit with a couple of PCI cards cannot take full responsibility of performing all the functions, but they are necessary to control the whole system. From now on, we will explain each of the peripherals and *hardware* available at the transmission side.

A *15H* GPS unit from **Garmin** is integrated into the *Cyanide* board, and responsible for providing a time synchronization to the transmitter [104]. The great novelty which incorporates this GPS device comparing to previous surveys is the Pulse Per Second (PPS) technology. A PPS is a mechanism to provide synchronization signal with an

accuracy of $\pm 1\mu$s. This new feature will greatly simplify the time synchronization between transmitter and receiver.

There is external oscillator with working frequency of 100 MHz called Oven Controlled Crystal Oscillator (OCXO) that is noted for the high stability and its small drift over time. The assistance of this clock was very important, since if the clock frequency at both transmitter and receiver is not equal, the *Doppler frequency shift* measurements will not be reliable.

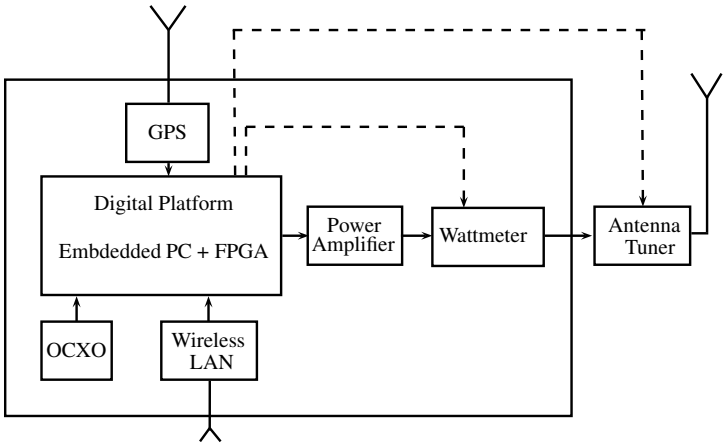

Figure 3.12: A simplified block diagram of the transmitter.

Two main subsets of peripherals are handled through the *embedded*-PC at the transmitter side - the power devices (amplifier, antenna adapter, and Wattmeter); the network devices. The first group are are controlled by a *software* that is providing system information. On the other hand, the network devices provide remote access to the whole system. A simplified block diagram of the transmitter is illustrated in Figure 3.12.

The Wattmeter unit is based on four-port directional coupler, and it is responsible for measuring the power delivered from the amplifier to the antenna adapter and calculate how much of this power is reflected due to the impedance mismatch. It provides the measurements to the *embedded*-PC through one of the four *RS-232* serial ports it has. So that, it is a key verification instrument to ensure that the transmitter works properly.

The RF signals are amplified through an amplifier unit with a nominal power of 200 Watts. These signals are controlled through an *RS-232* serial port with which it can open/close the amplifier and shows their current state.

The transmitter has an *Ethernet* module at the *Pico Radio* location that is required to access the *embedded*-PC remotely, check the status of the system, and apply new configurations. Alternatively, it is equipped with series of modules that provide wireless connectivity (IEEE 802.11 b/g), and additional optical fiber cable used as a backup to the WLAN connection.

Figure 3.13 shows the network diagram in which all the network components appear. Inside the waterproof case, you can find *switch*, wireless access point, and UTP to fiber optic converters. As shown in Figure 3.13, such architecture provides connectivity with the scientific module of the SAS and the electronic cottage located in *Punta Polaca*.

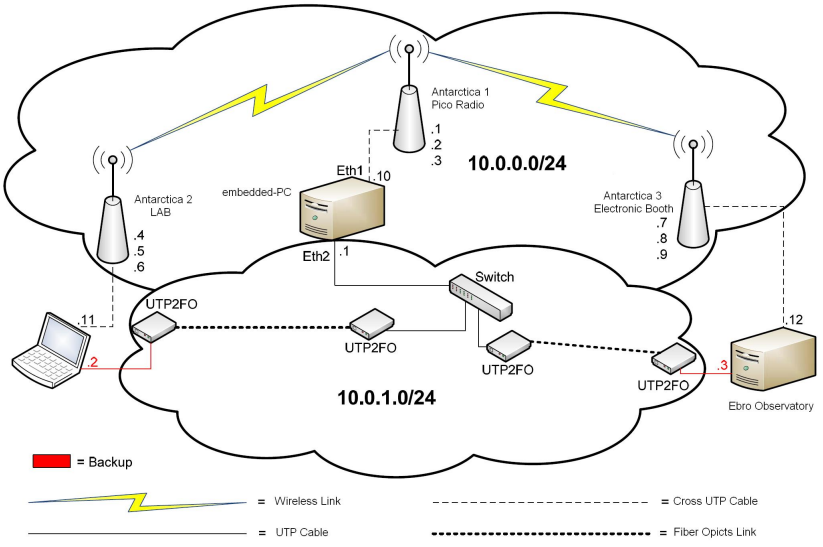

Figure 3.13: A diagram of the wireless network installed at SAS.

Therefore, it is not only possible to remotely access the *embedded*-PC of the transmitter, but the transmitter can access to the geomagnetic sensors' data. Using a client/server application, can implement a TCP/IP application to provide the geomagnetic sensor data to the transmitter; so that, it can be prepared before the transmission.

3.4.5 *Hardware* description of the receiver

Since the receiver in placed in a cabinet at the OE where the conditions are less critical than the ones in the transmitter location; therefore, there is no need for waterproof case to ensure the integrity and protection of the equipment. We have followed the same philosophy of placing all the transmitter components in one closet. So that, all

the receiver's components are located in one cabinet in order to transport the receiver comfortably without time wasting of mounting and dismounting the components of the receiver. The cabinet of the receiver contains all the components as it is depicted in Figure 3.14.

Figure 3.14: The cabinet where the receiver placed.

The receiver is able to control the power of the received signal, and several stages of amplification to handle the very low received signals. A simplified block diagram of the receiver is illustrated in Figure 3.15.

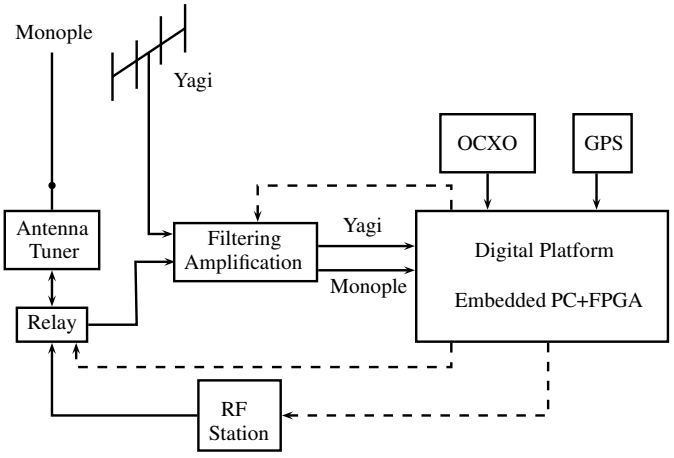

Figure 3.15: A simplified block diagram of the receiver.

The antenna adapter (*SG-230*) does the same function as the *SG-232* unit in the transmitter, with only one difference that this adapter does not support the adaptation block feature [98]. Each of the two receiving antennas (monopole and yagi) has independent amplification and filtering stages. The whole chain of filters and amplifiers that are handling the received signal is shown in Figure 3.16.

Figure 3.16: The filtering and amplification unit at the closet of the receiver.

The most notable update in the receiver of the POTASIO platform is the simultaneous reception by the two different antennas. Therefore, it takes twice as electronics intended to regenerate the small signal coming through the antenna and more control signals so far. Figure 3.17 defines in more detail the filtering and amplification block that appears in Figure 3.15.

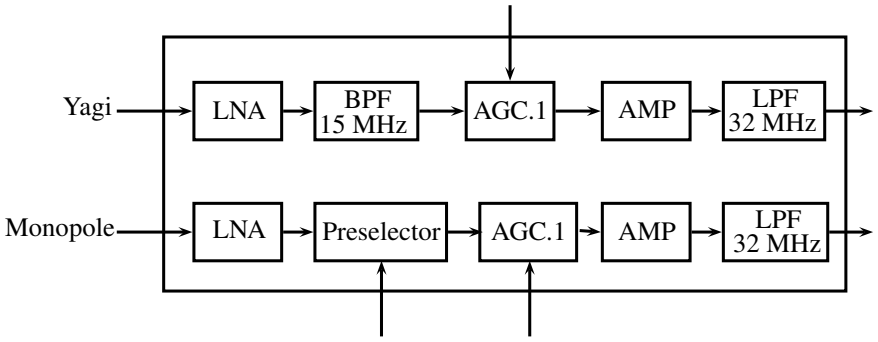

Figure 3.17: Filtering and amplification block of the receiver.

The RF station is responsible for generating RF tone of sufficient amplitude to force the antenna adapter unit (*SG-230*) to adapt the impedance of the monopole antenna. The relay appears in Figure 3.15 acts as a switch between passing the adapting tone on one direction and passing the received signal in the other direction.

Firstly, during the adaptation process, the relay releases the RF tone to the adapter unit. Secondly, once the antenna adapted, the relay lets the received signal passes to the amplification and filtering block.

The filtering and amplification block showed in Figure 3.17 consists of the following components:

- Low Noise Amplifier (LNA) deployed with noise figure of 2.5 dB and gain of 20 dB. The interception point at 1 dB is 22 dBm; therefore, this amplifier is rarely saturated despite the interference that may have happened [105].
- A 15 MHz bandpass filter tuned to the resonance frequency of the yagi antenna, and a pre-selector filter bank consists of three tunable filters that cover the whole HF band from 1.5 MHz to 30 MHz [99]. For each filter, there are 251 different adjustments, and there is a *software* installed at the receiver to determine the pass frequency for each moment. However, the major drawback of this device is the 17 dB of insertion losses.
- Two low pass filters of 32 MHz installed after each stage of amplification, with the aim of eliminating distortions or nonlinearities that may be added from the previous amplifier.
- The Automatic Gain Amplifier (AGC) provides a variable gain between -10 dB and +35 dB. Also, it offers the maximum possible dynamic range without distortion [96]. This type of amplifier is crucial to the system, because interference level that is received, is varying with time and frequency. However, it cannot always amplify as much as the maximum, otherwise there is a risk of saturating the A/D converter. So that, this AGC is controlled through the FPGA that configures the amplification levels, which means uses the maximum number of bits, without the risk of reaching the distortion point.

Part II

Contributions

Chapter 4

Oblique sounding of the ionospheric HF radio link

This Chapter is organized as follows, first in Section 4.2, there is a brief description of the SAS-OE link. Next, fundamentals of the wideband channel and wideband sounding techniques are provided in Section 4.3. Consequently through Section 4.5, the algorithms dedicated to process the received narrowband and wideband signals to determine the characteristics of the SAS-OE ionospheric link. Finally, the measurements from the narrowband and wideband sounding, such as Signal to Noise Ratio (SNR) estimation, channel availability, composite multipath spread, composite Doppler spread, propagation time, and Doppler frequency shift, are introduced in Section 4.6.

4.1 Introduction

The communications from north and south poles highlight the importance of using the ionosphere as transmission medium for the HF electromagnetic waves, since the line of sight from geostationary satellite is not totally feasible. In that sense, our research group (GRECO) was develop communications system using the ionosphere from the Spanish Antarctica Station Juan Carlos I (SAS) in Antarctica to the Ebro Observatory (OE) in Spain, to transmit magnetic data gathered from geomagnetic sensors installed in Livingston Island (South Shetland Islands) to the OE. The research project has been launched during 2003 with three main objectives:

1. sounding and modeling the SAS-OE ionospheric link, taking into account the variation of the solar activity;

2. design the best digital modulation scheme for low-power and -interference communications system;

3. implement very robust *hardware* and *software* combination that is able to run under hard environmental conditions, such as in Antarctica.

A more detailed description of this project's components can be found previously in Chapter 3 and [106]. Important contributions regarding high-latitude projects can be found in [107, 108], mid-latitude in [109, 110], and low-latitude in [111, 112].

The first channel model that has been accepted for narrowband transmissions was developed by *Watterson* [33]. Besides that, *Vogler* from the Institute of Telecommunication Science (ITS) introduced a wideband ionospheric HF channel model with *non-Gaussian* statistics and *multipath spread* parameters [113]. An HF channel simulation system that is well operative with both narrowband and wideband HF channels model was provided by *Mastrangelo* [35].

The *radiomodem* platform of the system has been updated several times since the first survey of the project during 2003/2004. Through deploying the *Software Defined Radio* (SDR) technique, three main *radiomodem* platforms have been installed at both transmitter and receiver locations. Full description of the first SDR platform, SANDICOM, can be found in [100].

During the 2005/2006 survey [96], the second generation of SDR platforms, SODIO, had been operated with a new digital platform consisted of Field Programmable Gate Arrays (FPGA), Application Specific Integrated Circuits (ASIC), and multiple high speed D/A converters as explained in Chapter 3. Measurements obtained during the 2006/2007 survey had been published in [48]. The SODIO platform had some limitations in sounding time (00:00 UTC to 11:00 UTC and 18:00 UTC to 23:00 UTC), sounding frequency (4.5 MHz to 16.5 MHz), and the measurement capability. For these reasons, the daytime data, such as channel availability, *composite mutipath spread*, and *composite Doppler spread*, had not been obtained due to changing the configuration of the system, which was carried out manually by the staff in the SAS. Other parameters could not be measured, such as *Doppler frequency shift* and propagation time, on account of *hardware* lack.

Finally, since 2009/2010 survey, third generation SDR platform called POTASIO has been installed in both SAS and OE. The new system is easier to handle and maintain than the previous one, and is able to operate during 24 hours per day with an extended frequency range from 2 MHz to 30 MHz. Therefore, the results obtained by using this platform represent a substantial improvement to the previous work.

4.2 Link description

This section discusses some important characteristics of the SAS-OE ionospheric link, such as the locations of the transmitter and receiver, study of the trajectory of the wave, and the solar variation influence in terms of the sunrise and sunset during the 2009/2010 survey. Figures 4.1, 4.2, and 4.3 show the maps of the geographical locations of the transmitter, the receiver, and the geodesic path of the link, respectively.

First, the transmitter is located at the SAS, South Bay (Hurd Peninsula) of Livingstone Island (South Shetland Archipelago), with coordinates of 62.6 S, 60.4 W. As mentioned in Chapter 3, the actual location of the antenna is near the peak of *Pico Radio*, which is around 500 meters far from the SAS at altitude of approximately 100 meters, and it has been selected due to the minimization of the orographic obstacles presence in the direction of the receiver.

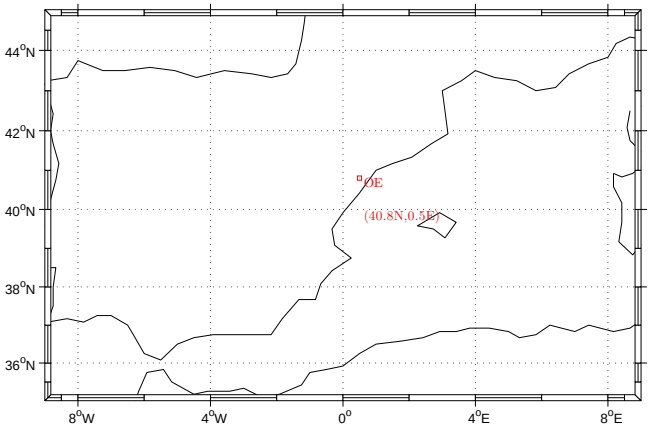

Figure 4.1: The location of the receiver at OE, Spain.

Second, the receiver is installed at the OE, Roquetes, Spain, with coordinates of 40.8 N, 0.5 E, and the trajectory in the direction of the transmitter (azimuth 206.2 SW) is free of obstacles. The length of the transmission link measured on the surface

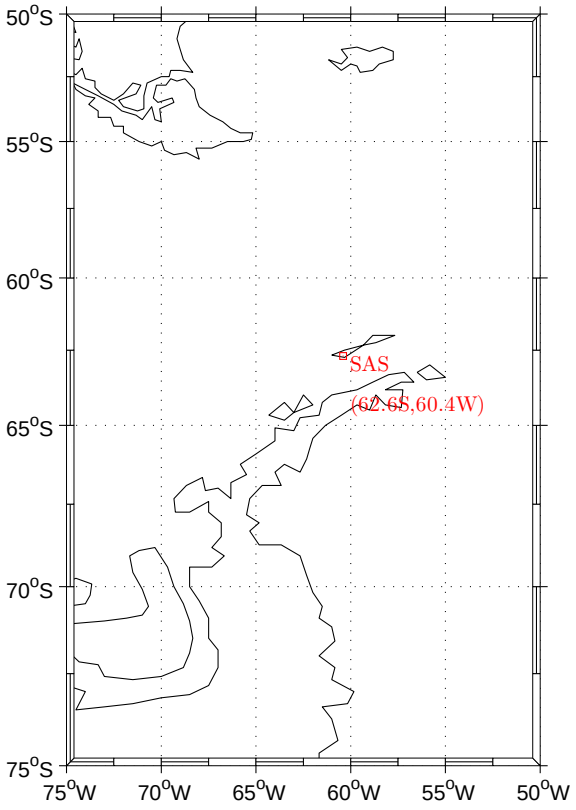

Figure 4.2: The location of the transmitter at the SAS, Antarctica.

Station	Latitude	Longitude	Distance from the TX (km)
SAS(TX)	62.7 S	60.4 W	0
H1	50.4 S	43.6 W	1580
H2	21.1 S	27.4 W	4755
H3	1.3 N	17.3 W	7930
H4	28.2 N	7.1 W	11105
OE(RX)	40.8 N	0.5 E	12700

Table 4.1: The locations of the transmitter, receiver, and the four reflection hop.

of the Earth is about 12700 km, crossing the Equator, 103.4 degrees latitude and 60.9 degrees longitude with a 4 time zones.

Since the maximum distance can be established by an ionospheric link is about 3000 km [114], we supposed that link is segmented into four segments of around 3000 km long. Table 4.1 shows the approximated location of each reflection hop.

The solar activity on the portion of the ionosphere has a major role to be taken into account, in order to perfectly interpret the channel sounding results of each survey. Over the period of the austral summer (November to March), Figures 4.4 and 4.5

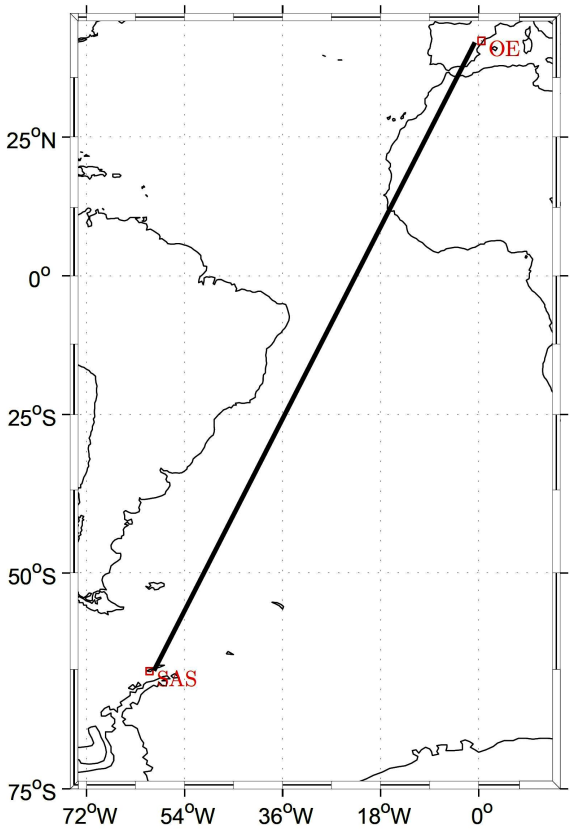

Figure 4.3: The locations of the transmitter, receiver, and the approximation path of the link.

illustrate graphically the evolution of the sunrise and sunset at the four reflection hops. Regarding the sunrise, as shown in Figure 4.4, it is observed that every day, the Sun is rising with a maximum time gap slightly over half an hour in all reflection hops, and the vanish of the Sun is practically simultaneous over the link and during all the days of the survey. To carry out the narrowband channel sounding using the whole HF band, it takes one hour for utilizing around 60 different frequencies from 2 MHz to 30 MHz with a step of 500 kHz.

Similarly, with respect to the sunset, we noticed that the Sun goes down with a time difference of four to five hours between the first and the last reflection hop. Therefore, the effect of the sunset is progressive over the link with a total duration of the process between 4 and 5 hours. Additionally, the inter-day behavior of the ionosphere towards the electromagnetic waves propagation is virtually equivalent for all the days of the survey.

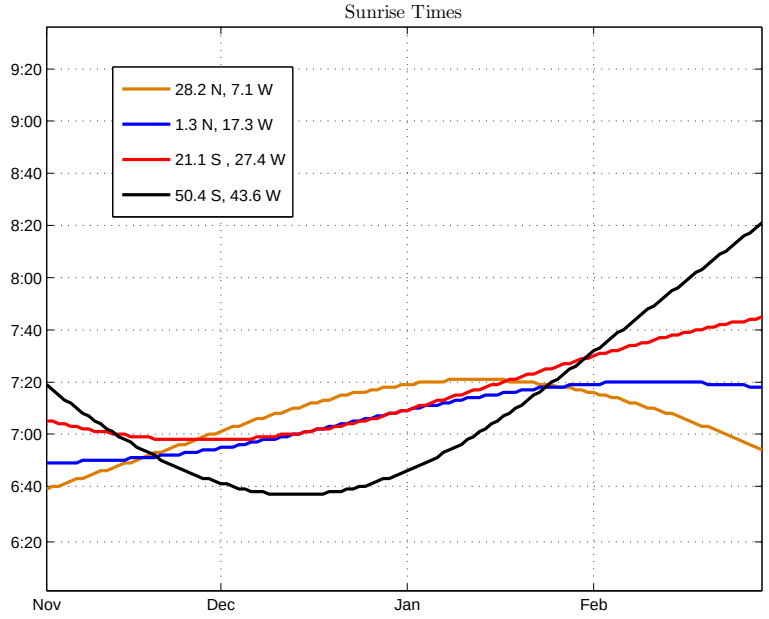

Figure 4.4: The sunrise times at the four reflection hops.

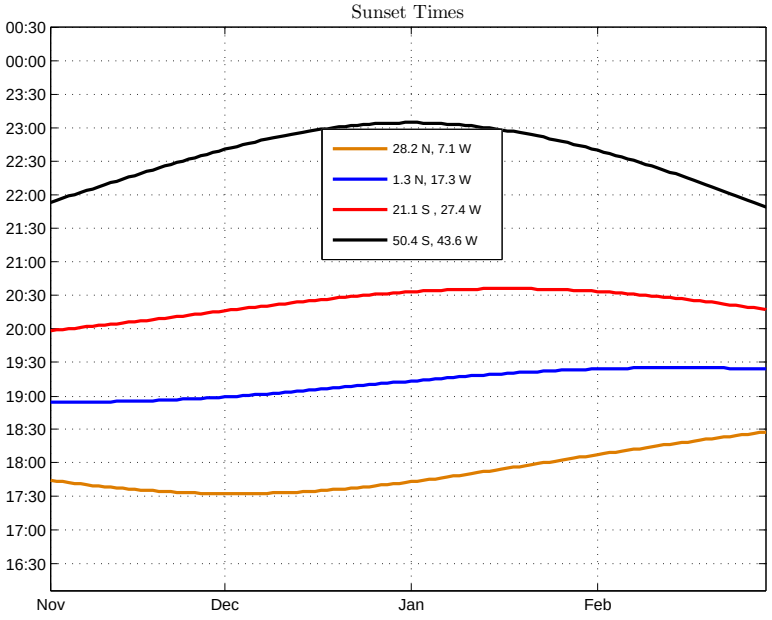

Figure 4.5: The sunset times at the four reflection hops.

4.3 Wideband theoretical basics

Sounding an ionospheric channel is carried out through two main techniques according the demanded parameters, narrowband and wideband. The narrowband sounding will result in the estimation of the SNR and the channel availability, in addition to the wideband sounding, which is responsible for measuring the wideband SNR, *composite*

multipath spread, *composite Doppler spread*, propagation time, and *Doppler frequency shift*. Practically, the wideband channel sounding needs more computations due to high levels of complexity. In this section, we are reviewing the theoretical fundamentals of the wideband channel and the techniques used to wideband sounding the ionosphere.

This section is organized as following, a brief comparison is presented between the narrowband and wideband channel; then, there will be an introduction of the linear time-variant characterizations, such as imposing the conditions of stationary in the wide sense. Consequently, we will describe the ionospheric channel in terms of the *scattering function*, *power delay profile*, and *Doppler power profile*. Finally, we will review several wideband sounding methods, with particular emphasis on technique based on *pulse compression*, which is applied through the project.

The channel characterization defines the behavior of the ionosphere on towards the radio waves propagation. There are several parameters that should be determined in order to characterize any type of channel, these include: time and frequency dispersion; interference levels; noise.

Regarding the time dispersion of the channel, the transmission bandwidth B_s compared to the coherence bandwidth of the channel B_c distinguishes two different situations, which will be discussed below.

The first is the wideband situation, which is occurred only if the $B_s > B_c$. Then the frequency components of the signal undergo different variations; and consequently, produces a *frequency selective fading*, which in the time domain expressed in form of *intersymbol interference* (ISI). In this case, the behavior of the channel is described using functions in the time or frequency domain, which obtain information about the channel dispersion, such as *composite multipath spread* and *composite Doppler spread*. The wideband channel sounding can be performed using different techniques based on sending periodic pulses (e.g., *pseudo random* sequences (PN-sequences)) as we will describe later.

The second one is called narrowband, which will take place only if the $B_s < B_c$. In such condition, the different frequency components of the signal experiment similar variations in amplitude and phase, which result in a phenomena called *flat fading*. The narrowband sounding can be carried out through sending unmodulated carriers; and then, the time evolution of the envelope and phase are measured at the reception. If the channel is variant in time:

- The slow variation of the envelope called *slow fading*, *shadow fading* or *long term fading*, and usually, it can be modeled by a *lognormal* probability distribution.
- The rapid variation of the envelope named *fast fading* or *short-term fading*, which become accustomed to model through a *Rayleigh* or *Rice* probability distribution in the absence or presence of direct ray, respectively.

4.3.1 Characterizations of wideband channel

The characterizations of a wideband communications channel are framed within the paradigm of the description of linear time-varying system that introduces four channel functions for this purpose. The study starts with a deterministic channel, and later on, this assumption will be modified to more realistic situation with random variations of the channel. The baseband complex signal $s(t)$ interacts with the bandpass signal $x(t)$ through the following expression:

$$x(t) = \Re\{s(t)e^{j2\pi f_c t}\} \tag{4.1}$$

where f_c defines the carrier frequency.

For example, let the $s(t)$ is the input to a linear deterministic channel, which is time variant with impulse response $h(t,\tau)$; so that, the output $r(t)$ is expressed with the following equation as mentioned in [115, 116]:

$$r(t) = \int_{-\infty}^{\infty} s(t-\tau)h(t,\tau)d\tau \tag{4.2}$$

where t represents the time variable and τ is the *delay*. Although, in real systems, the integration limits of the previous equation should be bounded between 0 (the function $h(t,\tau) = 0$ for $\tau < 0$) and T.

We will keep the notation of Equation 4.2 for simplicity and consistency with the literature. The $h(t,\tau)$ function, which relates the input and output in time domain, is often found in the literature under the name of *input delay-spread function*.

Similarly we usually define the function $H(f,\nu)$ from the following expression that connects the input and output in the frequency domain:

$$R(f) = \int_{-\infty}^{\infty} S(f-\nu)H(f-\nu,\nu)d\nu \tag{4.3}$$

where ν is the *Doppler* variable. Then the $T(f,t)$ function will connect the input in the frequency domain and output in the time domain as:

$$r(t) = \int_{-\infty}^{\infty} S(f)T(f,t)e^{j2\pi ft}df \tag{4.4}$$

where f defines the frequency variable. Equation 4.3 is called the *output Doppler-spread function*, and Equation 4.4 is the *time-variant transfer function*.

The fourth function of the channel characterization will be obtained through replacing $h(t,\tau)$ in equation 4.2 by its dual frequency function $S(\tau,\nu)$ that is going to result in the *delay-Doppler spread function*:

$$h(t,\tau) = \int_{-\infty}^{\infty} S(\tau,\nu)e^{j2\pi\nu t}d\nu \tag{4.5}$$

and then,

$$r(t) = \int_{-\infty}^{\infty}\int_{-\infty}^{\infty} s(t-\tau)S(\tau,\nu)e^{j2\pi\nu t}d\nu d\tau \tag{4.6}$$

The four functions represent different views of the same phenomenon. Taking into account that $\tau \leftrightarrow f$ and $t \leftrightarrow \nu$ are often $time \leftrightarrow frequency$ dual variables. Those four functions of channel characterization are being interrelated through the Fast Fourier Transform (FFT) of one of its variables. Through the work of the project, $S(\tau,\nu)$ will be the most usable function, since it permits the characterization of the channel, and explanation of the dispersive behavior in both time and frequency domains.

It seems more convenient; however, to use statistical tools in case of modeling an ionospheric communications channel. As the variations of the ionosphere are highly complex, a comprehensive knowledge of all the phenomenas that intervene is not possible; therefore, this is perceived as random variation. A statistical approach involves a review of the nature of the previous functions, which will now be stochastic processes.

A complete description of the channel requires the knowledge of the joint probability density functions of the channel. As this knowledge is not generally acceptable, a more realistic and sufficiently careful in most cases is based only on obtaining the correlation functions of the channel functions, which will be defined as:

$$R_h(t, s; \tau, \eta) = E[h(t, \tau)h^*(s, \eta)] \tag{4.7}$$

$$R_H(f, m; \nu, \mu) = E[H(f, \nu)H^*(m, \mu)] \tag{4.8}$$

$$R_T(f, m; t, s) = E[T(f, t)T^*(m, s)] \tag{4.9}$$

$$R_S(\tau, \eta; \nu, \mu) = E[S(\tau, \nu)S^*(\eta, \mu)] \tag{4.10}$$

The first function that expressed in Equation 4.7, called the *input delay-spread function*. The second one named as *output Doppler-spread function*, and defined in Equation 4.8. The third function determined in Equation 4.9, and called the *time-variant transfer function*. Finally, the fourth called the *delay-Doppler spread function* and expressed in Equation 4.10. Furthermore -

- t and s are the time variables;
- τ and η are of the *delay*;
- f and m are the frequency variables;
- ν and μ are of the *Doppler*.

A common assumption in characterizing any communications channel is to consider that the contributions of the amplitude and phase from different paths are uncorrelated (*uncorrelated scattering*). Thus, the correlation functions evaluated by two different *delays* τ, where η will be zero whenever $\tau \neq \eta$.

The four correlation functions that will be defined below, depend on each of the four variables. This description can be simplified, assuming a stationary channel behavior at wide sense (WSS: *wide-sense stationary*), i.e., assuming that the correlation functions are invariant to a time translation. So the dependence with the time variables (t and s) is of the following form:

$$\zeta = s - t \tag{4.11}$$

In addition, the WSSUS channel has a dual time-frequency behavior, as the dependency of the frequency variables (f and m) will be in form of $\Omega = m - f$, and the correlation functions evaluated for two *Doppler frequency shifts* (ν and μ) will

be neglected as $\nu \neq \mu$. So that, through incorporating the two conditions of the WSSUS (*wide-sense stationary, uncorrelated scattering*) to the definition of the correlation functions, we will obtain:

$$R_h(t, s; \tau, \eta) = \delta(\tau - \eta) R_h(\zeta; \tau) \tag{4.12}$$

$$R_H(f, m; \nu, \mu) = \delta(\nu - \mu) R_H(\Omega; \nu) \tag{4.13}$$

$$R_T(f, m; t, s) = R_T(\Omega; \zeta) \tag{4.14}$$

$$R_S(\tau, \eta; \nu, \mu) = \delta(\mu - \tau)\delta(\nu - \mu) R_S(\tau, \nu)] \tag{4.15}$$

The well-known *scattering function* $R_S(\tau, \nu)$ presents the characterization of the channel in terms of time and frequency dispersion. In addition to, it is related with the $R_h(\zeta; \tau)$ through the Fourier transformation:

$$R_S(\tau, \nu) = \int_{-\infty}^{\infty} R_h(\zeta, \tau) e^{-j2\pi\zeta\nu} d\zeta \tag{4.16}$$

From Equation 4.16, we will determine the *multipath intensity profile* or *power delay profile* according to the following expression [117]:

$$\phi(\tau) = \int_{-\infty}^{\infty} R_S(\tau, \nu) d\nu \tag{4.17}$$

The *power delay profile* gives the distribution of the power at the output of the channel as a function of *delay*. In general, the range of *delays* for which the *power delay profile* is different from zero determines the *delay spread* of the channel (τ_m). The inverse of τ_m called the *coherence bandwidth* of the channel (B_c), and corresponding to the maximum separation of two frequencies for experiencing equal distortion when passing through it, which is exactly the condition of the narrowband channel.

For consistency with the literature [107], we are measuring the time dispersion of the channel as the *composite multipath spread* τ_c, which is defined as the width of the *power delay profile* region comprising 80% of total power.

Similarly, the *Doppler power profile* or the *Doppler power spectrum* can be obtained from the *scattering function* $R_S(\tau, \nu)$ according to this expression:

$$\phi(\nu) = \int_{-\infty}^{\infty} R_S(\tau, \nu) d\tau \tag{4.18}$$

The *Doppler power profile* gives the distribution of power at the output as a function of *Doppler* values. In general, the range of *Doppler* for which the *Doppler power profile* is different from zero determines the *Doppler spread* of the channel (ν_m). The inverse of ν_m called the *coherence time* of the channel (T_c), which determines the time interval as the channel considered stationary.

For the same reasons as in the case of *delay spread*, we will measure the frequency dispersion of the channel by the *composite Doppler spread* parameter ν_c that is presenting the width of the *Doppler power profile* region including 80% of total power.

4.3.2 Wideband sounding techniques

The importance of the channel sounding comes when experimental data needed to derive the necessary parameters for the channel characterization. This section describes two groups of wideband sounding techniques [115]. Generally, both of these groups aimed to obtain any of the channel functions that have been described previously (in the first instance, usually the $h(t, \tau)$) through sending appropriate wideband signals. The techniques for the wideband sounding are classified into, *pulse compression sounding* and *periodic pulse sounding*.

4.3.2.1 Pulse compression techniques

This type of sounding is based on the power distribution of the sounding signal through longer time intervals avoiding power surges that will be produced in the other group. Thus, sounding signals will not be short pulses but sequence with specific properties, which ideally are of white noise. Recall that if white noise $n(t)$ is applied to the input of a linear system $h(t)$; then, the output will be correlated with a delayed replica of the noise $n(t - \tau)$, and the corresponding correlation coefficient will be proportional to the channel impulse response for this *delay* value ($h(\tau)$), i.e.,

$$\begin{aligned}\phi_n(\tau) &= E\Big[\int_{-\infty}^{\infty} n(t-t_0)h(t_0)dt_0 n^*(t-\tau)\Big] \\ &= \int_{-\infty}^{\infty} E\big[n(t-t_0)n^*(t-\tau)\big]h(t_0)dt_0 \\ &= N_0 h(\tau) \end{aligned} \tag{4.19}$$

In practice, deterministic sequences are typically used with correlation properties similar to those of white noise [118], such as *m-sequences*, *Barker*, complementary chirp, etc. Thus, for example, the *m-sequences* $s_l(t)$ of length l have the following property:

$$\phi_s(t_0) = E[s_l(t)s_l(t-t_0)] = \begin{cases} l & t_0 = 0 \\ -l & t_0 \neq 0 \end{cases} \tag{4.20}$$

which approximates the autocorrelation of a white noise. Generally, a sequence length that each time increases the total transmission energy associated with the sequence, will improve the detection at the receiver. On the other hand, when the channel is time variant, the sequence transmission must be periodic and frequent enough to properly follow the variations.

In order to obtain the characterization of the channel, the *pulse compression* techniques used at the reception side are classified into three categories:

1. Convolutional based techniques - that accustomed to apply matched filter to the sounding sequence at reception. This filter is usually implemented through *Surface Acoustic Wave* (SAW) technology. Therefore, it will significantly simplify the complexity and the cost of the receiver, since at the reception, is not necessary to regenerate a replica of the transmitted sequence and correlate it to obtain the channel impulse response.

   The major drawbacks associated to this method are:

   - The performance of the SAW filters is limiting the goodness of the estimation; and thus, reducing the sensitivity.
   - The channel impulse response obtained at the output of the SAW filter tuned to a high frequency. Thus, the amount of the resulted *real-time* data is not easily storable using moderate cost devices.

- Additionally, this data corresponds already to the channel impulse response; so that, it is not possible to store unprocessed data of the survey.

2. *Swept time-delay cross-correlator* - it is based on the use of PN-sequence of chip period T_c coincides with the resolution obtained in estimation of the channel impulse response. The *Swept time-delay cross-correlation* method allows obtaining the same resolution using much larger chip periods (or get higher resolutions without increasing the chip period), for the sake of the performance in monitoring the variability of the channel.

   Let's demonstrate an example, suppose that we have a sounding signal $s(t)$ based on a PN-sequence with chip period of T_c and period of T. The baseband signal in the reception $r(t)$ has a relation with the $s(t)$ as expressed in Equation 4.2. We consider the correlation of the sounding signal at reception (r_{co}) centered at intermediate frequency f_{if} that has expressed as:

$$f_{if}(r_{co} = r(t)e^{j2\pi f_{co}t}) \tag{4.21}$$

   with a replica of the sounding sequence modulated at frequency:

$$f_{co} - \delta f_{if}(s(t)e^{j2\pi(f_{co}-\delta f_{co})}) \tag{4.22}$$

   The value of $k = \frac{f_{co}}{\delta f_{co}}$ must be sufficiently high in order to make the difference between $s(t)e^{j2\pi f_{co}t}$ and $s(t)e^{j2\pi(f_{co}-\delta f_{co})t}$ small enough in an interval T; hence, the degradation due to the correlation of the frequency difference will be negligible.

   It is usual to consider that a value of $k = 5000$ is sufficient for that purpose [119]. Suppose we take an integration period kT while the channel is considered stationary. Therefore, if the width of the Fourier transform mainlope of the autocorrelation function of $s(t)$ is $2/T_c$, the same measure for the correlation of the two signals slightly displaced in frequency, will be $2k/T_c$. Therefore, you will get an estimation of the channel impulse response with a resolution of k times better, without increasing the chip period T_c of the sounding sequence. Now, the channel is not monitored every T but at each kT.

   Referencing to the computational cost, systems applying this type, is more complex than the first one that based on correlation, since it requires higher signal processing to generate a replica of the modulated sounding sequence $f_{co} - \delta f_{co}$.

3. Techniques based on the utilization of correlation algorithm to figure out the channel impulse response at the receiver. These techniques have been classified into two types according to the sequence that will be applied:

   - Methods using *chirp* signals, will lead to sounding signal $s(t)$ taking this form:

$$\begin{aligned} s(t) &= \sum_{n=0}^{N-1} s_x(t-nT) \\ &= \sum_{n=0}^{N-1}\sum_{i=0}^{l-1} e^{j2\pi B(\frac{i^2}{l}-i)} p(t-i\frac{T}{l}-nT) \end{aligned} \tag{4.23}$$

     where T is the transmission period of the *chirp*, $p(t)$ determines the signaling pulse, $\Delta t = NT$ defines the time interval of the sounding, and $[-B, B]$ represents the sounding bandwidth.

   - Methods that utilizing PN-sequences; hence, the sounding signal $s(t)$ will be defined as below:

$$\begin{aligned} s(t) &= \sum_{n=0}^{N-1} s_{pl}(t-nT) \\ &= \sum_{n=0}^{N-1}\sum_{i=0}^{l-1} b_i p(t-iT_c-nT) \end{aligned} \tag{4.24}$$

     where T is the transmission period of the sequence, $T_c = \frac{T}{l}$ determines the chip period, $s_{pl}(t)$ defines PN-sequence of l length interpolated with signaling pulse $p(t)$, $\Delta t = NT$ represents the time interval of the sounding signal, and $b_i \in \{-1, 1\}$ are the sequence chips. The sounding bandwidth takes the form of $1/T_c$. This technique allows sounding channels unambiguously with impulse response of length less than T, and provides a resolution of *delay* T_c, supports a *Doppler* resolution of $\frac{1}{\Delta t}$ and maximum *Doppler* of $\frac{1}{2T}$.

   Some advantages of the techniques based on the use of correlation algorithms in reception are:

   - the signal generation is very simple. In the case of the PN-sequence, it uses feedback shift registers or memory;
   - they have higher robustness against the noise and interference;

- if the signaling pulse response is not considered, the sounding signal will have a constant envelope.

4.3.2.2 Periodic pulses sounding technique

The *periodic pulses sounding* technique is mainly based on sending high power pulses of very short duration, such as the *pseudo-impulse*, which is being transmitted periodically towards the ionosphere. The channel impulse response $h(\tau)$ is obtained from the received signal, and through repetitive transmission we can track the variability of the channel. The transmitted pulses are widely separated in time; so that, the echoes of the signal can be resolved without ambiguity. Meanwhile, it should be frequent enough to allow sufficient monitoring of the channel variability.

The most important advantage of this sounding technique is the simplicity. On the other hand, the main disadvantage is the need to generate pulses with extremely high power, in case of sounding highly attenuated channel or having to resolve underpowered echoes of the signal. Besides that, it presents low immunity against the noise and interference. Such method has been used successfully in the past, especially in the mobile environments [120]. However, its disadvantages did not encourage the utilization for the ionospheric channel sounding.

In the work framed in this chapter, we have used wideband sounding method based on the correlation algorithm with PN-sequences as it will be explained later on through this chapter.

4.4 Structure of the channel sounding

Herein, there will be a general description of the sounding structure of the ionsopehric link between the SAS and OE throughout each survey, starting from the 2009/2010 survey. The time period of each step of the sounding process depends on predefined working plan with the ability to *real-time* changing.

Figure 4.6 shows the used structure of the sounding. Briefly the main points of the structure are below:

- A survey means the time period during the austral summer while the channel sounding is taking place.

- The survey consists of several consecutive or alternative days.
- Each day of the sounding survey is comprising 24 hours of sessions, one hour is the time period of each session.
- Each session is divided into 56 sub-sessions of one minute each and one sounding frequency. Generally, all the sub-sessions of one session are identical except for the sounding frequency and eventually some other configuration parameters of the transceiver. The process of changing the parameters developed along with the project lifetime. It started from suspending all the sounding actions to *real-time* reconfigurations since the 2009/2010 survey.
- Each sub-session consists of three time intervals:
  - there are few seconds to adapt the antenna with the frequency of the sub-session, both in emission and reception when using a monopole, through a low power tone;
  - a time interval for the narrowband sounding of the channel by using un-modulated tones;
  - a time interval dedicates to wideband sounding by sending PN-sequence.

  The duration for each interval is configurable, and among the first and second intervals, the system automatically adjusts the gain of Variable Gain Amplifier (VGA) for this sub-session.

  The sounding intervals (both narrowband and wideband) in reception starting one second before and one second after the transmission (called *Guard time*). This property makes it robust to inaccuracies in time synchronization between transmitter and receiver and also allows evaluating the SNR at the reception.

4.5 Analysis algorithms of channel sounding

This section is dedicated to explain several algorithms, which are used to analyze the received signal regarding both types of experiments (narrowband and wideband). These algorithms upgraded from both theoretical and programmable point of view throughout the project lifetime.

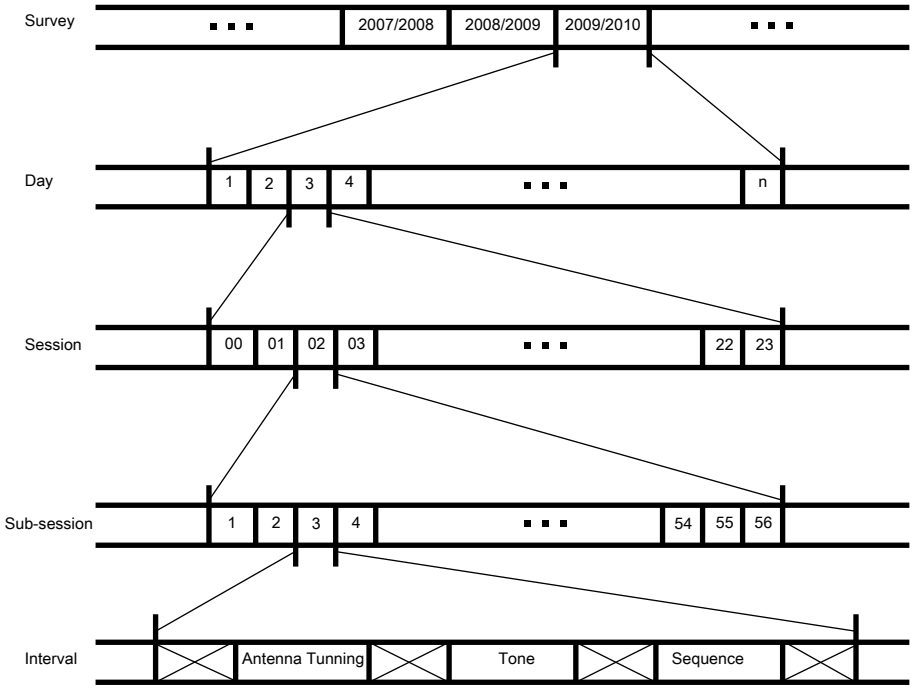

Figure 4.6: The sounding organization.

4.5.1 Algorithms of the narrowband sounding

First of all, the configuration of the narrowband sounding experiment used during the 2009/2010 survey is shown in Table 4.2. Generally, for each narrowband sounding interval, the link availability $a_n(f, h, d)$ is binary evaluated in the following form:

$$a_n(f,h,d) = \begin{cases} 1 & \text{if the tone detected in reception} \\ -1 & \text{otherwise} \end{cases} \tag{4.25}$$

The detection process of the narrowband sounding tone is based on the measurements of the SNR at a given bandwidth (SNR_B). The SNR_B is estimated in the time domain, taking advantage of the received narrowband sounding interval I_{rx}, which begins a second before and a second after the transmission I_{tx}. The *Guard time* raises the detection probability of the received narrowband sounding signal. Then:

$$\text{SNR}_B = 10\log_{10}\left(\frac{P(t \in I_{tx})}{P(t \in I_{rx}, t \notin I_{tx})}\Big|\Big|_B\right)[\text{dB}] \tag{4.26}$$

Before calculating the SNR_B, the tone frequency must be detected in reception. In theory, the tone frequency at the output of the Digital Down Converter (DDC) should be centered at zero. Practically, there will be *Doppler frequency shift* caused by frequency drift between the clocks that govern the transmitter and the receiver. At the reception, such drift makes the tone being observed in different positions, within a frequency range called Δf. Due to the previous factor, the frequency at which the tone is detected (δf) increases along with the sounding frequency f increment. Prior to the 2009/2010 survey, Δf was observed of around tens of Hz; however, since the 2009/2010 survey, it is decreased to less than 1 Hz because of the deployment of the Oven Controlled Crystal Oscillator (OCXO) unit. It is found that the relationship between δf and f is approximately a straight line and defined as:

$$\delta f = x + y.f \tag{4.27}$$

where the values of x and y vary every session. Below we will discus four algorithms used to be applied consecutively or alternatively to the received signal from the narrowband sounding experiment before 2009/2010 survey (4.5.1.1, 4.5.1.2, 4.5.1.3, and 4.5.1.4), to firstly, detect the frequency of the tone in reception δf; and then, estimate the SNR_B.

Due to the large frequency drifts between the transmitter and the receiver, the first step for analyzing the received narrowband tones was dividing the Δf into certain number of subbands. Then start looking for the subband with the highest frequency component, apply the rest of the analysis on the selected subband. From the δf and SNR_B, the availability of SAS-OE link is determined for each sounding interval $a_n(f, h, d)$.

However, the utilization of a high stable clock at both transmitter and receiver, such as the OCXO, is decreasing the frequency drifts to very low levels. So that, since 2009/2010, there was no need to divide the Δf, and we can calculate the SNR_B directly from the received tones after applying just two algorithms, i.e., 4.5.1.5 and 4.5.1.6.

It is noteworthy mentioning that the application of those algorithms over the narrowband signal depends on the capabilities of the system. Prior to the 2009/2010 survey, the first four algorithms were implemented in MATLAB. Consequently, from the 2009/2010 survey all the algorithms were being implemented in C++, which gives

Sampling Frequency	100000	Hz
Time Interval	1–11	s
Guard time	1	s
Window Filter	*Kaiser*	
Window Bandwidth	12	Hz
Portion length	0.5	s
Threshold values	3, 6, 9, 15	dB

Table 4.2: The configuration setup for the narrowband sounding during the 2009/2010 survey.

us the ability to observe the measurements in a daily base due to the high speed of execution.

4.5.1.1 First algorithm

To overcome the effect of the frequency drifts, this algorithm has operated on each narrowband sounding interval independently. It calculates the SNR_B for the most powerful components of the N_{sb} equal subbands. Subsequently, it choses the estimation of the tone frequency in reception δf regarding to the subband with the highest SNR_B.

Empirically, it has been observed that the interval $\Delta f = (10, 160)$ Hz always includes δf for the entire sounding frequency range. We selected the number of subbands as $n_{sb} = 5$. High value of n_{sb}, improves the probability of reception; but at the same time, slows the execution time.

The higher bandwidth values will increase the amount of noise in the measurement; therefore, the probability of detection will be declined. Finally, a bandwidth value of $B = 10$ Hz has been selected since 2005/2006 survey.

In spite of subband division technique, sometimes the sounding tone can be masked. For that reason, we implemented the second algorithm.

4.5.1.2 Second algorithm

This algorithm has operated together with the first one over all narrowband sounding intervals of a session. For each session, it calculates the line that best approximates the relationship between (δf) and sounding frequency f.

4.5.1.3 Third algorithm

This algorithm operates on each narrowband sounding interval independently. It maximizes the probability of detecting the tone at reception in the presence of high level of interference within the Δf interval, which forces the detection to be carried out in a setup of suitable δf.

4.5.1.4 Fourth algorithm

This algorithm operates jointly on all the narrowband sounding intervals of the session. The availability value assigned under the following conditions (all values of the SNR_B expressed in dB):

$$a_n(f,h,d) = \begin{cases} 1 & \text{if } \mathrm{SNR}_{B_{f,h,d}} \geq 6 \\ 1 & \text{if } \mathrm{SNR}_{B_{f,h,d}} \in (3,6) \cap (\mathrm{SNR}_{B_{f_{-1},h,d}} \geq 3 \cup \mathrm{SNR}_{B_{f_{+1},h,d}} \geq 3) \\ -1 & \text{otherwise} \end{cases} \tag{4.28}$$

where the notations f_{-1} and f_{+1} make reference to the measure on the previous and subsequent sounding frequency.

4.5.1.5 Windowing algorithm

The previous four algorithms were applied to mitigate the effect of the high frequency drifts, and then calculate the SNR_B, but along with installing the OCXO clock, which is highly notable for its frequency stability, the errors in the frequency synchronization become very low (essentially less than one Hz). Instead of usually executing four algorithms to calculate the SNR_B values of the received tones; from the 2009/2010 survey, we defined two consecutive algorithms to handle the received narrowband tones; and then, calculate the SNR_B and accordingly, the narrowband channel availability. So that, the philosophy of the analysis has been changed completely to install highly notable hardware components instead of apply multiple algorithms, which if applied, will be or will not be able to recover the non synchronized signals.

In order to have a useful received signal power profile, the first step is filtering the received signal properly. In our case, this is carried out in the frequency domain by multiplying the Fast Fourier Transform (FFT) of the received signal by the frequency response of several window filters. Such a filter has two main features:

1. It should eliminate signals at frequencies apart from the reception frequency.

2. It should have a good time response to avoid creating transients from the impulsive interferences that fall far away from the reception frequency.

An example of a perfectly received narrowband signal filtered by an ideal rectangular window is shown in Figure 4.7, while a highly interfered one is shown in Figure 4.8. The window filter should deal with both cases. In the literature, several window functions can be found. However for the reason of simplicity, we have just applied four windows which are *Blackman*, *Hanning*, *Flattop*, and *Kaiser*.

A comparison between the four window functions is illustrated in Figure 4.9 and Table 4.3. The windows' time domain response is derived as:

1. The *Blackman* window function depicted in [121], is calculated as:

$$w_B(n) = a_0 - a_1 \cos\left(\frac{2\pi n}{N-1}\right) + a_2 \cos\left(\frac{4\pi n}{N-1}\right) \tag{4.29}$$

   where $a_0 = 1 - \alpha/2,\ a_1 = 1/2,\ a_3 = \alpha/2$;

2. The *Hanning* window function mentioned in [121], is determined as:

$$w_H(n) = 0.5\big(1 - \cos(\frac{2\pi n}{N-1})\big) \tag{4.30}$$

3. The *Flattop* window function according to [122], is defined as:

$$\begin{aligned} w_F(n) &= a_0 - a_1 \cos\left(\frac{2\pi n}{N-1}\right) + a_2 \cos\left(\frac{4\pi n}{N-1}\right) \\ &- a_3 \cos\left(\frac{6\pi n}{N-1}\right) + a_4 \cos\left(\frac{8\pi n}{N-1}\right) \end{aligned} \tag{4.31}$$

   where $a_0 = 0.215,\ a_1 = 0.416,\ a_2 = 0.277,\ a_3 = 0.083,\ a_4 = 0.006$;

4. The *Kaiser* window function defined in [123] as:

$$w_K(n) = \frac{I_0(\pi\alpha\sqrt{1 - (\frac{2n}{N-1} - 1)^2})}{I_0(\pi\alpha)} \tag{4.32}$$

   where I_0 referred to zero-th order modified *Bessel* function of the first kind, and usually $\alpha = 3$.

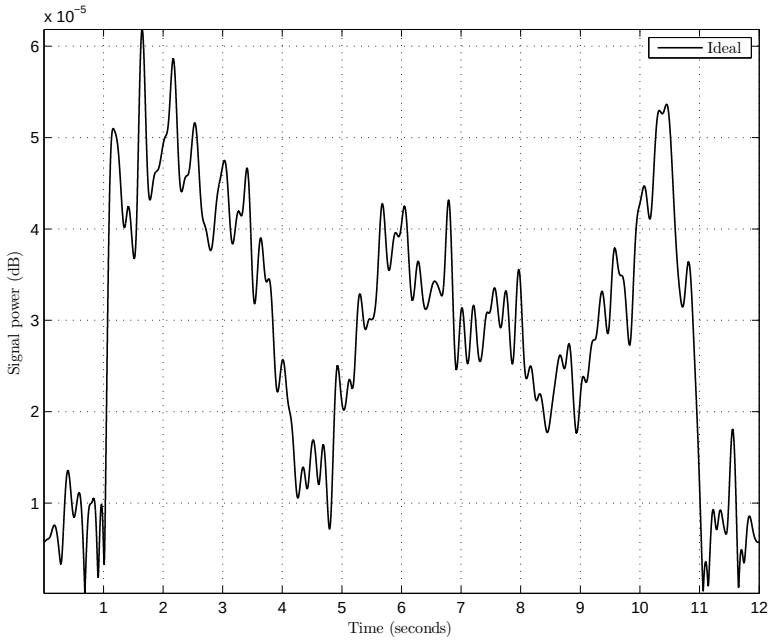

Figure 4.7: Narrowband signal filtered with the ideal rectangular window function with a carrier frequency of 15.5 MHz at 10:00 UTC.

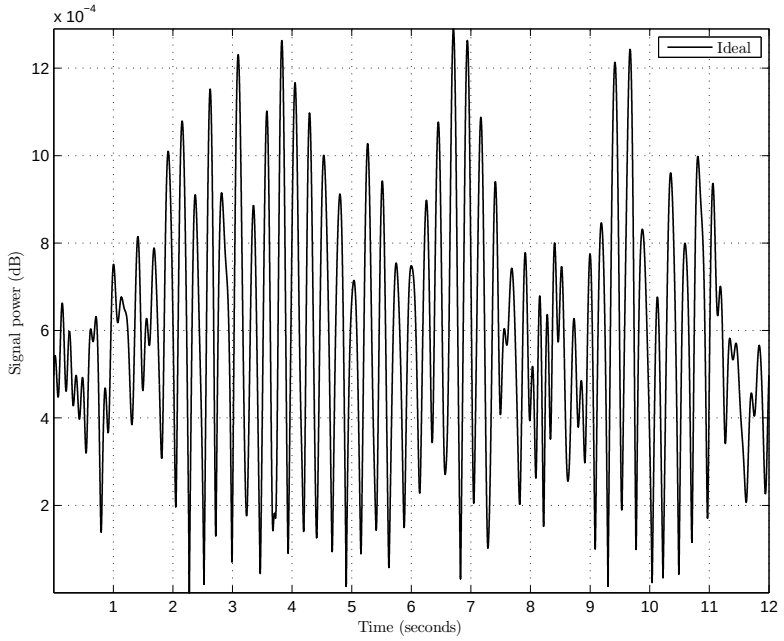

Figure 4.8: Highly interfered narrowband signal filtered with the ideal rectangular window function with a carrier frequency of 20 MHz at 17:00 UTC.

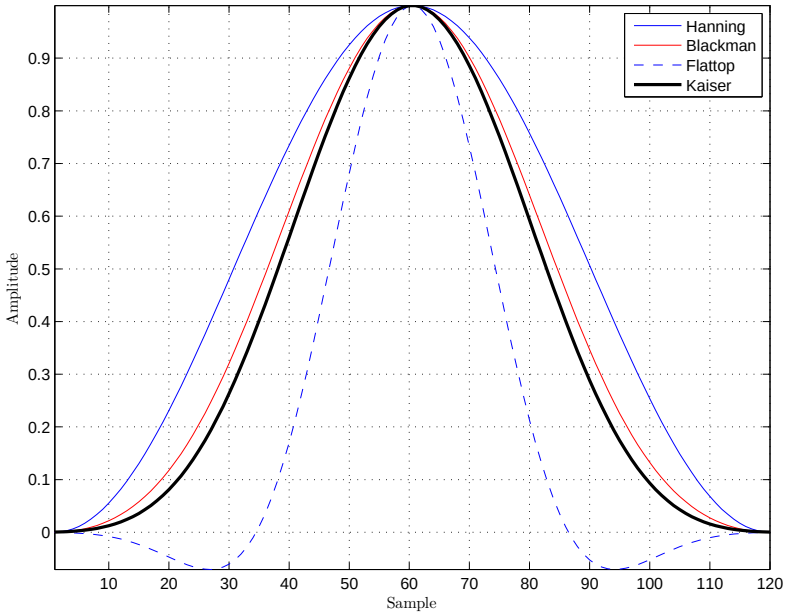

Figure 4.9: The time response of the four window functions (*Blackman*, *Hanning*, *Flattop*, and *Kaiser*).

Window	Best for these signal type	Frequency resolution	Spectral leakage	Amplitude accuracy
Blackman	Random or mixed	Poor	Best	Good
Flattop	Sinsoids	Poor	Good	Best
Hanning	Random	Good	Good	Fair
Kaiser	Random	Fair	Good	Good

Table 4.3: A brief comparison between the four window functions.

Then, after the refinement stage of the signal in the frequency domain, we will apply Inverse Fast Fourier Transform (IFFT) to recover the signal in the time domain, e.g., Figures 4.11 and 4.13. Figure 4.11 shows narrowband tone, perfectly received, filtered with the ideal rectangular filter along with the other four window functions. The signal appeared in Figure 4.7 has been received correctly with minimum effect of interference and noise. So that, applying the windowing technique will not provide a significant improvement as illustrated in Figure 4.11. However, highly interfered signal such as in Figure 4.8, will be significantly improved by applying any of the four window filters as shown in Figure 4.13, specially the *Kaiser* window as depicted in Figure 4.14.

The results of applying those different windows are much better than the ideal one that was used in previous surveys published in [48], specially in case of highly interfered

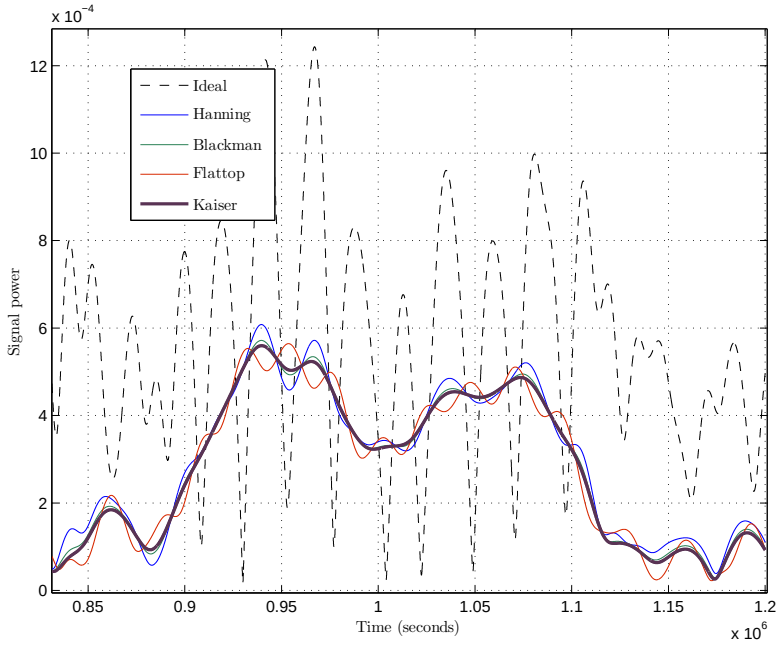

Figure 4.10: 4 seconds of 20 MHz narrowband signal at 17:00 UTC shows the difference between the four window functions.

signal.

Figure 4.10 depicts that *Kaiser* window has a slightly better and smoother response than the rest of the windows; for that reason, the *Kaiser* window is the preferred one throughout the surveys from 2009/2010 to 2011/2012. Figures 4.12 and 4.14 illustrate the application of *Kaiser* window function on an excellent received signal and a highly interfered signal, respectively. Previously, narrowband signal such as the one in Figure 4.13 was discarded since the channel is considered unavailable; however, such signal is actually received correctly and the SAS-OE link is available.

4.5.1.6 Time framing algorithm

The SNR_B computation can be easily distorted by the presence of high-level interfering signals. In order to exclude the interfering signal from being considered as a good received signal, the presented time framing technique shall be used. This technique is applied consecutive to the windowing algorithm, in order to have an effective method to mitigate the effects of the presence of both interference and noise. As shown in Figure 4.15, an interfering signal present during some seconds of the analyzed interval will lead to false SNR_B calculations.

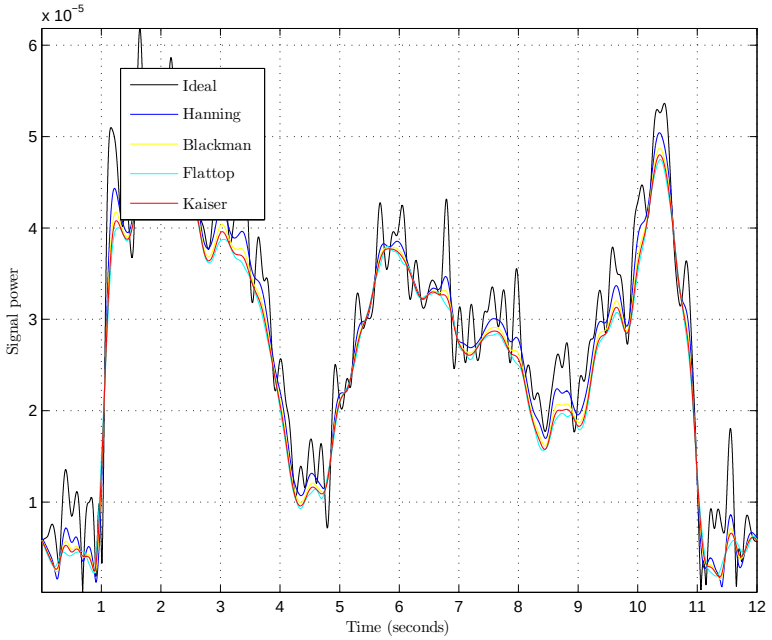

Figure 4.11: Narrowband signal filtered with the four different window functions with a carrier frequency of 15.5 MHz at 10:00 UTC.

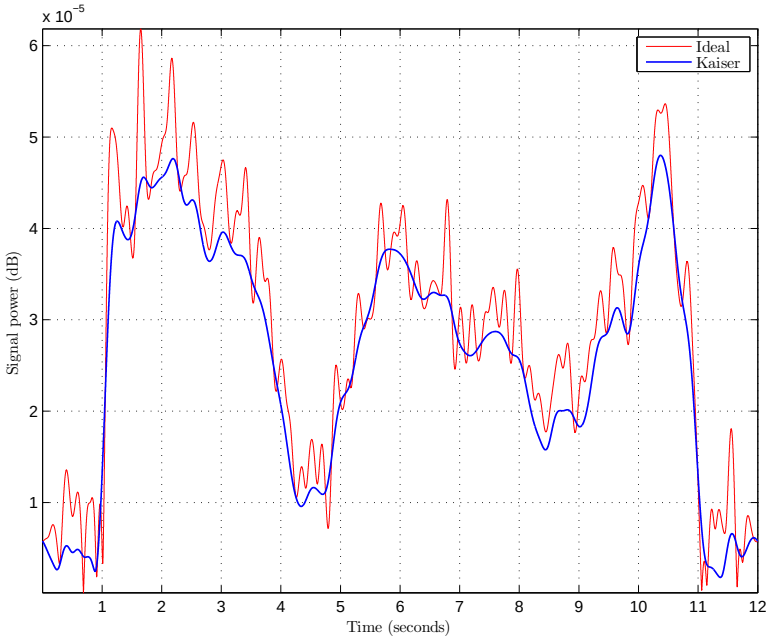

Figure 4.12: Narrowband signal filtered with the ideal and *Kaiser* window functions with a carrier frequency of 15.5 MHz at 10:00 UTC.

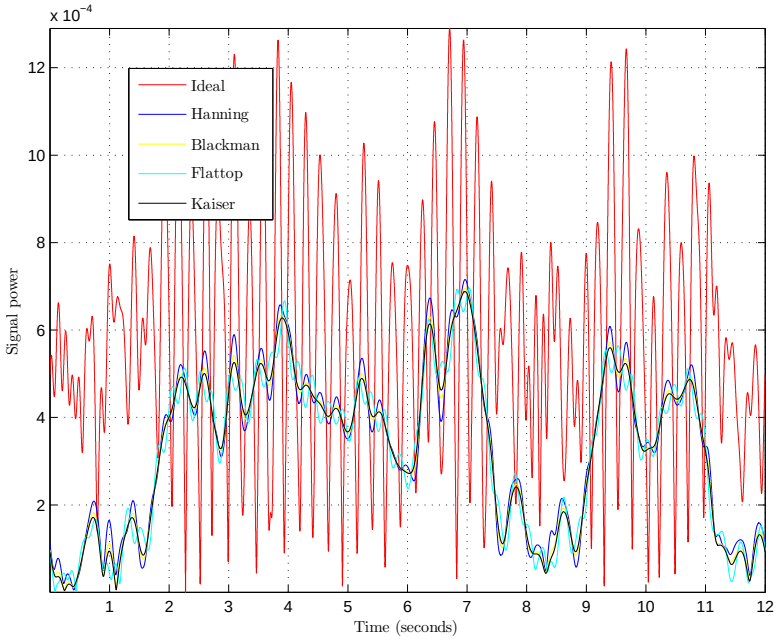

Figure 4.13: Ideal window compared with the other four window filters on a highly interfered narrowband signal with a carrier frequency of 20 MHz at 17:00 UTC.

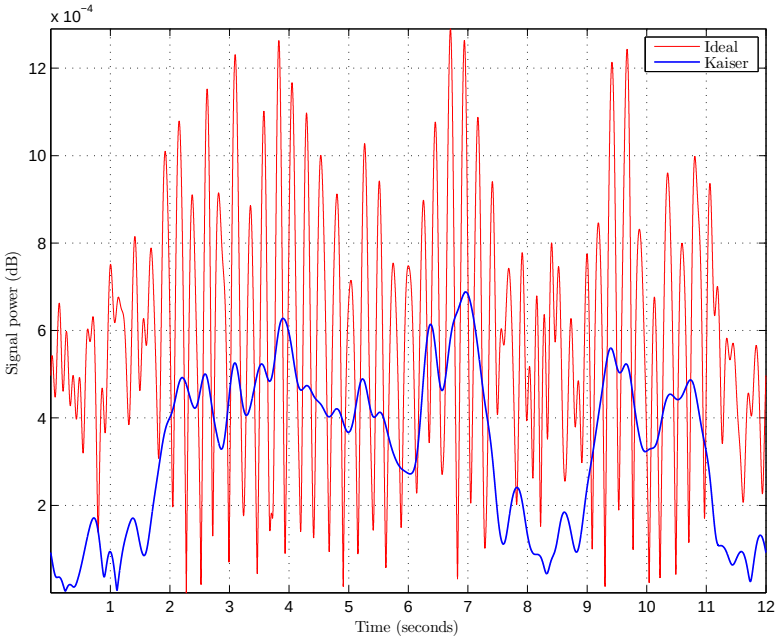

Figure 4.14: Ideal window compared with the *Kaiser* window on a highly interfered narrowband signal with a carrier frequency of 20 MHz at 17:00 UTC.

To overcome this problem, the whole received signal period has to be segmented into certain number of periods, e.g., 10 periods as shown in Figure 4.15. Usually, the SNR_B is calculated as the ratio between the information signal interval (period from 1 to 11) and the waiting interval (periods from 0 to 1 and from 11 to 12). As an example, see, Figure 4.15, due to the existence of high noise signal over the time period that goes from second 8 to 10, the SNR_B value will be very large. So that, previously it had been considered a perfectly received signal according to its SNR_B value; however, it is a perfect noise signal and has no information what so ever.

From the 2009/2010 survey, the SNR_B is computed as the ratio of the signal power on every information segment over the noise power measured at the segments of the waiting period. So we have an evolution of the SNR_B along the observation interval. In case of having wideband signal of 12 seconds, we will obtain 20 different SNR_B computations. The next step in the time framing technique is going to define two threshold values that the SAS-OE channel will be available, if certain percentage of computations exceed the two threshold values.

According to several previous experiments, the two threshold values have been defined, i.e., $Th_{low} = 3$ dB and $Th_{high} = 6$ dB. In order to have a high detection reliability, only signals have $SNR_B \geq Th_{low}$ over 70% of the segments and $SNR_B \geq Th_{high}$ over 50% of the segments are considered to be correctly received and we able to rely on. Therefore, no high power noise can be considered as useful signal, which is a great development step in refinning the channel availability scheme.

4.5.2 Algorithms of the wideband sounding

A simple block diagram of the algorithms that have been executed for obtaining the characteristics of the wideband channel is shown in Figure 4.16. The algorithms of the wideband sounding signals can be found in [48, 49]. The process is carried out in the following order:

1. frequency correction;
2. the correlation process of the received signal with the original sent sequence;
3. obtain the channel matrix from the correlated version of the signal;
4. calculate the *scattering function* from the channel matrix;

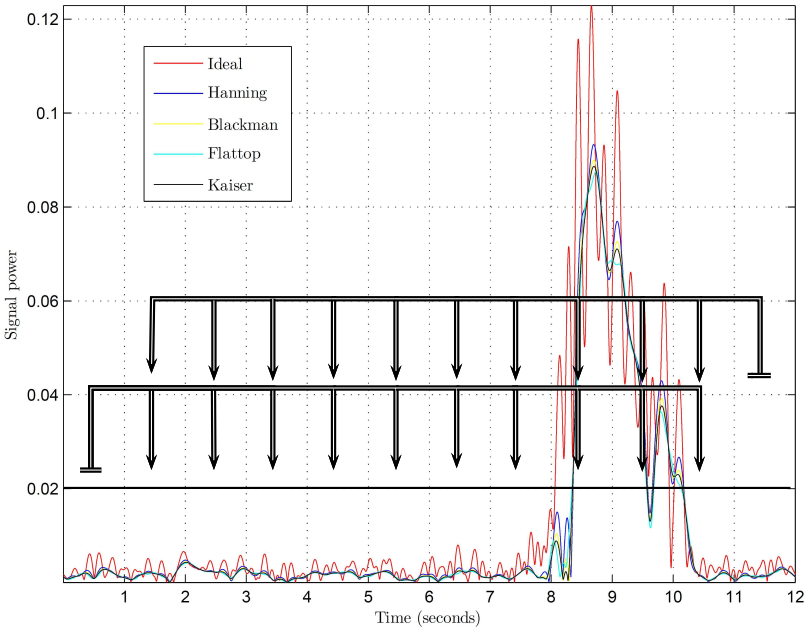

Figure 4.15: Ideal window compared with the other four window filters on a noisy narrowband signal with a carrier frequency of 3 MHz at 00:00 UTC.

5. measure the *power delay profile* and *Doppler power profile*, and consequently the *composite multipath spread* and *composite Doppler spread*.

A part from the correlated version of the received signal, there is a dedicated algorithm that measures the propagation time of the received electromagnetic signal. Starting from the 2009/2010 survey, the *Doppler frequency shift* measurements can be obtained from the *scattering function*. The configuration of the wideband sounding experiment during the 2009/2010 survey is illustrated in Table 4.4.

Let $r[n]$ be the signal at the output of the DDC during the wideband sounding interval. Hence, it has a duration of Δt seconds, which is corresponding to number of samples ($\Delta t F_m$) where F_m is the sampling frequency at reception. In the wideband experiment that has been conducted throughout the 2009/2010 survey, the duration of the signal $\Delta t = 12$ s and the sampling frequency $F_m = 100$ kS/s.

Firstly, the $r[n]$ signal is converted to its baseband through multiplication by complex exponential of frequency δf. Then, the received $r[n]$ signal is correlated with a replica of the original wideband sounding signal $S_e[n]$. The $S_e[n]$ is the corresponding sequence of length l chips, sampled at N_c Sample per chip, and interpolated with signaling pulse $p[n]$ of *root raised cosine* type:

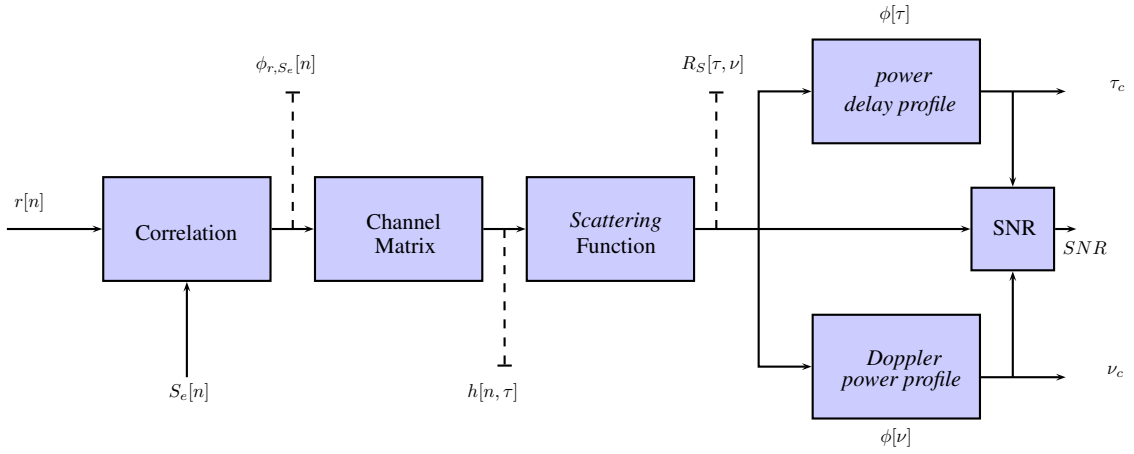

FIGURE 4.16: A block diagram of the analysis algorithms of the wideband received signal.

Sampling Frequency	100000	Hz
Time Interval	1–11	s
Chip Frequency	5000	Hz
Sequence length	127	
Doppler frequency window	(-4 4)	Hz
multipath window	(-3 3)	ms
Minimum SNR threshold value	6	dB
Roll-off factor of the RCC filter	0.65	

TABLE 4.4: The configuration setup for the wideband sounding during 2009/2010 survey.

$$S_e[n] = \sum_{i=0}^{l-1} b_i p[n - iN_c] \tag{4.33}$$

The signal $S_e[n]$ has a length of $N_s = lN_c + N_p - 1$ Samples where N_p is the number of samples of the signaling pulse, and defined as $N_p = 2N_sN_c + 1$ where $2N_s$ determines the number of chips covering the *root raised cosine* filter. The correlation process is carried out as:

$$\phi_{r,S_e}[n] = \sum_{k=0}^{N_s-1} r[n+k]S_e[k] \tag{4.34}$$

Consequently, the channel matrix is obtained as following:

$$h[n,\tau] = \phi_{r,S_e}[nlN_c+\tau],\ n \in \left[0, \left\lfloor \frac{\Delta t F_m}{lN_c} \right\rfloor\right], \tau \in [0, lN_c-1] \tag{4.35}$$

An example of $\phi_{r,S_e}[n]$ of 10 seconds long is shown in Figure 4.17, and another clipped version of 2 seconds long is illustrated in Figure 4.18. Both 3D and 2D implementations of the corresponding channel matrix of the previous correlated signal are shown in Figures 4.19 and 4.20, respectively.

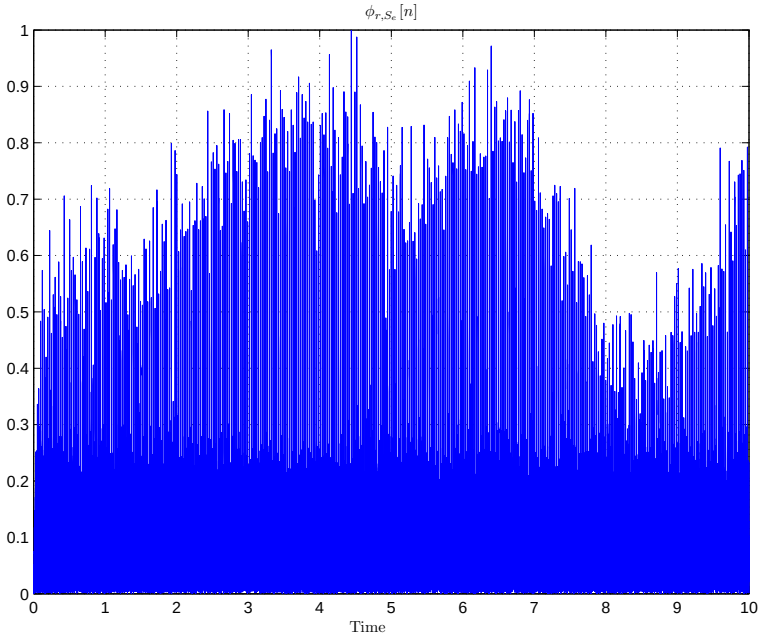

Figure 4.17: A correlated version of the received sounding signal (10 seconds long).

According to Equation 4.16, the *scattering function* will be calculated from the channel matrix as following:

$$R_S[\tau,\nu] = \sum_{\zeta} R_h[\zeta,\tau]e^{-j2\pi\zeta\nu} \tag{4.36}$$

The $R_S[\zeta,\tau]$ term is refereeing to an estimation of the autocorrelation of the channel matrix and it is defined as:

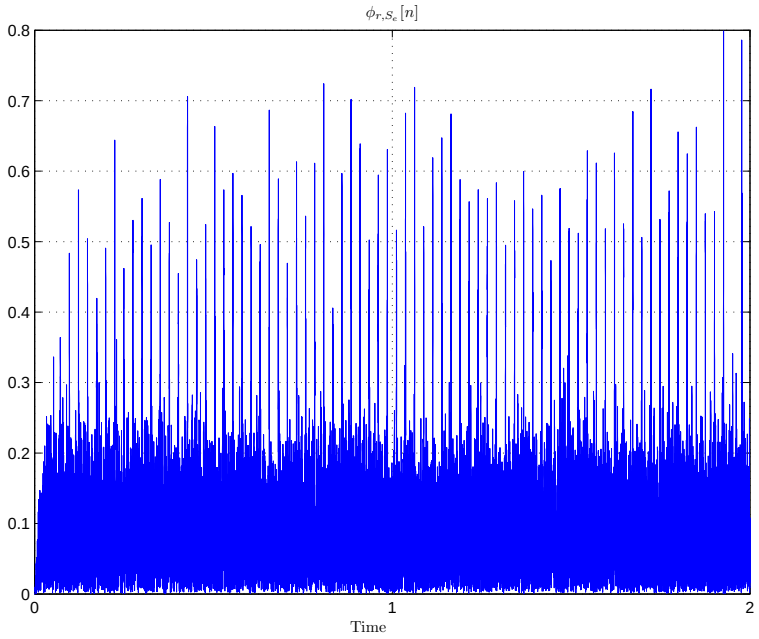

Figure 4.18: A correlated version of the received sounding signal (clipped to 2 seconds long).

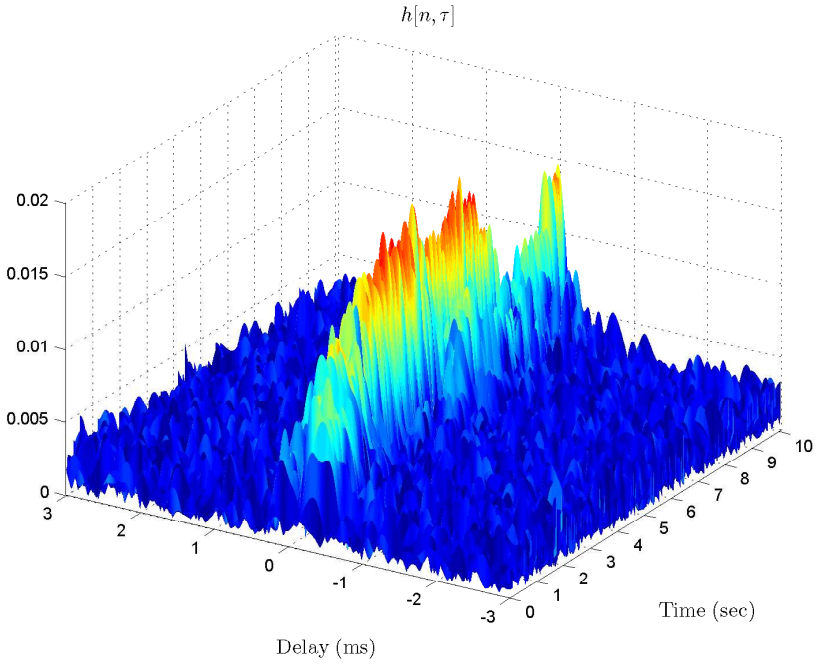

Figure 4.19: An example of the channel matrix in 3D view.

$$R_S[\zeta,\tau] = \sum_n h*[n,\tau]h[n+\zeta,\tau] \tag{4.37}$$

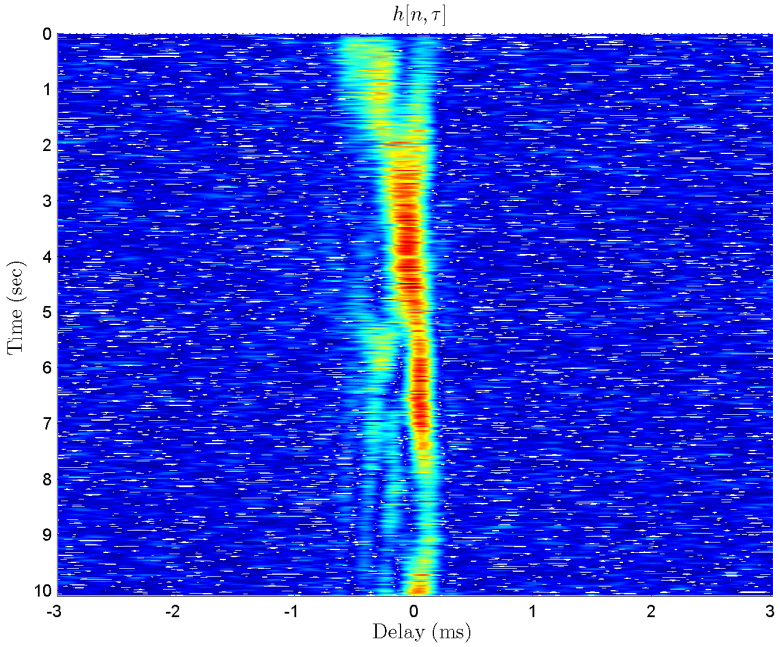

Figure 4.20: An example of the channel matrix in 2D view.

By substituting 4.37 in 4.36, that will result in:

$$\begin{aligned} R_S[\tau,\nu] &= \sum_{\zeta}\sum_{n} h*[n,\tau]h[n+\zeta,\tau]e^{-j2\pi\zeta\nu} \\ &= \sum_{n} h*[n,\tau]e^{j2\pi n\nu}\sum_{\zeta} h[n+\zeta,\tau]e^{-j2\pi(\zeta+n)\nu} \end{aligned} \tag{4.38}$$

Moreover, the *scattering function* $R_S[\tau,\nu]$ can be obtained from the *Fourier* transformation ($n \leftrightarrow \nu$) of the channel matrix as following:

$$R_S[\tau,\nu] = ||H(\tau,\nu)||^2 \tag{4.39}$$

By applying Equation 4.39 to the signal appeared in Figure 4.19, the *scattering function* $R_S[\tau,\nu]$ will be obtained as shown in Figures 4.21 and 4.22, which are illustrating 3D and 2D representations, respectively.

From now on, we will assume that the channel impulse response contained in $R_S[\tau,\nu]$ is centered, both on *delay* and *Doppler* axis. Two different examples of correlated

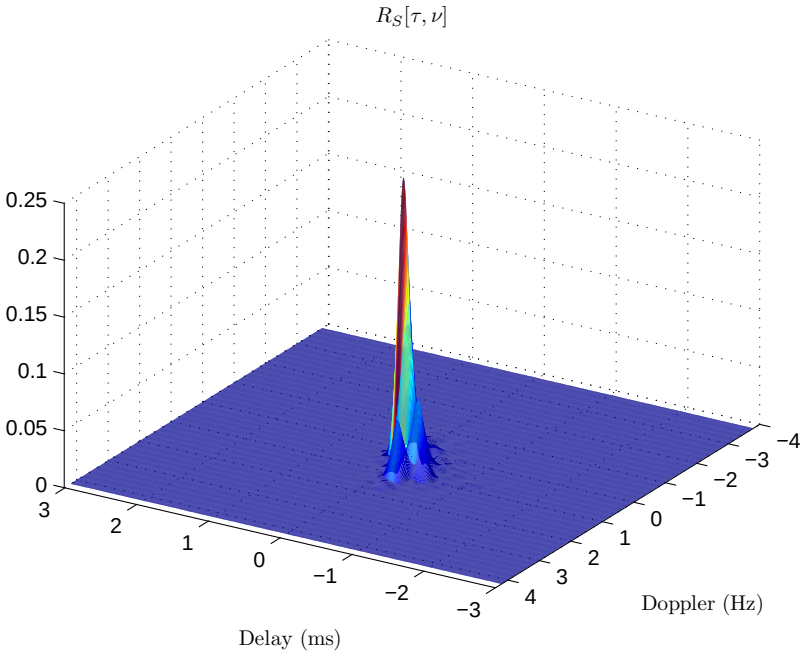

Figure 4.21: A 3D representation of the *scattering function* of a received sounding signal.

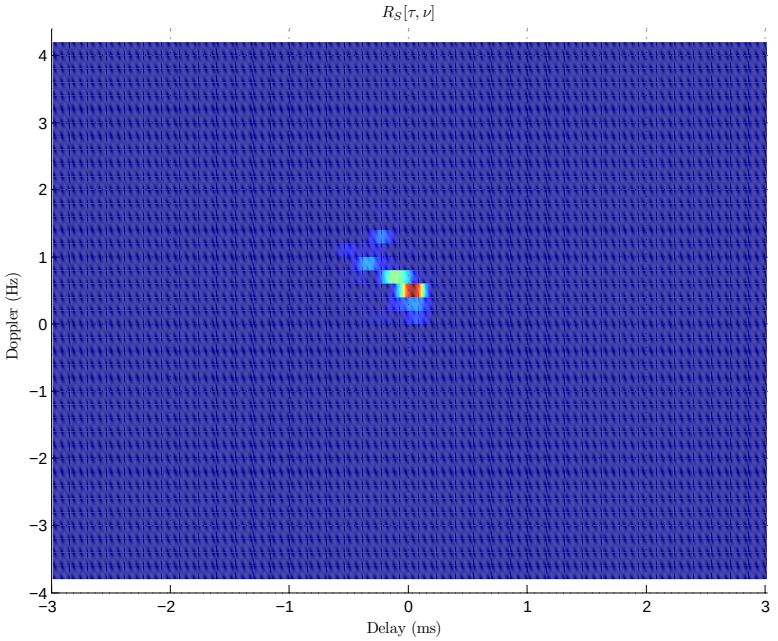

Figure 4.22: A 2D representation of the *scattering function* of a received sounding signal.

version of received wideband signal, the corresponding channel matrix, and *scattering function* are shown in Figures 4.23 and 4.24.

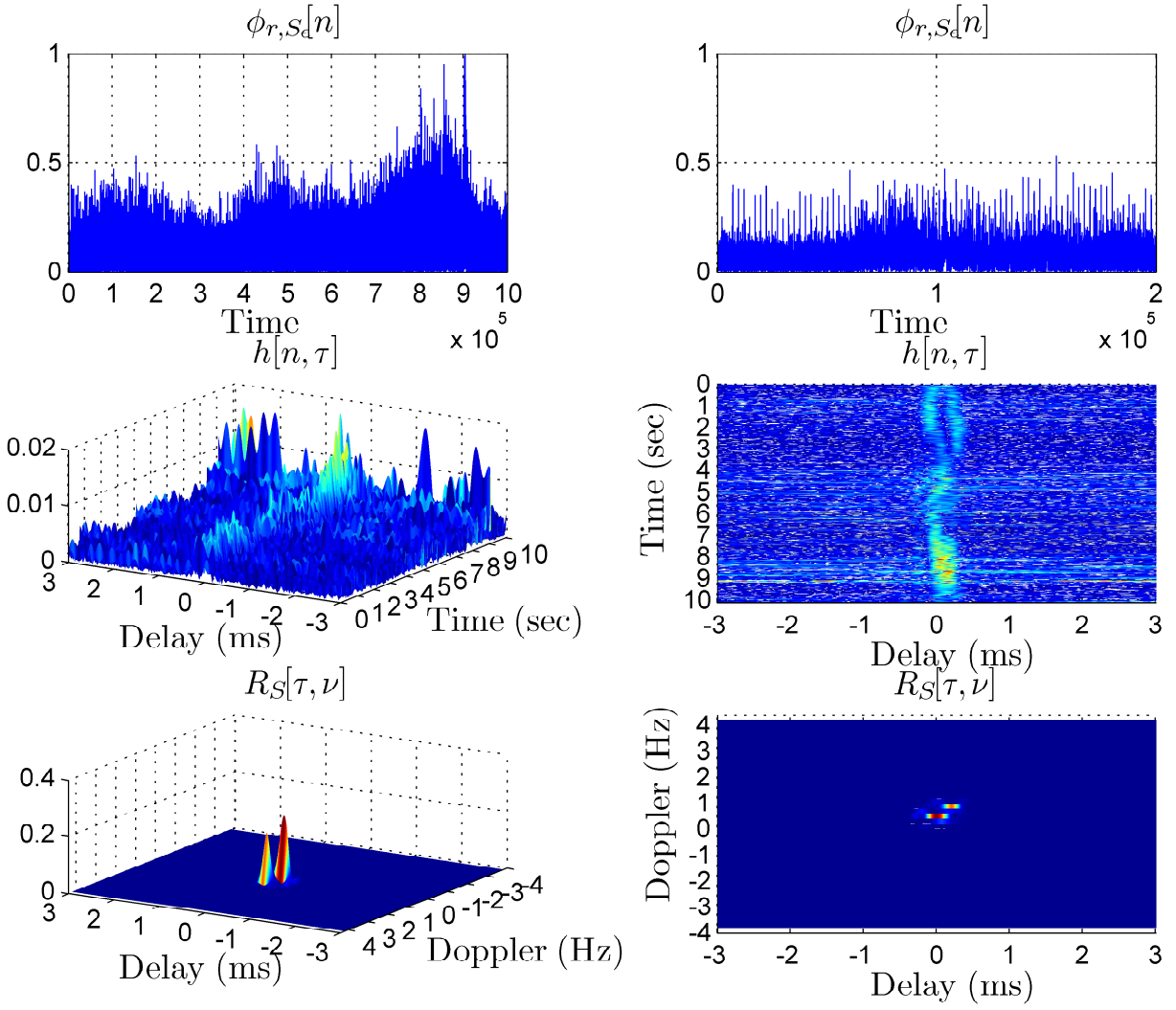

Figure 4.23: Sounding signal of 18.5 MHz at 11:00 UTC. A correlation of 10 seconds and 2 seconds of the received signal with the original sequence depicted at the top right and left frames respectively. At the middle right and left frame, channel impulse response in 3D and top-view. *Scattering function* in 3D and top-view are depicted at the bottom right and left frames respectively.

As mentioned in Table 4.4, we define the two observation windows of both the *multipath* $[\tau_1, \tau_2]$ and the *Doppler* $[\nu_1, \nu_2]$ based on the expected maximum values of dispersion. Thus, the *power delay profile* is calculated from the *scattering function* as:

$$\phi[\tau] = \sum_{\nu=\nu_1}^{\nu_2} R_S[\tau, \nu] \tag{4.40}$$

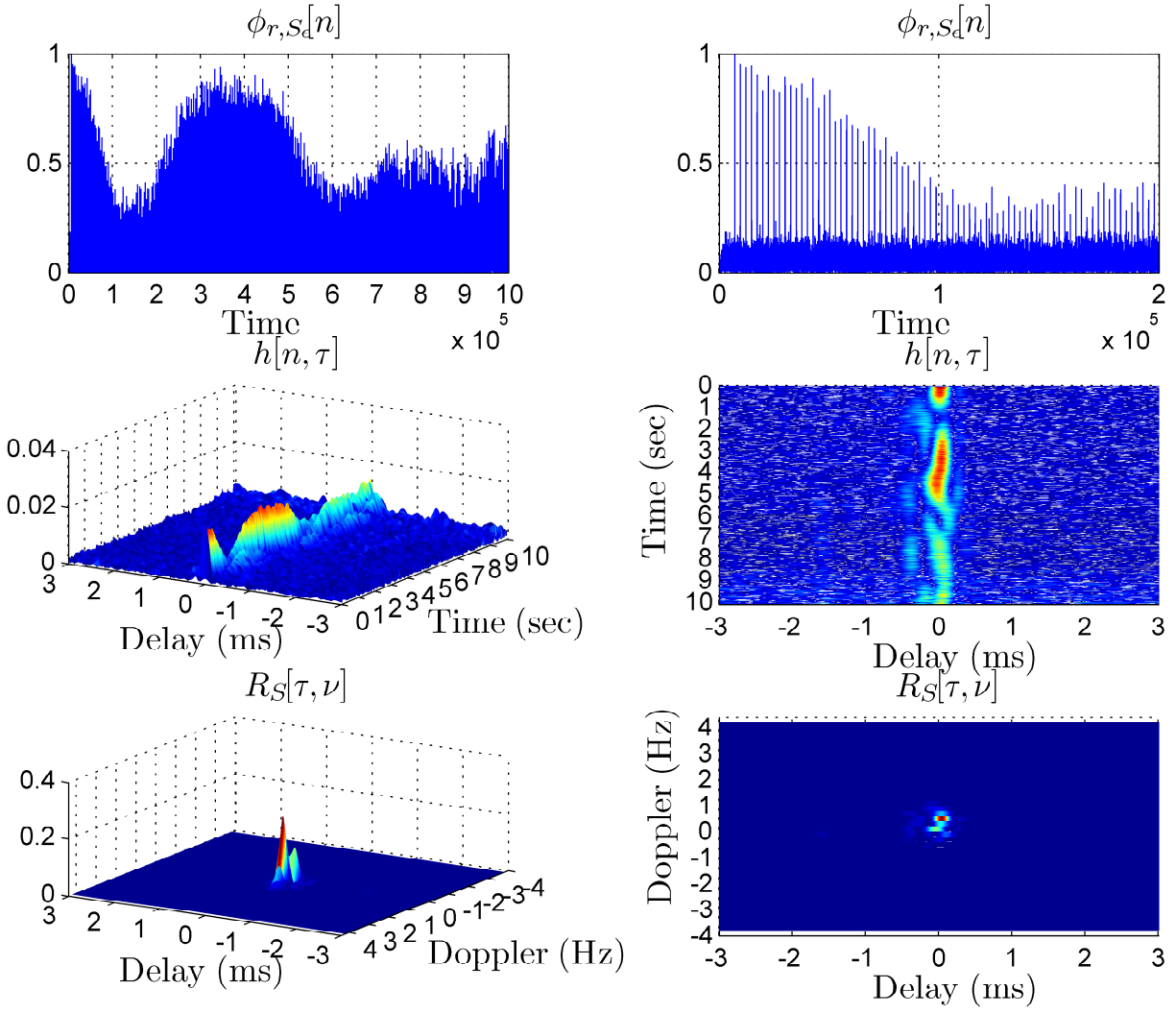

Figure 4.24: Sounding signal of 16 MHz at 17:00 UTC. A correlation of 10 seconds and 2 seconds of the received signal with the original sequence depicted at the top right and left frames respectively. At the middle right and left frame, channel impulse response in 3D and top-view. *Scattering function* in 3D and top-view are depicted at the bottom right and left frames respectively.

Similarly, the *Doppler power profile* will be computed as:

$$\phi[\nu] = \sum_{\tau=\tau_1}^{\tau_2} R_S[\tau,\nu] \tag{4.41}$$

After defining the expected dispersion windows, the dynamic range of the measurement can be calculated with respect to the noise. Indeed, if the $r[n]$ received with

SNR_{Bw}, the *maximum dynamic range* of the *multipath* measurement with respect to noise and interference will be:

$$\mathrm{MDR}_n^{\tau} = \mathrm{SNR}_{Bw} + 10\log_{10}\frac{\Delta t}{T} + 10\log_{10} l - 10\log_{10}\frac{\nu_2 - \nu_1}{1/\Delta t} \tag{4.42}$$

where Δt is the duration of the wideband sounding interval, T determines the period of the sequence in seconds, l represents the length (measured in number of chips), and ν_1, ν_2 expressed in Hz. The second term ($10\log_{10}\frac{\Delta t}{T}$) of the previous expression (4.42) is the gain of the sequence process [117]. The third term ($10\log_{10} l$) is the maximum gain that could be obtained in the frequency transformation process to calculate the *scattering function*. In case of ideal and static channel, the width of the *Doppler* observation window would coincide with the resolution of the measurement. Otherwise, if the channel is observed in the $[\nu_1, \nu_2]$ window, this gain has to be corrected downward $\left(10\log_{10}\frac{\nu_2-\nu_1}{1/\Delta t}\right)$; so that, the two terms of Equation 4.42 will result in:

$$10\log_{10}\frac{\Delta t}{T} - 10\log_{10}\frac{\nu_2 - \nu_1}{1/\Delta t} = 10\log_{10}\frac{1}{T(\nu_2 - \nu_1)} \tag{4.43}$$

Quantifying the actual gain for this concept, will lead to the final expression for the *maximum dynamic range* of the *multipath* measurement with respect to noise and interference through substituting 4.43 into 4.42. Hence, the *maximum dynamic range* (MDR_n^{τ}) is expressed as:

$$\begin{aligned} \mathrm{MDR}_n^{\tau} &= \mathrm{SNR}_{Bw} + 10\log_{10} l + 10\log_{10}\frac{1}{T(\nu_2 - \nu_1)} \\ &= \mathrm{SNR}_{Bw} + 10\log_{10}\frac{f_c}{\nu_2 - \nu_1} \end{aligned} \tag{4.44}$$

where f_c is the chip frequency. Also, the *maximum dynamic range* of the *Doppler* measurement with respect to the noise (MDR_n^{ν}), is defined as:

$$\mathrm{MDR}_n^{\nu} = \mathrm{SNR}_{Bw} + 10\log_{10} l + 10\log_{10}\frac{\Delta t}{T} - 10\log_{10}\frac{\tau_2 - \tau_1}{T_c} \tag{4.45}$$

where T_c is the chip time that expressed in seconds and the *multipath* values of the observation window (τ_1, τ_2) are expressed in seconds. Now combining the second and fourth terms on the right of equality of Equation 4.45:

$$10\log_{10} l - 10\log_{10}\frac{\tau_2 - \tau_1}{T_c} = 10\log_{10}\frac{l \cdot T_c}{\tau_2 - \tau_1} = 10\log_{10}\frac{T}{\tau_2 - \tau_1} \tag{4.46}$$

Configuration	SNR	MDR_n^{τ}	MDR_n^{ν}
$l = 127,\ f_c = 5000$	SNR_{5000}	$SNR_{5000} + 30$	$SNR_{5000} + 32$

Table 4.5: The dynamic range of the *multipath* and *Doppler* measurements (all values expressed in dB).

The process gain can be obtained by calculating the *Doppler power profile* of a dispersive channel observed through *multipath* window $[\tau_1, \tau_2]$. Substituting 4.46 into 4.45 and operand reaches the final expression for the *maximum dynamic range* of the *Doppler* measurement with respect to noise and interference (MDR_n^{ν}) as following:

$$\begin{aligned} MDR_n^{\nu} &= SNR_{Bw} + 10\log_{10}\frac{\Delta t}{T} + 10\log_{10}\frac{\Delta t}{\tau_2 - \tau_1} \\ &= SNR_{Bw} + 10\log_{10}\frac{\Delta t}{\tau_2 - \tau_1} \end{aligned} \tag{4.47}$$

Table 4.5 shows the total dynamic ranges for the wideband sounding experiment determined in Table 4.4. The analysis of the wideband sounding during 2009/2010 survey carried out by using an observation window of [-3, 3] ms for *multipath* and [-4, 4] Hz for the *Doppler*.

Consequently, there are two algorithms have to be applied for calculating the *composite multipath spread* (τ_c) from the *power delay profile* and the *composite Doppler spread* (ν_c) from the *Doppler power profile*. Since these two algorithms are equivalent, we will describe only the one dedicated to calculate the *composite multipath spread*. It should be noted that, if the observation window of the *multipath* is properly adjusted, $\phi[\tau]$ will contain the noise outside this window; therefore,

$$\tilde{\phi}[\tau] = \phi[\tau] - \frac{1}{T - (\tau_2 - \tau_1)} \sum_{m \notin [\tau_1, \tau_2]} \phi[m] \tag{4.48}$$

Then we calculate the integral function of $\tilde{\phi}[\tau]$ within the *multipath* observation range:

$$\Phi[\tau] = \sum_{m=\tau_1}^{\tau_s} \tilde{\phi}[m], \quad \tau \in [\tau_1, \tau_2] \tag{4.49}$$

Consequently, we normalized $\Phi[\tau]$ with respect to its maximum value:

$$\bar{\Phi}[\tau] = \frac{\Phi[\tau]}{\max(\Phi[\tau])} \tag{4.50}$$

Finally, the *delay* values obtained for which the $\bar{\Phi}[\tau]$ reaches 10% and 90% of the maximum value:

$$\tau_{min} = \min_{\tau} \bar{\Phi}[\tau] \geq 0.1 \tag{4.51}$$

$$\tau_{max} = \max_{\tau} \bar{\Phi}[\tau] \leq 0.9 \tag{4.52}$$

Therefore, the *composite multipath spread* is defined as:

$$\tau_c = \frac{\tau_{\max} - \tau_{\min}}{F_m} \tag{4.53}$$

where the term $\tau_{max} - \tau_{min}$ in the previous expression is defined in number of Samples.

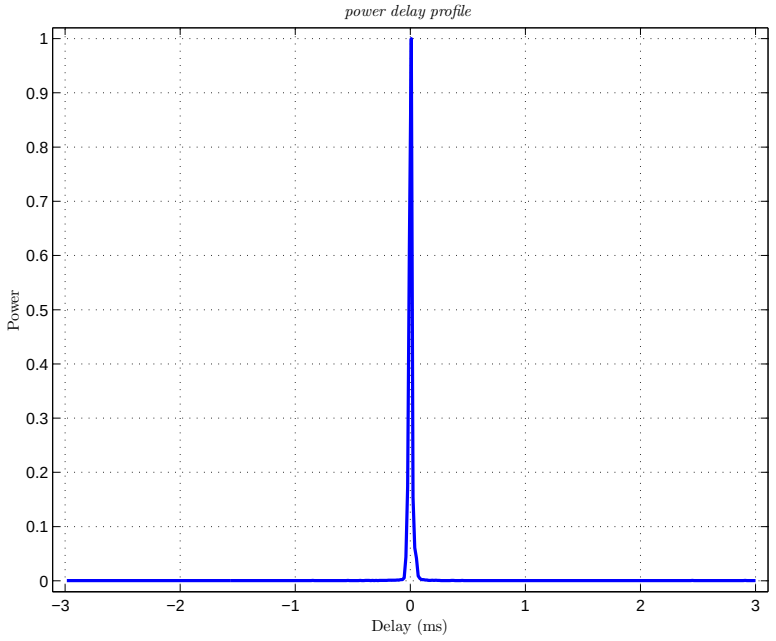

Figure 4.25: The *power delay profile* of a received sounding signal.

For the *Doppler power profile* calculation, the same algorithm is used; so that, ν_c as a function of the maximum and minimum values of the *Doppler* will be:

$$\nu_c = \frac{\nu_{\max} - \nu_{\min}}{\Delta t} \tag{4.54}$$

and $\nu_{\max} - \nu_{\min}$ is also expressed in number of Samples.

Figures 4.25 and 4.26 show the *power delay profile* parameter and the corresponding integral functions. The *Doppler power profile* and the corresponding integral function

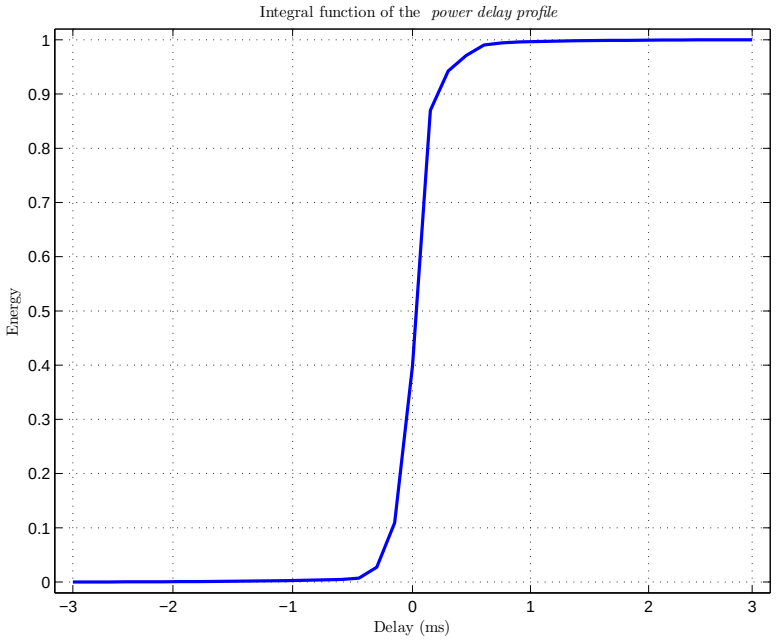

Figure 4.26: An example of the corresponding integral function (*power delay profile*).

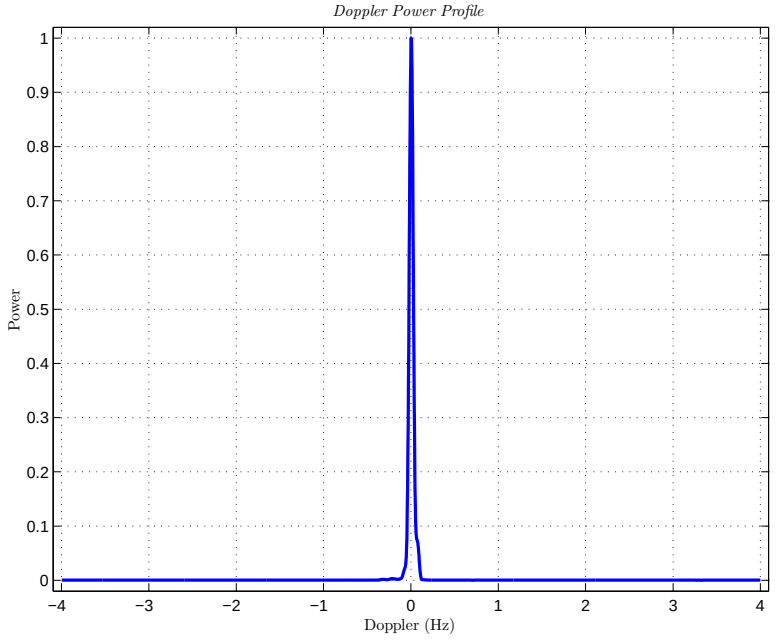

Figure 4.27: The *Doppler power profile* of a received sounding signal.

are illustrated in Figures 4.27 and 4.28, respectively. The $\tau_{\max}$, $\tau_{\min}$, $\nu_{\min}$, and $\nu_{\max}$ parameters are limiting the region of the *scattering function*, which contains the signal. Taking into account that this property along with the previous relationships, we will calculate the SNR_{Bw} from Figure 4.29 as:

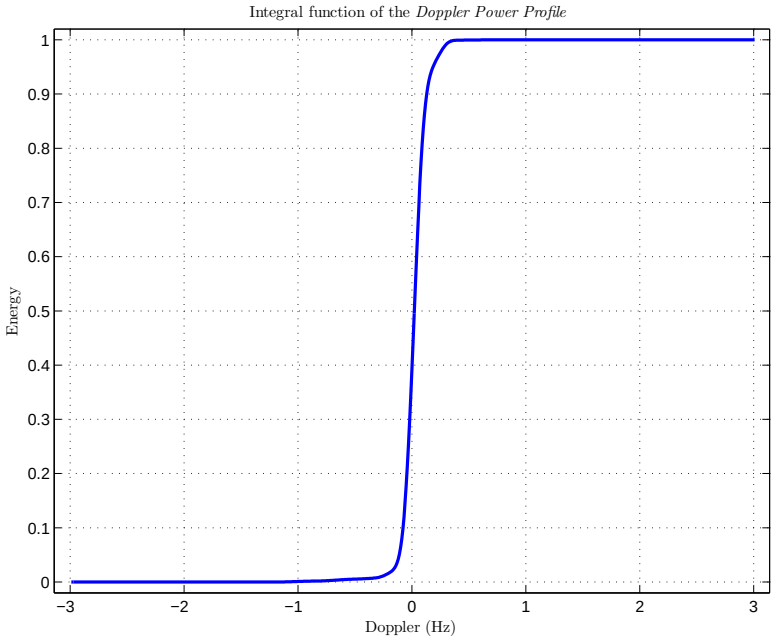

FIGURE 4.28: An example of the corresponding integral function (*Doppler power profile*).

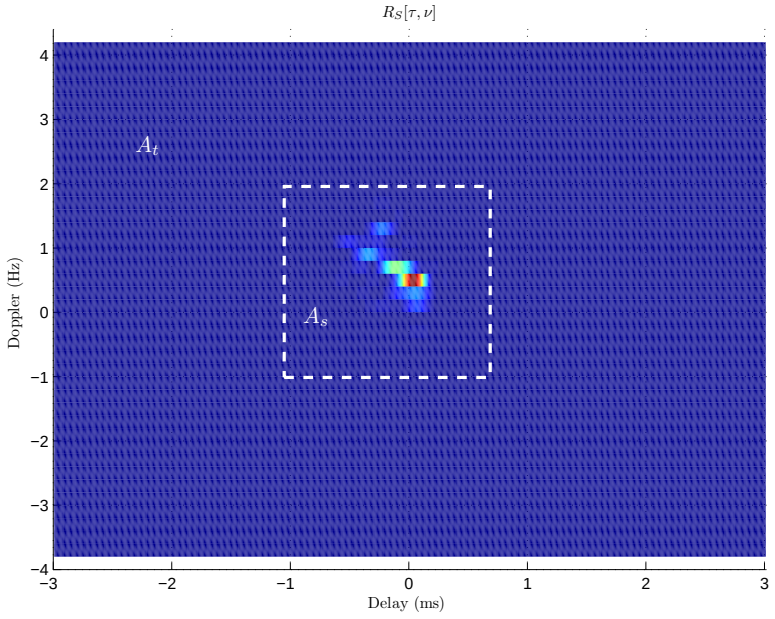

FIGURE 4.29: An example of the *scattering function.*

$$\mathrm{SNR} = \frac{P|_{A_s} - \rho_n A_s}{\rho_n A_t}, \quad \rho_n = \frac{P|_{\bar{A}_s}}{\bar{A}_s} \tag{4.55}$$

where P is the power of the signal, A_s defines the area of the *scattering function* limited by $\tau_{\max}$, $\tau_{\min}$, $\nu_{\min}$, and $\nu_{\max}$, A determines the total area of the *scattering function*, and $\bar{A}_s$ represents the complementary area to A_s. The ρ_n term is the noise per unit of the area of the *scattering function*. Finally, and in accordance with the described algorithms, consider that the waveform is detected during the wideband interval when both verified the following equations simultaneously:

$$\frac{\max(\Phi[\tau]), \quad \tau \in [\tau_{\min}, \tau_{\max}]}{\text{mean}(\Phi[\tau]), \quad \tau \notin [\tau_{\min}, \tau_{\max}]} \geq \text{SNR}^{\tau}_{\min} \tag{4.56}$$

$$\frac{\max(\Phi[\nu]), \quad \nu \in [\nu_{\min}, \nu_{\max}]}{\text{mean}(\Phi[\nu]), \quad \nu \notin [\nu_{\min}, \nu_{\max}]} \geq \text{SNR}^{\nu}_{\min} \tag{4.57}$$

The values of $\text{SNR}^{\nu}_{\min}$ and $\text{SNR}^{\tau}_{\min}$ are set empirically with the aim of reaching good compromise between minimizing the detection of false receptions and maximizing the detection of certain receptions. Specifically, the following values are selected:

$$\text{SNR}^{\nu}_{\min} = 6 \text{ dB}, \quad \text{SNR}^{\tau}_{\min} = 6 \text{ dB} \tag{4.58}$$

4.6 Results

The frequency range that has been utilized for obliquely sounding the SAS-OE link throughout the 2006/2007 survey was from 4.6 MHz to 16.6 MHz and the sounding time was extending from 18:00 UTC to 11:00 UTC, which is mainly the nighttime period of the day. So that, to complete the time series of the oblique soundings, the SO-DIO platform, which was operating has to be replaced with much more advanced one (POTASIO). The new platform is able to carry out soundings with the whole HF band (2 MHz - 30 MHz) and during 24 hours per day. New measurements of the *Doppler frequency shift* and propagation time have been recorded during 2009/2010 survey, are introduced herein regarding the improvements in the *hardware* of the POTASIO platform.

All the results that will be explained through this section were measured during time period of around 10 complete days (the system was working properly throughout 24 hours per day) at the 2009/2010 survey. Firstly, we will introduce the narrowband SNR_B calculations and the availability of the SAS-OE link by using the windowing and

time framing algorithms that aimed to completely refine the received signal, then, compute the SNR_B values. Secondly, there will be the measurements from the wideband sounding of the SAS-OE link:

- from the *scattering function*, we have estimated the SNR_{Bw} of the wideband channel, *composite multipath spread*, *composite Doppler spread*, and *Doppler frequency shift*;
- from the correlated version of the wideband signal, we have calculated the propagation time.

4.6.1 Narrowband sounding

Herein, we will define the term "availability", and the associated notation. In addition, we are introducing the availability scheme of the SAS-OE link throughout the 2009/2010 survey by using the narrowband sounding technique. Through the explanation of the narrowband channel availability, we have estimated the SNR_B conventionally as the ratio between signal power in the information interval and the waiting intervals. Besides that, we have calculated the availability as the percentage of time frames that have SNR_B values larger than 6 dB. Moreover, and to have more reliable availability scheme, the channel is considered available if 70 % of the time frames have SNR_B values higher than 3 dB and 50 % more than 6 dB.

In order to consider that measuring the channel availability will support the establishment of an ionospheric link, several aspects should be taken into account, such as the constraints of the equipment (*sensitivity* and *blocking*), the noise and interference levels that imposed at the reception, which was already studied before.

Figure 4.30 is an example of the inter-day estimation of the SNR_B for all the sounding frequencies and during 24 hours per day. Figure 4.31 illustrates the availability of the SAS-OE link obtained during the 2009/2010 survey using the windowing and time framing techniques, for which it is the percentage of the time frames having SNR_B larger than 6 dB. Practically, we are estimating the availability as the percentage of detected receptions with respect to the total number of transmissions under the conditions specified with the variables (f, h, and d). As it can be observed, there are some discontinuities that cannot be attributed to the ionospheric channel behavior.

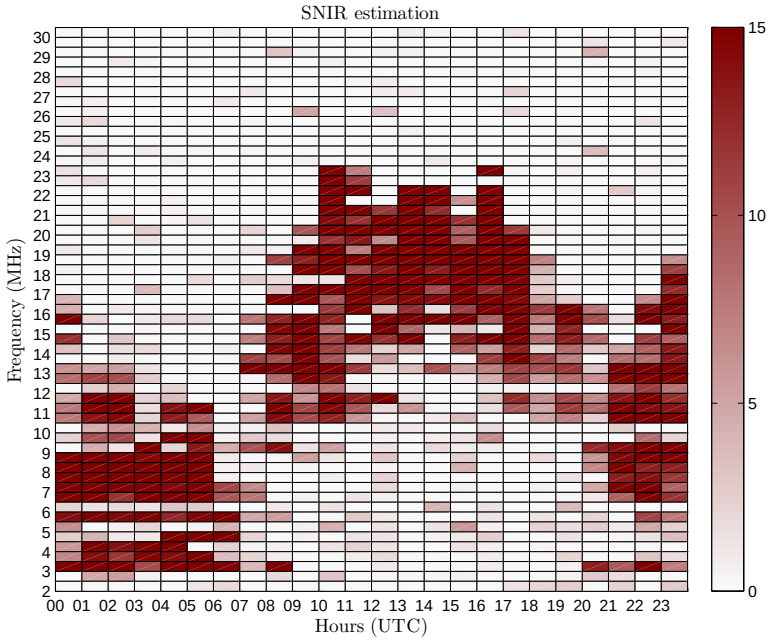

Figure 4.30: SNR estimation of the narrowband ionospheric channel as a function of hour and frequency of sounding.

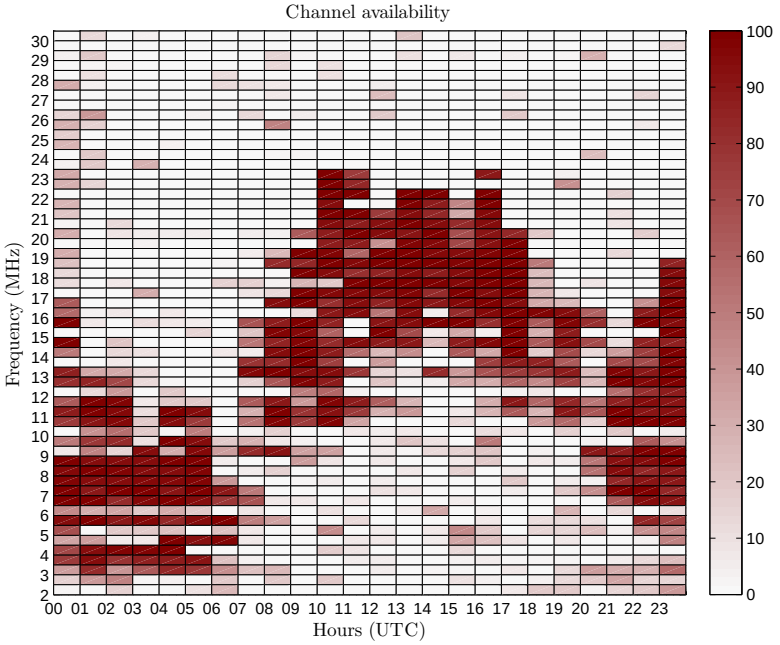

Figure 4.31: The channel availability measured over 2009/2010, as a percentage of the time frames that exceeded 6 dB.

To overcome this problem, after several surveys and further analysis of the narrowband received signals, we suggested new availability definition of the SAS-OE link based on the time framing the received signal. For which the channel is considered available if 50% of the time frames show SNR_B values higher than 6 dB and 70% of the time frames show SNR_B values higher than 3 dB. The availability of the SAS-OE link after applying the new difinition of the channel availability is illustrated in Figure 4.32.

The red slots mean that no signal could be detected due to the presence of other strong interfering signals. This fact may not be interpreted as a failure of the method since such signals could not be detected neither by time framing nor by any other technique. According to its position and well-known propagation theories, these red slots should be considered as points of potential availability of the channel. The blue slots mean that the channel is available, i.e., $SNR_B \geq 6$ dB the 50% of the time slots and $SNR_B \geq 3$ dB the 70% of the time slots. The position of the blue slots plus the red slots (global availability) is much more consistent than the availability estimated in previous works [48].

Finally we have small amount of non-detected available slots (green ones), where the method failed to detect the presence of weak signals, and a single false alarm slot (black slot), where the method erroneously detected a good reception.

From Figures 4.30, 4.31, and 4.32, we can distinguish two propagation regions with the following characteristics:

1. The nighttime region - it starts at sunset (around 17:00 UTC) and ends at sunrise (around 07:00 UTC). As the sunset time extends for around four four hours and half along the whole SAS-OE link path, frequencies from 10.5 MHz to 16.5 MHz during the time period from 18:00 UTC to 20:00 UTC have high channel availability. Then, the channel tends to be available with frequency range from 6.5 MHz to 17.5 MHz over around three hours from 21:00 UTC to 23:00 UTC.

   Due to the complete D layer absence during the nighttime period, low frequency range from 3 MHz to 13 MHz is highly propagated from midnight to 7:00 UTC. High frequency range above 13 MHz is completely useless during the nighttime period the termination of all the ionic recombination, and the decrement of the ionization levels over the ionosphere.

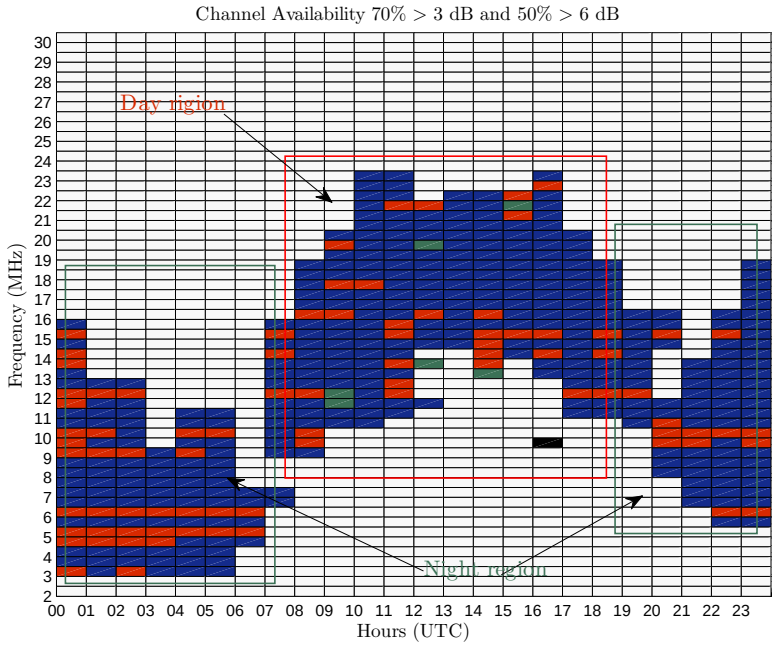

Figure 4.32: The channel availability during 2009/2010, where 70% of the time frames have SNR higher than 3 dB and 50% higher than 6 dB.

2. The daytime region - it lasts from around sunrise to sunset (around 17:00 UTC). Generally, the D layer absorbs the frequencies below 10 MHz, which makes the propagation of the low frequency band impossible during the daytime period. Over the time period from sunrise to 11:00 UTC, frequency range from 10 MHz to 17 MHz is highly propagated, and consequently, it changes throughout the period from 11:00 UTC to 18:00 UTC to frequency range starts from 13 MHz to 23.5 MHz.

   The ionospheric propagation during the daytime region is largely supported by existence of the Sun, and subsequently the highly ionization conditions that lead to the the F2 layer existence. An important notation is that the daytime region had not been analyzed prior to the 2009/2010 survey.

A clear observation had been noted that frequencies higher than 23.5 MHz could not propagate throughout the daytime region (07:00 UTC to 17:00 UTC), and larger than 18 MHz during the nighttime region (18:00 UTC to 06:00 UTC). Previously, the daytime region appeared in Figure 4.32 was not be tested due to several lacks of the SODIO platform, which was operating from 2005/2006 to 2008/2009. As a great achievement has been obtained that frequencies ranged from 11 MHz to around 23 MHz are highly propagated, and the SAS-OE link can be used for transmission.

Sounding the SAS-OE link throughout the daytime region added around 6 hours to the operator of the SAS-OE link; so that, the link can be used over the whole day, which we considered a large step in the project.

4.6.2 Wideband sounding

The analysis of the wideband sounding signals of the SAS-OE link has been carried out through the algorithms explained in Section 4.5.2, in order to obtain the *scattering function* of the received signals. Consequently, from the *scattering function*, the SNR_{Bw} can be estimated, besides that, the time and frequency dispersion parameters can be obtained, such as *composite multipath spread*, *composite Doppler spread*, propagation time, and the *Doppler frequency shift*.

4.6.2.1 Wideband SNR estimation

The calculation of the SNR_{Bw} from the *scattering function* will lead to the wideband channel availability. The wideband SNR_{Bw} is estimated according to Equation 4.55, and the wideband channel availability of the SAS-OE ionospheric link ((D_w)) at a bandwidth Bw where $Bw \ggg Bn$, is defined as following:

$$D_w(f,h,d) = p(\mathrm{SNR}_{Bw} \geq \mathrm{SNR}_{\mathrm{min},Bw})\Big|\Big|_{f,h,d} \text{ for a determined value of } Bw \qquad (4.59)$$

The $\mathrm{SNR}_{\mathrm{min},Bw}$ often refers to the minimum necessary SNR_{Bw} value for a particular physical layer to be able to provide the desired quality of service, and the bandwidth Bw is the available bandwidth for establishing the SAS-OE ionospheric link. This concept is determined in the literature by using the term "availability" or "reliability" [124]. In this work, neither the physical layer nor the transmission bandwidth were defined; and therefore, the wideband channel availability is calculated as function of various $\mathrm{SNR}_{\mathrm{min},Bw}$ and different Bw.

The availability the *multipath* measurement (D_τ) defines the probability of obtaining an SNR^τ (measurement about the *power delay profile*) more or equal to the minimal $\mathrm{SNR}^\tau_{\mathrm{min}}$ at a determined hour (h), frequency (f) and day (d):

$$D_\tau(f,h,d) = p(\mathrm{SNR}^\tau \geq \mathrm{SNR}^\tau_{\min})\Big|\Big|_{f,h,d} \text{ in the bandwidth of } Bw \tag{4.60}$$

where the Bw is the bandwidth occupied by the sounding PN-sequences during the wideband sounding interval. According to the algorithms described previously in 4.5.2, D_τ can be estimated using the following expression:

$$D_\tau(f,h,d) = p\Big(10\log_{10}\Big(\frac{\max(\Phi[\tau]), \quad \tau \in [\tau_{\min},\tau_{\max}]}{\mathrm{mean}(\Phi[\tau]), \quad \tau \notin [\tau_{\min},\tau_{\max}]}\Big) \geq \mathrm{SNR}^\tau_{\min}\Big) \tag{4.61}$$

The availability condition of the *multipath* measurement may be related to the SNR_{Bw}, identifying in the Equation 4.47, the *maximum dynamic range* of the *multipath* measurement with respect to noise and interference with the $\mathrm{SNR}^\tau_{\min}$:

$$\mathrm{SNR}_{Bw} + 10\log_{10}\frac{f_c}{\nu_2-\nu_1} \geq \mathrm{SNR}^\tau_{\min}(\mathrm{dB}) \tag{4.62}$$

Then, substitute $\nu_2 - \nu_1 = 5$ Hz, $T_c = 0.2$ ms, and $Bw = 5000$ Hz, then take the value of $\mathrm{SNR}^\nu_{\min}$ indicated by Equation 4.58, we obtain the minimum SNR_{Bw}, which produces the availability of the *multipath* measurement:

$$\mathrm{SNR}^\tau_{\min} = 6 \text{ dB} \Longrightarrow SNR_{\min,5000} \geq -24 \text{ dB} \tag{4.63}$$

Similarly, the availability of the *Doppler* measurement (D_ν) is the probability of obtaining an SNR^ν (measurement about the *Doppler power profile*) more or equal to the minimal SNR^ν_{min} at a determined hour (h), frequency (f), and day (d):

$$D_\nu(f,h,d) = p(\mathrm{SNR}^\nu \geq \mathrm{SNR}^\nu_{\min})\Big|\Big|_{f,h,d} \text{in the bandwidth of } Bw \tag{4.64}$$

where the Bw is the bandwidth, which is occupied by the sounding signal during the wideband sounding interval. According to the algorithms described in 4.5.2, D_ν can be estimated using the following expression:

$$D_\nu(f,h,d) = p\Big(10\log_{10}\Big(\frac{\max(\Phi[\nu]), \quad \nu \in [\nu_{\min},\nu_{\max}]}{\mathrm{mean}(\Phi[\nu]), \quad \nu \notin [\nu_{\min},\nu_{\max}]}\Big) \geq \mathrm{SNR}^\nu_{\min}\Big) \tag{4.65}$$

The availability condition of the *Doppler* measurement may be related to the SNR_{Bw}, identifying in the Equation 4.47 the *maximum dynamic range* of the *Doppler* measurement with respect to noise and interference with the SNR^{ν}_{min}:

$$\mathrm{SNR}_{Bw} + 10\log_{10}\frac{\Delta t}{\tau_2 - \tau_1} \geq SNR^{\nu}_{\mathrm{min}}(\mathrm{dB}) \tag{4.66}$$

Then, substitute $\tau_2 - \tau_1 = 7$ ms and $\Delta t = 12$ s, taking the value of $\mathrm{SNR}^{\nu}_{\mathrm{min}}$ indicated by Equation 4.58: so that, we will obtain the minimum SNR_{Bw}, which produces the availability of *Doppler* measurement:

$$\mathrm{SNR}^{\nu}_{\mathrm{min}} = 6 \text{ dB} \Longrightarrow \mathrm{SNR}_{\mathrm{min},5000} \geq -26 \text{ dB} \tag{4.67}$$

Finally, we will define the availability of the wideband measurement $D_m w$ as the probability of which the availability of *multipath* and *Doppler* is simultaneously produced:

$$D_m w(f,h,d) = p(\mathrm{SNR}^{\tau} \geq \mathrm{SNR}^{\tau}_{\mathrm{min}}, \mathrm{SNR}^{\nu} \geq \mathrm{SNR}^{\nu}_{\mathrm{min}})\Big|\Big|_{(f,h,d)} \text{ in the bandwidth } Bw \tag{4.68}$$

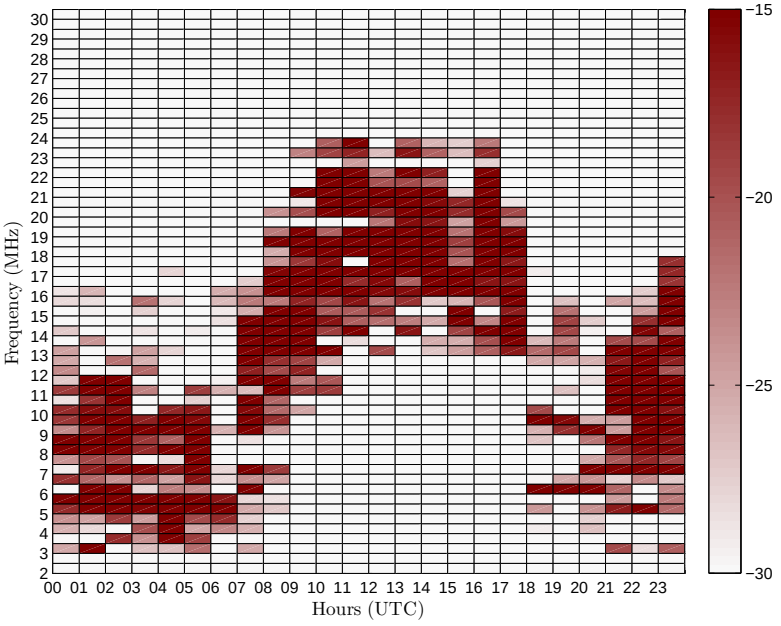

Figure 4.33: Wideband SNR values estimated during 2009/2010, as a function of the hour and the frequency of sounding.

This will be the parameter used for measuring the probability of reception of the sounding signal during the wideband interval.

An estimation of the wideband SNR_{Bw} derived from the *scattering function* as computed in Equation 4.55, is depicted in Figure 4.33. As expected, there are no significant differences between the wideband SNR_{Bw} estimation in Figure 4.33 and the narrowband SNR_{B} estimation showed in Figure 4.30. However, since the wideband signals are more susceptible to noise than the narrowband signals, some frequencies propagated narrowband signals and failed to propagate wideband signals during the same moment.

High SNR values had been estimated during the period that goes from 00:00 UTC to 06:00 UTC with frequency range starts at 3 MHz and ends at 11 MHz. During the daytime region, which had not been analyzed before, the SNR values were raised largely over frequency range from 12.5 MHz to 23.5 MHz. From 18:00 UTC to 20:00 UTC (during the sunset period), high SNR_{Bw} values were observed at 6 MHz and 9.5 MHz. Finally, wideband signals with frequency range from 6.5 MHz to 15 MHz were received with high SNR_{Bw} values throughout time period from 21:00 UTC to 23:00 UTC.

4.6.2.2 *Composite multipath spread*

The propagation of the HF electromagnetic waves through the ionosphere is perfect situation of the *multipath* propagation, since the receiver is receiving several replicas of the original transmitted signal. Reflection from more than one ionospheric layer, and/or after multiple reflections between the ionosphere and the ground are the main causes of the multiple receptions. Each replica of the transmitted signal is generally arriving with a different time *delay*, causing either constructive or destructive interference.

Two replicas of the same electromagnetic radio wave moving simultaneously through the ionosphere will advance independently, each producing a disturbance as if the other is not present. If the two replicas have the same frequency, in phase with each other, and are moving in the same direction, they are additive and are said to interfere constructively. If the two replicas have the same frequency and are moving in the same direction, but out of phase, they are subtractive and are said to interfere destructively.

If these two subtractive replicas have equal amplitudes, these two waves will cancel each other.

In order to measure the *composite multipath spread* of an ionospheric channel, two measures are used (*composite multipath spread* and *effective multipath spread*), which will be explained as below:

- *Composite multipath spread* - measures of the overall temporal spread of the received signal; however, the relative powers contained within the various detected replicas are not taken into account. Specifically, it is taken as the temporal separation between the rising edge of the first detected replica and the falling edge of the last detected replica of the original signal.
- *Effective multipath spread* or *delay spread* - is calculated for a pair of replicas by determining the *multipath* separation between the rise edge of the central 80% power region of the first replica and the trail edge of the central 80% power region of the last replica. Then weight the separation with the ratio of the two replicas' total powers, taking into account that it should be equal or less than unity. This procedure is applied to each pair of replicas in turn and the equivalent *multipath spread* is taken as the maximum value.

Figures 4.34 and 4.35 illustrate the *composite multipath spread* from the *scattering function* of the received signal according to Equation 4.53. Each figure is consisting of six subfigures defining the *composite multipath spread* values of two consecutive hours as a function of the sounding frequencies. The zero values appeared in Figures 4.34 and 4.35 are representing null data, where no successful propagation is taken place.

Looking at the summary of data introduced in Table 4.7, we can state that *composite multipath spread* takes values as minimum as 0.2 ms to the maximum of around 3.1 ms, decreasing with increasing the sounding frequency. The *composite multipath spread* values have been reached 3.1 ms (maximum observed value) at two occasions around midnight: 6.5 MHz at 23:00 UTC; 10.5 MHz at 00:00 UTC. During the nighttime period, the *composite multipath spread* values have exceeded 2.5 ms as depicted in Table 4.6.

From the sunrise at 07:00 UTC to around noontime, where the ionization levels becomes more significant, the *composite multipath spread* values are decreasing along with increasing the sounding frequencies.

Hour (UTC)	F_c (MHz)
00:00	11
02:00	4.5
03:00	12 to 14
20:00	14
21:00	13.5
23:00	6.5

Table 4.6: Maximum *composite multipath spread* values that exceeded 2.5 ms.

Hour (UTC)	Start F_c (MHz)	End F_c (MHz) (MHz)	Max τ_c (ms)	Min τ_c (ms)
05:00	3.5	10.5	2.1	0.4
07:00	8	17	1.6	0.3
08:00	8.5	19.5	2.5	0.2
09:00	10.5	19.5	1.9	0.2
10:00	13.5	23.5	1.7	0.4
11:00	13.5	22.5	1.5	0.25
15:00	10.5	21	2.1	0.2
23:00	5	18.5	3.1	0.6

Table 4.7: The degradation of the *composite multipath spread* values throughout the day.

During the daytime region, after noontime from 12:00 UTC to 17:00 UTC, minimum *composite multipath spread* of 0.25 ms has occurred in a higher frequency range from 12.5 MHz to 23 MHz. It is noteworthy to mention that the measurements over the time periods from 00:00 UTC to 11:00 UTC and from 18:00 UTC to 23:00 UTC with the frequency range from 4.5 MHz to 16.5 MHz agree with the results presented in [48].

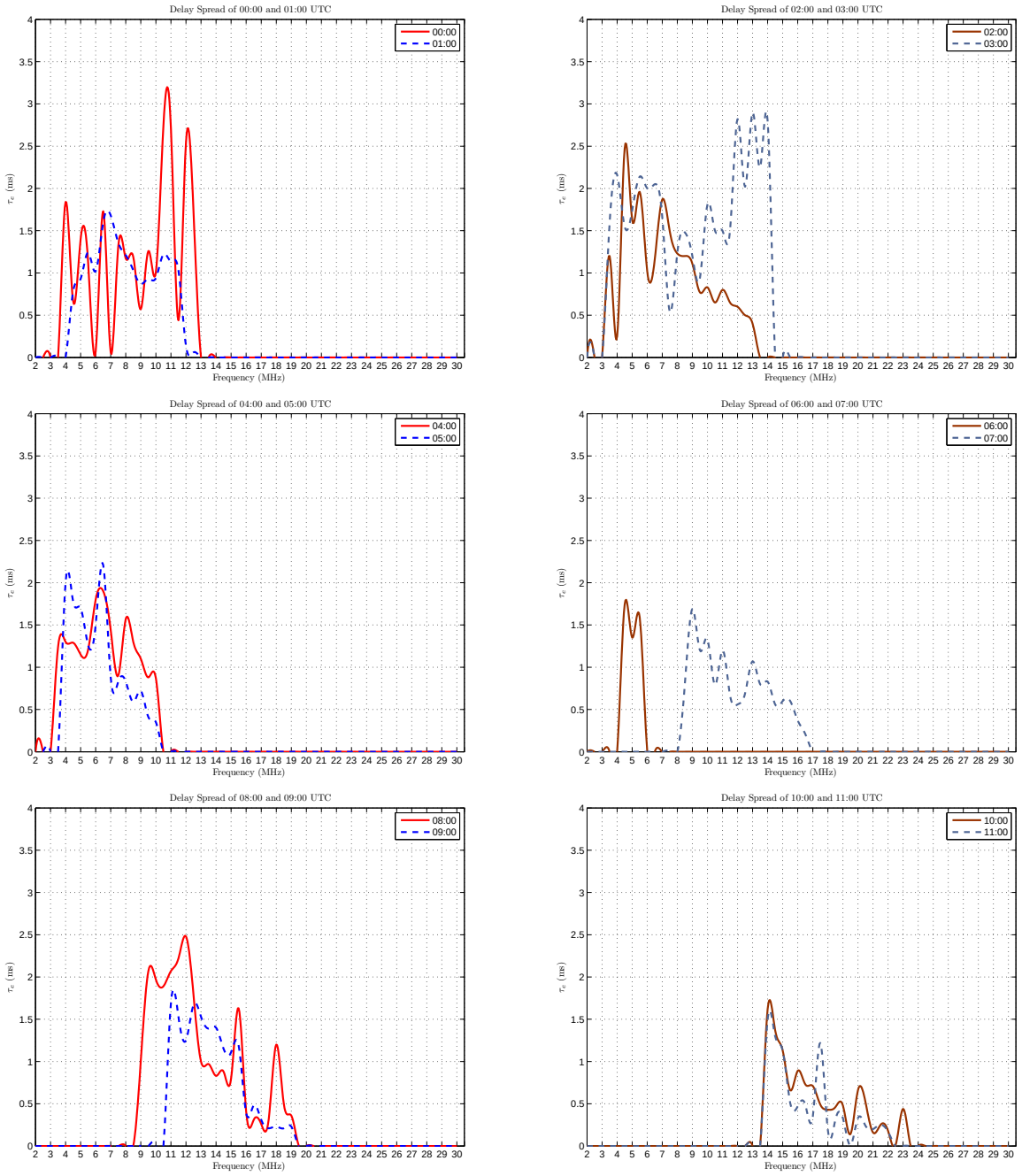

Figure 4.34: The *composite multipath spread* measurements as a function of the sounding frequency and hour from 00:00 to 11:00 UTC.

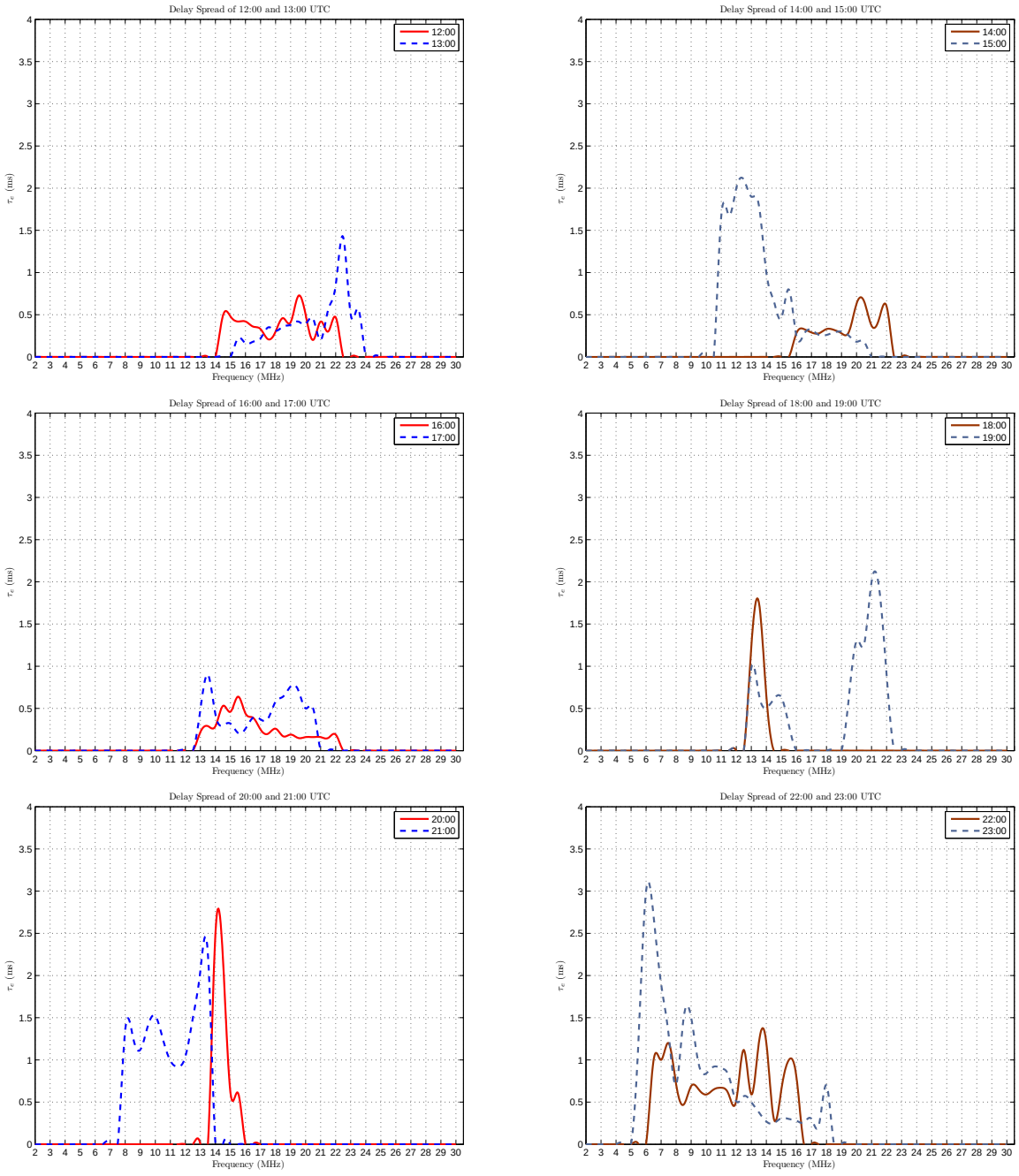

Figure 4.35: The *composite multipath spread* measurements as a function of the sounding frequency and hour from 12:00 to 23:00 UTC.

4.6.2.3 *Composite Doppler spread*

Frequency dispersion usually occurs jointly with time dispersion, although it can exist in the absence of substantial time dispersions as mentioned in [125]. The *composite Doppler spread* is defined as the narrowest spectral width containing 80% of the received signal power. In 4.5.2, we explained the calculation of the *composite Doppler spread*, and measurements from the 2009/2010 survey representing two consecutive hours are illustrated in each subfigure of Figures 4.36 and 4.37.

Maximum *composite Doppler spread* values from 2 Hz to 2.4 Hz have been measured in the frequency range from 3.5 MHz to 14 MHz from 00:00 UTC to 04:00 UTC. So that, the ionospheric channel becomes more wide spread in frequency during the nighttime with low- and mid-frequency range. Table 4.8 shows the *composite Doppler spread* values that exceeded 2 Hz.

Hour (UTC)	F_c (MHz)
00:00	10
01:00	7
03:00	10
04:00	7.5

Table 4.8: Maximum *composite Doppler spread* values that exceeded 2 Hz.

The *composite Doppler spread* values were decreasing from 2.1 Hz to 0.6 Hz with increasing frequency from 8.5 MHz to 23 MHz, during the time period from 08:00 UTC to 11:00 UTC along with the increment of the ionization levels over the ionosphere. Minimum *composite Doppler spread* values from 0.1 Hz to 0.24 Hz measured during the daytime region from 10:00 UTC to 17:00 UTC, in a higher frequency range starts at 15 MHz and ends at 22.5 MHz.

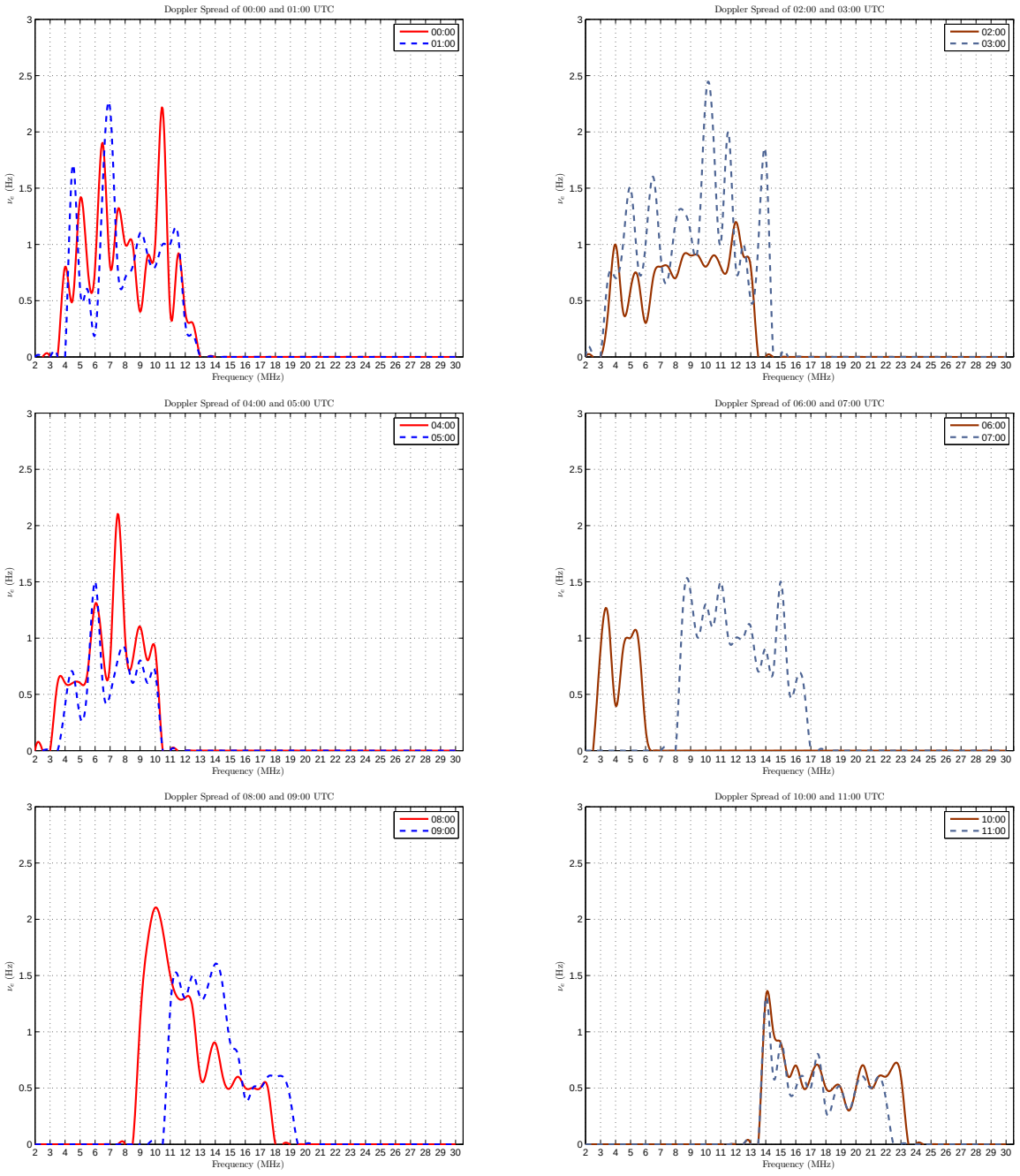

Figure 4.36: The *composite Doppler spread* measurements as a function of the sounding frequency and hour from 00:00 to 11:00 UTC.

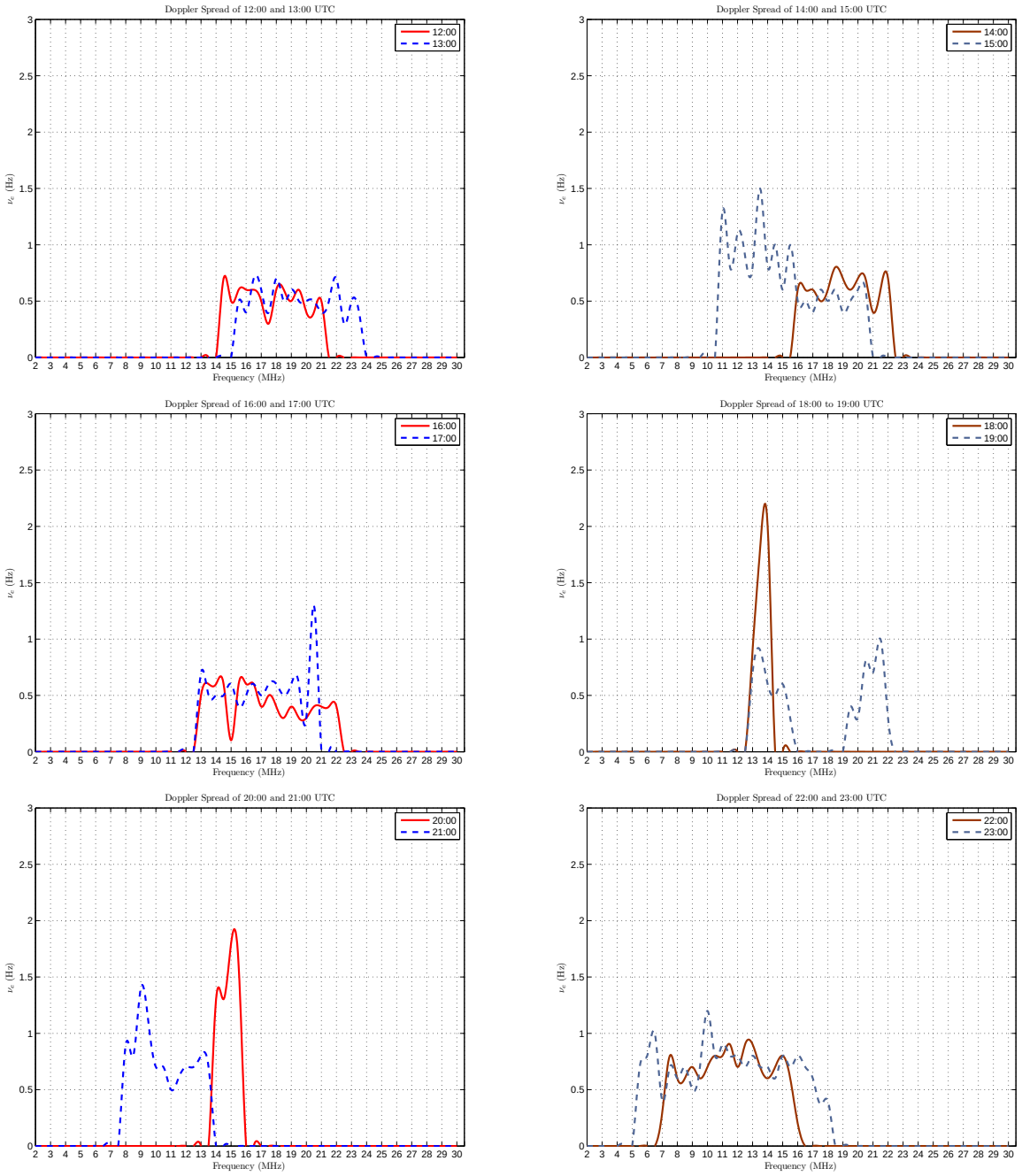

Figure 4.37: The *composite Doppler spread* measurements as a function of the sounding frequency and hour from 12:00 to 23:00 UTC.

It is possible to have a better overview of the behavior of the channel by looking to the *scattering function* that combines information of the time *delay* and the *Doppler* frequency in single graph. *Scattering functions* for several sounding frequencies and times are shown in Figure 4.38. As it has been previously mentioned, the ionospheric channel is wide spread both in time and frequency during the nighttime at lower frequencies, while becomes narrow spread in both time and frequency during the day at higher frequencies.

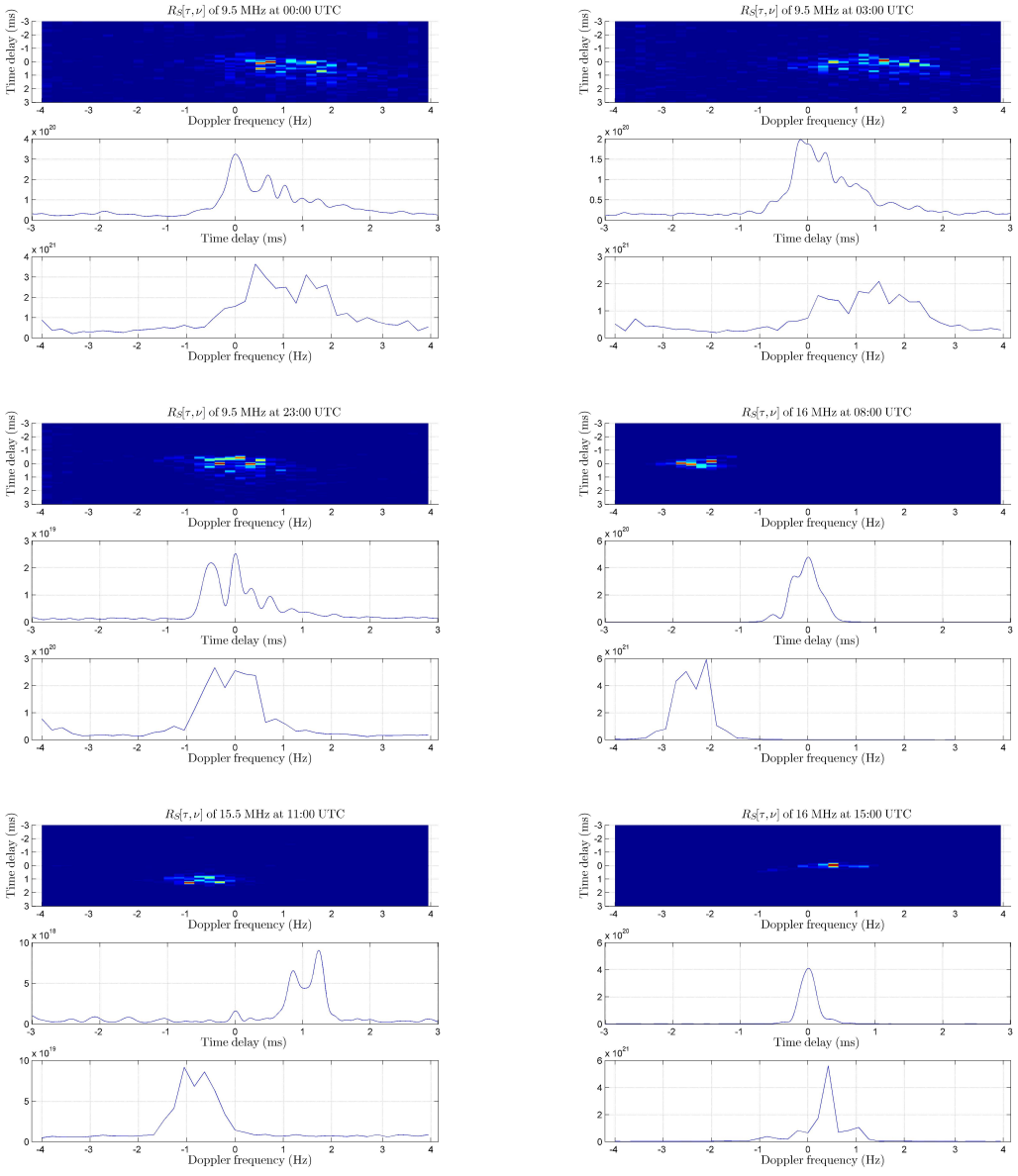

Figure 4.38: *Scattering functions* and their corresponding time *delay* and *Doppler* frequency for different sounding frequencies and times.

4.6.3 Propagation Time

The propagation time means the time it takes for the electromagnetic radio wave to travel from the SAS to OE (12700 km). As initial approach, we assumed the radio waves are moving through free space; so that, the propagation speed is equal to speed of light $(3 * 10^8)$ m/s. The propagation time can be defined as :

$$T = 12700 * 10^3 / 3 * 10^8 = 42.3 \text{ ms} \tag{4.69}$$

In practice, the electromagnetic waves are propagating through the ionosphere, which is different from free space; therefore, we are expecting slightly lower propagation speeds. That will lead to higher propagation times that is already assured by the prediction models, such as the Voice of America Coverage Analysis Program (VOACAP). All the specifications of the SAS-OE ionospheric link were provided to the VOACAP *software*, such as the antenna type, the length of the link, the Smoother Sunspot Number (SSN), etc. Consequently, a propagation time range from 42.8 ms to 45.8 ms have been obtained from the VOACAP *software*.

In order to measure the propagation time of the received signals, we have adapted the measuring technique that mentioned in [114]. The technique mainly deals with the correlated version of the received wideband signals, which is the result of correlating the received signal with the original transmitted PN-sequence. Then, obtains the propagation time through measuring the time *delay* of the first peak of the correlated version of the received signal as shown Figure 4.39.

An accurate time reference is needed at both transmitter and receiver; so that, during the design and implementation stages of the 2009/2010 survey, a new GPS unit from **Garmin** with a Pulse Per Second (PPS) signal of an accuracy of 1 μs was installed to the POTASIO platform (for further details, see, Chapter 3).

The average, maximum, and minimum values of the propagation time as a function of frequency are given in Figure 4.40. As expected, higher average values from 45 ms to 50 ms have been recorded. The variation from minimum to maximum values at each frequency is due to changing the reflection heights propagation modes (e.g., four or five reflection hops). In all cases, the practical propagation times are higher than the one obtained from the VOACAP prediction *software*.

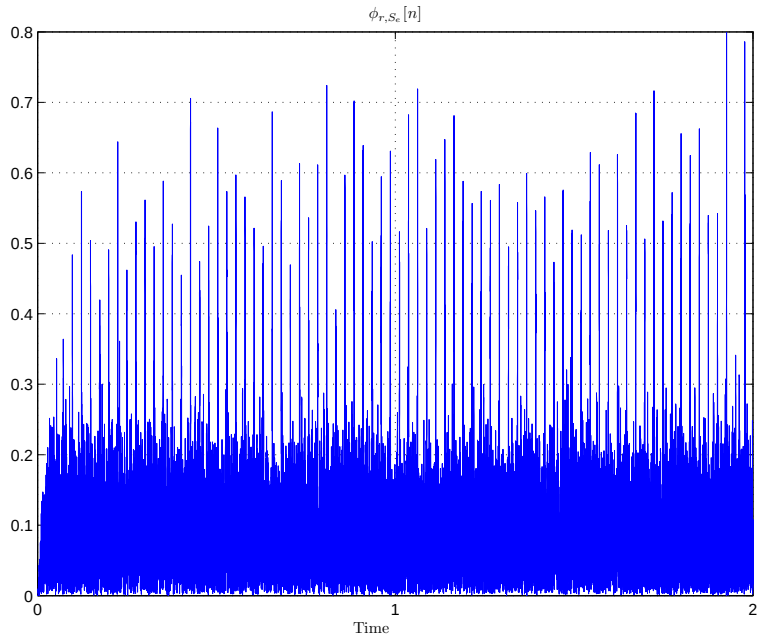

Figure 4.39: A correlated version of the received sounding signal (clipped to 2 seconds long).

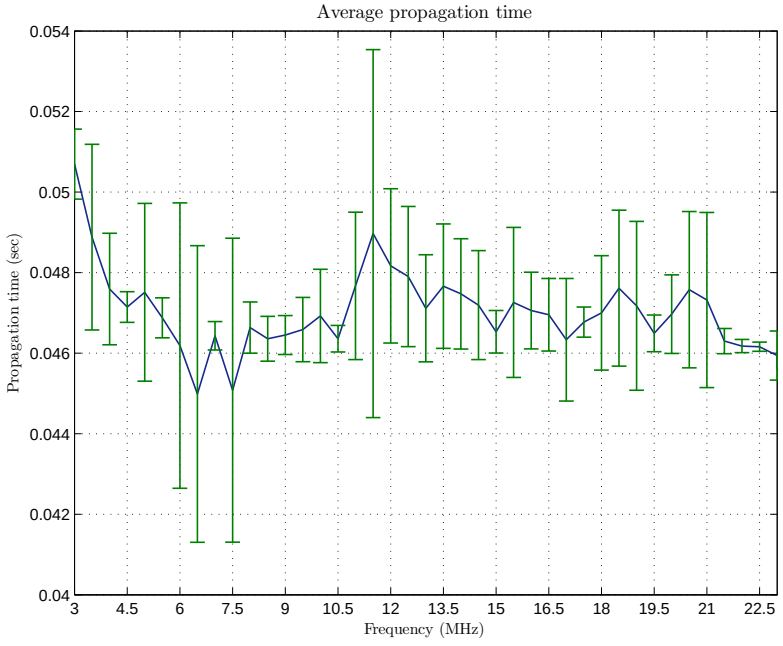

Figure 4.40: Average propagation time as a function of sounding frequencies.

4.6.4 *Doppler frequency shift*

Doppler frequency shift arises due to the mobility in the source or destination or any other objects in between that may change the length of the ray as mentioned in [125]. This can be formulated by a shift in the carrier frequency as follows:

$$f_D = \frac{\nu_a}{\lambda} \tag{4.70}$$

where ν_a is the apparent velocity and λ defines the wavelength. In our case both the transmitter and the receiver are static, while the reflective ionospheric layers are in continuous movement during 24 hours per day.

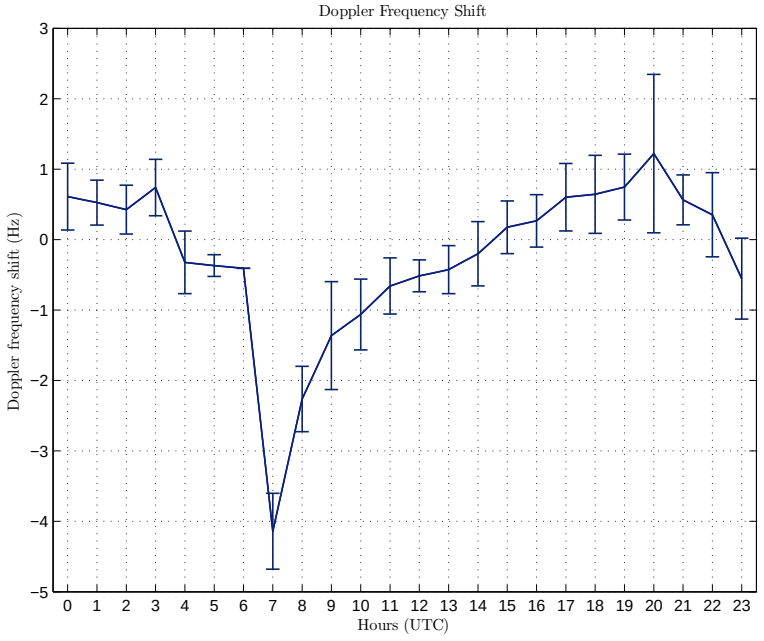

Figure 4.41: Average *Doppler frequency shift* during the 24 hours.

The apparent velocity depends on the refractive index changes over the ionosphere and the real velocity of the wavefront. The refractive index is changing due to the variation of the electron density throughout the ray path; so, the apparent velocity (ν_a) will be given as:

$$\nu_a = \frac{\nu}{\cos\theta} \tag{4.71}$$

where ν represents the velocity of the wavefront and θ is the angle formed by the wavefront and the antenna.

The differences in *Doppler frequency shift* that contribute to a single channel tap is known as the *composite Doppler spread*, which is the measure of the spectral broadening. In the situation of the narrowband signals, the *composite Doppler spread* is usually equal to the maximum *Doppler frequency shift*, while in the wideband signals situation, the *composite Doppler spread* is proportional to the inverse value of the coherence time.

In order to have enough accuracy in our measurement system, an OCXO with a frequency precision of $\pm 30.10^{-9}$ was installed during the 2009/2010 survey. The average *Doppler frequency shift* values as function of time of day are shown in Figure 4.41. As expected, the *Doppler frequency shift* changes are directly related to the changes of ionization levels through the ionospheric layers due to the changes in the solar radiation.

Generally, larger ionization levels result in reflections at lower heights and shorter ray paths. During the daytime period, *Doppler frequency shift* values increased from -4 Hz at 07:00 UTC to 1.2 Hz at 20:00 UTC. During the nighttime period, the values are ranging from -0.5 Hz to 1.2 Hz from 20:00 UTC to 06:00 UTC.

We would like to highlight the sudden *Doppler frequency shift* variations at sunrise. As seen in Figure 19, *Doppler frequency shift* values suddenly change from -0.5 Hz at 06:00 UTC to -4 Hz at 07:00 UTC, due to the fact that sunrise takes only 24 minutes along the 4 reflection hops as mentioned by [48]. On the contrary, the sunset takes 4 hours and 24 minutes along the 4 hops. That is the reason for the smooth transition from 17:00 UTC to 21:00 UTC.

Through [126], *Doppler frequency shift* values observed over the Qaanaaq to Ny-Ålesund (QN) link, which is entirely within the polar cap. Values of around 10 Hz have been measured at the starting of the reception (mid-day of Oct. 25th, 2011), then it decreased to a range from 2 Hz to 5 Hz for around 4 consecutive days.

4.7 Concluding remarks

Through this chapter, we have presented a comprehensive analysis of sounding the SAS-OE link by using narrowband and wideband sounding techniques. All the results introduced previously in this chapter were obtained during the 2009/2010 survey.

The narrowband and wideband sounding parameters, such as the availability of the SAS-OE link, *composite multipath spread*, *composite Doppler spread*, etc., were measured by using the whole HF band and during 24 hours per day. So that, inter-day variations of channel characteristics have been obtained during the 2009/2010 survey.

The propagation time of the received signal and the *Doppler frequency shift* were be able to be measured due to the last *hardware* updates of the transmitter and the receiver. Below we will introduce the concluding remarks, which we came up with, regarding narrowband and wideband sounding parameters, propagation time, and *Doppler frequency shift*.

Narrowband sounding

During the analysis stage of the received signal, we have tested several window filters (*Kaiser*, *Blackman*, *Hanning*, and *Flattop*) to refine the received signal. The *Kaiser* window filter was the most appropriate option. Consequently, the signal will be segmented into a certain number of portions that are equal in length.

The SNR_B has been calculated by comparing the power at the information portions and the waiting portions of the received signal. Two threshold values were defined in order to mitigate the effect of the noise signals on the SNR_B calculations. So, both windowing and time framing techniques proved in several ways their importance.

Regarding the availability of the SAS-OE ionospheric link:

- The frequency range from 10.5 MHz to 21 MHz provided availability from 70% to 90% over the time period from 7:00 UTC to 11:00 UTC.
- Throughout seven consecutive hours starts at noontime (12:00 UTC) to 18:00 UTC, the SAS-OE link was largely available (70% to 90%) with high frequency range from 14 MHz to 23 MHz.
- The SAS-OE link was 50% to 80% available with low frequency range from 3 MHz to 13 MHz over the nighttime period from 00:00 UTC to 06:00 UTC.
- During 19:00 UTC and 20:00 UTC, and with frequency range from 8 MHz to 16 MHz, the link was available from 40% to around 80%.
- Over the time period that goes from 21:00 UTC to 23:00 UTC, the availability of the SAS-OE link was highly available (70% to 90%) with frequency range from 6 MHz to 19 MHz.

The description of the link availability can be summarized into two main time and frequency regions. First, relevant region of high availability existed from 7:00 UTC to around sunset in frequency range from 10 MHz to 23 MHz, which had not been analyzed before the 2009/2010 survey. Second, during the nighttime period from 20:00 UTC to 06:00 UTC, frequencies from 3.5 MHz to 16 MHz showed the best degree of availability, which was totally agree with previous results obtained during the 2006/2007 survey [48]. Finally, the investigations that have been conducted regarding the availability, offered the following:

1. The extension of the oblique soundings to the whole day showed that the SAS-OE link is highly available during the time period that goes from 11:00 UTC to 17:00 UTC.

2. Throughout the daytime period, high frequency range from 13 MHz to around 23.5 were highly propagating over the SAS-OE link.

Wideband sounding

Below, there will be a summarize of the concluding remarks of the wideband sounding parameters that we reached with during 2009/2010 survey.

The wideband SNR_{Bw} estimation over the SAS-OE link as a function of the sounding frequency and time followed the form of the narrowband SNR_{B} estimation and the link availability as well. We can break down the description of the wideband SNR_{Bw} estimation as the following time and frequency regions having high SNR_{Bw} values (15 dB to 20 dB):

- Nighttime period -

    1. from 00:00 UTC to 05:00 UTC with low frequency range that starts at 3 MHz and ends at 11.5 MHz;
    2. from 21:00 UTC to 23:00 UTC with low frequency range that starts at 7 MHz and ends at 16 MHz.

- Daytime period -

    1. from 10:00 UTC to 17:00 UTC with high frequency range from 13 MHz to 23.5 MHz;

2. from 07:00 UTC to 09:00 UTC with frequency range of minimum values varying from 9 MHz to 11 MHz and maximum values varying from 15 MHz to 20 MHz.

The *composite multipath spread* values showed clear differences between nighttime and daytime periods. The maximum *composite multipath spread* values have been obtained from 20:00 UTC to 03:00 UTC and just after sunrise at frequencies lower than 14 MHz, while the minimum values have been observed during the day from 12:00 UTC to 17:00 UTC, in a higher frequency range from 12.5 MHz to 23 MHz.

Maximum *composite Doppler spread* values from 2 Hz to 2.4 Hz were measured from 00:00 UTC to 04:00 UTC, with frequency range from 3.5 MHz to 14 MHz. The *composite Doppler spread* values decreased along with increasing the sounding frequency from 8.5 MHz to 23 MHz. A degradation in the *composite Doppler spread* values from 2.1 Hz to 0.6 Hz was noticed during the time period from 08:00 UTC to 11:00 UTC. The minimum *composite Doppler spread* values from 0.1 Hz to 0.24 Hz were measured during the daytime hours from 10:00 UTC to 17:00 UTC. Such minimum values have been noticed with higher sounding frequency range from 15 MHz to 22.5 MHz.

Propagation time

The average propagation time values were ranging from 45 ms to 50 ms throughout 24 hours per day. These values are slightly higher than the results of the VOACAP *software* (42.8 ms to 45.8 ms). The difference between the simulation and the *real-time* measurements could be related to the *multipath* propagation of the electromagnetic waves through the ionosphere (receive the signals through various paths with different lengths).

Doppler frequency shift

The movement of each of the ionospheric layers over the 24 hours per day causes the *Doppler frequency shift*. During the daytime period, the values of the *Doppler frequency shift* varied from -4 Hz to 1.2 Hz; on the other hand, it changed from -0.5 Hz to 1.2 Hz during the nighttime period.

The sunrise takes around half an hour to be completed; so that, the ionization levels will increase rapidly to the maximum through the ionosphere. That lead to change the *Doppler frequency shift* values from -0.5 Hz (06:00 UTC) to around -4 Hz (07:00 UTC). Consequently, during the daytime period, the D layer is appearing and high

frequency range is the only usable range. The *Doppler frequency shift* values started to decrease smoothly from sunrise (-4 Hz) to around sunset (1.2 Hz), which is might be regarded to changing the reflection layers.

Chapter 5

Vertical and Oblique soundings variation

Herein this chapter, starts with an introduction followed by Sections 5.2 and 5.3 that is giving descriptions of both sounding systems, the Oblique Incidence Sounding (OIS) and the Vertical Incidence Sounding (VIS), respectively. Thereafter, the measurements of the solar activity during three surveys (2009/2010, 2010/2011, and 2011/2012) is discussed in Section 5.4. Then parameters, such as the channel availability and Frequency of Largest Availability (FLA) are compared to the MUF from Rec533 model (MUFRec533) in Section 5.5. Section 5.6 is dedicated to explain the day-to-day and inter-day variations of the Total Electron Content (TEC), critical frequency of the F2 layer (foF2), and Maximum Usable Frequency for ground distance reflected at the F2 layer (MUF(3000)) recorded at VIS stations located close to the SAS-OE link path. The likeness between the MUF(3000) and FLA measurements is explained in Section 5.7. Finally, a summary and the concluding remarks are given in Section 5.8.

5.1 Introduction

The transmitter of the OIS system has been installed in the Spanish Antarctic Station (SAS) (62.6 S, 60.4 W) and collocated with a VIS unit. Besides that, the receiver of the OIS system has been located at the Ebro Observatory (OE) (40.8 N, 0.5 E) where another VIS system is operating. The distance between SAS and OE is around 12700 km; therefore, four reflection hops of 4000 km are established with approximate latitudes and longitudes appeared in Figure 5.1 and illustrated in Table 5.1.

Currently, several types of ground-based ionospheric sounding systems are being developed and experimented around the world, such as the Oblique-Backscatter Sounding [127, 128], OIS [129, 130], and VIS [131]. The utilization of a sounding system among the others is depending on the capabilities and limitations of each system.

The Oblique-Backscatter Sounding technique is suitable for monitoring large area as discussed in [128]; however, recognize the echo propagation paths is the major drawback of this technique. In order to overcome this issue, the Oblique-Backscatter Sounding system has to be operate together with anther VIS or OIS unit as explained in [132]. One of the recent systems is the Wuhan Ionospheric Oblique Backscattering Sounding System (WIOBSS), which is a combination of an OIS system besides the Oblique-Backscatter Sounding system as introduced in [133].

The OIS system that is being utilized over the SAS-OE link has been upgraded several times since the first establishment at 2003, with three main *Software Defined Radio* (SDR) platforms (SANDICOM, SODIO, and POTASIO). The description of the SANDICOM and SODIO were introduced in [49, 106], while an extensive description of the last platform (POTASIO) can be found in Chapter 3. The main objective of the OIS system is establishing a long-haul HF link between SAS and OE, in order to transmit the information gathered by the geomagnetic sensors located at SAS to its final distention at OE.

Both the SAS and the OE have two different VIS systems operating for more than a decade to analyze the physics of the ionosphere, for further details about the structure of those systems, we are refereeing the reader to [134, 135]. The physical behavior of the ionosphere at the locations of both the OIS transmitter and receiver is being investigated through two different VIS systems. Later on, during the next two sections, the OIS and VIS systems will be discussed in deep.

The parameters that we can obtain form the OIS systems present important knowledge about the electromagnetic wave propagation through the ionosphere, but less information from the physical point of view. Otherwise, the VIS systems provide better prediction of the usable HF frequencies for achieving high quality long-haul link.

In [134], there is a presentation of the Maximum Received Frequency (MRF), channel availability, and the FLA data that were measured from the OIS system throughout the 2006/2007 survey. Besides that, the inter-day and day-to-day variations of the foF2 and MUF(3000) parameters were presented, which have obtained from four different VIS stations located along the SAS-OE link path during the same period. Finally, in

Station	Latitude	Longitude	URSI code
SAS	62.7 S	60.4 W	
Port Stanley	51.6 S	57.9 W	PSJ5J
H1	50.4 S	43.6 W	
H2	21.1 S	27.4 W	
Ascension Island	7.95 S	14.4 W	AS00Q
H3	1.3 N	17.3 W	
El Arenosillo	37.1 N	6.7 W	EA036
H4	28.2 N	7.1 W	
OE	40.8 N	0.5 E	EB040

TABLE 5.1: The locations of the VIS stations and the reflection hops of the OIS link from the SAS to OE (SAS-OE).

order to analyze the behavior of the ionosphere from both physical and communications engineering point of view, there are comparisons between the outcomes of the VIS and OIS systems, and HF propagation models.

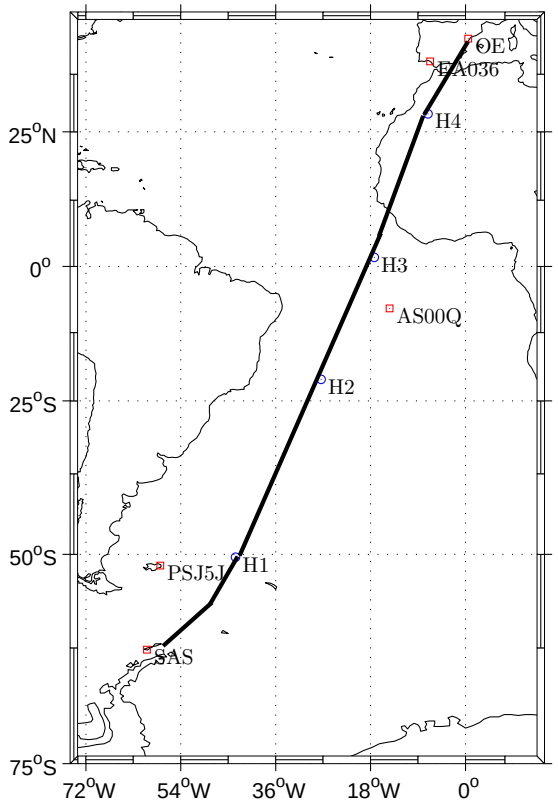

FIGURE 5.1: The SAS-OE ionospheric link path and the approximate locations of the VIS stations and reflection hops.

All the measurements that will be explained through this chapter were measured during three consecutive surveys (2009/2010, 2010/2011, and 2011/2012). Ideally,

the survey starts at November and ends at March of the next year, which is called the austral summer; however, in practice the OIS system is usually operating over a period of one month. That is regarding several technical, forecast, environmental, and logistical issues. Selecting the austral summer to conduct the survey is due to having the best weather conditions. Usually, all the components of the transmitter are ready to be shipping towards the SAS before November.

5.2 Oblique incidence sounding

The OIS system is working continuously for a complete decade since 2003, providing great knowledge about the SAS-OE link. All the updates that have been taken place to the OIS system during the 2009/2010 survey, along with the results (channel availability, *composite multipath spread*, *composite Doppler spread*, propagation time, and *Doppler frequency shift*) are previously explained in deep through Chapter 4 and in [49]. This system is able to operate during 24 hours per day and using the whole HF band (2 MHz to 30 MHz), which was a large development step comparing to the previous platform (SODIO). Another great feature is having the lowest frequency drifts between transmitter and receiver due to installing highly stable clock called Oven Controlled Crystal Oscillator (OCXO) with a working frequency of 100 MHz.

During the last three surveys, narrowband sounding has been carried out over the SAS-OE link in order to estimate the SNR_B, and consequently the availability of the link. Besides that, the wideband sounding has been allowing measurements of *Doppler frequency shift*, *composite multipath spread*, *composite Doppler spread*, and propagation time.

Referring to the availability of the SAS-OE link obtained during the 2009/2010 survey, it can be summarized into two main time regions (daytime and nighttime). A substantial availability of the link has been observed during the daytime from 07:00 UTC to around sunset through a frequency range from 10 MHz to 23 MHz, which had not been analyzed before, due to some degrees of lack in the SODIO platform. The nighttime period goes from 20:00 UTC to 06:00 UTC with a frequency range from 3.5 MHz to 16 MHz resulted in significant availability, which is considered a confirmation of the previous results measured during the 2006/2007 survey and published in [48].

Survey	Start	End	No. of days
2009/2010	1/1/2010	2/2/2010	33
2010/2011	22/1/2011	26/2/2011	35
2011/2012	30/12/2011 17/2/2012	9/1/2012 22/2/2012	17

TABLE 5.2: The start, end, and number of operating days for each of the three surveys.

The FLA parameter indicates which frequency has the greatest chance to reach the receiver at certain moment; so that, it is quite important parameter for the propagation of the HF electromagnetic waves through the ionosphere. In order to highlight the likeness between the OIS and VIS measurements, FLA that has been calculated during three surveys (2009/2010, 2010/2011, and 2011/2012) will be compared with the MUF(3000), which has been recorded at VIS stations located along the SAS-OE ionospheric link path throughout the same period.

It should be noted that the results of the 2009/2010 survey were measured during 33 days from the 1st of January to the 2nd of February 2010. Regarding the 2010/2011 survey, the measurements have been recorded throughout 35 days from the 22nd of January 2011 to 26th of February 2011. Finally, for the 2011/2012 survey, 17 days from 30th of December 2011 to 9th of January 2012 then from 17th of February 2012 to 22nd of February 2012 were the active period of the system. The previous time periods indicating the working time of the sounding system are summarized in Table 5.2.

5.3 Vertical incidence sounding

The VIS systems are used to transmit sounding pulses vertically towards the ionosphere, then the reflected pulses are processed by the receiver unit to produce the ionograms that is appeared in Figure 5.2. In [136], a VIS system was introduced with a Dynasonde software for data acquisition. Since then, several automated scaling techniques for handling these ionograms were introduced, such as in [137].

Some of the parameters of the VIS systems may be predicted by the propagation models for short distance sky-wave ionospheric paths. However, apply some geometrical factors to the ionograms will lead to the propagation properties of longer OIS ionospheric paths. The reliability of these properties depends on how much the reflection points of the OIS link are close to the VIS stations as mentioned in [134].

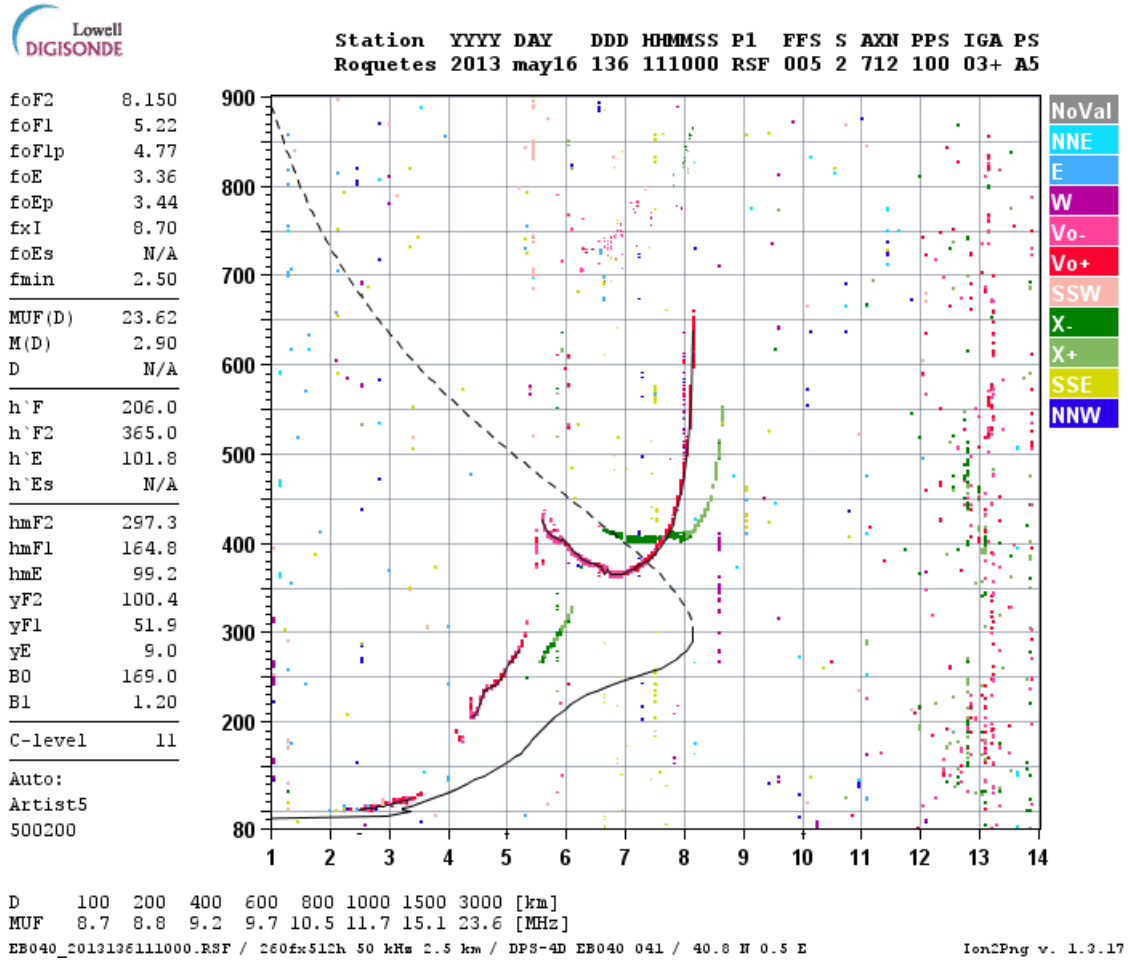

FIGURE 5.2: An ionogram obtained from the VIS system in OE, Roquetes, Spain at 16 of May 2013, 11:10 UTC

Also, in [138, 139], there are several discussions on how the observation at one point could clarify the ionospheric conditions at other closer points. This is the concept that fostered the idea of comparing the MUF(3000) parameter from multiple VIS stations with the FLA from the OIS system.

There are three different techniques to carry out vertical sounding, the *Pulse ionosonde*, *Chirp Sounder*, and the *Digisonde*. We highlight the *Digisonde* system over the rest of the system, since it has being used in the work presented in this thesis. The *Digisonde* is the well-known system developed by the center for Atmospheric Research at the University of Massachusetts Lowell (UMLCAR). Currently, *Digisonde* systems are operating in several VIS stations around the world. In both SAS and OE, there are two different type of VIS systems in order to monitor the ionosphere at these positions.

An Advanced Ionospheric Sounder (AIS) system developed by Istituto Nazionale di

Geofisica e Vulcanologia (INGV) of Rome has been used in the SAS since the 2004/2005 survey (For extensive description of the AIS, see, [140]). Since ever, the AIS system has not been upgraded, because of the logistic limitations, low investment budget, limited operation time, etc.

At the OE, there was *Digisonde* model (DGS-256) of the University of Massachusetts at Lowell (http://ulcar.uml.edu/digisonde.html), which was operating throughout seven consecutive surveys from 2004/2005 to 2010/2011. In September 2011, the VIS system that located in OE had been upgraded from DGS-256 to the Digital Portable Sounder (DPS) 4D. Both systems are products of Lowell *Digisonde* International. As explained in [141], the DPS-4D is HF radar system for ionospheric research and monitoring (http://ulcar.uml.edu/digisonde-manual.html), and it has the same principles of the previous *Digisonde* VIS family.

The *hardware* and *software* of the DPS-4D model have been upgraded over the previous version (DGS-256). The signal is received by an electronically switched crossed loop antennas. Fast 16-bit Analogue/Digital (A/D) converters were installed, in addition to 15 dB signal processing gain from phase coded pulse compression. Besides that, there is a signal processing gain of 21 dB from coherent *Doppler* integration. Also, it has an RF interference mitigation algorithm, which is resulting in signal gain up to 35 dB. Additional two embedded computing platforms have been added for *hardware* control, data acquisition, processing, storage, publishing, and dissemination. Signal processing functions applied to the time domain data through *software* implementation. An embedded expert system was installed to automatically identify the ionospheric layers and parameter scaling. Figure 5.2 shows an example of VIS ionogram obtained from DPS-4D system located at OE, Spain. Finally, there is an additional ability of accessing the *real-time* measurements by using the Internet.

Several parameters, such as foF2, MUF(3000), TEC, etc., were recorded by the VIS systems over the three surveys. The VIS systems usually generate a large amount of data that is difficult to be processed manually. Therefore, to handle the required parameters, the University of Massachusetts Lowell has developed a Read/Display Digisonde data tool called *SAOExplorer* v.3.4.1.9., which will significantly simplify the analysis of the demanded VIS parameters.

5.4 Solar activity

The activities associated with the Sun have a period of rise and fall of around 11 years. The magnetic fields of the sunspots result in more *Ultraviolet* (UV) radiation towards the Earth, which will increase the electron density in the ionosphere. Figure 5.3 illustrates an overview of the Smoother Sunspot Number (SSN) values from 1995 to 2012. In order to understand the ionospheric propagation, a considerable effort has to be dedicated to figure out the relationship between the solar activity (SSN, Solar Flux, etc.) and the state of the ionospheric characteristics. So that, the correlation between SSN, Solar Flux values, and ionospheric daily, monthly, and annually parameters has to be studied in deep.

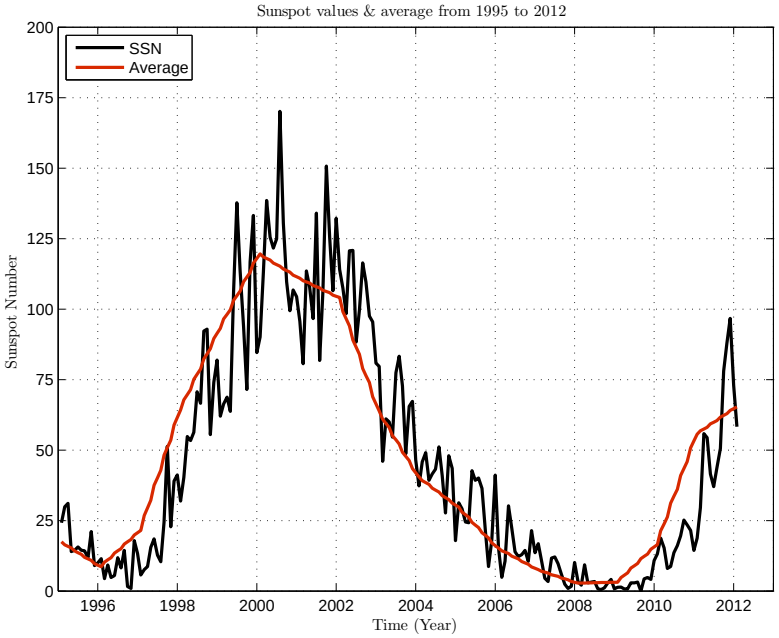

FIGURE 5.3: SSN values and the average during the period from 1995 to 2012.

During the period of maximum sunspot numbers, the highly ionized F2 layer acts like a mirror, refracting the higher HF frequencies above 20 MHz. As the Sun is very active and more radiation being emitted, backscatter propagation either from the ionosphere or the auroral layers could be possible. Besides that, there is a greater likelihood of occurring large *Solar Flares*, which ionizes the D layer, causing more absorption of electromagnetic waves with lower HF band. Since the D layer presents only during the day, only those communications paths that pass during the daytime period will be effected.

Otherwise, throughout the period of minimum sunspot numbers, the chromosphere becomes very quiet and its UV emission is very low. Consequently the MUF(3000) decreases, even it is rarely rising to 20 MHz, and the majority of the long distance ionospheric communications must be conducted on lower HF bands.

Figure 5.3 shows average SSN values of 11.68, 21.1, and 65.3 measured over the 2009/2010, 2010/2011, and 2011/2012 surveys, respectively. In addition to the SSN measurements, the solar activity can be monitored by the Solar Flux, the larger the Solar Flux number, the greater the Sun's influence on the ionospheric propagation. Throughout the 2009/2010, 2010/2011, and 2011/2012, average Solar Flux values of 79, 86, and 134 Solar Flux Unit (SFU) have been measured. Since the Sun represents the ionization source of the ionosphere, the propagated range of frequencies is overturning during the sunrise and sunset periods of the day. Figures 5.4 and 5.5 show the sunrise and sunset times, during the austral summer, of the four reflection hops and the VIS stations located along the link path. The sunrise takes an average of one hour to be finished as illustrated in Figure 5.4. On the other hand, Figure 5.5 shows that the Sun takes around four hours and half to be vanished along the path.

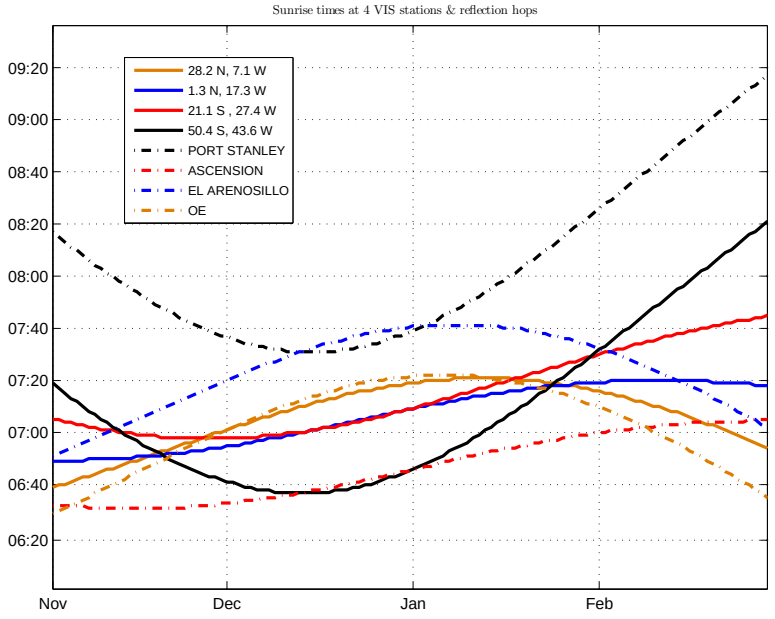

FIGURE 5.4: The sunrise times at four reflection hops of the SAS-OE link and four VIS stations located along the link path.

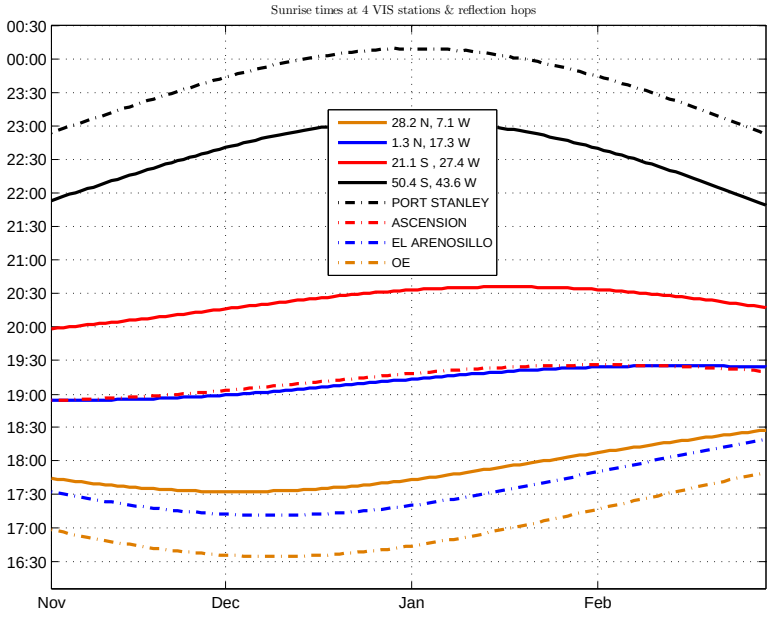

FIGURE 5.5: The sunset times at four reflection hops of the SAS-OE link and four VIS stations located along the link path.

5.5 Oblique incidence sounding, data, and results

As explained in Section 5.2, the OIS analysis focuses on the SNR_B estimation and consequently the channel availability, using new method of computation based on filtering the received signal through window filter, in addition to framing the time envelope of the received signal, as clarified in [49]. Generally, high propagation conditions associated with the daytime period are largely supported by the high ionization conditions, and the existence of the F2 layer. The D layer complete absence during the night leads to high propagation conditions at low HF range; however, frequencies lower than 10 MHz did not propagate over the daytime because of the existence of the D layer.

The channel availability, FLA, and MUFRec533 [134, 142] obtained during the three surveys are illustrated in Figures 5.6, 5.7, and 5.8. These figures can be interpreted in terms of two main time region: the daytime region that lasts from around sunrise (07:00 UTC) and vanishes at sunset (18:00 UTC); the nighttime region starts at around the sunset (18:00 UTC) and finishes at sunrise (07:00 UTC).

Prior to the 2009/2010 survey, the OIS was sounding only 18 hours per day, which is one of the drawbacks of the SODIO platform, that besides the inability to used the whole HF band. However, the ability of the new OIS platform (POTASIO) to operate throughout 24 hour per day and with the whole HF band represented a large step

forward to have a complete study of the channel. So that, as explained in [49], the channel is highly available at high frequencies (10 MHz to around 25 MHz) during the daytime period from 07:00 UTC to 18:00 UTC, which was not analyzed before the 2009/2010 survey.

5.5.1 2009/2010 survey

The 2009/2010 survey was the first occasion to investigate the performance of the new platform, which was fully operational (24 hours per day with the whole HF band). The results obtained in 2009/2010 are extensively explained in [49]. Figure 5.6 shows the channel availability, inter-day variability of the FLA, and MUFRec533 of the whole HF band during the 2009/2010 survey. There are two differentiated regions have been observed with the following characteristics:

1. The daytime region - high channel availability has been recorded from 08:00 UTC to 10:00 UTC with frequency range from 10 MHz to 17 MHz, then it has changed from 13 MHz to 23.5 MHz during the time interval from 11:00 UTC to 17:00 UTC.

2. The nighttime region - the channel was around 40% available from 10.5 MHz to 16.5 MHz over the period that goes from 18:00 UTC to 20:00 UTC. Then, the channel availability has increased to around 90% from 6.5 MHz to 17.5 MHz from 21:00 UTC to 23:00 UTC. Finally, frequency range from 6.5 MHz to 13 MHz were highly propagated throughout the time period from 00:00 UTC to 7:00 UTC.

Frequencies higher than 23.5 MHz did not propagate throughout the whole survey. Generally, the FLA is about 5 MHz below the MUFRec533 as shown in Figure 5.6. An average FLA of 8 MHz has been measured from midnight to sunrise, which then increased quickly to 13 MHz because of the sudden sunrise. Thereafter, it has gradually increased along with the Sun rising to 18.5 MHz at 16:00 UTC, and it decreased again during the sunset period along the link. From 20:00 UTC to midnight, an FLA average of 11 MHz has been measured. As an observation, the difference between the FLA and the MUFRec533 has reached the highest value (7 MHz) at midnight (00:00 UTC). Also, as illustrated in Figure 5.6, the MUFRec533 is approximately limiting the channel availability scheme, especially during the period from 00:00 UTC to 16:00 UTC.

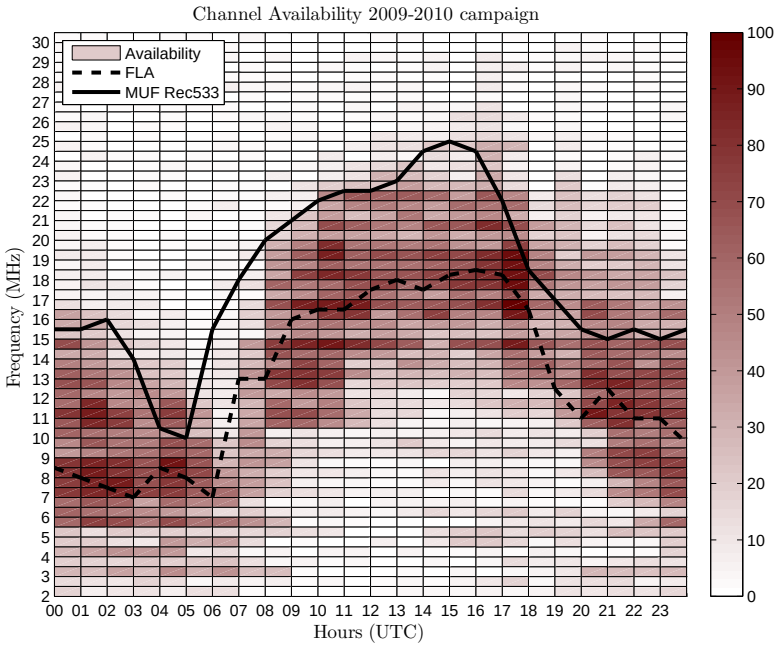

FIGURE 5.6: Comparison between the inter-day variation of the FLA, MUFRec533, and the channel availability of the SAS-OE link during the 2009/2010 survey.

5.5.2 2010/2011 survey

Figure 5.7 shows comparison between both the availability of the SAS-OE link, the corresponding inter-day FLA variation from the OIS system, and the MUFRec533 throughout the 2010/2011 survey. As a first observation, the frequency availability scheme of the SAS-OE link throughout the 2010/2011 survey is slightly higher than during the previous survey. The main two time/frequency propagation regions can be described as:

1. The daytime region - during the time period from 7:00 UTC to 10:00 UTC, high channel availability has been recorded from 12 MHz to 17.5 MHz. Then during the second segment of the daytime region from 11:00 UTC to 18:00 UTC, the channel was highly available within the frequency range from around 15 MHz to 25.5 MHz.

2. The nighttime region - from 00:00 UTC to 03:00 UTC, the HF ionospheric propagation started to increase gradually with frequency range from 6 MHz to 13.5 MHz. Then, the frequency range from 7 MHz to around 10 MHz had good propagation properties during the period that goes from 04:00 UTC to 06:00 UTC.

The Sun, which is the main source for ionizing the ionosphere starts to disappear from 18:00, and the channel became less available at 19:00 UTC with frequency range from 14.5 MHz to 20 MHz. Consequently, the significant channel availability changed from 8.5 MHz to 16.5 MHz over 20:00 UTC and 21:00 UTC. Finally, high propagation has been observed at 22:00 UTC and 23:00 UTC through the frequency range that starts at 8.5 MHz to around 14.5 MHz.

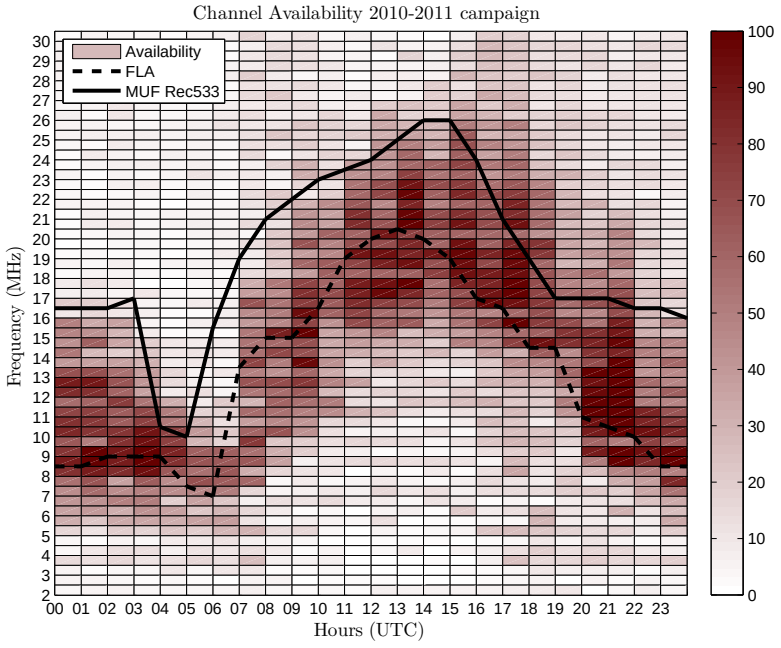

FIGURE 5.7: Comparison between the inter-day variation of the FLA, MUF Rec 533, and the channel availability of the SAS-OE link throughout the 2010/2011 survey.

During the 2010/2011 survey, 25.5 MHz was the upper bound of the propagated frequencies during the daytime period and 18 MHz over the nighttime. Regarding the FLA measurements, average of 9 MHz has been recorded from midnight to 04:00 UTC; then, it decreased to 7 MHz. Consequently along with the sunrise, FLA raised from 7 MHz to 13 MHz at 06:00 UTC. Throughout the daytime period from 07:00 UTC to 18:00 UTC, the FLA values have increased to around 21 MHz at 13:00 UTC, and then decreases to 14 MHz at 18:00.

The sunset has been completed, and the FLA values continued the decrementing stage to 10 MHz at around midnight. Similarly, as observed during the previous survey (2009/2010), the average FLA values have followed the scheme of the MUFRec533, and the MUFRec533 values were bounding the channel availability scheme approximately throughout the 24 hours.

5.5.3 2011/2012 survey

Prior to the initiation of the 2011/2012 survey, three different antennas have been installed at the receiving side (monopole, yagi, and V-antenna); so that, we can investigate the correlations between the *Ordinary* and *Extraordinary* versions of the received signals. Figure 5.8 represents illustration of the channel availability, the inter-day variation of FLA, and the MUFRec533 measured throughout the 2011/2012 survey. The availability of the SAS-OE link throughout the two propagation regions may be summarized into:

1. The daytime region - immediately after sunrise, the availability raised significantly from low frequency range (3.5 MHz to 9.5 MHz) to mid frequency range (9 MHz to 21.5 MHz) due to the sudden increment of the ionization levels over the ionosphere. The emissions from the Sun become more stable during the daytime period (08:00 UTC to 17:00 UTC); so that, the SAS-OE link has been strongly available through frequency range starts at 11 MHz and ends at 28 MHz.

2. The nighttime region - the SAS-OE link was highly available during the time period that goes from 00:00 UTC to 04:00 UTC with frequency range starts from 5 MHz to the maximum of 18 MHz, which then decreased to around 13.5 MHz. Frequencies lay on the 3.5 MHz to 10 MHz range have propagated through the SAS-OE link over 05:00 UTC and 06:00 UTC. The SAS-OE link was around 60% available with a frequency range starts at 11 MHz to almost 18 MHz throughout the time period that goes from 18:00 UTC to 20:00 UTC. Consequently, before midnight, the channel was 50% available with frequency range from 9 MHz to 18 MHz.

In [143], generally the real time observations are similar to the predictions, however, there are some discrepancies. In February, while we are usually carrying out the surveys, the predicted median MUF is higher than the real-time observations. Also, as discussed in [134], throughout the nighttime period, the MUFRec533 values were higher than the observations of FLA and MUF(3000) obtained at several VIS stations along the SAS-OE link.

Regarding the average FLA during the 2011/2012 survey, from midnight to 04:00 UTC, an average FLA of 10 MHz has been obtained; then, has declined to around 7

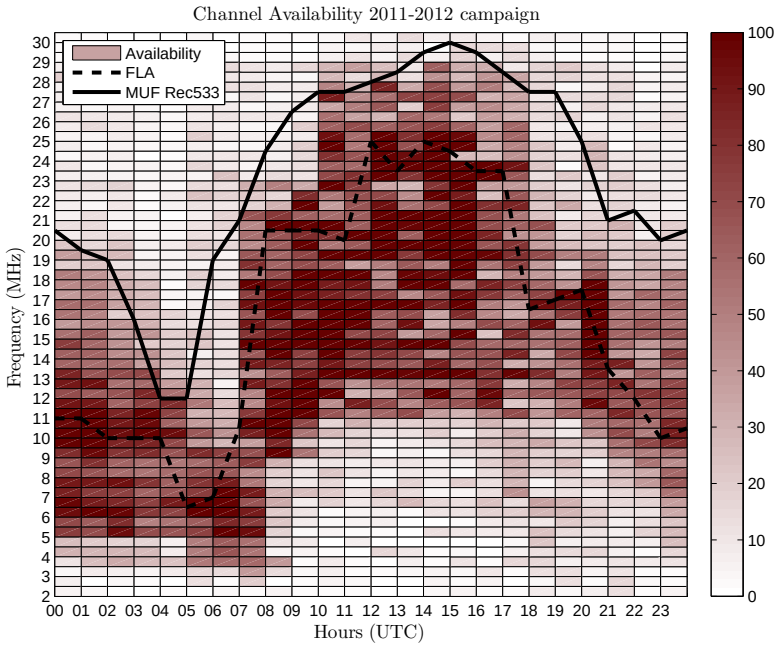

FIGURE 5.8: Comparison between the inter-day variation of the FLA, MUFRec533, and the channel availability over the 2011/2012 survey.

MHz just before starting the sunrise. The average FLA started to increase substantially to almost 20 MHz throughout the time period that goes from 08:00 UTC to 11:00 UTC.

The maximum FLA of 25 MHz has been measured at exact noontime, and then it started to be stable until 16:00 UTC. At 18:00 UTC, average FLA was decreased instantly form 23.5 MHz to 16 MHz at 17:00 UTC because of the large drop that was happened to the ionization levels. Small increment is observed from 16 MHz to 16.5 MHz throughout the time period that goes form 18:00 UTC to 20:00 UTC; then, it was decreased to 11 MHz at exactly midnight.

As shown in Figure 5.8, throughout the 2011/2012 survey, the highest frequency where the SAS-OE link is available was around 28 MHz during the daytime region, and 19 MHz at the nighttime region. The average FLA and the SAS-OE link availability have followed the scheme of the MUFRec533 during 2011/2012 survey as noted previously during 2009/2010 and the 2010/2011. Table 5.3 summarizes the frequency ranges where the SAS-OE link was available over the three surveys segmented into the two time regions.

A comparison is illustrated in Figure 5.9 between the inter-day FLA variations that have been measured during the three surveys 2009/2010, 2010/2011, and 2011/2012 survey, where we noticed that the average FLA measurements of 2009/2010 are similar

Survey	Daytime	Nighttime		
	08 to 17	00 to 04	05 to 07	18 to 23 (UTC)
2009/2010	10 to 23.5	5.5 to 14	10 to 17	10.5 to 17.5 (MHz)
2010/2011	12 to 25.5	6.5 to 15	8 to 17.5	8.5 to 16.5 (MHz)
2011/2012	10 to 28	5 to 18	3.5 to 21	11 to 18 (MHz)

TABLE 5.3: The frequency range where the channel was available during the three surveys summarized into 4 time segments of the daytime and nighttime regions.

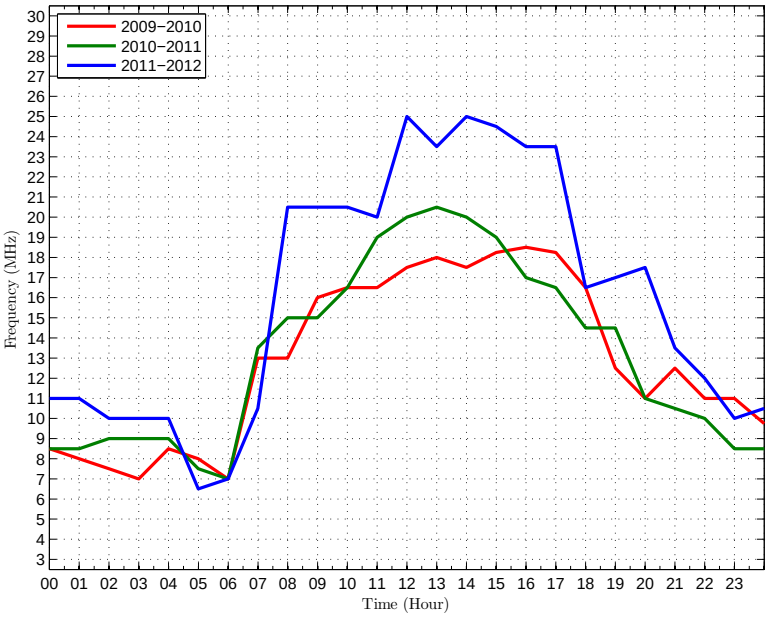

FIGURE 5.9: The FLA inter-day variation during the 2009/2010, 2010/2011, and 2011/2012 surveys.

to the 2010/2011 surveys. However, during the 2011/2012 survey, the average FLA values were 20% higher. Specifically, the inter-day variation of the FLA increased throughout the daytime period with around 23% and 15% over the nighttime period.

The average FLA reached a maximum value of 18.5 MHz at 16:00 UTC during the 2009/2010 survey, 20.5 MHz at 13:00 UTC throughout the 2010/2011 survey, and 25 MHz at the midday interval over the 2011/2012 survey. During the afternoon period, the average FLA began to decrease significantly due to the large drop in the electron density through the ionosphere. Important observation we came up with from Figure 5.9, is that the increment of the SSN during the three surveys (11.6, 21, and 65.3) and the Solar Flux numbers over the same period (79, 86, and 134) are strongly affecting the availability of the ionospheric SAS-OE link. Hence, the increment in the inter-day variation of FLA is proportionally relative to solar activity over the three surveys.

5.6 Vertical incidence sounding, data, and results

A relationship between the channel availability from OIS system and VIS parameters, such as TEC, foF2 and MUF(3000) can be found; so that, through this section, we will analyze the recorded inter-day variation of the TEC, along with the inter-day and day-to-day variations of foF2 and MUF(3000) parameters.

5.6.1 Day-to-day variation

This section presents the day-to-day variations of the most important parameters that can be measured by VIS system, foF2 and MUF(3000), during a time period of around two consecutive weeks. Firstly, there will a description of the day-to-day variation of the foF2 measurements over the time period that goes from 13^{th} to 26^{th} of January of each survey; then, the description of the MUF(3000) day-to-day variation during the same period.

Figures 5.10, 5.11, and 5.12 depict the day-to-day variations of the foF2 measurements that have been recorded at the four VIS stations (OE, El Arenosillo, Ascension, and Port Stanley) over the 2009/2010, 2010/2011, and 2011/2012 surveys, respectively. In addition, the day-to-days variation of the MUF(3000) are illustrated in Figures 5.17, 5.18, and 5.19 during 2009/2010, 2010/2011, and 2011/2012 surveys, respectively. These day-to-day variations can be considered as an indicator for the characterizations of the ionosphere during the whole period of the survey, which is usually longer than two weeks.

As a notation, the amount of ionospheric data recorded from the VIS system located in SAS was not significant to rely on during the three surveys in account on several technical issues. Therefore, depending on the results that explained in [134], the measurements from Port Stanley station would be very similar to the SAS station due to its nearby location.

5.6.1.1 foF2 day-to-day results

Among the parameters that we are able to measure from the VIS systems, the foF2 is one of the most critical parameters that shows up the behavior of the ionosphere at a

certain location. The inter-day and monthly median foF2 values are increasing with the solar activity in a complicated way as explained in [144].

As illustrated in Figures 5.10, 5.11, and 5.12, the day-to-day variations of the foF2 that have been recorded at the Ascension, El Arenosillo, and OE stations were characterized by clear diurnal harmonic over the three surveys. However, the foF2 day-to-day variation of the Port Stanley has semi-diurnal harmonic according to its high-latitude location. From one survey to the next, as shown in Figures 5.10, 5.11, and 5.12, the maximum foF2 value that was measured at each station is increased annually.

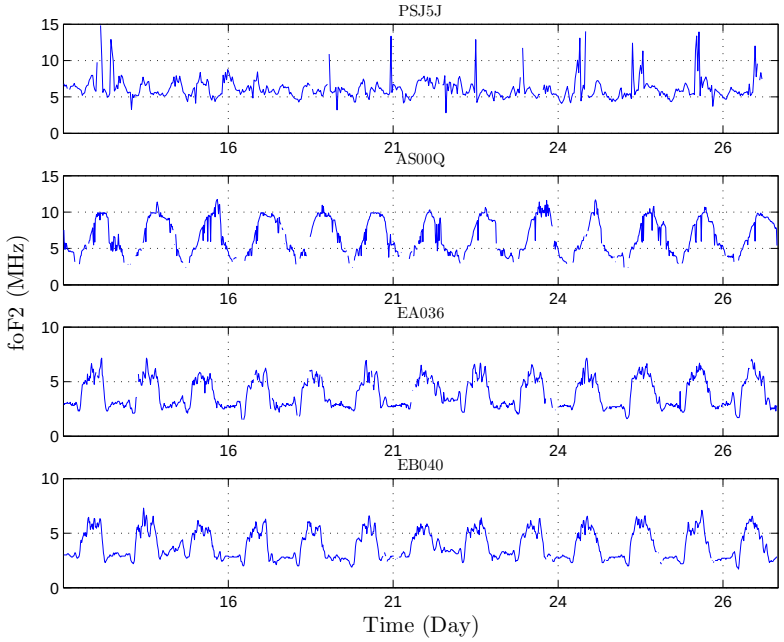

FIGURE 5.10: The day-to-day variation of the foF2 during two weeks of January 2010 (2009/2010 survey) at the four VIS stations (PSJ5J, AS00Q, EA036, and EB040).

The evolution of the foF2 measurements that have been obtained at each VIS station throughout the three surveys will be explained, and then there is a discussion of the solar activity effects on the foF2 values. Figures 5.10, 5.11, and 5.12 illustrate the foF2 values that were obtained throughout the 2009/2010, 2010/2011, and 2011,2012 surveys, respectively.

The Port Stanley station (51.6 S, 57.9 W) has a maximum foF2 value of around 15 MHz during the three surveys as depicted in Figures 5.10, 5.11, and 5.12.

A maximum foF2 value of 10 MHz has been measured during the 2009/2010 survey at the Ascension station (7.95 S, 14.4 W) as shown in Figure 5.10. Consequently,

throughout the 2010/2011 survey, the maximum foF2 increased from 10 MHz to around 12.75 MHz with 20% of increment as illustrated in Figure 5.11. Thereafter, over the 2011/2012 survey, the maximum foF2 has raised to 14.8 MHz (14% more than the 2010/2011 survey) as depicted in Figure 5.12.

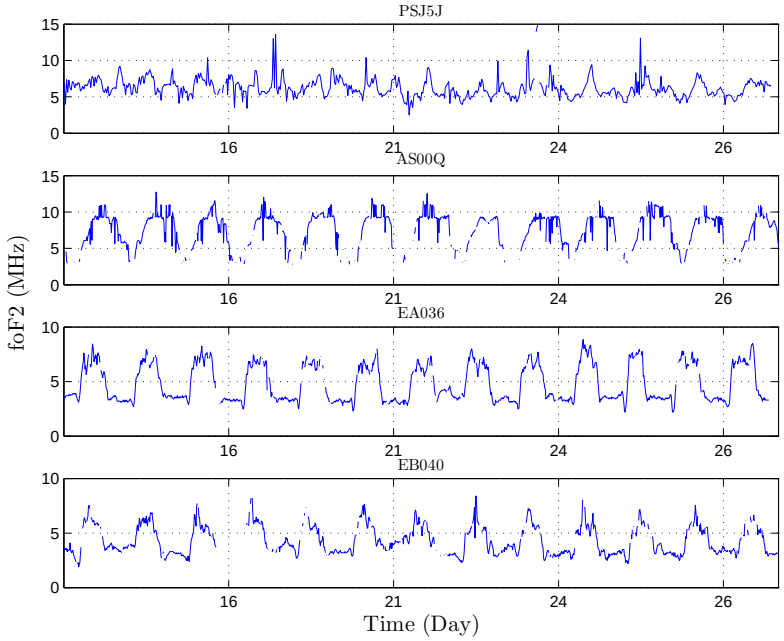

FIGURE 5.11: The day-to-day variation of foF2 throughout two weeks of January 2011 (2010/2011 survey) at the four VIS stations (PSJ5J, AS00Q, EA036, and EB040).

With respect to El Arenosillo station (37.1 N, 6.7 W), during the 2009/2010 survey, Figure 5.10 illustrates a maximum foF2 value of 7.3 MHz. That is consequently increased by around 17.5% to 8.85 MHz throughout the 2010/2011 survey as illustrated in Figure 5.11. As shown in Figure 5.12, over the 2011/2012 survey, the foF2 reached its maximum value of 11.9 MHz with approximately 25.5% increment compared to the 2010/2011 survey.

A maximum foF2 value of 7 MHz has been obtained during 2009/2010 at the OE station (40.8 N, 0.5 E) as shown in Figure 5.10. Over the 2010/2011 survey, Figure 5.11 showed a maximum foF2 value of 8.5 MHz with around 15% increment compared to the 2009/2010 survey. Then, an increment of approximately 21.7% from 8.5 MHz to 10.75 MHz is observed during the 2011/2012 survey as depicted in Figure 5.12. The maximum foF2 that was obtained at the OE station increased with around 35% over the three surveys.

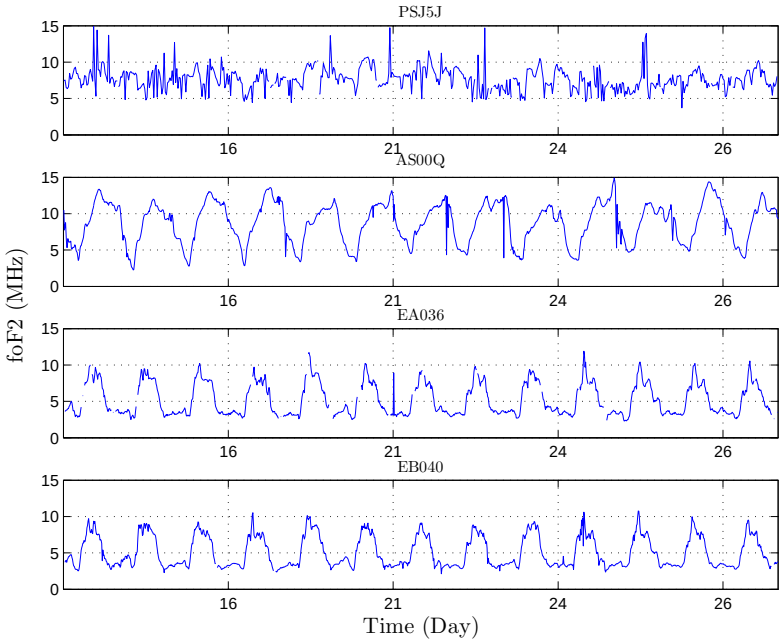

FIGURE 5.12: The day-to-day variation of foF2 during two weeks of January 2012 (2011/2012 survey) at the four VIS stations (PSJ5J, AS00Q, EA036, and EB040).

The evolution of the foF2 day-to-day variation regarding each VIS station (Port Stanley, Ascension, El Arenosillo, and OE) are illustrated in Figures 5.13, 5.14, 5.15, and 5.16.

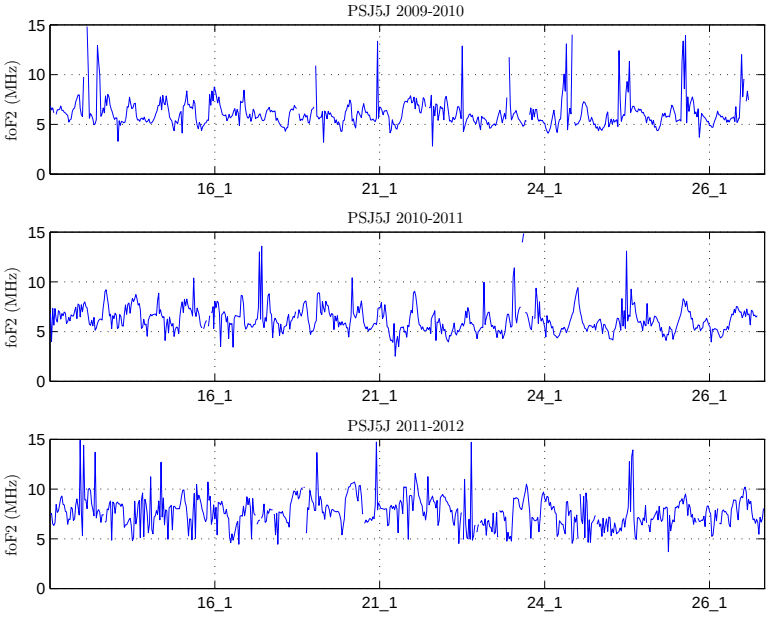

FIGURE 5.13: The day-to-day variation of foF2 during three surveys at Port Stanley station.

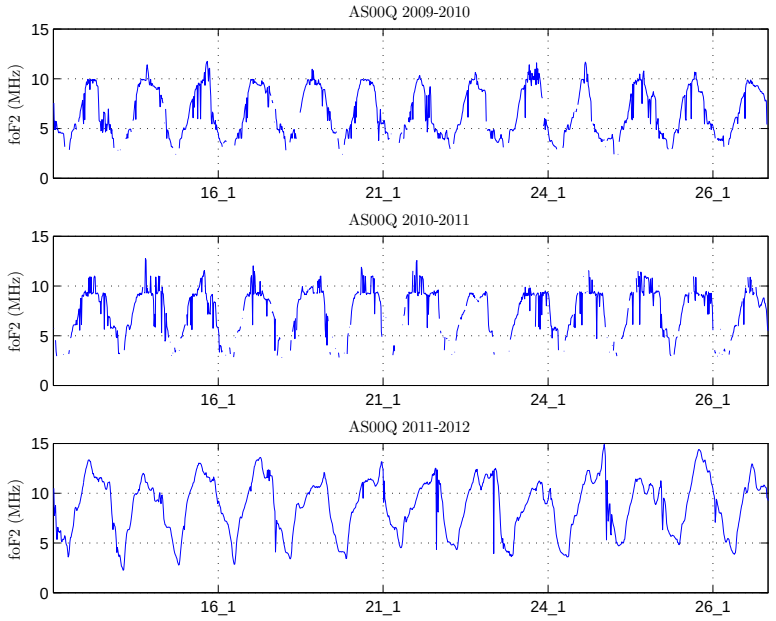

FIGURE 5.14: The day-to-day variation of foF2 over three surveys at Ascension station.

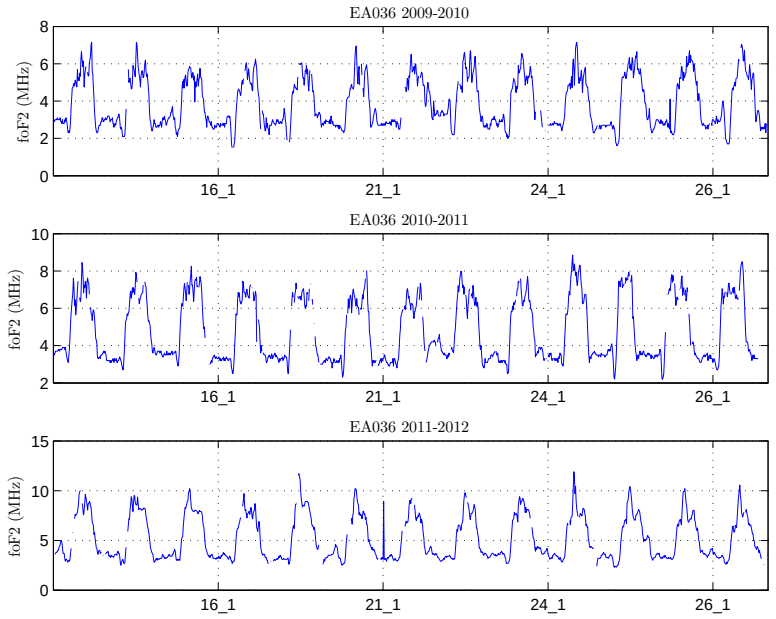

FIGURE 5.15: The day-to-day variation of foF2 throughout three surveys at El Arenosillo station.

The minimum foF2 values that have been observed at Port Stanley, Ascension, El Arenosillo, and OE are around 5 MHz, 4 MHz, 3 MHz, and 3 MHz, respectively. Throughout the three surveys, the minimum foF2 value, which is usually occurred during the night has not been changed at the four VIS station. The maximum foF2

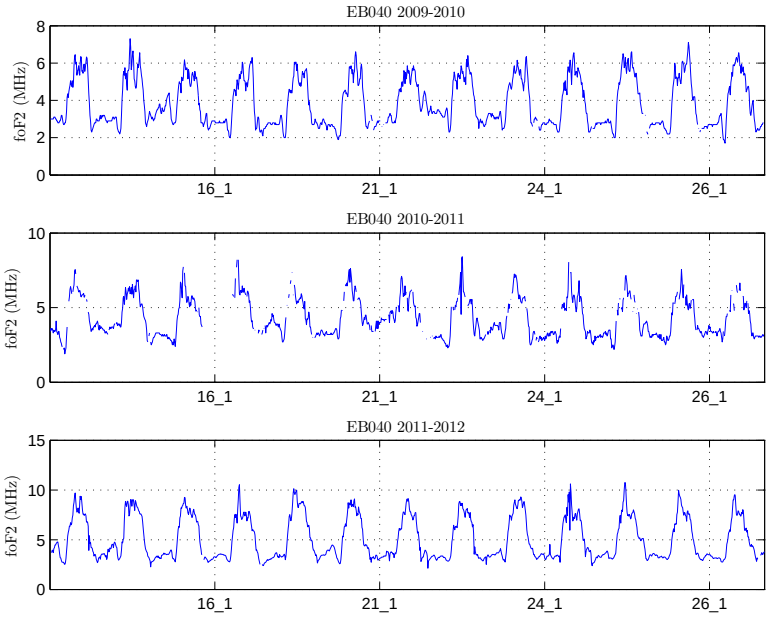

FIGURE 5.16: The day-to-day variation of foF2 during three surveys at OE station.

values, which have been recorded during the three surveys are summarized in Table 5.4.

Station	foF2 (MHz)		
	2009/2010	2010/2011	2011/2012
PSJ5J	15	15	15
AS00Q	10	12.75	14.8
EA036	7.3	8.85	11.9
EB040	7	8.5	10.75

TABLE 5.4: Maximum foF2 values measured at the four VIS stations during three surveys.

As mentioned previously, the average SSN values that have been recorded over the three surveys were 11.6, 21, and 76 for the 2009/2010, 2010/2011, and 2011/2012 survey, respectively. The increment of the SSN values were affecting significantly the maximum foF2 values with around 35% of increment at the Ascension, El Arenosillo, and OE. However, no change has been noticed in the minimum foF2 day-to-day values during the three surveys at the four VIS stations.

5.6.1.2 MUF(3000) day-to-day results

As observed in the day-to-day variation of foF2, the MUF(3000) day-to-day variations that have been recorded at the Ascension, El Arenosillo, and OE stations throughout the three surveys were characterized by clear diurnal harmonic, e.g., Figures 5.21, 5.22, and 5.23. On the other hand, the measurements at the Port Stanley station have semi-diurnal harmonic characterizations as shown in Figure 5.20. This section is organized as following, first, there will be an explanation of MUF(3000) day-to-day variations over the three surveys (Figures 5.17, 5.18, and 5.19), and then discussing the influence of solar activity upon the MUF(3000) measurements.

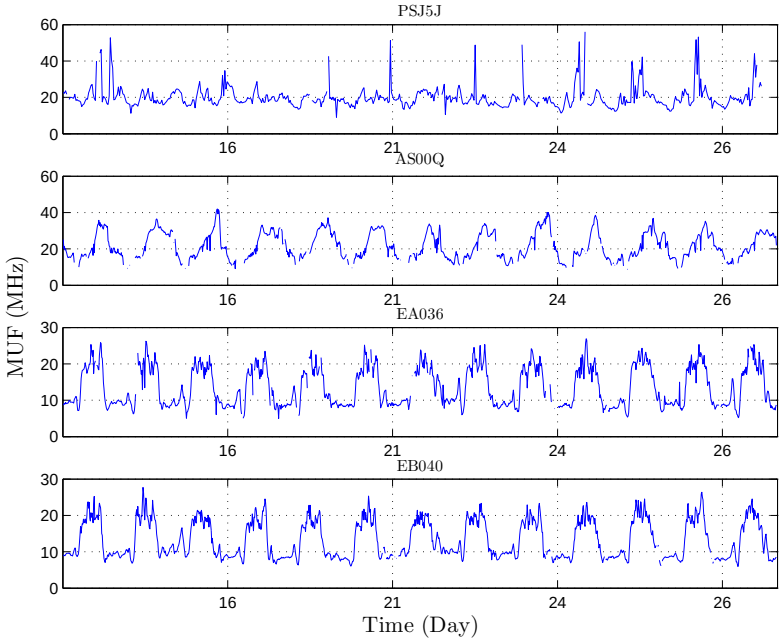

FIGURE 5.17: The day-to-day variation of MUF(3000) during two weeks of January 2010 (2009/2010 survey) at the four VIS stations (PSJ5J, AS00Q, EA036, and EB040).

A maximum MUF(3000) value of around 56 MHz has been measured during the 2009/2010 survey at the Port Stanley station (51.6 S, 57.9 W) as shown in Figure 5.17. During 2010/2011, the maximum value has reached 62.8 MHz with an increment of around 11% as illustrated in Figure 5.18. Consequently, the maximum MUF(3000) has raised with 2% from 62.8 MHz to 64 MHz during the 2011/2012 survey compared to the 2010/2011 survey as depicted in Figure 5.19.

Regarding the MUF(3000) recordings that have been measured at the Ascension station (7.95 S, 14.4 W), Figure 5.17 shows the day-to-day variation of MUF(3000)

with a maximum value of around 42 MHz during the 2009/2010 survey. Then, it has raised with around 5.5% from 42 MHz to 44.5 MHz throughout the 2010/2011 survey as depicted in Figure 5.18. Finally, over the survey of 2011/2012, an increment of 4% has been observed from 44.5 MHz to 46.5 MHz as illustrated in Figure 5.19.

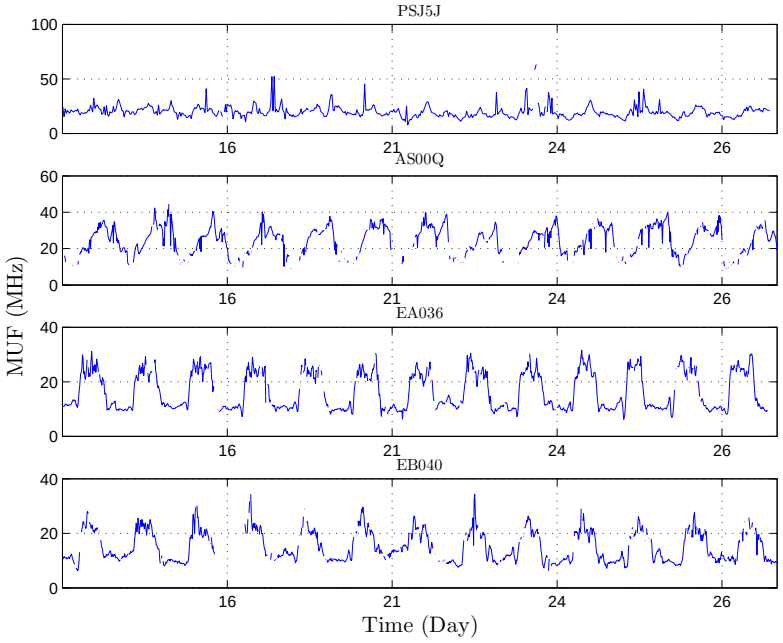

FIGURE 5.18: The day-to-day variation of MUF(3000) throughout two weeks of January 2011 (2010/2011 survey) at the four VIS stations (PSJ5J, AS00Q, EA036, and EB040).

During the 2009/2010 survey, a maximum MUF(3000) value of 27 MHz has been recorded at El Arenosillo station (37.1 N, 6.7 W) as shown in Figure 5.17, and then it increased to almost 31.5 MHz with 14.7% throughout the 2010/2011 survey as depicted Figure 5.18. Finally, the maximum MUF(3000) that has been measured is raised with around 29.5% from 31.5 MHz to 44.7 MHz during the 2011/2012 survey compared to the 2010/2011 survey as illustrated in Figure 5.19.

At the OE station (40.8 N, 0.5 E), Figure 5.17 shows that the maximum MUF(3000) value reached over 27.6 MHz over the 2009/2010 survey. Consequently, during the 2010/2011 survey, the maximum MUF(3000) raised with 19.3% from 27.6 MHz to 34.3 MHz as shown in Figure 5.18. Figure 5.19 illustrates the day-to-day variation during 2011/2012 survey with a maximum value of 41.5 MHz with 16.8% increment more than the 2010/2011 survey.

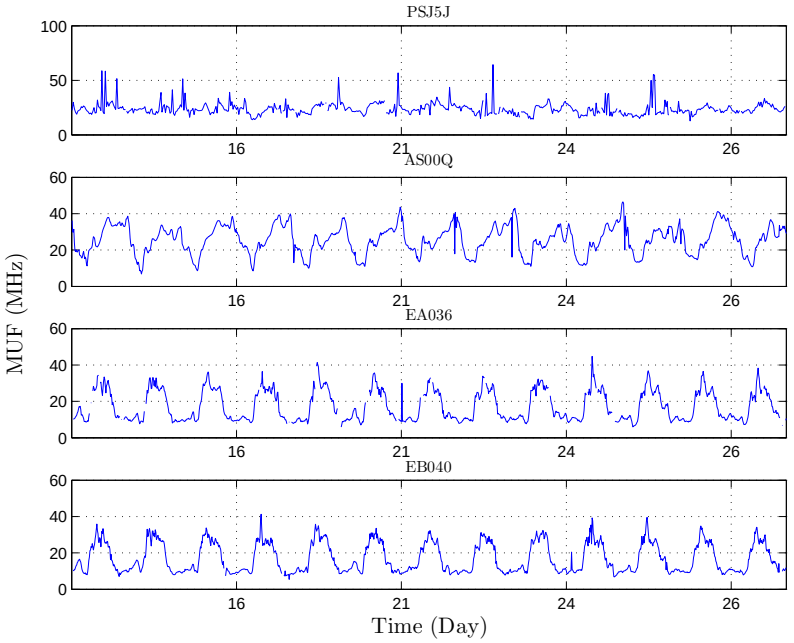

FIGURE 5.19: The day-to-day variation of MUF(3000) during two weeks of January 2012 (2011/2012 survey) at the four VIS stations (PSJ5J, AS00Q, EA036, and EB040).

Two consecutive weeks of MUF(3000) measurements have been recorded at Port Stanley, Ascension, El Arenosillo, and OE stations are illustrated in Figures 5.20, 5.21, 5.22, and 5.23, respectively.

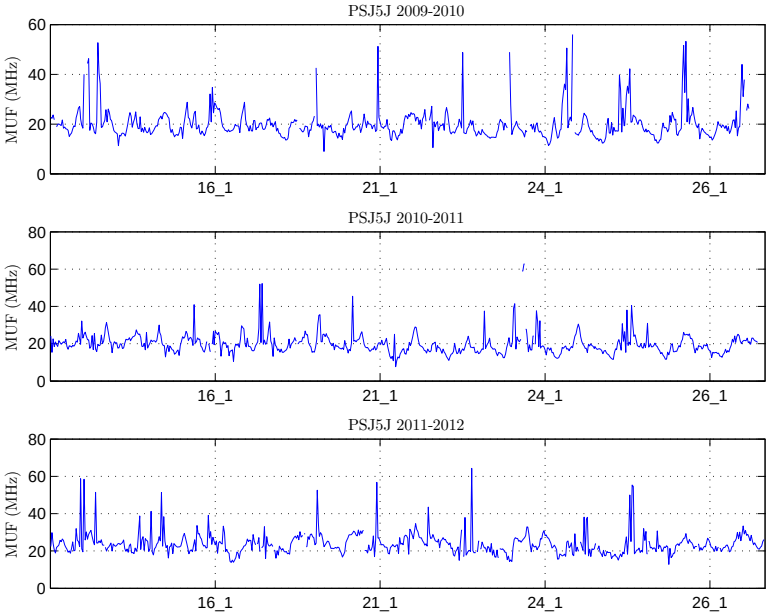

FIGURE 5.20: The day-to-day variation of MUF(3000) throughout three surveys at Port Stanley station.

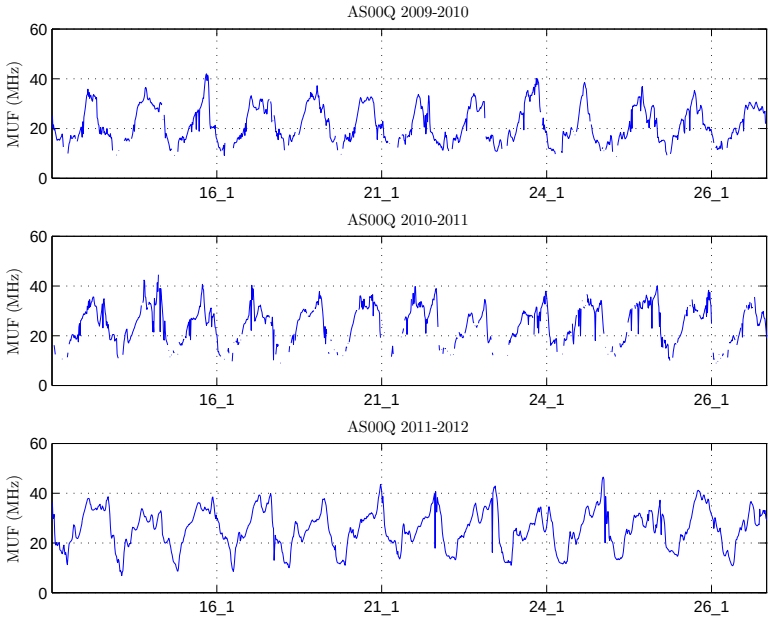

FIGURE 5.21: The day-to-day variation of MUF(3000) over three surveys at Ascension station.

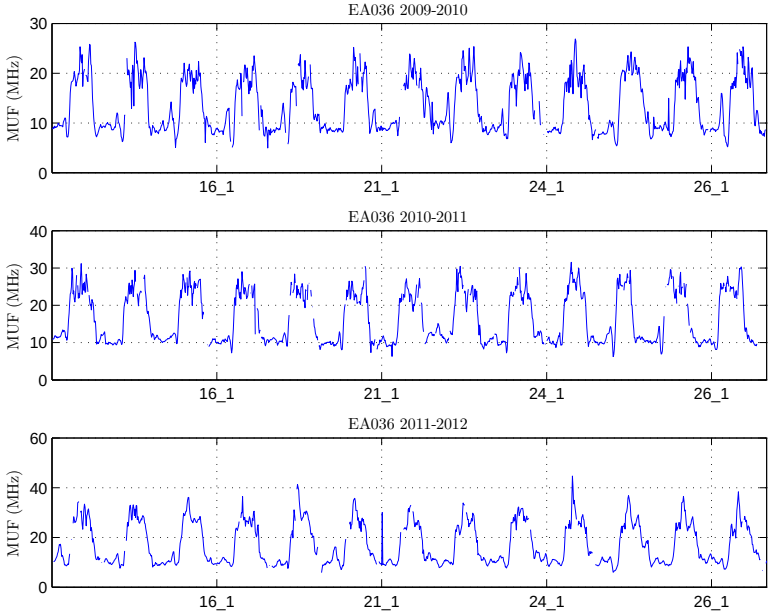

FIGURE 5.22: The day-to-day variation of MUF(3000) during three surveys at El Arenosillo station.

The minimum values of MUF(3000) that have been recorded at the Port Stanley, Ascension, El Arenosillo, and OE VIS station were 20 MHz, 15 MHz, 10 MHz, and 10 MHz, respectively. A clear observation is that the minimum MUF(3000) values measured at each VIS station have not raised over the three surveys. Such observation is consistent with the persistence of the minimum foF2 values throughout the three

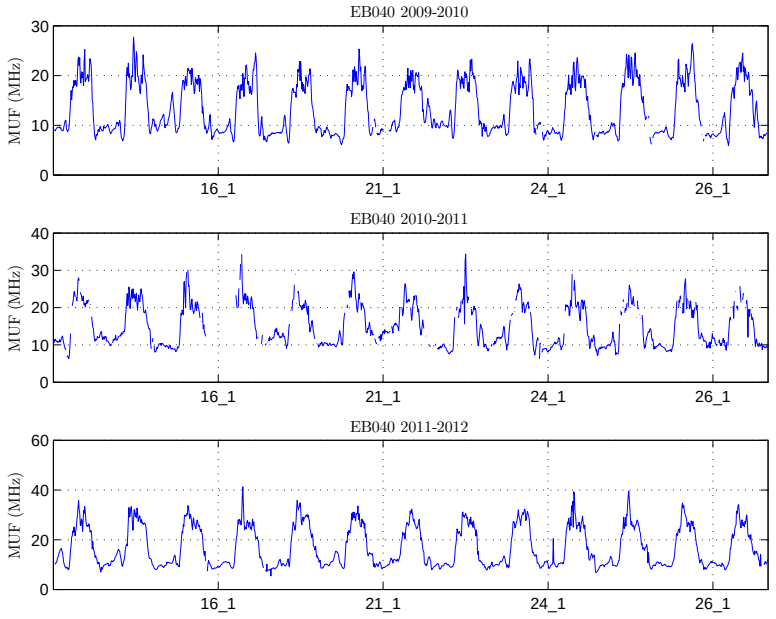

FIGURE 5.23: The day-to-day variation of MUF(3000) during three surveys at OE station.

surveys as mentioned previously. The raise of the SSN from 11.6 to 21.1 and then 65.3, was largely affecting the maximum MUF(3000) values with an average increment of 23.5%.

The maximum foF2 values, which have been measured during the three surveys are summarized in Table 5.5. By looking to Table 5.5, we have noted that the maximum MUF(3000) values are increased from a survey to the next, and move towards the high-latitude areas of the Earth as well.

Station	MUF(3000) (MHz)		
	2009/2010	2010/2011	2011/2012
PSJ5J	56	62.8	64
AS00Q	42	44.5	46.5
EA036	27	34.3	44.7
EB040	27	31.5	41.5

TABLE 5.5: Maximum MUF(3000) values recorded at the four VIS stations during three consecutive surveys.

5.6.2 Inter-day variation

Within this section, we will discuss the inter-day measurements of the TEC that were forming the ionospheric propagation throughout three surveys from 2009 to 2012, along with investigate the effects of different SSN values on the TEC measurements. Besides that, the evolution of foF2 and MUF(3000) inter-day variations, which have been recorded at the four VIS stations (Port Stanley, Ascension, El Arenosillo, and OE) throughout three surveys, will be presented later on. Finally, there will be an explanation of the solar activity effects on the foF2 and MUF(3000) data over the three surveys.

5.6.2.1 TEC inter-day variation results

The balance of the plasma production, loss, and transport is affecting the behavior of the electron density of the ionospheric layers. So that, the ionospheric plasma redistribution process influences significantly the electron density profile through the ionosphere. Both monthly and inter-day patterns of the solar activity are significantly affecting the ionospheric variability definition as explained in [145]. Previous studies have showed that electron density is increased along with the solar activity in complicated ways [146, 147]. The electron density profile of the F1 and F2 layers in the ionosphere tends to increase along with the annual increment of the solar activity that is due to the enhanced photo-ionization as explained in [146, 148].

The TEC measurements represent the total number of electrons per square meter through the path between the transmitter and the receiver. There are several methods to measure the TEC values through the ionosphere, such as the dual frequency GPS, the ionospheric models that is based on ionosonde data, the incoherent scatter radar, the Faraday rotation of geostationary satellite signals [149], etc. Herein, we are introducing the TEC values, which have been recorded from the ionosondes located at four VIS stations over the SAS-OE link path.

In [150, 151], there are comparisons between TEC data obtained from the GPS measurements and from the VIS ionosonde stations. Usually, the TEC measurements, which are being obtained from the VIS ionosonde stations have high vertical resolution. However, the high number of GPS stations, which are located around the Earth can present TEC measurements with high spatial resolution.

The TEC values can be calculated through the electron density $N(h)$ measurements or the foF2 measurements. First, calculate the TEC values from the electron density distribution $N(h)$:

$$\text{TEC} = \int_0^h N(h)\, dh \tag{5.1}$$

where h denotes the height and $N(h)$ is the ionospheric electron density distribution. On the other hand, it can be obtained with respect to the foF2 measurements as:

$$\text{TEC} = 1.2410^{-6}\tau(foF2)^2 \tag{5.2}$$

where τ determines the slab thickness, which defines the relation between the TEC and the maximum electron density N_{max}, and is defined as:

$$\tau = \frac{\text{TEC}}{N_{\max}} \tag{5.3}$$

where TEC is measured in TEC unit (TECU) (1 TECU = 10^{16} $electrons/m^2$), foF2 in MHz, and τ in meters [114].

Figures 5.24, 5.25, 5.26, and 5.27 show the inter-day variations of the TEC that have been measured at the four VIS stations located along the SAS-OE link path over the three surveys. Thereafter, we conclude how the TEC measurements are changing along the SAS-OE link path (12700 km long).

The TEC inter-day variation that has been recorded at Port Stanley station (51.6 S, 57.9 W) is illustrated in Figure 5.24 with an average of 7 TECU over the first interval of the nighttime period that goes from 00:00 UTC to 08:00 UTC at the 2009/2010 survey. That has increased to around 9 TECU over the 2010/2011 survey and 10 TECU during the 2011/2012 survey.

At 07:00 UTC, the sunrise starts and the ionization levels through the ionosphere become very high; therefore, the TEC values have reached almost 10 TECU from 08:00 UTC to 18:00 UTC at the 2009/2010 survey, and then increased to 12 TECU and 17 TECU throughout the 2010/2011 survey and 2011/2012 survey, respectively.

Finally, during the second interval of the nighttime period from 19:00 UTC to 23:00 UTC, an average of 9 TECU has been recorded during the 2009/2010 survey, that has changed to 10 TECU over the 2010/2011 survey, and then raised to approximately 13 TECU over the 2011/2012 survey.

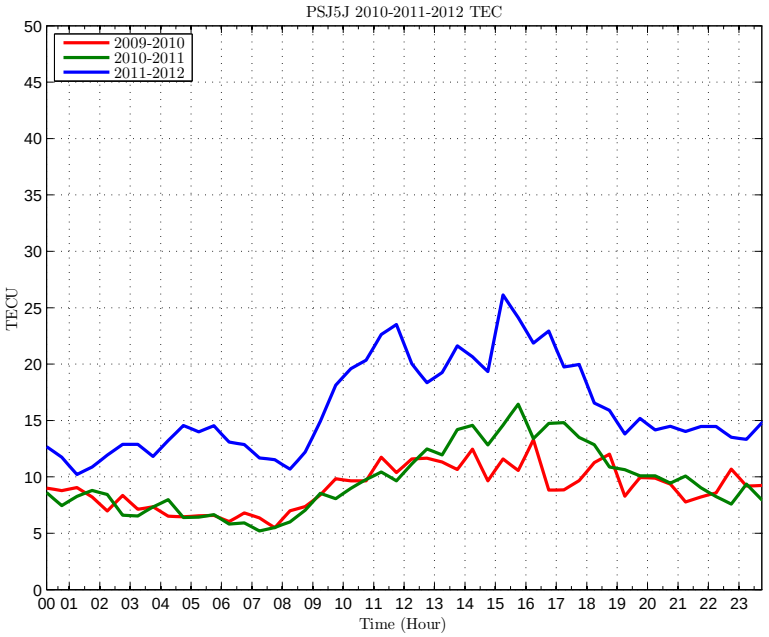

FIGURE 5.24: Inter-day variation of the TEC at Port Stanley station during 2009/2010, 2010/2011, and 2011/2012.

As a final observation form Figure 5.24, throughout the nighttime period, the average TEC that has been recorded over 2010/2011 survey was around 16% higher than 2009/2010. Also, over the 2011/2012 survey, the measurements were 16% larger than 2010/2011. Meanwhile, during the daytime period, from 2009/2010 to 2010/2011, the average TEC values were increased with around 16%, and with 30% from 2010/2011 to 2011/2012. That all can be related to the strong increment of the solar activity throughout the three surveys.

The inter-day variation of the TEC that has been recorded at the Ascension station (7.95 S, 14.4 W) during the three survey is shown in Figure 5.25. Firstly from midnight (00:00 UTC) to around sunrise (07:00 UTC), an average of 2 TECU has been calculated throughout the 2009/2010 survey, and then it has increased to around 3 TECU during the 2010/2011 survey and 8 TECU over the 2011/2012 survey.

Then, the daytime region starts; so that, from sunrise to around 18:00 UTC at the 2009/2010 survey, high average TEC of 13.5 TECU has been recorded due to the enhanced ionization levels; consequently, it has raised to around 16.8 during 2010/2011 and 36.8 TECU at the 2011/2012 survey. As shown in Figure 5.25, an increment of around 20% is observed in the average TEC values from 2009/2010 to 2010/2011, and 54% from 2010/2011 to 2011/2012.

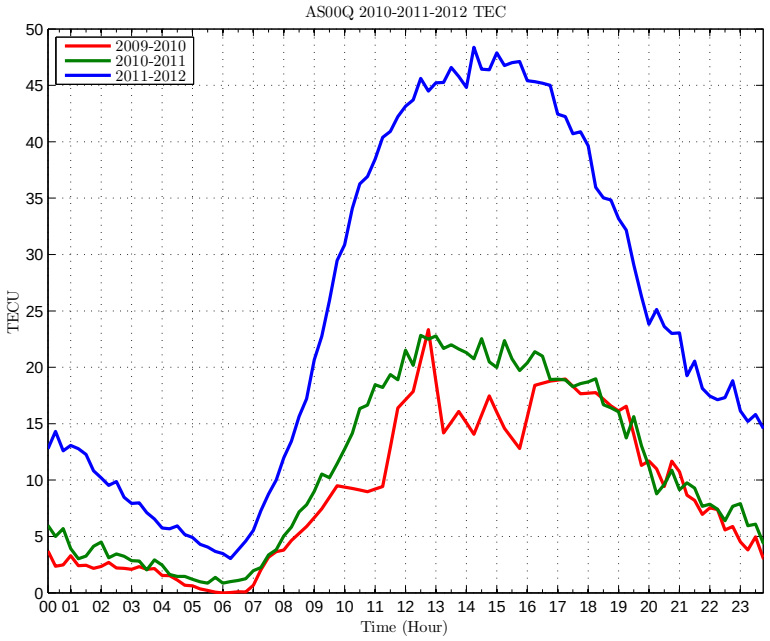

FIGURE 5.25: Inter-day variation of the TEC at Ascension station throughout 2009/2010, 2010/2011, and 2011/2012.

The sunset is completed at around 19:00 UTC; thereafter, the average TEC has reached 8 TECU at the period that goes from 19:00 UTC to around midnight during the 2009/2010 survey; then, it has increased to 9 TECU and 20 TECU throughout the 2010/2011 and 2011/2012 survey, respectively. Over the nighttime period, the TEC measurements were increased with around 22% and 59% from 2009/2010 to 2010/2011 and from 2010/2011 to 2011/2012, respectively.

The maximum inter-day value of TEC reached almost 22.5 TECU over both the 2009/2010 and the 2010/2011 survey. During the 2011/2012 survey, the maximum value has increased significantly to around the double (50 TECU), which was not consistent with the increment observed previously or even at other stations. Finally, as depicted in Figure 5.25, the average TEC incremented with 27% from the 2009/2010 survey to the 2010/2011, which even has raised substantially with around 53% from the 2010/2011 survey to the 2011/2012.

Figure 5.26 illustrates the TEC inter-day variation that has been recorded at El Arenosillo station (37.1 N, 6.7 W) during the three surveys. An average of the TEC measurements equal to 2 TECU has been calculated from 00:00 UTC to around sunrise at 07:00 UTC throughout the 2009/2010 survey, and then it changed to around 2.5 TECU during the 2010/2011 survey and 3.2 TECU over the 2011/2012 survey.

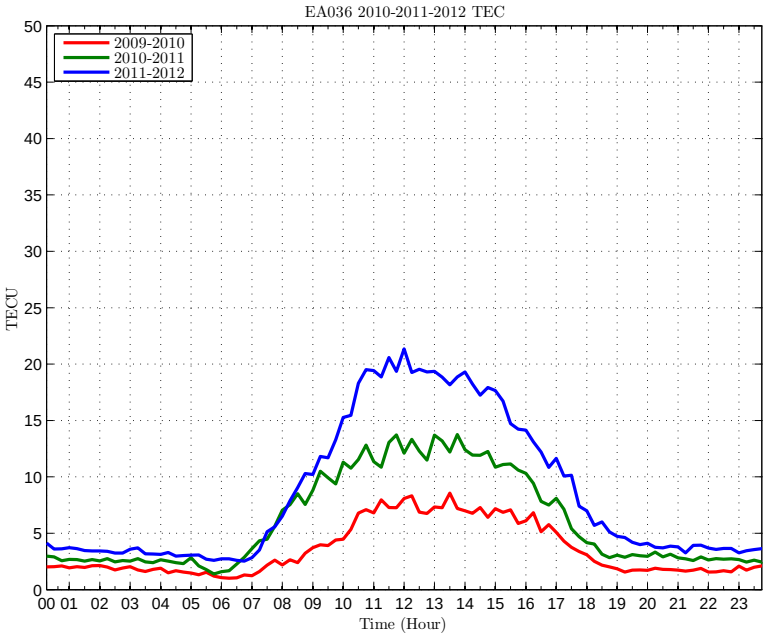

FIGURE 5.26: Inter-day variation of the TEC at El Arenosillo station during 2009/2010, 2010/2011, and 2011/2012.

During 2009/2010, 6 TECU was the average value, which has been computed throughout the time period that goes form around sunrise to sunset, and consequently, it increased to 10 TECU and 14.5 TECU over 2010/2011 survey and 2011/2012 survey, respectively. Along with high levels of ionization during daytime period, the average TEC has raised with 40% from 2009/2010 to 2010/2011, which then decreased slightly to 33% from 2010/2011 to 2011/2012.

From 17:30 UTC to almost midnight, an average TEC of around 2 TECU was measured during the 2009/2010 survey, and then it raised to 2.8 during the 2010/2011 survey, and 4 TECU throughout the 2011/2012 survey. Over the nighttime period, as appeared in Figure 5.26, the TEC measurements have increased with about 25% from 2009/2010 to 2010/2011 and similarly from 2010/2011 to 2011/2012.

Figure 5.27 depicts the TEC inter-day measurements from the OE station (40.8 N, 0.5 E) where an average of 1.5 TECU was recorded from 00:00 UTC to around sunrise during the 2009/2010 survey; consequently, it increased to around 2.5 TECU throughout 2010/2011 and 2011/2012 surveys.

The sunrise starts at 07:00 UTC along with increasing the electron density through the ionosphere, that lead to an average TEC of 5 TECU during the 2009/2010 survey. The SSN values increased; therefore, the average value of the TEC was raised from

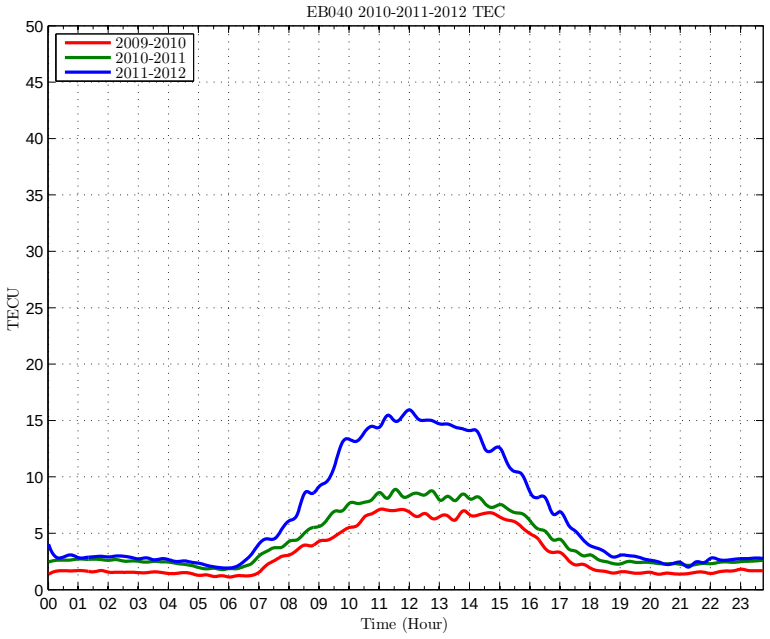

FIGURE 5.27: Inter-day variation of the TEC at the OE station throughout 2009/2010, 2010/2011, and 2011/2012.

5 TECU to around 7 TECU and 11 TECU during 2010/2011 and 2011/2012 survey, respectively. So that, the average TEC has increased with approximately 28% from 2009/2010 to 2010/2011 at the daytime period, which then raised with 36% during 2011/2012 over 2010/2011.

Finally, 1.5 TECU was the average of TEC measurements, which have recorded from 18:00 UTC to around midnight throughout the 2009/2010 survey. Thereafter, it changed to almost 2.5 TECU over both the 2010/2011 and the 2011/2012 surveys. As illustrated in Figure 5.27, over the nighttime period, the average TEC values have increased with 40% from 2009/2010 to 2010/2011 and 2011/2012.

The rising of the solar activity, which it can be measured by SSN and Solar Flux, will affect the electron density distribution through the ionosphere. A slightly increment in TEC inter-day average measurements, such as what has been observed during 2009/2010 and 2010/2011, could be related to low increment of SSN values (11.6 to 21.1) and Solar Flux (79 to 86 SFU).

Additionally, large increment from 21.1 to 65.3 of SSN and Solar Flux from 86 to 134 SFU during the 2010/2011 and 2011/2012 surveys, has resulted in large uplift of the average TEC measurements. With those observations in mind, we conclude that the solar activity is proportionally relative to the measurements of the TEC.

Also, at mid-latitude stations (e.g., El Arenosillo and OE) the ionization levels increment affects the measurements of the TEC throughout the daytime period. Otherwise, during the nighttime period, there are no major changes in the average TEC values. In high-latitude stations (e.g., Port Stanley and Ascension), the solar activity resulted in large TEC increment over the whole day (daytime and nighttime intervals).

5.6.2.2 foF2 inter-day variation results

The solar activity influence on the foF2 is varying depend on the location of the observation (high-latitude, mid-latitude, and low-latitude) as mentioned by [146] and the history of the solar activity as explained in [152]. Essentially, the foF2 inter-day variation differs significantly from the years of the minimum and maximum solar activity. Herein, there will be an investigation of the effect of the solar activity on the foF2 inter-day variation, which has been recorded at mid- and high-latitude VIS stations (Port Staley, Ascension, El Arenosillo, and OE) during three consecutive surveys from 2009 to 2012.

The inter-day variations of the foF2 during the 2009/2010, 2010/2011, and 2011/2012 surveys are illustrated in Figures 5.28, 5.29, 5.30, and 5.31, respectively. Each figure represents the average foF2 data that has been measured at different VIS station.

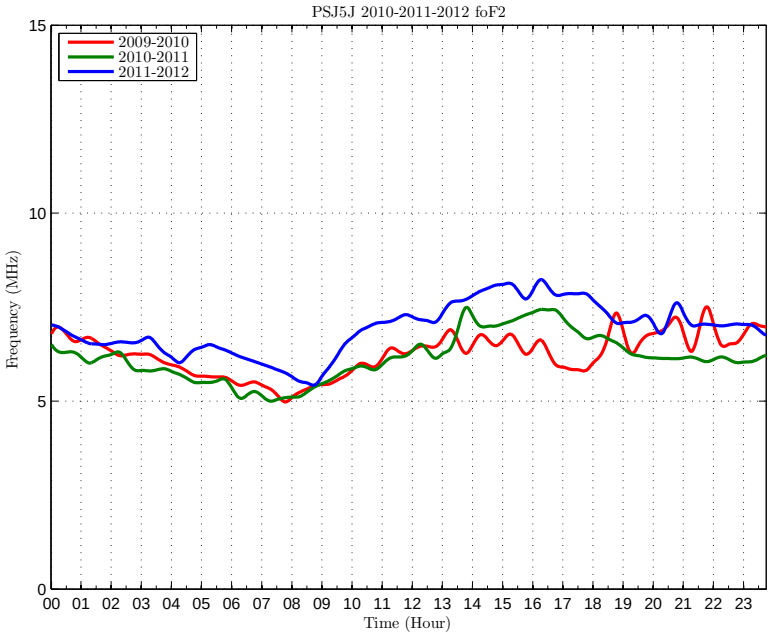

FIGURE 5.28: Inter-day variation of the foF2 at Port Stanley station during 2009/2010, 2010/2011, and 2011/2012.

The foF2 data, which has been recorded at the Port Stanley station (51.6 S, 57.9 W) showed that there was no significant increasing along with the solar activity raising (SSN form 11.6 to 21.1, and then 65.3, Solar Flux from 79 to 86, and then 134) as depicted in Figure 5.28. It has started with around 6 MHz at 00:00 UTC during both 2009/2010 and 2010/2011 surveys, and then decreased to 5 MHz just after sunrise at 08:00 UTC. During the 2011/2012 survey, inter-day variation of the foF2 of 7 MHz has been measured at 00:00 UTC; consequently, it has declined to 5.5 MHz at 09:00 UTC.

Along with the Sun appearance, maximum foF2 value of 7.5 MHz was recorded at 14:00 UTC and 19:00 UTC throughout 2009/2010 and 2010/2011, respectively. The solar activity has raised substantially from 2010/2011 to 2011/2012; thereafter, the maximum foF2 value increased from 7.5 MHz to around 8 MHz at 16:30 UTC.

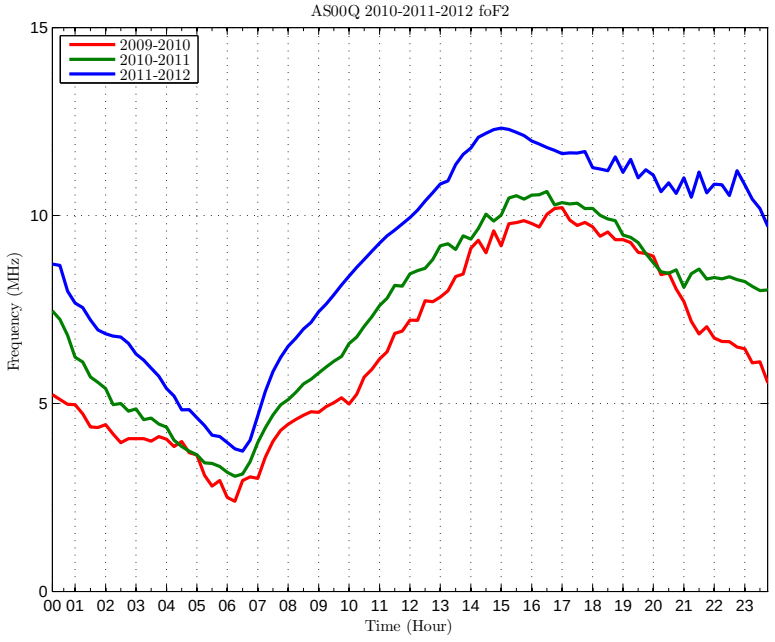

FIGURE 5.29: Inter-day variation of the foF2 at the Ascension station over 2009/2010, 2010/2011, and 2011/2012.

Regarding the Ascension station (7.95 S, 14.4 W), Figure 5.29 illustrates that the foF2 inter-day measurements during the 2009/2010 and 2010/2011 surveys have closer values at the sunrise and sunset intervals. Throughout the 2009/2010 survey, an inter-day variation of 5 MHz has been recorded at 00:00 UTC, and then it decreased to around 2.5 MHz just before starting the sunrise at 06:30 UTC. Along with an average SSN value of 21.1 during the 2010/2011 survey, the inter-day variation has started with 7.5 MHz, and consequently, at 06:30 UTC, the inter-day variation reached 3

MHz. Generally, the foF2 inter-day variation decreased from around 8.5 MHz at 00:00 UTC to 3.5 MHz at 06:30 UTC.

As illustrated in Figure 5.29, the inter-day variation has raised significantly just after the sunrise to the maximum values at 14:30 UTC, 16:00 UTC, and 14:30 UTC throughout the 2009/2010, 2010/2011, and 2011/2012 surveys, respectively. A maximum foF2 value of 10 MHz was recorded at 17:00 UTC over the 2009/2010 survey (SSN of 11.6), then it has raised to 10.7 MHz at 16:00 UTC over the 2010/2011 (SSN of 21.1). Finally, the maximum value became much higher (12.2 MHz) at 14:30 UTC throughout the 2011/2012 survey (SSN of 65.3).

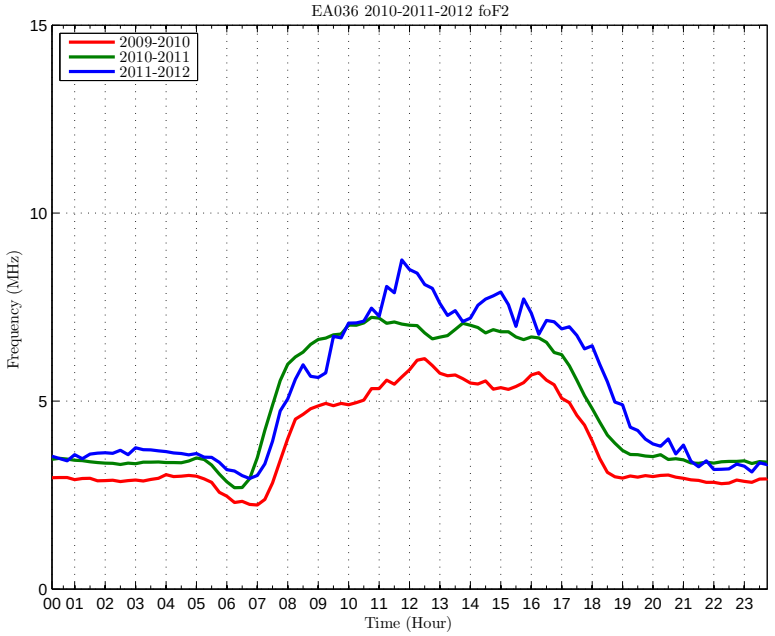

FIGURE 5.30: Inter-day variation of the foF2 at El Arenosillo station throughout 2009/2010, 2010/2011, and 2011/2012.

The inter-day values of the foF2 at both the Port Stanley and Ascension stations have semi-diurnal characteristics as shown in Figures 5.28 and 5.29. However, Figures 5.30 and 5.31 showed that the measurements at El Arenosillo and OE have clear diurnal characteristics, and lastly the inter-day variations over the three surveys are shaped according to the existence and absence of the Sun's radiation.

The foF2 data recorded at El Arenosillo station (37.1 N, 6.7 W) (see, Figure 5.30) has depicted that along with the SSN raising (11.6, 21.1, 65.3), the inter-day variation of the foF2 was increased throughout the three surveys. Starting from 00:00 UTC to 07:00 UTC, the average measurements of the foF2 has increased from around 3 MHz (2009/2010) and 3.5 MHz (2010/2011, 2011/2012) at 00:00 UTC to around 3

MHz, 4 MHz, and 5 MHz during the 2009/2010, 2010/2011, and 2011/2012 surveys, respectively.

During the 2009/2010 survey, the inter-day variation has raised to the maximum value of 6 MHz at 12:30 UTC, with an average of 5 MHz over the daytime period. Consequently, it increased to its maximum value (7 MHz) at 11:00 UTC with an average of 6 MHz throughout the time period that goes from 07:30 UTC to around 18:30 UTC. Throughout the daytime period, the inter-day variation reached the maximum of 8 MHz at 12:00 UTC with an average value of 7 MHz. Figure 5.30 illustrates that the SSN increment append around one hour to the daytime interval from one survey to the next.

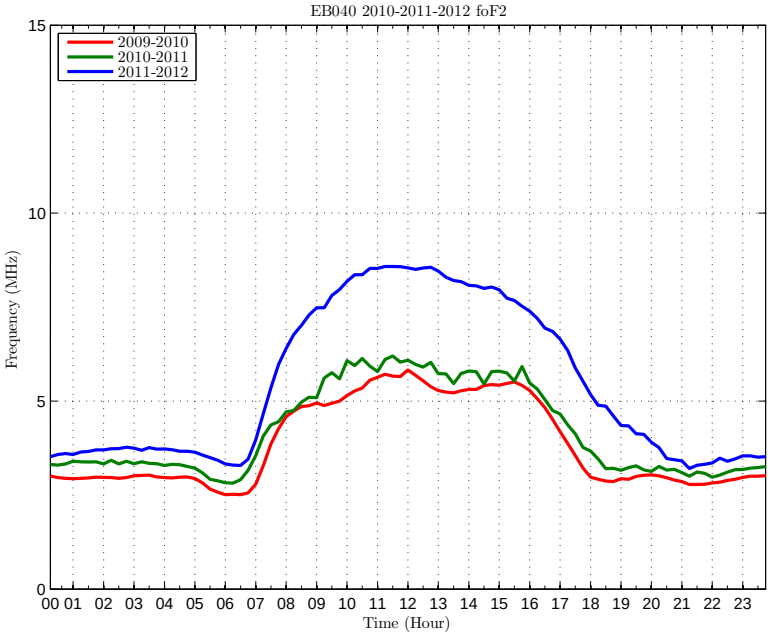

FIGURE 5.31: Inter-day variation of the foF2 at the OE station during 2009/2010, 2010/2011, and 2011/2012.

With respect to the OE station (40.8 N, 0.5 E), Figure 5.31 illustrates that along with the SSN raising, the inter-day variation of the foF2 was increased throughout the three surveys. Start from around 00:00 UTC, the inter-day measurements increased from around 3 MHz, 3.3 MHz, and 3.6 MHz throughout the time period that goes from 00:00 UTC to 07:30 UTC, to about 5 MHz, 5.5 MHz, and 8 MHz during the 2009/2010, 2010/2011, and 2011/2012 surveys, respectively. Throughout the noontime interval, maximum foF2 inter-day value of 5.8 MHz at 12:00 UTC (2009/2010), 6.3 MHz at 11:30 UTC (2010/2011), and 8 MHz at 11:00 UTC (2011/2012).

After sunset, over 2009/2010 and 2010/2011, the foF2 measurements have descended with an average of 5 MHz and 5.5 MHz to 3 MHz and 3.3 MHz within two hours (16:00 UTC to 18:00 UTC). However, during the 2011/2012 survey, the foF2 data has decreased from around 8 MHz to 3.6 MHz throughout three hours. Therefore, high SSN values (65.3) during the 2011/2012 survey resulted in adding one hour and half to the daytime period (i.e., foF2 of 5 MHz is the average critical frequency of the F2 layer over the 2011/2012 survey at 18:00 UTC, while it was at around 16:30 UTC during 2010/2011).

5.6.2.3 MUF(3000) inter-day variation results

The inter-day variations of the MUF(3000), which have been recorded at the four VIS stations are illustrated in Figures 5.32, 5.33, 5.34, and 5.35. Each figure presents three series of results for three consecutive surveys 2009/2010, 2010/2011, and 2011/2012.

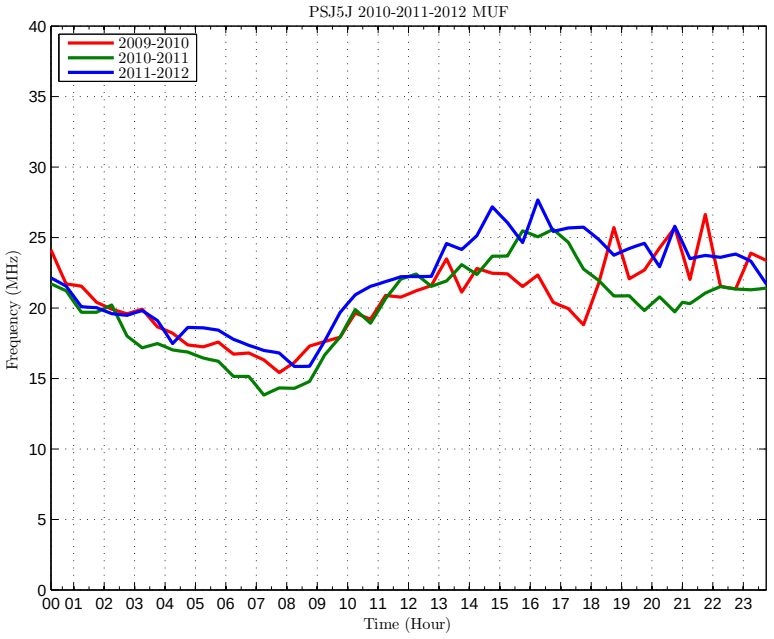

FIGURE 5.32: Inter-day variation of the MUF(3000) at the Port Stanley station during 2009/2010, 2010/2011, and 2011/2012.

Over the three surveys, Figure 5.32 shows that the MUF(3000) inter-day variation that measured at the Port Stanley VIS station (51.6 S, 57.9 W) were decreased from around 23 MHz at midnight to 16 MHz at 07:30 UTC. Meanwhile, the sunrise starts to take place for around half an hour, and consequently it increased to approximately 25 MHz throughout the time interval that goes from 08:00 UTC to 23:00 UTC. Usually,

the measurements regarding to a survey are higher than the measurements of the previous one due to the step up of the solar activity. However, the inter-day variation of the 2009/2010 survey was larger than the 2010/2011 survey throughout the time interval that starts at 18:00 UTC and ends at 23:00 UTC.

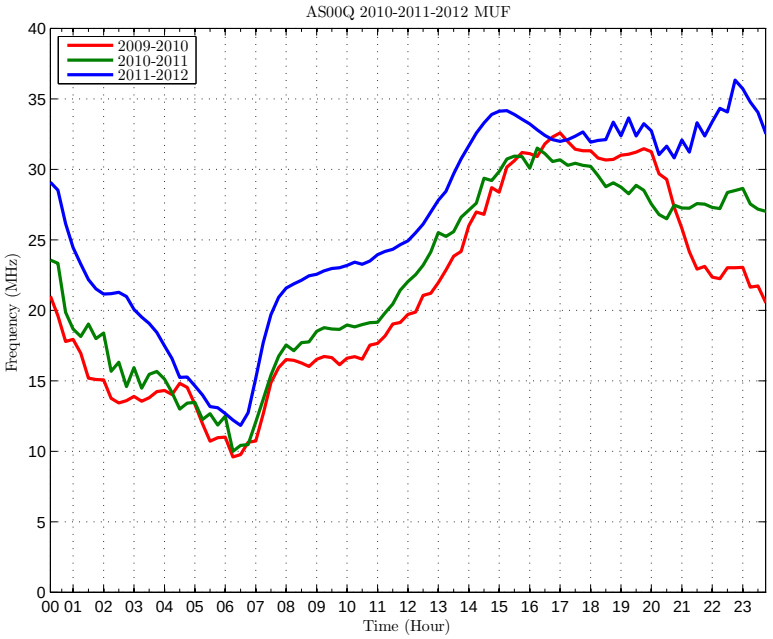

FIGURE 5.33: Inter-day variation of the MUF(3000) for the Ascension over 2009/2010, 2010/2011, and 2011/2012.

With respect to the Ascension station (7.95 S, 14.4 W), the inter-day variations of the MUF(3000) that has been obtained throughout the 2009/2010, 2010/2011, and 2011/2012 are illustrated in Figure 5.33. The results according both the 2009/2010 and 2010/2011 surveys were closer throughout the 24 hour and especially at sunrise and sunset time intervals, expect during the period from 21:00 UTC to 23:00 UTC where the measurements of 2010/2011 were higher than 2009/2010 with around 5 MHz. The result of the 2009/2010 survey exceeded those of 2010/2011 throughout the time interval that starts at 16:00 UTC and ends at 21:00 UTC.

However, the MUF(3000) inter-day measurements during 2011/2012 were slightly higher with an average increment of 5 MHz over the whole day except at sunrise and sunset intervals. The maximum value of the inter-day variation (36 MHz) was measured at the 2011/2012 survey around midnight time, whereas the minimum value of 12.5 MHz was observed around 07:00 UTC.

From 21:00 UTC to 23:00 UTC, the inter-day variations were raised from around 22.5 MHz to 27.5 MHz and 32.5 MHz over the three surveys due to the increasing SSN and Solar Flux values.

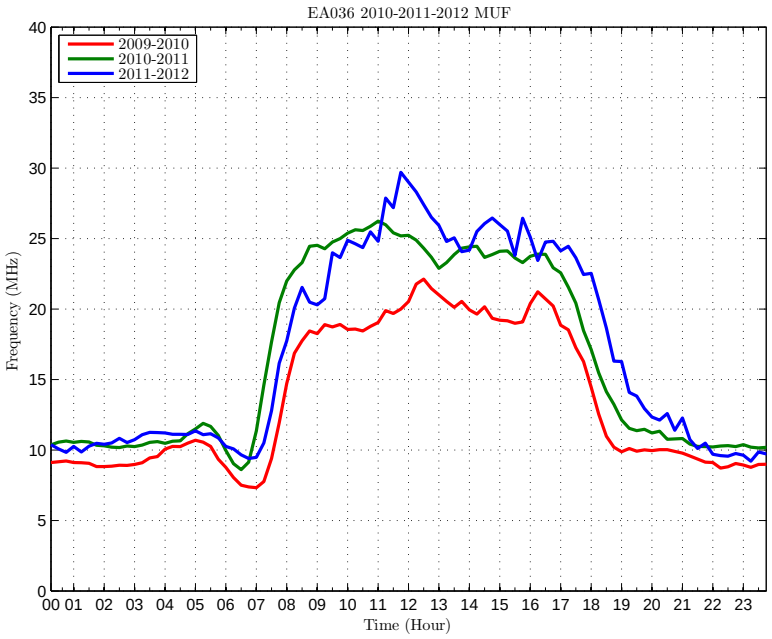

FIGURE 5.34: Inter-day variation of the MUF(3000) at El Arenosillo station throughout 2009/2010, 2010/2011, and 2011/2012.

Figure 5.34 illustrates the inter-day values of MUF(3000) recorded at El Arenosillo station (37.1 N, 6.7 W) during the three surveys. A maximum value of 30 MHz was measured at exact noontime (12:00 UTC) throughout the 2011/2012 survey, whereas over the 2010/2011, maximum MUF(3000) inter-day value of 26 MHz has been recorded at 11:00 UTC. At 12:30 UTC throughout the 2009/2010 survey, 22 MHz was the maximum MUF(3000) inter-day value that has been measured. During the nighttime of the three surveys, an average value of around 10 MHz was observed from 00:00 UTC to 07:00 UTC, and then started to increase to around 20 MHz at the 2009/2010 survey, 25 MHz throughout 2010/2011 and 2011/2012.

The MUF(3000) was decreased again after sunset to around 10 MHz at 19:00 UTC during the 2009/2010 survey, and then due to the raising of the SSN values, the MUF(3000) inter-day variation declined to 10 MHz at 20:00 UTC during the 2010/2011 survey, and at 21:00 UTC throughout the 2011/2012 survey. Herein, at El Arenosillo station, the daytime period was extended by around two hours from 2009/2010 to 2011/2012, and that can be related to the significant increment of the solar activity (SSN of 11.6, 21.1, and 65.3).

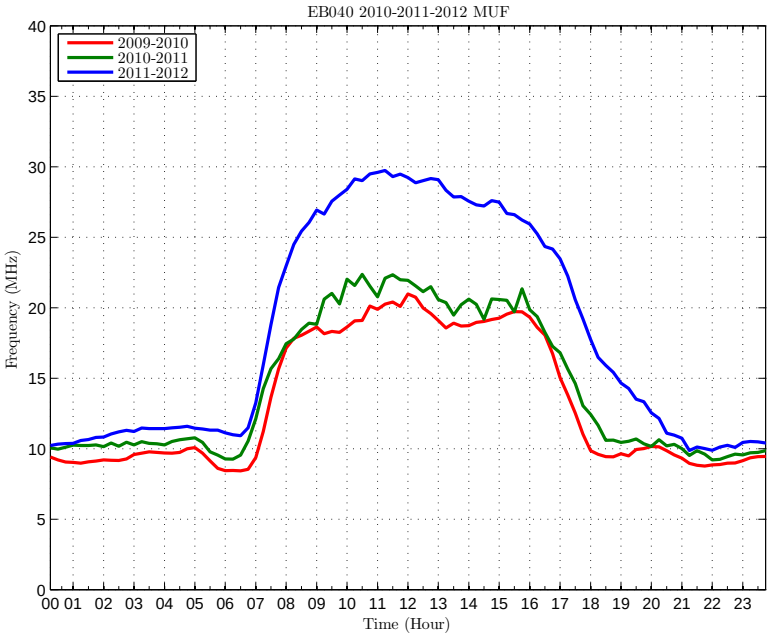

FIGURE 5.35: Inter-day variation of the MUF(3000) at the OE station during 2009/2010, 2010/2011, and 2011/2012.

Referencing the OE station (40.8 N, 0.5 E), the inter-day MUF(3000) variation, which has been recorded during the three survey are shown in Figure 5.35. The measurements regarding the 2009/2010 and 2010/2011 surveys were very close throughout the whole day. It started with around 9 MHz, 10 MHz, and 11 MHz at 00:00 UTC over the three surveys. Then, as observed in El Arenosillo station (see, Figure 5.34), the MUF(3000) variations were decreased with around 1 MHz just prior to the starting of the sunrise at (06:30 UTC).

During the daytime period, the MUF(3000) variation that has been measured during 2009/2010 was slightly smaller than 2010/2011. That was corresponding to the small increment in the SSN values during the first two surveys (11.6 and 21.1). During the 2011/2012 survey, the inter-day MUF(3000) measurements were clearly higher with an average of around 8 MHz larger than both the 2009/2010 and 2010/2011 surveys. The maximum MUF(3000) value that obtained during the 2011/2012 survey was around 30 MHz (at 11:00 UTC), 22 MHz (at 11:00 UTC) over the 2010/2011 survey, and 21 MHz (at 12:00 UTC) throughout the 2009/2010 survey.

The large SSN increment during the 2011/2012 (65.3) resulted in adding around two hours to the daytime propagation region that starts at sunrise and ends at sunset.

5.7 VIS and OIS parameters comparison

Herein, there will be an investigation on how to take advantage of the VIS station that spread all over the world in the establishment of the long-haul ionospheric link. In that context, we compare the likeliness between the inter-day variation of the MUF(3000), which was recorded at VIS stations close to the SAS-OE link path and the average FLA that has been obtained from the OIS system over three consecutive surveys.

Throughout the three surveys, Figures 5.36, 5.37, and 5.38 illustrate the MUF(3000) inter-day variation recorded at the Port Stanley, Ascension, and El Arenosillo stations along with the FLA of the OIS system and the minimum MUF(3000) among the VIS stations. The results explained through this section are representing the completion for the conclusions mentioned in [134] where the measurements were of 18 hours and HF band from 4.6 MHz to 16.6 MHz.

According to the behavior of the ionosphere during the day, Figures 5.36, 5.37, and 5.38 can be explained in terms of three time intervals, from 00:00 UTC to 06:00 UTC, from 07:00 UTC to 18:00 UTC, and from 19:00 UTC to 23:00 UTC.

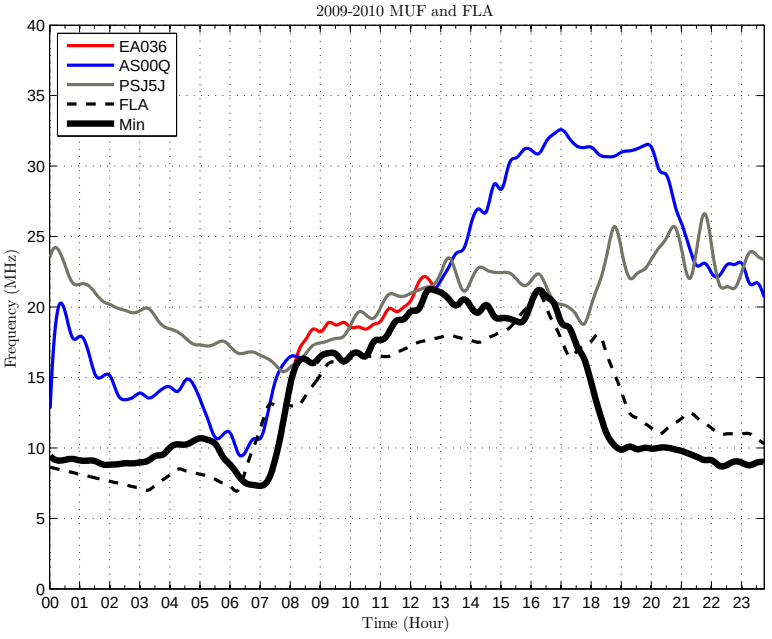

FIGURE 5.36: A comparison between MUF(3000) inter-day variation of the VIS stations throughout the 2009/2010 survey, the FLA of the OIS system, and the minimum MUF(3000).

Regarding the 2009/2010 survey, from Figure 5.36, we can see that from 00:00 UTC to 07:00 UTC, the measurements obtained at EL Arenosillo station (37.1 N, 6.7 W)

are the minimum inter-day variation of MUF(3000); so that, the stations located at mid-latitude zone have the minimum MUF(3000) values. However, after the sunrise from 08:00 UTC to 12:00 UTC, the results from the Ascension station (high-latitude) presented the minimum MUF(3000) values among the other VIS stations. During the time interval that goes from 13:00 UTC to 23:00 UTC, the minimum MUF(3000) inter-day variation was measured at El Arenosillo station.

Throughout the 2010/2011 survey, Figure 5.37 shows that the MUF(3000) inter-day measurements that obtained at El Arenosillo station, which is located at mid-latitude zone were the minimum ones from 00:00 UTC to 06:00 UTC and from 14:00 UTC to 23:00 UTC. On the other hand, stations placed at high-latitude areas (e.g., Port Stanley (51.6 S, 57.9 W)) had the minimum MUF(3000) inter-day variation.

After the sunrise until 13:00 UTC, Port Stanley station presented the minimum MUF(3000) values; although, the minimum values over the time periods that goes from 00:00 UTC to 06:00 UTC and from 14:00 UTC to 23:00 UTC were measured at El Arenosillo station.

During three consecutive surveys as shown in Figures 5.36, 5.37, and 5.38, the first time interval (00:00 UTC to 07:00 UTC) shows that the minimum MUF(3000) values were restricted the FLA that obtained over the SAS-OE link. That can be an assurance for the previous results measured during the 2006/2007 and discussed in [134].

The second time interval (07:00 UTC to 18:00 UTC) over the three surveys, which is illustrated in Figures 5.36, 5.37, and 5.38 depict that the FLA values are limited by the minimum MUF(3000) values, which mostly measured at El Arenosillo VIS station. Figure 5.36 shows an exception at 10:00 UTC and 16:00 UTC where the FLA is almost equal to the minimum MUF(3000).

During the 2010/2011 survey, the average MUF(3000) recorded at El Arenosillo station is approximately equal to the FLA values during 07:00 UTC to 09:00 UTC. Consequently, the minimum MUF(3000) becomes the upper bound to the FLA from 10:00 UTC to around 18:00 UTC as shown in Figure 5.37.

Regarding the 2011/2012 survey, the FLA measurement is equivalent to the minimum MUF(3000) values that have been recorded at El Arenosillo station. However, the time interval from 08:00 UTC to 10:00 UTC and at 12:00 UTC depicted that the FLA values have exceeded the minimum MUF(3000) values.

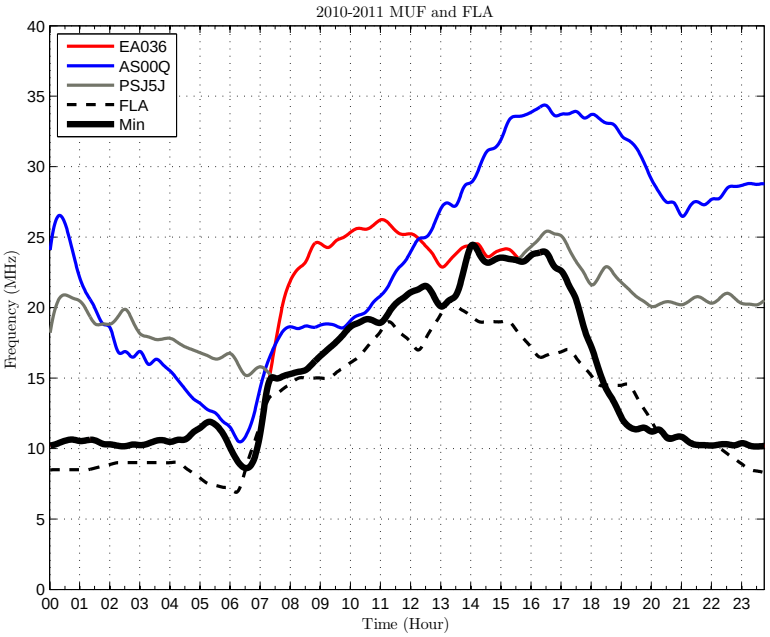

FIGURE 5.37: A comparison between MUF(3000) inter-day variation of the VIS stations during the 2010/2011 survey, the FLA of the OIS system, and the minimum MUF(3000).

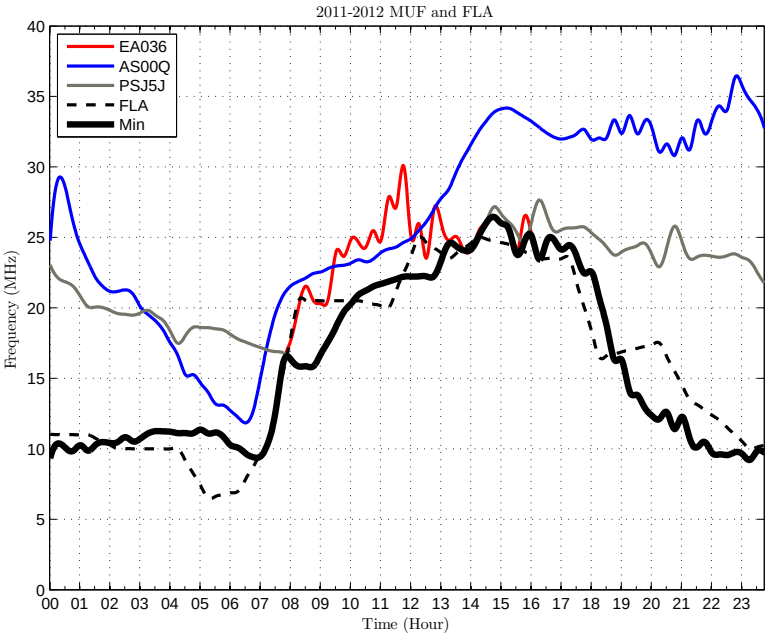

FIGURE 5.38: A comparison between MUF(3000) inter-day variation of the VIS stations over the 2011/2012 survey, the FLA of the OIS system, and the minimum MUF(3000).

The third time interval from 18:00 UTC to 23:00 UTC for the three surveys which illustrated in Figures 5.36 and 5.38, show that the FLA limitation outcome from the

previous two interval (00:00 UTC to 07:00 UTC and 07:00 UTC to 18:00 UTC) is not further applicable for the third interval (18:00 UTC to 23:00 UTC) during the 2009/2010 and 2011/2012 surveys. However during the 2010/2011 survey as shown in Figure 5.37, the FLA is bounded by the minimum MUF(3000).

Figure 5.36 illustrates that the FLA values were higher than the the minimum MUF(3000) values over the period that goes from 19:00 UTC to 23:00 UTC, then at 19:00 UTC as shown in Figure 5.37 and from 19:00 UTC to 23:00 UTC as depicted in Figure 5.38. This can be explained because the reflection points are not exactly the same as the ionosondes.

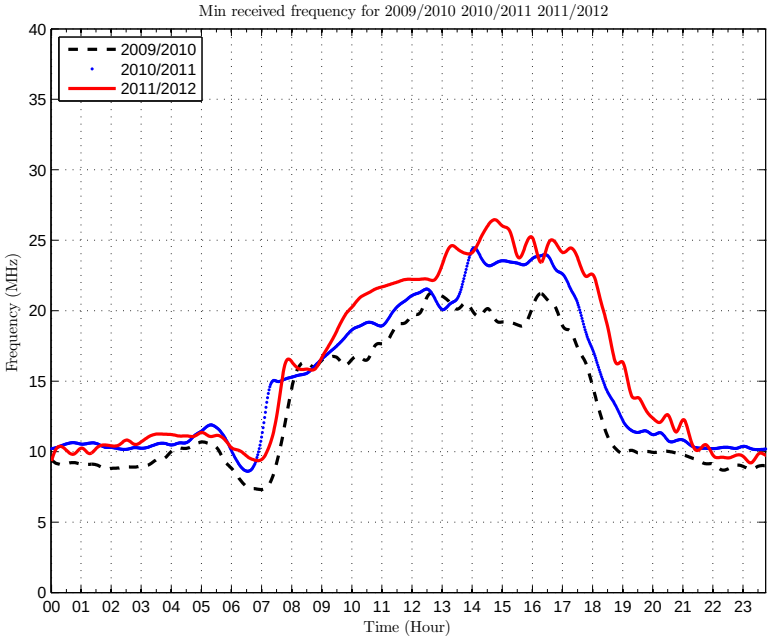

FIGURE 5.39: Comparison of the minimum inter-day variations of MUF(3000) throughout the 2009/2010, 2010/2011, and 2011/2012 surveys.

The evolution of the minimum MUF(3000) values that have been measured during the 2009/2010, 2010/2011, and 2011/2012 is illustrated in Figure 5.39. The explanation of Figure can be summarized into the following time interval:

- The first time interval from 00:00 UTC to 07:00 UTC - an average of 10 MHz can be usable for transmission during this interval, then at the sunrise period it decreased with an average of 2 to 5 MHz.
- The second time interval (08:00 UTC to 18:00 UTC) - shows that the minimum MUF(3000) values of the three surveys have increased from almost 15 MHz at

08:00 UTC to the maximum values of 22.5 MHz at 16:30 UTC (2009/2010), 24 MHz at 14:00 UTC (2010/2011), and 26.5 MHz at 15:00 UTC (2011/2012).

- The third time interval from 19:00 UTC to 23:00 UTC - the minimum values were progressively decreased to approximately 10 MHz.

Remarkably the minimum MUF(3000) values that obtained during the daytime propagation region extended by around one hour over the three surveys. That is highly related to the increasing in the SSN (11.6 to 65) and Solar Flux (79 to 134 SFU). So that, according to the previous results, the lowest MUF(3000) recorded at the VIS stations, which are located strategically close to the SAS-OE ionospheric link path will restrict the FLA values during almost the whole day. Prior to the establishment of an ionospheric link, knowing the minimum MUF(3000) values over the link path will help in optimizing the performance of the transmission platform.

5.8 Concluding remarks

Herein this chapter, there is a study of several OIS parameters that have been measuring over the oblique SAS-OE ionospheric link (12700 km) throughout three surveys (2009/2010, 2010/2011, and 2011/2012), besides other parameters from four VIS stations located close the SAS-OE link path. So that, it has been possible to understand the relationship between the availability of the SAS-OE ionospheric link and the MUF(3000) values that have been obtained at the VIS stations located along the path of the link.

All the results presented in this chapter were measured during three consecutive surveys with different SSN (11.6, 21.1, and 65.3) and Solar Flux (79, 86, and 134) values in order to investigate the influence of the solar activity on availability of the SAS-OE link (OIS) and the TEC, foF2, MUF(3000) (VIS). Finally, through this chapter, we include proofs of the validity of this infrastructure (i.e., using VIS stations located close to the reflection points of an oblique ionospheric link) for observing the ionospheric propagation over very log distance.

The availability of the SAS-OE link was measured from 2009 to 2012, with the corresponding inter-day variation of the FLA. Then, we compared *real-time* measurements

(link availability and corresponding FLA values) with the MUF(3000) from the prediction software Rec533, which is called MUFRec533 as shown in Figures 5.6, 5.7, and 5.8.

The propagated frequencies have reached maximum value of 18.5 MHz at 16:00 UTC during 2009/2010, 20.5 MHz at 13:00 UTC throughout the 2010/2011 survey, and 25 MHz at midday during the 2011/2012 survey. From the 2009/2010 and 2010/2011 surveys to the 2011/2012, the inter-day values of the FLA increased with around 23% over the daytime period and 15% throughout the nighttime period. Therefore, high frequencies that were not being able to propagate, along with the annual raising of the solar activity, start to propagate efficiently.

During the three surveys, as shown in Figures 5.6, 5.7, and 5.8, the Rec533 HF prediction *software* provided MUFRec533 values limiting the availability of the SAS-OE link over 24 hours per day. So that, the highest frequency that was propagating for a specific link throughout the whole day can be determined in advance by using the Rec533 prediction *software* (MUFRec533).

Station	foF2 (MHz)			MUF(3000) (MHz)		
	2009/2010	2010/2011	2011/2012	2009/2010	2010/2011	2011/2012
PSJ5J	15	15	15	56	62.8	64
AS00Q	10	12.75	14.8	42	44.5	46.5
EA036	7.3	8.85	11.9	27	34.3	44.7
EB040	7	8.5	10.75	27	31.5	41.5

TABLE 5.6: Maximum foF2 and MUF(3000) values that measured at the four VIS stations during three surveys.

The day-to-day variations of the foF2 and MUF(3000), which have been recorded along the SAS-OE link path, were characterized by clear diurnal harmonics at mid-latitude stations (El Arenosillo and OE) and semi-diurnal harmonics at high-latitude stations (Port Stanley and Ascension); therefore, the usable range of frequencies over 24 hours per day depends largely on the location of the VIS station will.

The maximum foF2 and MUF(3000) values that have been measured during the three surveys over a period of two weeks in January are summarized in Table 5.6. A clear observation is that the maximum foF2 and MUF(3000) values were increasing as moving from mid-latitude stations to high-latitude stations, and from a survey to the next.

The inter-day variation of the TEC showed that the Sun has affected the average TEC values during the daytime only at mid-latitude stations. However, at the high-latitude stations, the increasing of the solar activity resulted in stepping-up the inter-day TEC variation during the 24 hour per day (daytime and nighttime).

As explained previously, the inter-day variations of the foF2 and the MUF(3000), which were obtained at mid-latitude stations (El Arenosillo and OE) during the three consecutive surveys show that:

- The increment of the solar activity (e.g., SSN (11.6, 21.1, and 65.3) and Solar Flux (79, 86, and 134)) has added time period that goes from around one to two hours over the daytime interval of the MUF(3000) inter-day variation.
- The maximum inter-day values of the foF2 obtained at El Arenosillo station have increased with around 14.2% from the 2009/2010 to 2010/2011 survey and 12% from the 2010/2011 to 2011/2012 survey.
- The maximum inter-day values of the foF2 obtained at OE station have increased with around 7.9% from the 2009/2010 to 2010/2011 survey and 21.2% from the 2010/2011 to 2011/2012 survey.
- The maximum inter-day values of the MUF(3000) obtained at EL Arenosillo station have raised with around 15.5% from the 2009/2010 to 2010/2011 survey and 13.3% from the 2010/2011 to 2011/2012 survey.
- The maximum inter-day values of the MUF(3000) obtained at OE station have been stepped-up with around 4.5% from the 2009/2010 to 2010/2011 survey and 26.6% from the 2010/2011 to 2011/2012 survey.

So that, the maximum values of both the foF2 and MUF(3000) inter-day variations have been increased according to the raising of the solar activity.

Then, we have studied the likeliness between the FLA values from the OIS system operated over the SAS-OE, and the inter-day variation of MUF(3000) recorded at VIS stations close to the SAS-OE link path. The comparisons illustrated in Figures 5.36, 5.37, and 5.38 throughout three consecutive surveys have provided interesting conclusion, since, the inter-day measurements of the FLA were correlate quite well with the MUF(3000) variations obtained at mid-latitude stations nearby the receiver, e.g., El Arenosillo and OE.

Firstly, during the 2009/2010 survey, the inter-day variation of the MUF(3000) that has been measured at mid-latitude VIS stations, which are near the receiver unit (OE), and the average values of FLA were almost equal from 00:00 UTC to 07:00 UTC and from 13:00 UTC to 23:00 UTC. Otherwise, from 08:00 UTC to 12:00 UTC, the variation pattern of the MUF(3000) recorded at VIS stations close to the transmitter unit was more similar to the FLA values.

Secondly, over the 2010/2011 survey, the inter-day variation of the MUF(3000), which has been obtained at mid-latitude VIS stations close to the receiver and the average FLA are very close over the period that starts at 00:00 UTC and ends at 06:00 UTC and from 14:00 UTC to 23:00 UTC. However, the MUF(3000) pattern, which has been measured at VIS stations near the transmitter at SAS was almost equal the FLA values obtained from 07:00 UTC to 13:00 UTC.

Finally, throughout the 2011/2012 survey, the MUF(3000) inter-day variation that has been obtained close to the receiver and the FLA measurements were very similar during two time periods from 00:00 UTC to 07:00 UTC and from 14:00 UTC to 23:00 UTC. On the other hand, from 08:00 UTC to 13:00 UTC, the MUF(3000) patterns of VIS stations close to the transmitter were much more equal to the average FLA values.

Also, the average FLA values hardly exceeded the minimum MUF(3000) inter-day values that were recorded at VIS stations located along the SAS-OE link path as shown in Figures 5.36, 5.37, and 5.38. So that, we come up with clear conclusion that having VIS stations strategically located along the link path, the lowest MUF(3000) values, which are measured at those stations in a particular moment will represent the boundaries for the FLA values over the link. This fact does not mean that higher frequencies than the minimum MUF(3000) are not propagated, but received with very low power.

Chapter 6

Conclusions and future lines

This section is devoted to summarize the work conducted in this thesis; with special attention to the contributions that have been achieved. For further details about the results, we refer the reader to Sections 4.6, 5.5, 5.6, and 5.7.

The work in the scope of this thesis is considered a step in the Antarctica project, which has a goal of connecting the Spanish Antarctica Station Juan Carlos I (SAS) (62.6 S, 60.4 W) with the Ebro Observatory (OE) (40.8 N, 0.5 E). For almost a decade, the *radiomodem* platform of the Antarctica project has been upgraded several times to reach that goal.

There are three generations of *Software Defined Radio* (SDR) platforms with two main purposes, narrowband and wideband sounding of the SAS-OE link, and transmitting the collected measurements from the geomagnetic sensors located at SAS. In other words, firstly sounding the SAS-OE ionospheric link, and then depending on sounding measurements, the SAS-OE link can be used for transmitting the magnetic data. There are several features that make the SAS-OE ionospheric link a unique transmission link, these include:

- it has very long length of around 12700 km crossing high-latitude and mid-latitude areas, and four different time zones;
- very low available transmission power of around 200 watts as maximum due to the environmental restrictions at SAS;
- single monopole antenna at the transmitter and simultaneous reception through three types of antennas (monopole, yagi, and V-antenna).

Mainly, the results that have been presented through the contribution part of this thesis were obtained in three consecutive stages:

- sounding obliquely the SAS-OE link in order to obtain the narrowband and wideband characteristics of the link;
- study the influence of the solar activity on the parameters that have been measured from the Oblique Incidence Sounding (OIS) platform and at four Vertical Incidence Sounding (VIS) stations located over the SAS-OE link path throughout three consecutive surveys with different Smoother Sunspot Number (SSN) and Solar Flux values;
- investigate the likeliness between the inter-day Frequency of Largest Availability (FLA) values obtained from the OIS and the inter-day variation of the Maximum Usable Frequency for a single hop transmission reflected at the F2 layer (MUF(3000)) recorded at the four VIS stations;

In the first stage, the SAS-OE ionospheric link had been studied over the 2009/2010 (33 days from December 2009 to February 2010), the whole HF band was used for sounding the link during 24 hours per day; so that, we completed the time series of the oblique soundings. In order to have all the characteristics of the SAS-OE link, the study has covered both narrowband and wideband sounding techniques. The narrowband sounding has been carried out by transmitting narrowband pulses at the whole HF band in a step of 500 kHz for estimating the availability of the link as a function of time and frequency.

In order to refine the highly interfered narrowband tones, four window functions have been tested. Finally, the *Kaiser* function was selected after further experiments over different times and sounding frequency. Besides that, discontinuities in the link availability scheme (frequency/time), which could not be attributed to the channel behavior were solved by the time framing method. The SAS-OE link availability throughout the 2009/2010 survey can be summarized in the following two regions:

- First, the daytime propagation region that starts at 07:00 UTC to around sunset, such region had not been analyzed prior to the 2009/2010 survey. The SAS-OE link was strongly available over frequency range from 10 MHz to 23 MHz.

- Second, during the nighttime propagation region from 20:00 UTC to 06:00 UTC, the frequency band that starts at 3.5 MHz and ends at around 16 MHz showed the best degree of availability.

So, by handling the transmission frequency over the day, the SAS-OE ionospheric link can be used for transmission throughout the 24 hours per day. Finally, we have made measurements of the time and frequency dispersion as a function of sounding frequency and hour. For this purpose we have selected parameters, such as *composite multipath spread* and *composite Doppler spread*, *Doppler frequency shift*, and the propagation time for the aim of consistency with previous work and the fact that those parameters were demonstrating effectiveness in applying them to the design of HF modems.

The *composite multipath spread* values have reached the maximum of 3.2 ms, decreasing to the minimum of 0.25 ms, along with increasing sounding frequency. The maximum *composite multipath spread* values have ranged from 2.7 ms to 3.2 ms, and have been obtained throughout the nighttime period. Otherwise, the minimum *composite multipath spread* of 0.25 ms has occurred during the daytime period.

Maximum *composite Doppler spread* values have been obtained in low frequency range during the nighttime period. Meanwhile, over the daytime period, minimum *composite Doppler spread* values have been measured with high frequency range.

So, we conclude that the SAS-OE link is wide spread both in time and frequency during the nighttime at lower frequencies, while becomes narrow spread in both time and frequency during the daytime at higher frequencies.

Regarding the second stage, during three consecutive surveys (2009/2010, 2010/2011, and 2011/2012), we investigated the influence of the solar activity, e.g., SSN (11.6, 21.1, and 65.3) and Solar Flux (79, 86, and 134) on the SAS-OE link availability and FLA values, which were obtained from the OIS system, and the Total Electron Content (TEC), critical frequency of the F2 layer (foF2), MUF(3000) recorded at four VIS stations (Port Staley, Ascension, El Arenosillo, and OE) located close to the SAS-OE link path.

During the three surveys, the link availability and FLA values were compared to the MUFRec533 from the Rec533 HF prediction *software*, which we found out that the MUFRec533 values were the boundaries for the propagated frequencies over 24 hour per day as clarified in Chapter 4. During the daytime region, the highest frequency where

the SAS-OE link is available was around 23.5 MHz, 25.5 MHz, and 28 MHz throughout the 2009/2010, 2010/2011, and 2011/2012 surveys, respectively. The average FLA values have increased with around 23% over the daytime period and 15% throughout the nighttime period from the first two surveys (2009/2010 and 2010/2011) to the last one (2011/2012).

The VIS stations located at mid-latitude areas, such as OE and El Arenosillo, have provided day-to-day and inter-day variations with clear diurnal harmonics; while, the measurements from high-latitude stations (Port Stanley and Ascension) were characterized by semidiurnal harmonics. Also, it is observed that the maximum foF2 and MUF(3000) values raised along with increasing the activity of the Sun from survey to the next, and with changing the location of the VIS station from mid- to high-latitude areas. Moreover, the solar activity increment has added around one to two hours over the daytime propagation period depending relatively on the value of the SSN (11.6, 21.1, and 65.3) and Solar Flux (79, 86, and 134).

Additionally, the augmentation of the solar activity during the three surveys has raised the inter-day variation of the TEC that was measured at high-latitude stations over 24 hours per day; meanwhile, the measurements from the mid-latitudes stations have been increased strongly over the daytime period.

The discussion of the likeliness between the average FLA values and the MUF(3000) inter-day variation showed that - the average FLA values and the MUF(3000) inter-day values that measured at the mid-latitude stations (El Arenosillo and OE), have the same scheme. During the three surveys, the inter-day variations of the MUF(3000) at stations close to the receiver are very similar to the FLA values over the nighttime period. Otherwise, throughout the daytime period, the MUF(3000) patterns recorded at stations close to the transmitter (high-latitude) are the most similar to the FLA scheme.

The minimum MUF(3000) values that have been recorded among the VIS stations are limiting the inter-day FLA variation of the OIS system. Therefore, knowing in advance the minimum MUF(3000) values that have been measured at stations over an ionospheric link, will determine the FLA values of that ionospheric link. This conclusion does not mean that frequencies higher than the minimum MUF(3000) are not propagated, but received with much low power. Finally, we have proved the validity of this infrastructure for observing a very long ionospheric link, such as the SAS-OE link.

We have conducted a complete characterization study of the very long ionospheric link (SAS-OE) through measuring the channel availability, time and frequency dispersion parameters during 24 hours per day and using the whole HF band. Also, studied the solar activity influence on the OIS and VIS parameters through three consecutive surveys, and investigated how the MUF(3000) values recorded at stations close to the link path can help on determining the FLA of the link. Ultimately, we believe that is necessary to develop the following lines:

- The availability of the ionospheric link is mainly determined by the solar activity, and since we have only 4 surveys of a complete analysis of the SAS-OE link, the study has to be extended to a complete solar cycle of around 11 years. It is interesting to mention that the measurements obtained throughout the 2012/2013 survey, which is not included in this work, provided a large consistence with the previous surveys in term of the link availability (almost the whole HF band is highly propagating).

- The magnetic field of the Earth is dividing the electromagnetic waves, which pass through the ionosphere into two types of signal components, *Ordinary* and *Extraordinary*. The simultaneous reception through the monopole, yagi, and V-antenna, will help in investigating the correlations between the *Ordinary* and *Extraordinary* components of the received signals.

- As the Earth is spherical, there exist two paths from SAS to OE. First, the direct link (12700 km), which we have studied and a second link traveling through the opposite side of the Earth. The availability of this long link is less possible due to the higher number of hops, but also possible. There were several indications of the existence of this concept during the analysis process of the signals received over the SAS-OE link; so that this concept need to be studied comprehensively.

- Study how decisively the magnetic and ionospheric disturbances, such as the magnetic storms, *Coronal Mass Ejections* (CMEs), *Traveling Ionospheric Disturbances* (TIDs), can affect the oblique propagation of the electromagnetic waves over the SAS-OE ionospheric link.

Bibliography

[1] C. Vilella. Comunicaciones avanzadas en hf entre la base antártica espanola y el observatorio del ebro: caracterización de canal y transmisión de datos. *PhD dissertation, Ramon Llull University*, 2007.

[2] H. D. Arnold and L. Espenschied. Transatlantic radio telephony. *Transactions of the American Institute of Electrical Engineers*, XLII:718–729, August 1923. doi: 10.1109/T-AIEE.1923.5060906.

[3] O.Heaviside. *Encyclopedia Britannica (10th edition)*, 33:213, 1902.

[4] A. E. Kennelly. On the elevation of the electrically-conducting strata of the earth's atmosphere. *Elec. World mid Engr.*, 15:473, March 1902.

[5] D. Gauld and N. Arthur. On the nature of atmospherics. *Proceeding of the Royal Society A*, 111(756):615–653, July 1926. doi: 10.1098/rspa.1926.0085.

[6] E. V. Appleton and M. A. F. Barnett. On some direct evidence for downward atmospheric reflection of electric rays. *Proceeding of the Royal Society A*, 109 (752):621–641, December 1925. doi: 10.1098/rspa.1925.0149.

[7] S. S. Kirby, L. V. Berkner, and D. M. Stuart. Studies of the ionosphere and thier application to radio transmission. *Bureau of Standards Journal of Research*, 12: 15–51, January 1934.

[8] M. Emilio, J. R. Kuhn, R. I. Bush, and I. F. Scholl. Measuring the solar radius from space during the 2003 and 2006 mercury transits. *Astrophysical Journal*, 750(2), March 2012. doi: 10.1088/0004-637X/750/2/135.

[9] J. H. Dellinger. Sudden disturbances of the ionosphere. *Proceedings of the Institute of Radio Engineers*, 25(10):1253–1290, October 1937. doi: 10.1109/JRPROC.1937.228657.

[10] J. M. Spomenko and C. Lazovc. The disturbances of the solar-geomagnetic activity. *12th International Power Electronics and Motion Control Conference*, pages 2045–2050, August-September 2006. doi: 10.1109/EPEPEMC.2006.4778708.

[11] J. C. H. Wang. Solar activity and mf skywave propagation. *IEEE Transactions on Broadcasting*, 35(2):204–207, June 1989. doi: 10.1109/11.30836.

[12] S. Ostrow and M. Po-Kempner. The differences in the relationship between ionospheric critical frequencies and sunspot number for different sunspot cycles. *Transactions of the IRE Professional Group on Antennas and Propagation*, PGAP-3:213, August 1952. doi: 10.1109/T-AP.1952.28041.

[13] He Fengxia, Xie Yanjuan, and Ma Xuejun. Time series modeling and short-time forecasting for dst index of geomagnetic storm. *2nd International Workshop on Database Technology and Applications (DBTA)*, pages 1–4, November 2010. doi: 10.1109/DBTA.2010.5659064.

[14] J. Bartels, N. H. Heck, and H. F. Johnston. The three-hour-range index measuring geomagnetic activity. *Terrestrial Magnetism and Atmospheric Electricity*, 44(4):411–454, December 1939. doi: 10.1029/TE044i004p00411.

[15] M. C. Kelley. The earth's ionosphere. *Academic Press*, 1989.

[16] J. L. Fox, M. I. Galand, and R. E. Johnson. Energy deposition in planetary atmospheres by charged particles and solar photons. *Space Science Reviews*, 139:3–62, August 2008. doi: 10.1007/s11214-008-9403-7.

[17] J. J. Gibbons and A. H. Waynick. The normal d region of the ionosphere. *Proceedings of the IRE*, 47(2):160–161, February 1959. doi: 10.1109/JRPROC.1959.287261.

[18] T. R. Gilliland, G. W. Kenrick, and K. A. Norton. Investigations of kennelly-heaviside layer heights for frequencies between 1600 and 8650 kilocycles per second. *Proceedings of the Institute of Radio Engineers*, 20(2):286–309, February 1932. doi: 10.1109/JRPROC.1932.227522.

[19] L. E. Petrie and G. E. K. Lockwood. On the prediction of f-layer penetration frequencies. *Proceedings of the IEEE*, 57(6):1025–1028, June 1969. doi: 10.1109/PROC.1969.7147.

[20] D. D. Crombie. On the use of vlf measurements for obtaining information on the lower ionosphere (especially during solar flares). *Proceedings of the IEEE*, 53 (12):2027–2034, December 1965. doi: 10.1109/PROC.1965.4479.

[21] D. F. Webb. Coronal mass ejections: origins, evolution, and role in space weather. *IEEE Transactions on Plasma Science*, 28(6):1795–1806, December 2000. doi: 10.1109/27.902209.

[22] A. M. Gokov and O. F. Tyrnov. The features of the partial reflection signals, radionoises and electron density variations in the middle latitude d-region of the ionosphere during the magnetic storms in 2004-2006. *18th International Crimean Conference on Microwave Telecommunication Technology*, pages 882–883, September 2008. doi: 10.1109/CRMICO.2008.4676644.

[23] S. R. Prabhakaran Nayar, S. Yamini, R. Balachandran Nair, and P. B. Rao. Hf doppler spectrum under spread f and nonspread f conditions at magnetic equator. *Seventh International Conference on Antennas and Propagation*, 2: 902–905, April 1991.

[24] B. S. Lanchester, H. Rishbeth, T. Nygren, A. Huuskonen, and M. J. Jarvis. Interaction of winds, wave and sporadic e layers in the high latitude ionosphere. *IEE Colloquium on High Latitude Ionospheric Propagation*, 8:1–2, April 1992.

[25] M. H. Jusoh, F. N. Abu Bakar, A. A. Sulaiman, N. H. Baba, R. A. Awang, and Z. I. Khan. Determination of traveling ionospheric disturbances of geomagnetic storm by using dual frequency gps data. *IEEE International RF and Microwave Conference RFM*, pages 361–366, December 2008. doi: 10.1109/RFM.2008.4897352.

[26] Yu. V. Goncharenko, V. G. Gutnik, and F. V. Kivva. Experimental study of meteorological parameters variation using hf-signal during solar proton events. *The Fifth International Kharkov Symposium on Physics and Engineering of Microwaves, Millimeter, and Submillimeter Waves, 2004. MSMW 04*, 1:184–186, June 2004. doi: 10.1109/MSMW.2004.1345814.

[27] E. E. Johnson, R. I. Desourdis, G. Earle, J. C. Ostergaard, and S. Cook. *Advanced high frequency radio communications*. 1997.

[28] Characteristics and applications of atmospheric radio noise data, itu-r p.372-8. *International Telecommunication Union Std.*, 2003.

[29] H. Widmer. On the global emc aspect of broadband power line communications using the hf frequency band. *International Seminar on Broadband Communications*, 1998.

[30] P. S. Cannon. Ionospheric models and measurements required for hf communication system designers and operators. *IEE Colloquium on Propagation Characteristics and Related System Techniques for Beyond Line-of-Sight Radio*, pages 1–4, November 1997. doi: 10.1049/ic:19971348.

[31] P. S. Cannon. Ionospheric propagation and modeling for modern hf communication systems. *Nordic HF conference*, August 1998.

[32] J. P. Sudworth. Approaches to simulation of broadband ionospheric channels and some preliminary results. *Seventh International Conference on HF Radio Systems and Techniques*, pages 392–396, July 1997. doi: 10.1049/cp:19970829.

[33] C. C. Watterson, J. Juroshek, and W. D. Bensema. Experimental configuration of an hf channel model. *IEEE Transactions on Communication Technology*, 18: 792–803, December 1970. doi: 10.1109/TCOM.1970.1090438.

[34] R. Lindström. Wideband modelling of the ionospheric channel. *Proc. HF 92, Nordic Shortwave Conference*, pages 21–32, August 1992.

[35] J. F. Mastrangelo, J. J. Lemmon, L. E. Vogler, J. A. Hoffmeyer, L. E. Pratt, and C. J. Behm. A new wideband high frequency channel simulation system. *IEEE Transactions on Communications*, 45(1):26–34, 1997. doi: 10.1109/26.554283.

[36] D. N. Anderson, J. M. Forbes, and M. Codrescu. A fully analytic, low- and middle-latitude ionospheric model. *Journal of Geophysical Research*, 94(A2): 1520–1524, 1989. doi: 10.1029/JA094iA02p01520.

[37] Y. T. Chiu. An improved phenomenological model of ionospheric density. *Journal of Atmospheric and Terrestrial Physics*, 37(12):1563–1570, December 1975. doi: 10.1016/0021-9169(75)90035-5.

[38] R. E. Daniell, L. D. Brown, D. N. Anderson, M. W. Fox, P. H. Doherty, D. T. Decker, J. J. Sojka, and R. W. Schunk. A global ionospheric parameterization based on first principles models. *Radio Sci.*, 30(5):1499–1510, 1995. doi: 10.1029/95RS01826.

[39] J. R. Dudeney and R. I. Kressman. Empirical models of the electron concentration of the ionosphere and their value for radio communications purposes. *Radio Sci.*, 21(3):319–330, 1986. doi: 10.1029/RS021i003p00319.

[40] G. Banerjee and A. K. Mallick. A semi empirical model for low latitude hf ionospheric propagation prediction. *IEEE Transactions on Broadcasting*, 43(1): 89–95, march 1997. doi: 10.1109/11.566829.

[41] Reference ionospheric characteristics, itu-r p.1239-3. *International Telecommunication Union Std.*, 2012.

[42] S. Ganguly and A. Brown. Real-time ionospheric characterization and modelling. *International Ionospheric Effects Symposium*, 36:11811197, May 2002. doi: 10.1029/1999RS002412.

[43] J. D. Milsom, L. W. Barclay, and N. S. Wheadon. The evolution of an ionospheric forecasting service. *Eighth International Conference on HF Radio Systems and Techniques*, pages 181–185, July 2000. doi: 10.1049/cp:20000171.

[44] Asaps: Advanced stand-alone prediction system. *Ionospheric Prediction System, Radio and Space Services*, .

[45] T. F. Tascione, K. W. Kroehl, and B. A. Hausman. A technical description of the ionospheric conductivity and electron density profile model (iced, version 196-ii). *U.S. Air Force*, 1987.

[46] J. M. Ratzloff and G. R. Hand. User's guide and reference manual for the voacap and rec533 circuit analysis programs. *Institute for Telecommunication Sciences*, (TM-93-157), May 1993.

[47] L. R. Teters, J. L. Lloyd, G. W. Haydon, and D. L. Lucas. Estimating the performance of telecommunication systems using the ionospheric transmission channel-ionospheric communications analysis and prediction program user manual. *Institute for Telecommunication Sciences*, (TR-83-127), July 1983.

[48] C. Vilella, D. Miralles, and L. Pijoan. An antarctica-to-spain hf ionospheric radio link: sounding results. *Radio Sci.*, 43(4), August 2008. doi: 10.1029/2007RS003812.

[49] A. G. Ads, P. Bergadà, C. Vilella, J. R. Regué, J. L. Pijoan, R. Bardají, and J. Mauricio. A comprehensive sounding of the ionospheric hf radio link from antarctica to spain. *Radio Sci.*, 48(1):1–12, 2012. doi: 10.1029/2012RS005074.

[50] N. C. Davies, T. Wilink, M. J. Angling, and P. S. Cannon. Initial results from whisper; a wideband hf ionospheric sounder for propagation environment research. *Nordic Shortwave Conference*, 2001.

[51] P. S. Cannon, M. J. Angling, N. C. Davies, T. Wilink, V. Jodalen, B. Jacobson, B. Lundborg, and M. M. Broms. Damson hf channel characterization-a review. *IEEE Military Communications Conference*, 1:59–64, October 2000. doi: 10.1109/MILCOM.2000.904913.

[52] Y. M. L. Roux, J. Menard, J. P. Jolivet, P. Davy, and A. Bourdillon. Scipion: a flexible ionospheric digital sounder. illustration of its capabilities for spatial coherence studies of es and f regions. *Seventh International Conference on HF Radio Systems and Techniques*, pages 25–29, July 1997. doi: 10.1049/cp:19970754.

[53] V. E. Gherm, N. N. Zernov, H. J. Strangeways, and M. Darnell. Scattering functions for wideband hf channels. *8th International Conference on HF Radio Systems and Techniques*, pages 341–345, July 2000. doi: 10.1049/cp:20000199.

[54] A. G. Ads, P. Bergadà, J. R. Regué, J. L. Pijoan, D. Altadill, D. Badia, and S. Graells. Vertical and oblique soundings variation over long-haul link between antarctica and spain. *Manuscript submitted to Radio Sci.*, 2013.

[55] Use of high frequency ionospheric channel simulators, ccir-520-2. *International Telecommunication Union Std.*, 1992.

[56] W. Ñ. Furman and J. W. Nieto. Understanding hf channel simulator requirements in order to reduce hf modem performance measurement variability. *Nordic HF conference*, 6(1):1–13, 2001.

[57] Testing of hf modems with bandwidth of up to about 12 khz using ionospheric channel simulators. *International Telecommunication Union Std.*, (ITU-R F.1487), 2000.

[58] Radio noise. *Institute for Telecommunication Sciences*, (P.372-10), October 2009.

[59] A. D. Spaulding and R. T. Disney. Man-made radio noise, part 1: estimates for business, residential, and rural areas. *Office of Telecommunications Report*, 1974.

[60] Man-made radio noise. *International Telecommunication Union Std.*, (CCIR-258-3), 1986.

[61] J. J. Lemmon. Wideband model of hf atmospheric radio noise. *Radio Sci.*, 36 (6):1385–1391, 2001. doi: 10.1029/2000RS002364.

[62] J. J. Lemmon. Wideband model of man-made hf noise and interference. *Radio Sci.*, 32(2):525–539, 1997. doi: 10.1029/96RS03204.

[63] A. J. Gibson and L. Arnett. Measurements and statistical modeling of spectrum occupancy. *Sixth International Conference on HF Radio Systems and Techniques*, pages 150–154, July 1994. doi: 10.1049/cp:19940483.

[64] Interoperability and performance standards for data modems. *U.S. Department of Defense Std.*, (MIL-STD-188-110C), 2011.

[65] Interoperability and performance standards for medium and high frequency radio equipment. *U.S. Department of Defense Std.*, (MIL-STD-188-141C), 2011.

[66] NTIA. High frequency radio automatic link establishment (ale) application handbook. *National Telecommunications and Information Administration (NTIA)*, 1998.

[67] Profile for high frequency (hf) radio data communications. *North Atlantic Treaty Organization Std. (NATO)*, (STANAG-5066), 2000.

[68] Interoperability and performance standards for data modems. *U.S. Department of Defense Std.*, (MIL-STD-188-110A), 1991.

[69] Technical standards for non-hopping hf communications waveform. *North Atlantic Treaty Organization Std. (NATO)*, (STANAG-4539), 2005.

[70] Interoperability and performance standards for data modems. *U.S. Department of Defense Std.*, (MIL-STD-188-110B), 2000.

[71] Stanag 4406 edition 2: Military message handling system. *North Atlantic Treaty Organization Std. (NATO)*, (STANAG 4406 Edition 2), 2005.

[72] Stanag 5066 edition 3: The standard for data applications over hf radio. *North Atlantic Treaty Organization Std. (NATO)*, (STANAG 5066 Edition 3), 2008.

[73] Interoperability and performance standards for medium and high frequency radio equipment. *U.S. Department of Defense Std.*, (MIL-STD-188-141A), 1991.

[74] Hf radio automatic link establishment. *U.S. Department of Commerce National Telecommunications and Information Administration*, 58(199), October 1993.

[75] E. E. Johnson. Simulation results for third-generation hf automatic link establishment. *IEEE Military Communications Conference Proceedings*, 2:984–988, October-November 1999. doi: 10.1109/MILCOM.1999.821350.

[76] I. D. Taylor. Multi-station hf network - challenges and solution. *Nordic HF conference*, August 2004.

[77] High frequency (hf) global communications system (hfgcs), . URL http://www.globalsecurity.org/military/systems/aircraft/systems/hfgcs.htm.

[78] Shares home page, shared resources (shares) high frequency, . URL http://www.ncs.gov/shares.

[79] Fema national radio system (fnars) as-is architecture, . URL http://feacinstitute.org/feac_docs/fema-national-radio-system-fnars-as-is-architecture.

[80] H. Bergzen. Integrating automated hf systems in ip based networks. *Nordic HF conference*, August 2001.

[81] W. L. Beamish. Performance of hmtp based email using second and third generation hf data links. August 2001.

[82] L. Soyer. Hf messenger: european trials and research and development efforts. August 2001.

[83] Bushmail services, . URL www.bushmail.co.za.

[84] Globalink, . URL http://www.arinc.com/products/voice_data_comm/iridium.html.

[85] H. S. Sosa, L. P. Alvarez, S. Z. Bello, E. M. Otero, L. Raos, and J. Lopez-Perez. Performance over a real link of a hf software radio modem for interactive digital voice communications. *Ionospheric Radio Systems and Techniques*, pages 207–211, July 2006.

[86] G. Robertson and D. Arcoraci. Secure digital telophony over hf. *Nordic HF conference*, August 2004.

[87] F. Marie, L. B. Y. Erhel, D. Lemur, and M. Oger. Beam-forming techniques operating on hf collocated antennas. *IEE Electronics Letters*, 41(23):1261–1262, November 2005. doi: 10.1049/el:20052670.

[88] Y. M. Erhel, C. Perrine, D. Lemur, and A. Bourdillon. Image transmission through ionospheric channel. *IEE Electronics Letters*, 41(2):80–82, January 2005. doi: 10.1049/el:20056882.

[89] D. Gauld and N. Arthur. Implementation of an integrated hf voice and data network. August 2004.

[90] J. Stott. Digital radio mondiale: key technical features. *Journal on Electronics and Communication engineering*, 14(1):4–14, February 2002. doi: 10.1049/ecej: 20020101.

[91] J. Mitola. The software radio architecture. *IEEE Communications Magazine*, 33(5):26–38, May 1995. doi: 10.1109/35.393001.

[92] M. Cummings and S. Haruyama. Fpga in the software radio. *IEEE Communications Magazine*, 37(2):108–112, Febreuary 1999.

[93] X. Reves, V. Marojevic, R. Ferrus, and A. Gelonch. Fpgas middleware for software defined radio applications. *International Conference on Field Programmable Logic and Applications*, pages 598–601, August 2005. doi: 10.1109/FPL.2005. 1515794.

[94] N. C. Davies. A high performance hf software radio. *International Conference on HF Radio Systems and Techniques*, pages 249–256, July 2000. doi: 10.1049/cp: 20000183.

[95] N. Davies and M. Richards. A radio frequency hf channel simulator employing software radio techniques. *Nordic HF conference*, 2004.

[96] C. Vilella, P. Bergadà, M. Deumal, L. Pijoan, and R. Aquilué. Transceiver architecture and digital down converter design for long distance, low power hf ionospheric links. *Proc. Ionospheric Radio Systems and Techniques*, pages 95–99, July 2006. doi: 10.1049/cp:20060311.

[97] M. J. Bradley. Digital radio mondiale: system and receivers. *International Conference on HF Radio Systems and Techniques*, pages 198–202, June 2003. doi: 10.1049/cp:20030456.

[98] Cuadro nacional de atribucion de frecuencias. *Secretaria de Estado de Telecomunicaciones*, . URL http://www.mityc.es/Telecomunicaciones/Secciones/Espectro/cnaf/.

[99] C. Vilella, D. Badia, J. L. Pijoan, M. Deumal, M. Ribo, and J. R. Regue. On site receiver testing. application to long distance hf links. *Proc. International Symposium on Electromagnetic Compatibility EMC Europe*, September 2006.

[100] C. Vilella, D. Miralles, J. Socoró, L. Pijoan, and R. Aquilué. A new sounding system for hf digital communications from antarctica. *Proc. International symposium on, Antennas and Propagation*, pages 419–422, August 2005.

[101] I. Gutierrez, J.L. Pijoan, and C. Vilella. Caracterizacion del canal ionosfirico en la antartida. *Proc. of Simposium Nacional de la Union Cientifica Internacional de Radio (URSI)*, September 2004.

[102] Ad6620 67 msps digital receive signal processor datasheet. *Analog Devices*, . URL http://www.analog.com.

[103] Ad8369 600 mhz, 45 db digitally controlled variable gain amplifier datasheet. *Analog Devices*, . URL http://www.analog.com.

[104] Ad6622 65 msps, quad transmit signal processor (tsp) datasheet. *Analog Devices*, . URL http://www.analog.com.

[105] Sg-230 smartuner datasheet. *SGC*, . URL http://www.sgcworld.com.

[106] P. Bergadà, M. Deumal, C. Vilella, J. R. Regué, D. Altadill, and S. Marsal. Remote sensing and skywave digital communication from antarctica. *Sensors*, 9: 10136–10157, 2009. doi: 10.3390/s91210136.

[107] M. Angling, P. Cannon, N. Davies, T. Willink, V. Jodalen, and B. Lundborg. Measurements of doppler and multipath spread on oblique high latitude hf paths and their use in characterizing data modem performance. *Radio Sci.*, 33(1):97–107, January 1998. doi: 10.1029/97RS02206.

[108] E. M. Warrington. Observations of the directional characteristics of ionospherically propagated hf radio channel sounding signals over two high latitude paths. *IEE Proceedings, Microwaves, Antennas and Propagation*, 145(5):379–385, October 1998. doi: 10.1049/ip-map:19982068.

[109] M. J. Angling and N. C. Davies. On an ionospheric channel simulator driven by measurements of multipath and doppler spread. *Proc. IEE Colloquium on, Propagation Characteristics and Related System Techniques for Beyond Line-of Sight Radio*, pages 4/1–4/6, October 1997. doi: 10.1049/ic:19971351.

[110] E. M. Warrington and A. J. Stocker. Measurements of the doppler and multipath spread of the hf signals received over a path oriented along the midlatitude trough. *Radio Sci.*, 38(5):1080, 2003. doi: 10.1029/2002RS002815.

[111] H. Houpis and L. Nickisch. An ionospheric propagation prediction method for low latitudes and mid-latitudes. *Radio Sci.*, 26(4):1049–1057, 1991. doi: 10.1029/91RS00491.

[112] J. Fitzgerald, P. Argo, and R. Carlos. Equatorial spread f effects on an hf path: Doppler spread, spatial coherence, and frequency coherence. *Radio Sci.*, 34(1): 167–178, 1999. doi: 10.1029/1998RS900013.

[113] L. E. Vogler and J. A. Hoffmeyer. A model for wideband hf propagation channels. *Radio Sci.*, 28(6):1131–1142, 1993. doi: 10.1029/93RS01607.

[114] K. Davies. *Ionospheric radio*. 1996.

[115] J. D. Parsons. Mobile radio propagation channel. *John Wiley and Sons LTS*, 2000.

[116] P. A. Bello. Characterization of randomly time-variant linear channels. *IEEE Transactions on Communications*, 11(4):360–393, December 1963. doi: 10.1109/TCOM.1963.1088793.

[117] J. G. Proakis. Digital communications. *McGraw-Hill*, 1995.

[118] R. L. Peterson, R. E. Ziemer, and D. E. Borth. Introduction to spread spectrum communications. *Prentice Hall*, 1995.

[119] D. C. Cox. Delay doppler characteristics of multipath propagation at 910 mhz in a suburban mobile radio environment. *IEEE Transactions on Antennas and Propagation*, 20(5):625–635, September 1972. doi: 10.1109/TAP.1972.1140277.

[120] J. V. Rees. Measurements of the wide-band radio channel characteristics for rural, residential, and suburban areas. *IEEE Transactions on Vehicular Technology*, 36(1):2–6, Febreuary 1987. doi: 10.1109/T-VT.1987.24090.

[121] R. B. Blackman, J. Tukey, and J. Wilder. Discrete-time signal processing. *Dover Publications*, pages 98–99, 1959.

[122] A. V. Oppenheim and R. W. Shafer. Discrete-time signal processing. *Prentice Hall*, pages 444–447, 1989.

[123] J. F. Kaiser. Nonrecursive digital filter design using the i_0-sinh window function. *Proc. IEEE International Sump. on, Circuits and Systems*, pages 20–23, April 1974.

[124] J. Goodman, J. Ballard, and E. Sharp. A long-term investigation of the hf communication channel over middle- and high-latitudes paths. *Radio Sci.*, 32 (4):1705–1715, July-August 1997. doi: 10.1029/97RS01194.

[125] R. H. Clarke and D. V. Tibble. Measurement of the elevation angles of arrival of multicomponent h.f. skywaves. *Proc. Institution of Electrical Engineers*, 125 (1):17–24, January 1978. doi: 10.1109/ICCSN.2009.55.

[126] A.J. Stocker, E.M. Warrington, and D.R. Siddle. Observations of doppler and delay spread on hf signals received over polar cap and trough paths at various stages of the solar cycle. *Radio Sci.*, 2013. doi: 10.1002/2013RS005264.

[127] R. André, M. Pinnock, and A. S. Rodger. On the superdarn autocorrelation function observed in the ionospheric cusp. *Geophysical Research Letters*, pages 3353–3356, 1999. doi: 10.1029/1999GL003658.

[128] G. Chen, Z. Zhao, G. Zhu, and S. Shi. The wuhan ionospheric sounding systems. *IEEE letters on: Geoscience and Remote Sensing*, 6(4):748–751, October 2009. doi: 10.1109/LGRS.2009.2024439.

[129] P. S. Cannon, N. C. Davies, M. J. Angling, V. Jodalen, K. W. Moreland, and B. Lundborg. Initial results from damson–a system to measure multi-path, doppler spread and doppler shift on disturbed hf channels. *Ninth International Conference on: Antennas and Propagation*, 2:104–108, October 1995. doi: 10.1049/cp:19950393.

[130] B. Zolesi, G. Fontanaa, L. Perronea, M. Pietrellaa, V. Romanoa, G. Tutonea, A. Belehakib, I. Tsagourib, S. S. Kourisc, F. Vallianatosd, J. P. Makrisd, and M. J. Anglinge. New oblique-incidence ionospheric sounding campaign over europe and its data application. *Journal of Atmospheric and Solar-Terrestrial Physics*, 70(6):854–865, April 2008.

[131] B. W. Reinisch, D. M. Haines, K. Bibl, I. Galkin, X. Huang, D. F. Kitrosser, G. S. Sales, and J. L. Scali. New techniques in ground-based ionospheric sounding and studies. *Radio Sci.*, 21(3):331–341, 1986. doi: 10.1029/RS021i003p00331.

[132] S. V. Fridman. Reconstruction of a three-dimensional ionosphere from backscatter and vertical ionograms measured by over-the-horizon radar. *Radio Sci.*, 33 (4):1159–1171, February 1998. doi: 10.1029/98RS00477.

[133] S. Shi, Z. Zhao, F. Su, and G. Chen. A low-power and small-size hf backscatter radar for ionospheric sensing. *IEEE letters on: Geoscience and Remote Sensing*, 6(3):504–508, 2009. doi: 10.1109/LGRS.2009.2020700.

[134] C. Vilella, D. Miralles, D. Altadill, F. Acosta, J. G. Solé, J. M. Torta, and J. L. Pijoan. Vertical and oblique ionospheric soundings over a very long multihop hf radio link from polar to midlatitudes: Results and relationship. *Radio Sci.*, 44 (2), 2009. doi: 10.1029/2008RS004001.

[135] J. Torta, S. Marsal, J. Riddick, C. Vilella, D. Altadill, E. Blanch, O. Cid, J. Curto, A. De Santis, L. R. Gaya-Piqué, J. Mauricio, J. Pijoan, J. G. Solé, and A. Ugalde. An example of operation for a partly manned antarctic geomagnetic observatory and the development of a radio link for data transmission. *Annals Of Geophysics*, 52(1):45–56, February 2009. doi: 10.4401/ag-4572.

[136] J. W. Wright and M. L. V. Pitteway. Real-time data and interpretation capabilities of the dynasonde. 1. data acquisition and real-time display. *Radio Sci.*, 14(5):815–825, 1979. doi: 10.1029/RS014i005p00815.

[137] B. W. Reinisch and H. Xueqin. Automatic calculation of electron density profiles from digital ionograms 3. processing of bottom side ionograms. *Radio Sci.*, 18 (2):477–492, 1983. doi: 10.1029/RS018i003p00477.

[138] L. McNamara and P. Wilkinson. A cautionary note on the use of f2 layer correlation coefficients for short-term forecasting purposes. *Solar-Terrestrial Predictions: Proceedings of a Workshop at Meudon*, June 1984.

[139] J. Milsom. Towards improving a short-term ionospheric forecasting service. *Solar-Terrestrial Predictions: Proceedings of a Workshop at Meudon*, June 1984.

[140] E. Zuccheretti, G. Tutone, U. Sciacca, C. Bianchi, and B. J. Arokiasamy. The new ais-ingv digital ionosonde. *Annals Of Geophysics*, 46(4):647–659, 2003. doi: 10.4401/ag-4377.

[141] W. B. Reinisch, I. A. Galkin, G. M. Khmyrov, A.V. Alexander, I. A. Lisysyan, K. Bibl, G. Cheney, D. Kitrosser, S. Stelmash, K. Roche, Y. Luo, V. V.

Paznukhov, and R. Hamel. Advancing digisonde technology: the dps-4d. *Proc. of AIP Conference*, 974(1):127–143, 2008. doi: 10.1063/1.2885022.

[142] ITU-R. Method for the prediction of the performance of hf circuits. *Recomm. P.533-11*, February 2012.

[143] E. M. Warrington, A. Bourdillon, E. Benito, C. Bianchi, J-P. Monilié, M. Muriuki, M. Pietrella, H. Rothkaehl, V. Rannou, S. Saillant, O. Sari, A. J. J. Stocker, E. Tulunay, Y. Tulunay, and N. Y. Zaalov. Aspects of hf radio propagation. *Annals of Geophysics*, 52(3-4):301–321, 2009. doi: 10.4401/ag-4577.

[144] S. S. Kouris, P. A. Bradley, and P. Dominici. Solar cycle variation of the inter-day fof2 and m(3000)f2. *Ann. Geophys.*, 16:1039–1042, 1998.

[145] S. S. Kouris and D. N. Fotiadis. Ionospheric variability: a comparative statistical study. *Adv. Space Res.*, 29(6):977–985, 2002. doi: 10.1016/S0273-1177(02)00045-5.

[146] N. K. Sethi, M. K. Goel, and K. K. Mahajan. Solar cycle variations of fof2 from igy to 1990. *Ann. Geophys.*, 20(10):1677–1685, 2002. doi: 10.5194/angeo-20-1677-2002.

[147] J. Y. Liu, W. Wan, and B. Ning. Statistical modeling of ionospheric fof2 over wuhan. *Radio Sci.*, 39(2), 2004. doi: 10.1029/2003RS003005.

[148] J. Y. Liu, Y. I. Chen, and J. S. Lin. Statistical investigation of the saturation effect in the ionospheric fof2 versus sunspot, solar radio noise, and solar euv radiation. *J. Geophys. Res.*, 108(A2):1067, 2003. doi: 10.1029/2001JA007543.

[149] S. S. Kouris, T. Xenos, K. Polimeris, and D. Stergiou. Tec and fof2 variations: preliminary results. *Ann. Geophys.*, 47(4):1325–1332, 2004. doi: 10.4401/ag-3346.

[150] E. Sardon, G. Soler, L. F. Alberca, B. Morena, and A. Rius. Comparison of tec obtained using gps data and from a model based on ionosonde data. *Instituto de Astronomia y Geodesia*, (185):8–12, 1993.

[151] N. Jakowski, S. M. Stankov, V. Wilken, C. Borries, D. Altadill, J. Chum, D. Buresova, J. Boska, P. Sauli, F. Hruska, and Lj. R. Cander. Ionospheric behavior over europe during the solar eclipse of 3 october 2005. *Journal of Atmospheric and Solar-Terrestrial Physics*, 70:836–853, 2008. doi: 10.1016/j.jastp.2007.02.016.

[152] L. Triskova and J. Chum. Hysteresis in dependence of fof2 on solar indices. *Adv. Space Res.*, 18(6):145–148, 1996.